Electromagnetic Modelling and Signal Processing Algorithms for a Microwave-Tomography-Based Medical Device Prototype to Monitor Osteoporosis

A dissertation presented by:

Bilal Amin, M.Sc., B.Eng.

to:

Electrical and Electronic Engineering,

School of Engineering,

College of Science and Engineering,

National University of Ireland Galway.

in fulfilment of the requirements for the degree of

Doctor of Philosophy.

Supervised by:

Prof. Martin O'Halloran, Dr. Adnan Elahi and Dr. Atif Shahzad

July 27, 2021

Contents

Contents i
Declaration of Originality vi
Abstract vii
Acknowledgements ix
List of Figures xi
List of Tables xv
Acronyms xvii
1 Introduction 1
1.1 Motivation 3
1.2 Thesis Contributions 7
1.2.1 Journal Publications 9
1.2.2 Conference Publications 10
1.3 Thesis Structure 11
1.4 References 12
2 Literature Review 17
2.1 Introduction 17
2.2 Bone Anatomy and Physiology 18
2.3 Osteoporosis 20
2.4 Bone Imaging Modalities/Diagnostic Methods 22
2.4.1 Single-Photon Absorptiometry 23
2.4.2 Dual-Photon Absorptiometry 23
2.4.3 Quantitative Ultrasound 23
2.4.4 Radiographs and Magnetic Resonance Imaging 24
2.4.5 Dual Energy X-ray Absorptiometry 24
2.4.6 Quantitative Computed Tomography 25
2.5 Dielectric Properties of Bone 25
2.5.1 Dielectric Properties of Bone in Low-Frequency Range 27
2.5.1.1 Dielectric Properties of Animal Bone Tissue in Low-Frequency Range .. 29
2.5.1.2 Dielectric Properties of Human Bone Tissue in Low-Frequency Range .. 33
2.5.1.3 Comparative Analysis of Dielectric Properties of Bones in Low-Frequency Range 37

2.5.1.3.1 Variations in Dielectric Properties of Cortical Bone ……... 37
2.5.1.3.2 Variations in Dielectric Properties of Trabecular Bone …….. 40
2.5.1.4 Relationship between Bone Dielectric Properties and Bone Mineral Density … 42
2.5.2 Dielectric Properties of Bone in Microwave Frequency Range …….. 43
2.5.2.1 Dielectric Properties of Animal Bone Tissue in Microwave Frequency Range ……... 45
2.5.2.2 Dielectric Properties of Human Bone Tissue in Microwave Frequency Range ……... 51
2.5.2.3 Comparative Analysis of Dielectric Properties of Bones in Microwave Frequency Range …….. 55
2.5.2.3.1 Variations in Dielectric Properties of Cortical Bone ……... 55
2.5.2.3.2 Variations in Dielectric Properties of Trabecular Bone …….. 55
2.5.2.4 Relationship between Bone Dielectric Properties and Bone Mineral Density 58
2.5.2.5 Relationship between Bone Dielectric Properties and Bone Volume Fraction …… 59
2.6 Microwave Imaging …… 61
2.7 Microwave Tomography Imaging ……... 63
2.8 Experimental Prototypes ……. 66
2.9 Conclusion ……... 69
2.10 References ……. 70
3 Dielectric Characterisation of Diseased Human Trabecular Bones at Microwave Frequency 84
3.1 Introduction ……. 86
3.2 Methodology ……... 89
3.2.1 Experimental Design …….. 89
3.2.2 CT Scanning ……... 89
3.2.3 Dielectric Measurements …… 90
3.2.4 Measurement Protocol & System Uncertainty Analysis ……. 90
3.3 Results and Discussion …… 92
3.3.1 Trabecular Microarchitecture of Bone Samples …….. 92
3.3.2 Dielectric Properties of Trabecular Bone Samples ……. 94
3.3.2.1 Intra-patient Variation of Dielectric Properties ……. 94
3.3.2.2 Dielectric properties of Osteoporotic and Osteoarthritis Patient's Bones . 95

3.3.2.3 Comparison of Dielectric Properties with Literature ……..…….. 97
3.3.3 Relationship between dielectric properties and BV/TV of trabecular bone samples 98
3.3.4 Effect of PBS on Bone Samples ……..…….. 100
3.4 Conclusion ……. 100
3.5 References ……. 101

4 A Feasibility Study on Microwave Imaging of Bone for Osteoporosis Monitoring …….. 108
4.1 Introduction ……... 109
4.2 Methods ……. 112
4.2.1 Dielectric properties contrast of tissues present in the heel ……... 112
4.2.2 On the choice of frequency range and the matching medium ……... 113
4.2.2.1 Planar layered model …….. 114
4.2.2.2 Cylindrical layered model ……... 116
4.3 Results and Discussion …….. 118
4.3.1 Dielectric properties contrast of tissues present in the heel ……...…… 118
4.3.2 On the Choice of Frequency Range and the Matching Medium ……..……. 120
4.3.2.1 Planar Layered Model ……..……... 120
4.3.2.2 Cylindrical Layered Model ……..……... 122
4.3.2.3 E-field Distribution in Numerical Bone Models …… 124
4.4 Conclusion ……. 126
4.5 References ……. 127
5 Microwave Bone Imaging: A Preliminary Investigation on Numerical Bone Phantoms for Bone Health Monitoring …… 131
5.1 Introduction ……... 133
5.2 Mathematical Formulation …… 137
5.2.1 DBIM Formulation ……... 137
5.2.2 IMATCS Algorithm ……. 139
5.2.3 Parameter Selection of IMATCS Algorithm …… 141
5.2.4 Numerical Bone Phantoms ……... 142
5.3 Results and Discussion …….. 144
5.3.1 Simulation Testbed ……... 144
5.3.2 Performance Metrics …… 145

5.3.3 Choice of Number of IMATCS iterations, Number of DBIM iterations, and Threshold (A_0) …….. 147
5.3.4 Reconstruction of Numerical Bone Phantom 1 (P1) ……. 149
5.3.5 Reconstruction of Numerical Bone Phantom 2, 3, and 4 (P2, P3, P4) …….. 150
5.3.6 Reconstruction of Numerical Bone Phantom 5, 6, and 7 (P5, P6, P7) ……. 152
5.3.7 Robustness of L_2-IMATCS for Reconstruction of Bone Phantoms P1, P2, P3, P4, P5, P6, and P7 …… 154
5.3.8 Relative Error between Reference and Reconstructed Numerical Bone Phantoms 156
5.3.9 Impact of Signal-to-Noise Ratio (SNR) on Reconstructed Numerical Bone Phantoms ……... 157
5.4 Conclusion ……. 158
5.5 References ……. 159
6 Anthropomorphic Calcaneus Phantom for Microwave Bone Imaging Applications …….. 165
6.1 Introduction ……... 166
6.2 Methodology ……. 170
6.2.1 3-D Printed Structures …….. 170
6.2.2 Liquid Tissue Mimicking Mixtures Preparation …….. 170
6.2.3 Solid Tissue Mimicking Mixtures Preparation ……. 171
6.2.4 Dielectric Properties Measurement …….. 172
6.3 Results and Discussion …….. 173
6.3.1 3-D Printed Structures …….. 173
6.3.2 Liquid Tissue Mimicking Mixtures ……. 174
6.3.3 Solid Tissue Mimicking Mixtures …… 177
6.4 Conclusion ……. 180
6.5 References ……. 181
7 Experimental Validation of Microwave Imaging Prototype and DBIM-IMATCS Algorithm for Bone Health Monitoring …….. 185
7.1 Introduction ……... 187
7.2 Methodology ……. 191
7.2.1 Preparation of Calcaneus Bone Phantom and Liquid TMMs …… 191
7.2.2 Dielectric Properties Measurement …….. 193
7.2.3 Microwave Scanning of the Phantoms …….. 194
7.2.4 Image Reconstruction using DBIM Formulation and IMATCS Algorithm ….. 195

7.2.5 FDTD Modelling and Calibration of Measured Data 196
7.2.6 Evaluation of Reconstructed Images 197
7.2.6.1 Normalized Root Mean Square Error 197
7.2.6.2 Structural Similarity Index 197
7.2.6.3 Histogram-based Analysis 198
7.3 Results and Discussion 198
7.3.1 Dielectric Properties of Liquid TMMs 198
7.3.2 Reconstruction of Experimental Bone Phantoms P1, P2, and P3 199
7.3.3 Quantitative Evaluation of Reconstructed Profiles 203
7.3.4 Classification of Normal and Diseased Bones Based on Reconstructed Complex Permittivity Profiles 205
7.4 Conclusion 206
7.5 References 207
8 Conclusions and Future Work 213
8.1 Summary of Main Conclusions 213
8.2 Future Work 217
8.3 References 219

Declaration of Originality

I, the Candidate **Bilal Amin**, certify that this thesis entitled "**Electromagnetic Modelling and Signal Processing Algorithms for a Microwave-Tomography-Based Medical Device Prototype to Monitor Osteoporosis**":

- is all my own work;
- has not been previously submitted for any degree or qualification at this University or any other institution;
- and where any work in this thesis was conducted in collaboration, appropriate reference to published work by my collaborators has been made and the nature and extent of my contribution has been clearly stated.

Name:

Bilal Amin

Abstract

Osteoporosis, characterised as low bone mass, causes continuous systematic deterioration of the trabecular bone structure and leads to bone fragility and fractures. Current clinical practices widely employ dual-energy X-ray absorptiometry (DXA) to measure bone mineral density (BMD), which is considered to be the key clinical indicator of osteoporosis. However, DXA is not a portable device, moreover, due to the cumulative effect of repeated X-ray doses used for monitoring osteoporosis over time, the DXA scan may pose long-term health risks. Therefore, there is a need for a portable and non-ionising imaging modality for osteoporosis monitoring. Studies have reported that demineralisation of bones may also result in the change of dielectric properties of bones. Therefore, dielectric properties measurement technology may be employed for monitoring osteoporosis. Microwave imaging (MWI) can measure dielectric properties and exploit dielectric contrast between healthy and diseased tissues for diagnosis or disease monitoring. However, no previous study has reported dielectric contrast between healthy and diseased bones. While several studies have characterised the dielectric properties of both animal and human bones, no data on the dielectric properties of human diseased bones is available. Moreover, despite significant research on bone dielectric properties, no definite relationship between BMD and bone dielectric properties could be derived from the current literature. Regardless, two previous studies attempted to utilise bone dielectric properties and demonstrate proof-of-concept of MWI to monitor osteoporosis. However, no prototype MWI device for osteoporosis monitoring has been previously reported. Neither bone phantoms nor MWI algorithms have been specifically developed for osteoporosis monitoring.

The literature review suggested that variations exist in the dielectric properties of bone reported across different studies. The relationship between bone dielectric properties and different mineralisation levels was found to be inconsistent. Further, it was found that none of the studies have investigated and compared the dielectric properties of healthy and diseased human bones. To this end, this thesis has made the first attempt to characterise the dielectric properties of diseased (osteoporotic bones) and healthy (osteoarthritis bones) human trabecular bones. The availability of healthy human trabecular bones for *ex vivo* dielectric characterisation is scarce, therefore, this thesis has used osteoarthritis bones as a surrogate to healthy bone samples because osteoarthritis patients have compact and dense trabecular bone microarchitecture compared to osteoporotic patients. The findings of this study showed that there exists a significant dielectric contrast between osteoporotic and osteoarthritis bones. The difference in dielectric properties of osteoporotic and osteoarthritis bones can be exploited

using MWI to monitor osteoporosis. The development of the MWI system requires knowledge of a feasible frequency band, determining the dielectric contrast of tissues present in the human heel, and electric field (E-field) penetration in trabecular bone. The parameters (feasible frequency band, matching medium, and numerical modelling of bone) found in this study were used during the development of an MWI prototype for monitoring osteoporosis. To assess and determine the spatial distribution of dielectric properties of the numerical and experimental bone phantoms, a microwave tomography (MWT)-based imaging algorithm was developed. Firstly, the MWT algorithm was used to reconstruct the dielectric properties of diverse numerical bone phantoms under different noise levels. The numerical bone phantoms were developed based on the dielectric properties of osteoporotic and osteoarthritis bones reported in this thesis. The simulation results showed that osteoporotic and osteoarthritis bones can be differentiated based on the reconstructed dielectric properties even for low values of the signal-to-noise ratio (SNR). To evaluate the robustness of the adopted MWT approach for the reconstruction of dielectric properties under practical imaging scenarios, a simplified two-layered calcaneus bone phantom was developed along with a corresponding MWI prototype. The reconstruction of dielectric properties of bone phantoms has shown that the developed MWT algorithm provides a robust reconstruction of diverse bone phantoms with acceptable accuracy. Moreover, the osteoporotic and osteoarthritis bone phantoms were distinguished based on reconstructed dielectric properties. The findings have shown that this two-layered 3-D printed human calcaneus bone phantom and the imaging prototype can be used as a valuable test platform for pre-clinical assessment of calcaneus bone imaging for bone health monitoring.

Acknowledgements

I sincerely thank to all those whose help, support, and guidance over the years has been instrumental in the completion of this dissertation. With profound sense of gratitude I express my sincere thanks to my supervisors, Prof. Martin O'Halloran, Dr. Muhammad Adnan Elahi, and Dr. Atif Shahzad for their constant guidance, inspiration, valuable advice, education, and support during the course of research work. I would cordially thank Prof. Martin for allowing me to work in his Lab. and generously providing needed resources for my doctoral project. Particularly, I wish to express my special appreciation to Dr. Adnan and Dr. Atif for their patience, motivation, forbearance and the tremendous knowledge, of both research work and the write-up, which they have imparted to me during this project. This work would not have been possible without their guidance and persistent help. Their continued mentoring and invaluable advice, on both research and career-building, over the years has inculcated in me the essential skills needed for research pursuits. I convey my thanks to the graduate research committee members, Prof. Peter Corcoran, Dr. Maeve Duffy, and Dr. Barry Hayes for their guidance and encouragement during this project.

I cordially acknowledge and express my sincere thanks Dr. Lorenzo Crocco for organising a fruitful visit to IREA-CNR, Institute for Electromagnetic Sensing of the Environment, National Research Council of Italy, Naples, Italy which remained pivotal in the completion of this work. I would also like to thank Dr. Emily Porter, Dr. Adam Santorelli, Dr. Laura Farina, Dr. Declan O'Loughlin, and Dr. Bárbara L Oliveira for sharing their valuable knowledge and expertise on dielectric characterisation, phantoms, hardware, software, and research in general. I am also indebted to friends and colleagues in the TMDLab Marggie, Saqib, Alessandra, Barry, Eoghan, Anna B, Jiss, Ana G, Hamza, Niko, Nadia, Nuno, Farooq, Talha, and Haroon for their support, encouragement, and making my working hours more pleasant during my PhD.

From my heart and soul, I am immensely grateful to my loving mother Sajida who incessantly prayed and waited for the completion of this PhD journey, my supporting and admiring father Dr. Amin whose invaluable support and guidance gave me the strength to persistently endeavour during my academic career. I am extremely thankful to my loving and amicable sisters Madiha and Areesha who continuously missed me as I missed them during my stay in Ireland. The love, support, prayers, and guidance from my family throughout these 4 years and my life immensely contributed towards accomplishment of my doctoral program. Indeed, I would like to dedicate my PhD to my parents, siblings, and my country Pakistan. I would thank Dr. Syed Junaid Nawaz, who inspired me to contribute to humanity through

scientific knowledge and inspired in me the passion for research during my Master's program back in COMSATS, Islamabad, Pakistan.

I also thankfully acknowledge the European Research Council (ERC) for providing funding for this research project. I also express my gratitude to European COST Action TD1301, MiMed for providing grants to establish strong international collaborations through Short-term Scientific Missions.

Last but not the least, I would also thank the people of Ireland, more specifically Galway for being so kind, compassionate, and supportive. Being an international student from Pakistan, I always found Galway as my second home. The Irish people, their culture, and their hospitality were fabulous and unmatchable. The people of Ireland have imparted many good societal responsibilities in me that will surely shape me to become a productive and useful citizen of my country Pakistan.

List of Figures

2.1 Anatomical structure of bone [7] 20
2.2 Comparison of osteoporotic and non-osteoporotic bone [11] 22
2.3 Comparison of relative permittivity for human bone, apatite, and collagen [65] 34
2.4 Comparison of dielectric properties of cortical bone from reported studies. The graph shows a comparison between the dielectric properties of bones sourced from different species (human, bovine, porcine, and rat). The dielectric properties reported for Unal *et al.* are for the wet bone samples. HCB = Human Cortical Bone; BCB = Bovine Cortical Bone; PCB = Porcine Cortical Bone; RCB = Rat Cortical Bone 39
2.5 Comparison of dielectric properties of trabecular bone from reported studies. The reported studies exhibit variation in results and the dielectric properties of trabecular bones of human, bovine, porcine, and rat all vary from each other 41
2.6 Permittivity for normal and demineralised bone samples [47] 46
2.7 Permittivity and Conductivity for porcine cortical bone sample [42]. The dielectric properties of trabecular bone samples are higher than cortical bone samples 47
2.8 Permittivity and conductivity of ageing porcine tissues at selected frequencies [49]. The dielectric properties reduce as age increases 48
2.9 Reconstructed permittivity images (left) of the (a) 1st, (b) 2nd, and (c) 5th microwave scan of a saline-saturated bone specimen in a test tube at 1100 MHz, respectively. The images on the right are the corresponding conductivity images (from [23]). The dielectric properties are increasing as the mineralisation level of bones is decreasing after each microwave scan 50
2.10 Relationship between the relative permittivity (top) and conductivity (bottom) with bone mineral density [23]. The negative correlation between dielectric properties and BMD . 51
2.11 1300 MHz relative permittivity (top) and conductivity (bottom) soft-prior images for the first plane of the left and right heels of patient 1, respectively, (b) 1300 MHz permittivity (top) and conductivity (bottom) soft-prior images for the first plane of the left and right heels of patient 2, respectively (from [18]). Affected heel bone has higher dielectric properties compared to the normal heel bone. For Fig. 7, IEEE LICENSE received. License Number 4294280048384 52
2.12 Mean value of relative permittivity and conductivity [46] 54
2.13 Comparison of relative permittivity and conductivity from reported studies. The reported

studies exhibit variation in results; dielectric properties of trabecular bones are higher as compare to dielectric properties of cortical bones …… 57
2.14 Relationship between relative permittivity and conductivity against BVF [23],[46]. The black curves indicate the dielectric properties of humans and red curves indicate the same for porcine trabecular bones …… 60
2.15 The experimental prototype used by Meaney *et al.* in [18] for human bone imaging …. 67
2.16 The experimental prototype used by Gilmore *et al*. [107] for human forearm imaging .. 68
3.1 Photograph of the experimental setup …….. 92
3.2 Photograph of the bone sample. The arrows show the measurement points. Approximately similar locations were selected as measurement points on the other side of the sample . 92
3.3 Intra-patient variation of BV/TV for Osteoporotic Patients …… 93
3.4 Comparison of BV/TV between Osteoporotic and Osteoarthritis bone samples ……. 93
3.5 Intra-patient variation of (a) Relative Permittivity (b) Conductivity in 2 Osteoporotic Patients …… 94
3.6 Comparison of Osteoporotic and Osteoarthritis bone samples in terms of (a) Relative Permittivity (b) Conductivity ……... 95
3.7 Comparison of Osteoporotic and Osteoarthritis bone samples in terms of (a) Relative Permittivity (b) Conductivity at 0.5 GHz, 0.9 GHz, 2.42 GHz, 4.02 GHz, 6.02 GHz and 8.5 GHz. The red markers in plots represent the outliers in data ……. 96
3.8 Comparative analysis of trabecular bone dielectric properties with current study and literature (a) Relative Permittivity (b) Conductivity …… 98
3.9 Scatter plot between BV/TV and (a) Relative Permittivity (b) Conductivity at 900 MHz 99
4.1 (a) Anatomical structure of human heel (© 2014 WebMD, LLC. All rights reserved) (b) Anatomical structure of bone …… 113
4.2 The 1-D planar layered model of the human heel, which is composed of five layers: skin, fat, muscle, cortical bone, and trabecular bone. E_{inc} is the probing wave ……... 115
4.3 The transmission line model of 1-D heel structure. The $Z_{mm}, Z_{HH'}, Z_s, Z_f, Z_m, Z_{CB}$, and Z_{TB} represent impedance of matching medium, plane HH', skin, fat, muscle, cortical bone, and trabecular bone respectively …… 115
4.4 A five-layered human heel model …….. 116
4.5 Dielectric properties of considered tissues in human heel: (a) Relative Permittivity; (b) Conductivity. The values are taken from Gabriel *et al*. [15] ……... 119

4.6 The transmission coefficient as a function of frequency and relative permittivity of the matching medium …….. 120
4.7 Skin depth of considered tissues in the human heel. The values are taken from Gabriel *et al*. [14] ……... 122
4.8 Port signals for feasible and inconvenience frequency band …… 123
4.9 Power loss in dielectrics for five-layered medium ……. 124
4.10 Average E-field distribution at 1.3 GHz; (a) for Osteoporotic Bone (b) for Osteoarthritis Bone (c) for Gabriel *et al*. [15]'s Trabecular Bone ……. 125
5.1 Microwave imaging scenario. Γ denotes the contour with all EM sources, *V* denotes the overall imaging region, and Ω denotes the target to be imaged …….. 138
5.2 Simulation testbed ……. 145
5.3 Relationship between NRMSE and (a) number of IMATCS iterations, (b) number of DBIM iterations, and (c) value of threshold (A_0) ……... 149
5.4 Real and imaginary parts of complex permittivity of (a) and (b) reference P1, (c) and (d) reconstructed P1 at 1 GHz …….. 150
5.5 Real and imaginary parts of complex permittivity of (a) and (b) reference P2, (c) and (d) reconstructed P2 at 1 GHz …….. 152
5.6 Real and imaginary parts of complex permittivity of (a) and (b) reference P5, (c) and (d) reconstructed P5 at 1 GHz …….. 153
5.7 (a) Peak values of the real part of complex permittivity of reconstructed and reference bone phantoms (b) Peak values of the imaginary part of complex permittivity of reconstructed and reference bone phantoms at 1 GHz …… 155
5.8 Relative error maps for (a) Real part of complex permittivity (b) Imaginary part of complex permittivity for bone phantom P1 at 1 GHz ……. 156
5.9 Relative percentage error between peak values of reference and reconstructed real and imaginary parts of complex permittivity at 1 GHz for all bone phantoms ……. 157
6.1 Human calcaneus bone ……... 170
6.2 3-D printed two-layered cylindrical bone phantom (a) Top View (b) Side View and anatomically accurate human calcaneus structure (c) Interior View (d) Exterior View .. 174
6.3 Dielectric properties of liquid tissue-mimicking mixtures over 0.5 – 8.5 GHz frequency band: (a) Relative Permittivity (b) Conductivity. The measured dielectric data of TMMs (solid lines) are compared with reference data (dotted lines) from Gabriel *et al*. [27] .. 176

6.4 Dielectric properties of solid tissue-mimicking mixtures over 0.5 – 8.5 GHz frequency band: (a) Relative Permittivity (b) Conductivity. The measured dielectric data of TMMs (solid lines) are compared with reference data (dotted lines) from Gabriel *et al*. [27] .. 178
6.5 Cylindrical shaped calcaneus bone phantom (a) Side view (b) Top View …….. 179
6.6 Anatomically realistic calcaneus phantom (a) Interior view (b) Exterior View …….. 180
6.7 Anatomically realistic calcaneus bone phantom (a) Exterior View (b) Interior view …. 180
7.1 3-D printed cylindrical calcaneus bone structure (a) Top View (b) Side View ……..... 191
7.2 Realization of a 3-D MWI system prototype. A VNA is connected to a switching matrix. The switching matrix is connected to the cylindrical imaging prototype through cables.195
7.3 Dielectric properties of liquid TMMs over 1.5 – 4.5 GHz frequency band: (a) Relative Permittivity (b) Conductivity. The measured dielectric data of TMMs (solid lines) are compared with reference data (dotted lines) from Gabriel *et al*. [45] and Amin *et al*. [10] 199
7.4 Real and imaginary parts of complex permittivity of (a) and (b) reference bone phantom P1, (c) and (d) reconstructed bone phantom P1 at 3 GHz …… 201
7.5 Real and imaginary parts of complex permittivity of (a) and (b) reference bone phantom P2, (c) and (d) reconstructed bone phantom P2 at 3 GHz ……... 202
7.6 Real and imaginary parts of complex permittivity of (a) and (b) reference bone phantom P3, (c) and (d) reconstructed bone phantom P3 at 3 GHz ……... 203
7.7 Distribution of reconstructed real part of complex permittivity of (a) bone phantom P1 (b) bone phantom P2 (c) bone phantom P3 at 3 GHz ……... 205
7.8 (a) Peak values of the real part of complex permittivity of reconstructed and reference bone phantoms (b) Peak values of the imaginary part of complex permittivity of reconstructed and reference bone phantoms at 3 GHz …… 205
7.9 Distribution of reconstructed real part of complex permittivity of (a) bone phantom P1 (b) bone phantom P2 (c) bone phantom P3 at 3 GHz ……... 206

List of Tables

2.1 Comparative description of reported studies ……..… 28
2.2 Permittivity and conductivity values of rat bones at 37° C ……..…. 30
2.3 Permittivity values of bovine cortical bones …….…... 30
2.4 Permittivity values of the bovine femur at proximal, distal epiphysis, and diaphysis of bovine cortical bones …….…... 31
2.5 Permittivity and conductivity values of bovine cortical bone in three principal directions 32
2.6 Relative permittivity and conductivity values of trabecular and cortical bone samples in three orthogonal directions at 10 kHz …….. 36
2.7 Comparative description of reported studies ……..…….. 44
2.8 Measurements on cortical and trabecular bone discs [48] …… 49
2.9 Dielectric Properties against BMD values of two patients [18] ……... 53
3.1 Percent uncertainty in accuracy and repeatability of measurements ……. 91
3.2 Mean percentage difference between osteoporotic and osteoarthritis bone samples …... 97
4.1 Dielectric properties and thickness of considered tissues of the human heel. The dielectric properties are reported at 1.3 GHz. The values are taken from Gabriel *et al*. [15] ……... 117
4.2 Dielectric Properties of osteoporotic and osteoarthritis human trabecular bone samples at 1.3 GHz …….. 117
5.1 Numerical bone phantoms for simulations …….. 142
5.2 Single-pole Debye parameters of bone tissues. The values of ε_r and σ are given for 1 GHz 143
5.3 NRMSE between original and reconstructed bone phantoms …… 146
5.4 SSIM between original and reconstructed bone phantoms ……. 147
5.5 NRMSE between original and reconstructed bone phantoms for the real part of complex permittivity …… 158
5.6 NRMSE between original and reconstructed bone phantoms for the imaginary part of complex permittivity ……. 158
6.1 Percent uncertainty in accuracy and repeatability of measurements …….. 173
6.2 Composition of liquid TMMs …… 175
6.3 Average percentage difference between TMM and reference tissue dielectric data ….. 176
6.4 Composition of solid TMMS ……. 177

6.5 Average percentage difference between TMM and reference tissue dielectric data ….. 179
7.1 Composition of liquid TMMs …… 192
7.2 Experimental bone phantoms …… 192
7.3 The relative permittivity and conductivity for liquid TMMs at 3 GHz …….. 193
7.4 Percent uncertainty in accuracy and repeatability of measurements …….. 194
7.5 NRMSE and SSIM between original and reconstructed bone phantoms …… 204

Acronyms

2-D	two-dimensional
3-D	three-dimensional
aBMD	areal BMD
BMD	bone mineral density
BVF	bone volume fraction
CS	compressed sensing
CSI	contrast source inversion
CG	conjugate gradient
DBIM	distorted Born iterative method
DXA	Dual-energy X-ray absorptiometry
DPA	dual-photon absorptiometry
EM	electromagnetic
E-field	electric field
FBTS	forward-backward time-stepping
FEM	finite-element method
IMATCS	iterative method with adaptive thresholding for compressed sensing
MWI	microwave imaging
MWT	microwave tomography
MRI	magnetic resonance imaging
NRMSE	normalised root mean square error
OECL	open-ended coaxial probes
PLA	polylactic acid
QUS	quantitative ultrasound
QCT	quantitative computed tomography
SD	standard deviation
SPA	single-photon absorptiometry
SNR	Signal-to-Noise Ratio
SAR	specific absorption rate
TL	transmission line
TMDLab	Translational Medical Device Lab.
TMMs	tissue-mimicking mixtures

UWB	ultra-wideband
vBMD	volumetric BMD
WHO	World Health Organization

Chapter 1

Introduction

Osteoporosis, characterised as low bone mass, causes continuous systematic deterioration of the trabecular bone and hence leads to bone fragility and fractures [1]. Osteoporotic fractures are a significant cause of morbidity and mortality, particularly in developed countries. Osteoporosis causes more than 8.9 million fractures annually worldwide, resulting in an osteoporotic fracture every 3 seconds [2]. Approximately 50% of women and 20% of men over the age of 50 years will suffer from osteoporosis-related bone fracture [3].

According to the Irish osteoporosis society guidelines published in 2012, approximately 300,000 Irish people aged above 50 years suffer from osteoporosis. If the same trends continue then the expected cost for the treatment of osteoporosis will rise to €1,587- €2,043 million per annum by 2030 in Ireland [4]. Moreover, about 20% of the people aged above 60 years die within six to twelve months, and about 50% lose their independence due to hip fractures caused by osteoporosis in Ireland. Despite this, only 15% of the people in Ireland are diagnosed with bone loss, leaving 280,000 undiagnosed with the potential to lose their independence due to osteoporotic fractures [4]. The report further states that in the EU a hip fracture is reported every 30 seconds approximately, with about 1700 fractures reported per day. In the US, osteoporosis is considered the most commonly-encountered bone disease [5]. Almost 50% of American women and 25% of men over 50 years of age have an osteoporosis-related bone fracture, and around 43.6 million suffer from osteopenia, a precursor to osteoporosis [6]. Approximately two million osteoporotic fractures are reported annually resulting in 432,000 hospital admissions in the US [7].

The majority of the fractures occur in the hip, with other sites including the spine and wrist [6]. A hip fracture is a very common and serious outcome of osteoporosis, having a mortality rate of 14 – 36% during the first year after fracture. Economically, hip fractures account for 72% of fracture costs [3] and 24% of the fracture-related mortality rate [6]. By 2050 the incidence of hip fracture will increase by 310% for men and 240% for women worldwide compared to rates in 1990. The disease substantially affects the life of the people, and thus burdens the national health cost worldwide. Due

to an ageing population, the cost spent on osteoporosis by 2025 will be around $25.3 billion [8].

Osteoporosis is mainly caused due to the demineralisation of bones [3]. The World Health Organization (WHO) has defined bone mineral density (BMD, g/cm^2) as the key indicator for diagnosing osteoporosis [9]. Dual-energy X-ray absorptiometry (DXA) is used as a standard clinical modality for measuring BMD worldwide [1]. DXA calculates the BMD of central bone sites (hip, lumbar spine) and also peripheral sites (heel and distal forearm) [7]. DXA offers an insight into BMD but does not provide information on the structure and biology of the trabecular bone pattern, which are also considered key indicators for diagnosing osteoporosis; hence, using BMD solely for clinical care of overall fracture risk has limitations [10]. Moreover, the DXA scan uses standard X-ray doses up to 0.86 mrem, therefore frequent DXA scans are associated with long-term health risks [11]. Alternative technologies include quantitative ultrasound (QUS) and quantitative computed tomography (QCT). In QUS, the speed of sound and broadband attenuation in the patient's bone is observed, to estimate bone mass. The QUS technique was developed for bone imaging due to low health risks since the technique is non-invasive and does not use ionising radiation. However, this technique has not been well adopted by the clinicians because QUS is unable to penetrate through the bone, and hence the bone mass is measured only by considering the outer bone surface [6]. The QCT measures volumetric BMD (vBMD, g/cm^3) and measures BMD of trabecular bones separately from cortical bone, and is therefore less prone to soft tissue errors [12]. However, QCT is rarely used in clinical practice settings due to the high intensity doses of X-ray required, expensive equipment, poor availability, and the high cost of the test [12].

Recent studies have suggested a significant dielectric contrast between the dielectric properties (relative permittivity (ε_r) and conductivity (σ (S/m))) of healthy and diseased human bones [11],[13]–[17]. Therefore, the dielectric properties may be used to diagnose osteoporosis. Dielectric properties are also important parameters in the development of novel electromagnetic (EM) diagnostic and therapeutic medical devices for various other diseases [18], such as time-domain microwave radar for breast health monitoring [19], microwave ablation for treating liver, lung, kidney, bone and adrenal tumours [20], and microwave hyperthermia for breast cancer treatment [21]. The dielectric contrast between the healthy and diseased human bones

can be potentially exploited to develop a microwave tomography (MWT) based imaging device for monitoring of osteoporosis. MWT has been previously used to measure *in vivo* dielectric properties of the breast, and it has been recently proposed to measure the dielectric properties of the calcaneus bone for monitoring of osteoporosis [11],[17],[22],[23]. Encouraging results from the operational microwave imaging (MWI) systems and early-stage clinical studies for breast cancer detection have motivated researchers towards microwave bone imaging for monitoring of osteoporosis. However, the development of a MWI system needs initial investigation before *in vivo* monitoring of bone health. This new stage of development motivates the work in this thesis, and the specific challenges addressed are discussed in detail in the following section.

1.1 Motivation

The limitations of DXA in terms of sensitivity, lack of information about the structure and biology of the trabecular bone, ionising radiations, high cost, and non-portable equipment have motivated the researchers to propose and evaluate MWI as an alternative imaging modality for monitoring bone health. MWI is being investigated for a range of medical applications. The key advantages of MWI for diagnosing and monitoring various diseases compared to existing imaging modalities are non-ionising radiation, portability, and potential low cost [1],[2]. One of the notable applications of MWI is in the area of breast cancer detection [25]–[27], with four clinical systems being tested in clinical trials [27]. The detection of breast cancer relies on the inherent dielectric contrast between normal and malignant breast tissues [19], [28], [29]. Besides breast cancer detection, various studies have employed MWI for the diagnosis of brain stroke, exploiting the dielectric contrast between ischemic and healthy brain tissues [30]. Recent studies have investigated the feasibility of using MWI for osteoporosis monitoring [4],[11] based on the notable contrast between the dielectric properties of healthy and diseased bones [31]. Moreover, the dielectric properties of bone are found to be influenced by the mineralisation level of the bone [4],[17], thus the dielectric properties of bones can potentially be used to monitor osteoporosis [15],[16]. The non-ionising nature of microwave technology provides the capability to perform multiple scans over time for monitoring of bone health with a portable and cost-effective MWI based EM device in comparison to the DXA and QCT [32],[3].

Only one study to date has reported *in vivo* dielectric properties of human calcaneus bone by using MWT. In this study, Meaney *et al.* [11] used their breast imaging prototype for imaging the human calcaneus of two patients suffering from lower leg injury [11]. While Meaney *et al.* [11] achieved promising results with two patients using their breast imaging prototype, a dedicated MWI system for bone imaging application would further improve the results for monitoring osteoporosis. Future patient imaging studies will likely include larger and more diverse study populations, including a variety of calcaneus injuries, different aged patients, and different trabecular bone composition. Despite the promising initial evidence that dielectric properties can be potentially used for osteoporosis diagnosis, no dedicated MWI system exists to measure *in vivo* dielectric properties of human bone in the microwave frequency range.

The composition of trabecular bone varies substantially between osteoporotic and healthy human trabecular bones. Studies have found a significant difference between osteoporotic and healthy human trabecular bone samples in terms of trabecular number, trabecular thickness, and trabecular spacing [33]. The empty spaces in the trabecular microarchitecture of bones are filled with bone marrow. The quality of bone marrow changes as a function of age [34]. The bone marrow can be classified either as: red marrow that constitutes red and white blood cells, or yellow marrow that constitutes fat and connective tissues and which produces white blood cells [34]. As the person ages, the red marrow is replaced by the yellow marrow. Since the red marrow has higher dielectric properties compared to the yellow marrow, the bulk dielectric properties of bone reduce as a function of disease [34]. It has been reported in [4], that the dielectric properties of bone vary between different species since the fractional water content of bone is similar among bones of the same type; but in a single species, the water content of bone varies with age, sex, and disease state [34]. During the mineralisation of osteoid, water is replaced by the calcium apatite which ultimately fills the water spaces. This reduction of water content and hence the calcification of bone results in an overall decrease of dielectric properties of bone as a function of age [34]. MWI could potentially exploit the contrast between the dielectric properties of the osteoporotic and healthy human bone samples. Healthy human bones have high dielectric properties compared to osteoporotic bones.

MWI can be classified into two main categories: radar-based and tomographic MWI [35]. In radar-based MWI techniques, images are constructed based on the

scattered waves that arise due to the contrast between normal and malignant tissues [19]. Radar-based techniques are mainly used to localise strong scatterer/pathology in the biological tissues without reconstructing the full image of biological tissues [36]. Contrary to this, the tomographic MWI techniques aim to retrieve the spatial distribution of dielectric properties of biological tissues by processing the measured scattered EM field data [37]. The tomographic-based MWI techniques are computationally expensive compared to radar-based MWI techniques [37]. However, with the development of fast parallel tomography solutions, the computational cost of MWT approaches have reduced significantly [38].

Tomographic MWI is a leading technique for image reconstruction from scattered microwave energy. In MWT, the backscattered signals are used for the quantitative reconstruction of the dielectric profile of the breast using inverse scattering algorithms [25]. The EM inverse scattering problem is inherently ill-posed and non-linear. The regularisation and linearization techniques are applied to deal with the non-linearity and ill-posedness of the EM inverse scattering problem [37],[39]. To this end, various non-linear iterative techniques have been proposed in the literature such as the forward-backward time-stepping method [40], Gauss-Newton optimisation approach [11],[41], and microwave tomography using the dielectric Debye model [42]. The computational cost of these algorithms primarily depends upon the forward solver and the regularization techniques for the stabilization of the inversion method [37]. Moreover, the Gauss-Newton approaches are sensitive to the "initial guess", which makes this approach less favourable in scenarios where less *a priori* information is available [43]. In EM inverse scattering problems, an "initial guess" provides the starting point of the convex optimisation problem; hence, an inaccurate "initial guess" would lead to a solution that has no significance to the solution of the problem [43]. Besides non-linear iterative techniques, several linear approximation methods also exist, such as the Born and Rytov approximations [44]. These linear approximation methods help in reconstructing the dielectric profile of targets, that have a lower dielectric contrast compared to high contrast imaging scenarios [37]. In bone imaging applications, the cortical bone has lower dielectric properties compared to the trabecular bone [45], therefore the amount of energy penetrating trabecular bone is considerably higher than the reflected energy. Therefore, the contribution of the measured scattered EM signals due to the trabecular bone would dominate the behaviour of the objective function in the minimisation problem. Although numerous

studies have proposed MWT for breast cancer detection, the use of MWT for monitoring osteoporosis needs to answer the following specific questions:

1. Whether there exists any dielectric contrast between osteoporotic and non-osteoporotic bones that can be exploited by MWT, and what is the magnitude of the dielectric contrast?
2. Which frequency band should be feasible for bone imaging applications?
3. Which MWT algorithm would reconstruct the dielectric properties of the trabecular bone layer with optimum efficacy and sensitivity in terms of maintaining a sufficient dielectric contrast between cortical bone and trabecular bone?
4. What would be the practical implications and limitations of imaging bone phantoms with a dedicated MWI system?

These unanswered questions motivate the primary research objective of this thesis, namely to investigate the dielectric contrast between different diseased human trabecular bone samples and hence to develop an MWT algorithm to reconstruct the dielectric properties of numerical and experimental bone phantoms to monitor bone health. The primary research objectives are achieved in the following stages:

1. Investigating the dielectric contrast between osteoporotic and non-osteoporotic bones;
2. Initial feasibility analysis for developing an MWI system for bone imaging applications;
3. Analysing and developing MWT algorithm to reconstruct the dielectric properties of trabecular bone;
4. Developing an MWI prototype and bone phantoms to evaluate the efficacy of MWT for experimental scenarios.

To facilitate the primary research objectives, the dielectric characterisation of diseased human trabecular bones was performed, cortical bone and trabecular bone phantoms were developed, an MWT based algorithm was developed to reconstruct the dielectric properties of numerical bone phantoms, finally, the experimental evaluation of MWI prototype and bone phantoms was performed. The specific contributions described in this thesis are summarised in the following section, including the publications arising from these contributions.

1.2 Thesis Contributions

This thesis presents significant contributions to bone health monitoring by employing MWI. The specific novel contributions and the corresponding journal publications are summarised and listed below:

- The dielectric properties of bone across species from the literature were gathered and compared. This contribution aimed to summarise all available dielectric data of bone in the low-frequency range and the microwave frequency range, and also to analyse any confounders that may have resulted in variations in the reported data.

  Publication: Bilal Amin, Muhammad Adnan Elahi, Atif Shahzad, Emily Porter, Barry McDermott, and Martin O'Halloran, "Dielectric properties of bones for the monitoring of osteoporosis," Medical & biological engineering & computing, 57(1), pp.1-13. 2019.

  Publication: Bilal Amin, Muhammad Adnan Elahi, Atif Shahzad, Emily Porter, and Martin O'Halloran, "A review of the dielectric properties of the bone for low frequency medical technologies," Biomedical Physics & Engineering Express, 5, p.022001. 2019.

- The *in vitro* dielectric characterisation of various diseased human trabecular bone samples was performed. This contribution aimed to investigate whether there exists any dielectric contrast between different diseased human trabecular bone samples.

  Publication: Bilal Amin, Atif Shahzad, Laura Farina, Eoin Parle, Laoise McNamara, Martin O'Halloran, and Muhammad Adnan Elahi, "Dielectric characterization of diseased human trabecular bones at microwave frequency," Medical Engineering & Physics, pp. 1–8. 2020.

- The initial feasibility assessment of the MWI device was performed. This contribution aimed to investigate the operational frequency range, the relative permittivity of the matching medium, the numerical modelling of bone, and finally to analyse the penetration of the electric field in the human trabecular bone.

  Publication: Bilal Amin, Atif Shahzad, Lorenzo Crocco, Mengchu Wang, Martin O'Halloran, Ana González-Suárez, and Muhammad Adnan Elahi. "A feasibility study on microwave imaging of bone for osteoporosis monitoring,"

Medical & biological engineering & computing. 2021 Mar 30:1-12.

- Diverse numerical bone phantoms were developed based on the dielectric properties of human trabecular bones.

  Publication: Bilal Amin**,** Atif Shahzad, Martin O'Halloran, and Muhammad Adnan Elahi. "Microwave Bone Imaging: A Preliminary Investigation on Numerical Bone Phantoms for Bone Health Monitoring." Sensors. 20(21), p.6320. 2020.

- The development of the MWT algorithm for reconstructing the dielectric properties of human numerical bone phantoms was performed.

  Publication: Bilal Amin, Atif Shahzad, Martin O'Halloran, and Muhammad Adnan Elahi. "Microwave Bone Imaging: A Preliminary Investigation on Numerical Bone Phantoms for Bone Health Monitoring." Sensors. 20(21), p.6320. 2020.

- The fabrication and dielectric characterisation of cortical bone and trabecular bone phantoms was performed, along with the development of realistic three-dimensional (3-D) printed and carbon black-based human calcaneus structures. This contribution aimed to develop the liquid and solid based tissue-mimicking mixtures (TMMs) to mimic the dielectric properties of cortical bone and trabecular bone over 0.5 – 8.5 GHz frequency range.

  Publication: Bilal Amin, Atif Shahzad, Daniel Kelly, Martin O'Halloran, and Muhammad Adnan Elahi. "Anthropomorphic Calcaneus Phantom for Bone Imaging Applications." IEEE Journal of Electromagnetics, RF and Microwaves in Medicine and Biology. 2020.

- The designing, building, and testing of an experimental MWT based imaging system hardware, following the current state of the art operational system design was performed.

  Publication: Bilal Amin, Atif Shahzad, Martin O'Halloran, Barry McDermott, and Muhammad Adnan Elahi. "Experimental validation of microwave imaging prototype and DBIM-IMATCS algorithm for bone health monitoring." Medical Physics [Under Review].

- A system evaluation to image calcaneus and calcaneus bone phantoms was performed. This contribution aimed to evaluate the MWI prototype to image bone phantoms and hence to evaluate the constraints before investigating the

in vivo dielectric properties of human bone.

Publication: Bilal Amin, Atif Shahzad, Martin O'Halloran, Barry McDermott, and Muhammad Adnan Elahi. "Experimental validation of microwave imaging prototype and DBIM-IMATCS algorithm for bone health monitoring." Medical Physics [Under Review].

1.2.1 Journal Publications

[1] **Bilal Amin**, Muhammad Adnan Elahi, Atif Shahzad, Emily Porter, Barry McDermott, and Martin O'Halloran, "Dielectric properties of bones for the monitoring of osteoporosis," *Medical & biological engineering & computing*, *57*(1), pp.1-13. 2019.

[2] **Bilal Amin**, Muhammad Adnan Elahi, Atif Shahzad, Emily Porter, and Martin O'Halloran, "A review of the dielectric properties of the bone for low frequency medical technologies," *Biomedical Physics & Engineering Express*, *5*, p.022001. 2019.

[3] **Bilal Amin**, Atif Shahzad, Laura Farina, Eoin Parle, Laoise McNamara, Martin O'Halloran, and Muhammad Adnan Elahi, "Dielectric characterization of diseased human trabecular bones at microwave frequency," *Medical Engineering & Physics*, pp. 1–8. 2020.

[4] **Bilal Amin**, Atif Shahzad, Lorenzo Crocco, Mengchu Wang, Martin O'Halloran, Ana González-Suárez, and Muhammad Adnan Elahi. "A feasibility study on microwave imaging of bone for osteoporosis monitoring," *Medical & biological engineering & computing*. 2021 Mar 30:1-12.

[5] **Bilal Amin**, Atif Shahzad, Daniel Kelly, Martin O'Halloran, and Muhammad Adnan Elahi. "Anthropomorphic Calcaneus Phantom for Bone Imaging Applications." *IEEE Journal of Electromagnetics, RF and Microwaves in Medicine and Biology*. 2020.

[6] **Bilal Amin,** Atif Shahzad, Martin O'Halloran, and Muhammad Adnan Elahi. "Microwave Bone Imaging: A Preliminary Investigation on Numerical Bone Phantoms for Bone Health Monitoring." *Sensors*. 20(21), p.6320. 2020.

[7] **Bilal Amin**, Atif Shahzad, Martin O'Halloran, Barry McDermott, and Muhammad Adnan Elahi. "Experimental validation of microwave imaging prototype and DBIM-IMATCS algorithm for bone health monitoring," *Medical Physics* [Under Review].

1.2.2 Conference Publications

[1] **Bilal Amin**, Muhammad Adnan Elahi, Emily Porter, Atif Shahzad, and Martin O'Halloran. “Dielectric Properties of Bones: A Potential Indicator for Osteoporosis”, *Bioengineering in Ireland[24] Conference*, January 26-27, 2018.

[2] **Bilal Amin**, Muhammad Adnan Elahi, Atif Shahzad, Eoin Parle, Laoise McNamara, and Martin O’Halloran. “An insight into bone dielectric properties variation: a foundation for electromagnetic medical devices.” *EMF-Med 1st World Conference on Biomedical Applications of Electromagnetic Fields (EMF-Med)*, pp. 1-2. IEEE, 2018.

[3] **Bilal Amin**, Atif Shahzad, Laura Farina, Eoin Parle, Laoise McNamara, Martin O'Halloran, and Muhammad Adnan Elahi. “Investigating human bone microarchitecture and dielectric properties in microwave frequency range.” *In Proceedings of the 13th European Conference on Antennas and Propagation (Eu-CAP)*, pp. 1-5. IEEE, 2019.

[4] Daniel Kelly, **Bilal Amin**, and Muhammad Adnan Elahi, “Development of Bone Phantoms for Evaluation of a Novel Osteoporosis Monitoring Device.” *Atlantic Corridor Medical Student Research Conference* 2019, Brookfield Health Sciences Complex University College Cork.

[5] **Bilal Amin**, Daniel Kelly, Atif Shahzad, Martin O'Halloran, and Muhammad Adnan Elahi. “Microwave calcaneus phantom for bone imaging applications.” *In Proceedings of the 14th European Conference on Antennas and Propagation (Eu-CAP)*, pp.1-5. IEEE, 2020.

[6] **Bilal Amin**, Daniel Kelly, Atif Shahzad, Martin O'Halloran, and Muhammad Adnan Elahi. “Multilayered Human Calcaneus Phantom for Microwave Imaging of Bone.” *In Proceedings of the 42nd International Conferences of the IEEE Engineering in Medicine and Biology Society*. IEEE, 2020.

[7] **Bilal Amin**, Colin Sheridan, Daniel Kelly, Atif Shahzad, Martin O'Halloran, and Muhammad Adnan Elahi. "Microwave bone imaging: experimental evaluation of calcaneus bone phantom and imaging prototype.” *International Microwave Biomedical Conference*. IEEE, 2020.

[8] **Bilal Amin**, Atif Shahzad, Martin O'Halloran, and Muhammad Adnan Elahi. “Microwave Tomographic Imaging of Experimental Bone Phantoms for Bone Imaging Application.” *IEEE International Symposium on Antennas and Propagation* (*APS-URSI)* IEEE, 2021.

1.3 Thesis Structure

The remainder of this thesis is structured to describe the background, experimental methods, and results to address the primary research objective of this thesis.

Chapter 2 describes the anatomy and physiology of human bone; a clinical description of osteoporosis; an overview of bone imaging modalities; a literature review on dielectric properties of bones in the low-frequency range and microwave frequency range; a comparative analysis of studies reporting bone dielectric properties and the related inconsistencies in the dielectric data reported in the literature; the relationship between the bone dielectric properties and bone quality parameters; the potential of MWI for monitoring bone health; and a finally a brief literature review on MWT, the experimental prototypes, and clinical studies performed for bone imaging.

Next, Chapter 3 presents the *in vitro* dielectric characterisation of human trabecular bones from osteoporotic and osteoarthritis patients; a comparison between trabecular bone microarchitecture for osteoporotic and osteoarthritis patients is presented; a comparison between the dielectric properties of the current study and the dielectric properties of human trabecular bone in the literature is presented, and finally, the relationship between the bone dielectric properties and bone volume fraction is presented.

Chapter 4 presents an initial feasibility study on an MWI device for monitoring of osteoporosis; the dielectric contrast of tissues present in the calcaneus is investigated; a transmission line formalism approach is adopted to investigate the feasible frequency band for the operation of MWI device; an analysis is presented to find the optimal matching medium for maximum EM waves penetration into the calcaneus; the numerical modelling of the human calcaneus is presented; the finite difference time domain simulations are performed to analyse electric field penetration in the five-layered human calcaneus.

Chapter 5 presents the development of numerical bone phantoms based on the dielectric properties of cortical bone and trabecular bone data acquired from the literature; the numerical bone phantoms for osteoporotic and osteoarthritis patients were developed based on their dielectric properties presented in Chapter 3; the performance of the distorted Born iterative method (DBIM) along with iterative method with adaptive thresholding for compressed sensing (IMATCS) for linear inversion of EM waves is evaluated for the reconstruction of numerical bone

phantoms, and the numerical bone phantoms were assessed for different settings of signal to noise ratio.

Chapter 6 presents the preparation and dielectric characterisation of liquid and solid tissue-based mimicking mixtures to mimic the dielectric properties of human calcaneus tissues; the polylactic acid (PLA) based 3-D printed and carbon black-based cylindrical bone and realistic human calcaneus structures are presented.

Chapter 7 presents the experimental data and hardware acquisition system developed to image bone phantoms presented in Chapter 6; the performance of DBIM along with IMATCS for linear inversion of EM waves is evaluated for the reconstruction of dielectric properties of experimental bone phantoms; special cases of trabecular bone phantoms were developed that mimic the dielectric properties of osteoporotic and osteoarthritis patients' dielectric data and reconstruction algorithm was employed to retrieve the spatial distribution of dielectric properties.

Finally, Chapter 8 discusses the conclusions and suggestions for future work.

1.4 References

[1] US Department of Health and Human Services, "Bone health and osteoporosis: a report of the Surgeon General," *US Heal. Hum. Serv.*, p. 437, 2004.

[2] O. Johnell and J. A. Kanis, "An estimate of the worldwide prevalence and disability associated with osteoporotic fractures," *Osteoporos. Int.*, vol. 17, no. 12, pp. 1726–1733, 2006.

[3] S. N. Makarov, G. M. Noetscher, S. Arum, R. Rabiner, and A. Nazarian, "Concept of a Radiofrequency Device for Osteopenia / Osteoporosis Screening," pp. 1–15, 2020.

[4] B. Amin, M. A. Elahi, A. Shahzad, E. Porter, B. McDermott, and M. O'Halloran, "Dielectric properties of bones for the monitoring of osteoporosis," *Med. Biol. Eng. Comput.*, Aug. 2018.

[5] A. J. Laster, "Dual-Energy X-Ray Absorptiometry:," vol. 75, no. 2, pp. 132–136, 2014.

[6] Office of the Surgeon General, "Bone Health and Osteoporosis - NCBI Bookshelf," 2004.

[7] F. Cosman *et al.*, "Clinician's Guide to Prevention and Treatment of Osteoporosis," *Osteoporos. Int.*, vol. 25, no. 10, pp. 2359–2381, 2014.

[8] R. Burge, B. Dawson-Hughes, D. H. Solomon, J. B. Wong, A. King, and A.

Tosteson, “Incidence and Economic Burden of Osteoporosis-Related Fractures in the United States, 2005-2025,” *J. Bone Miner. Res.*, vol. 22, no. 3, pp. 465–475, 2007.

[9] W. H. Organization, “WHO SCIENTIFIC GROUP ON THE ASSESSMENT OF OSTEOPOROSIS AT PRIMARY HEALTH Care Level,” *World Heal. Organ.*, vol. May, no. May 2004, pp. 5–7, 2004.

[10] J. R. Wilkie *et al.*, “Comparison of radiographic texture analysis from computed radiography and bone densitometry systems.,” *Med. Phys.*, vol. 31, no. 4, pp. 882–891, 2004.

[11] P. M. Meaney *et al.*, “Clinical microwave tomographic imaging of the calcaneus: A first-in-human case study of two subjects,” *IEEE Trans. Biomed. Eng.*, vol. 59, no. 12, pp. 3304–3313, 2012.

[12] E.-M. Lochmüller, R. Müller, V. Kuhn, C. A. Lill, and F. Eckstein, “Can Novel Clinical Densitometric Techniques Replace or Improve DXA in Predicting Bone Strength in Osteoporosis at the Hip and Other Skeletal Sites?,” *J. Bone Miner. Res.*, vol. 18, no. 5, pp. 906–912, 2003.

[13] R. M. Irastorza, E. Blangino, C. M. Carlevaro, and F. Vericat, “Modeling of the dielectric properties of trabecular bone samples at microwave frequency,” *Med. Biol. Eng. Comput.*, vol. 52, no. 5, pp. 439–447, 2014.

[14] A. Ivancich, J. R. Grigera, and C. Muravchik, “Electric behaviour of natural and demineralized bones. Dielectric properties up to 1 GHz,” *J. Biol. Phys.*, vol. 18, no. 4, pp. 281–295, 1992.

[15] J. Sierpow[1] J. Sierpowska, J. Töyräs, M. A. Hakulinen, S. S., J. S. Jurvelin, and R. Lappalainen, “Electrical and dielectric properties of bovine trabecular bone -- relationships with mechanical properties and mineral density,” Phys.\ Med.\ Biol., vol. 48, J. Töyräs, M. A. Hakulinen, S. S., J. S. Jurvelin, and R. Lappalainen, “Electrical and dielectric properties of bovine trabecular bone -- relationships with mechanical properties and mineral density,” *Phys.\ Med.\ Biol.*, vol. 48, pp. 775–786, 2003.

[16] R. Irastorza, M. Mayosky, R. Grigera, and F. Vericat, “Dielectric properties of natural and demineralized collagen bone matrix,” *IEEE Trans. Dielectr. Electr. Insul.*, vol. 18, no. 1, pp. 320–328, 2011.

[17] P. M. Meaney, T. Zhou, D. Goodwin, A. Golnabi, E. A. Attardo, and K. D. Paulsen, “Bone dielectric property variation as a function of mineralization at

microwave frequencies," *Int. J. Biomed. Imaging*, vol. 2012, 2012.

[18] E. Porter and M. OHalloran, "Investigation of Histology Region in Dielectric Measurements of Heterogeneous Tissues," *IEEE Trans. Antennas Propag.*, no. c, pp. 1–1, 2017.

[19] E. Porter, M. Coates, and M. Popović, "An Early Clinical Study of Time-Domain Microwave Radar for Breast Health Monitoring," *IEEE Trans. Biomed. Eng.*, vol. 63, no. 3, pp. 530–539, 2016.

[20] C. L. Brace, "Radiofrequency and Microwave Ablation of the Liver, Lung, Kidney, and Bone: What Are the Differences?," *Curr. Probl. Diagn. Radiol.*, vol. 38, no. 3, pp. 135–143, 2009.

[21] P. T. Nguyen, A. Abbosh, and S. Crozier, "Microwave hyperthermia for breast cancer treatment using electromagnetic and thermal focusing tested on realistic breast models and antenna arrays," *IEEE Trans. Antennas Propag.*, vol. 63, no. 10, pp. 4426–4434, 2015.

[22] R. M. Irastorza, C. M. Carlevaro, and F. Vericat, "Is there any information on micro-structure in microwave tomography of bone tissue?," *Med. Eng. Phys.*, vol. 35, no. 8, pp. 1173–1180, 2013.

[23] A. H. Golnabi, P. M. Meaney, S. Geimer, T. Zhou, and K. D. Paulsen, "Microwave tomography for bone imaging," *Proc. - Int. Symp. Biomed. Imaging*, vol. 9, pp. 956–959, 2011.

[24] R. Scapaticci, P. Kosmas, and L. Crocco, "Wavelet-Based Regularization for Robust Microwave Imaging in Medical Applications," *IEEE Trans. Biomed. Eng.*, vol. 62, no. 4, pp. 1195–1202, 2015.

[25] M. A. Elahi *et al.*, "Evaluation of image reconstruction algorithms for confocal microwave imaging: Application to patient data," *Sensors (Switzerland)*, vol. 18, no. 6, 2018.

[26] D. O. Loughlin *et al.*, "Sensitivity and Specificity Estimation Using Patient-Specific Microwave Imaging in Diverse Experimental Breast Phantoms," vol. 38, no. 1, pp. 303–311, 2019.

[27] D. O'Loughlin, M. O'Halloran, B. M. Moloney, M. Glavin, E. Jones, and M. A. Elahi, "Microwave Breast Imaging: Clinical Advances and Remaining Challenges," *IEEE Trans. Biomed. Eng.*, vol. 65, no. 11, pp. 2580–2590, 2018.

[28] M. Lazebnik *et al.*, "A large-scale study of the ultrawideband microwave dielectric properties of normal, benign and malignant breast tissues obtained

from cancer surgeries," *Phys. Med. Biol.*, vol. 52, no. 20, pp. 6093–6115, 2007.

[29] J. Bourqui and E. C. Fear, "System for Bulk Dielectric Permittivity Estimation of Breast Tissues at Microwave Frequencies," *IEEE Trans. Microw. Theory Tech.*, vol. 64, no. 9, pp. 3001–3009, 2016.

[30] R. Scapaticci, L. Di Donato, I. Catapano, and L. Crocco, "A feasibility study on microwave imaging for brain stroke monitoring," *Prog. Electromagn. Res.*, vol. 40, pp. 305–324, 2012.

[31] B. Amin *et al.*, "Dielectric characterization of diseased human trabecular bones at microwave frequency," in *2020 Medical Engineering and Physics*, 2020, pp. 1–8.

[32] B. Amin, M. A. Elahi, A. Shahzad, E. Parle, L. McNamara, and M. Orhalloran, "An insight into bone dielectric properties variation: A foundation for electromagnetic medical devices," *EMF-Med 2018 - 1st EMF-Med World Conf. Biomed. Appl. Electromagn. Fields COST EMF-MED Final Event with 6th MCM*, pp. 3–4, 2018.

[33] B. Amin *et al.*, "Investigating human bone microarchitecture and dielectric properties in microwave frequency range," in *2019 13th European Conference on Antennas and Propagation (EuCAP)*, 2019, pp. 1–5.

[34] a. Peyman, C. Gabriel, E. H. Grant, G. Vermeeren, and L. Martens, "Variation of the dielectric properties of tissues with age: the effect on the values of SAR in children when exposed to walkie-talkie devices.," *Phys. Med. Biol.*, vol. 54, no. 2, pp. 227–241, 2009.

[35] J. Bourqui, J. M. Sill, and E. C. Fear, "A prototype system for measuring microwave frequency reflections from the breast," *Int. J. Biomed. Imaging*, vol. 2012, 2012.

[36] B. L. Oliveira and M. O. Halloran, "Microwave Breast Imaging : Experimental tumour phantoms for the evaluation of new breast cancer diagnosis systems Biomedical Physics & Engineering Related content Microwave Breast Imaging : experimental tumour phantoms for the evaluation of new breast can," no. January, 2018.

[37] A. Shahzad, M. O'Halloran, E. Jones, and M. Glavin, "A multistage selective weighting method for improved microwave breast tomography," *Comput. Med. Imaging Graph.*, vol. 54, pp. 6–15, 2016.

[38] A. Shahzad, M. O'Halloran, M. Glavin, and E. Jones, "A novel optimized

parallelization strategy to accelerate microwave tomography for breast cancer screening," in *2014 36th Annual International Conference of the IEEE Engineering in Medicine and Biology Society*, 2014, pp. 2456–2459.

[39] R. Scapaticci, M. Bjelogrlic, J. A. T. Vasquez, F. Vipiana, M. Mattes, and L. Crocco, "Microwave technology for brain imaging and monitoring: physical foundations, potential and limitations," in *Emerging Electromagnetic Technologies for Brain Diseases Diagnostics, Monitoring and Therapy*, Springer, 2018, pp. 7–35.

[40] T. Takenaka, H. Jia, and T. Tanaka, "Journal of Electromagnetic Waves Microwave Imaging of Electrical Property Distributions By a Method," no. January 2015, pp. 37–41.

[41] A. Fhager, M. Gustafsson, S. Nordebo, and S. Member, "Image Reconstruction in Microwave Tomography Using a Dielectric Debye Model," *IEEE Trans. Biomed. Eng.*, vol. 59, no. 1, pp. 156–166, 2012.

[42] A. Fhager, M. Gustafsson, and S. Nordebo, "Image Reconstruction in Microwave Tomography Using a Dielectric Debye Model," *IEEE Trans. Biomed. Eng.*, vol. 59, no. 1, pp. 156–166, Jan. 2012.

[43] R. Scapaticci, P. Kosmas, and S. Member, "Wavelet-Based Regularization for Robust Microwave Imaging in Medical Applications," *IEEE Trans. Biomed. Eng.*, vol. 62, no. 4, pp. 1195–1202, 2015.

[44] B. Amin, A. Shahzad, M. O'halloran, and M. A. Elahi, "Microwave bone imaging: A preliminary investigation on numerical bone phantoms for bone health monitoring," *Sensors (Switzerland)*, vol. 20, no. 21, pp. 1–21, 2020.

[45] B. Amin, M. A. Elahi, A. Shahzad, E. Porter, and M. O'Halloran, "A review of the dielectric properties of the bone for low frequency medical technologies," *Biomed. Phys. Eng. Express*, vol. 5, no. 2, p. 022001, 2019.

Chapter 2

Literature Review

Work from this chapter has been published in Medical & Biological Engineering & Computing in 2018 in a review paper entitled "Dielectric properties of bones for the monitoring of osteoporosis.", Biomedical Physics & Engineering Express in 2019 in a review paper entitled "A review of the dielectric properties of the bone for low frequency medical technologies.", and in Bioengineering in Ireland[24] Conference in 2018 in a review paper entitled "Dielectric Properties of Bones: A Potential Indicator for Osteoporosis."

In this chapter, the clinical context is first considered, with an overview of normal bone anatomy and physiology. An overview of the clinical problem (osteoporosis) is then provided, followed by a review of existing bone imaging modalities. Next, as a basis for the development of a microwave bone imaging system, a literature review on dielectric properties of bones both for low frequency and microwave frequency range is presented. The variation of dielectric properties of bones is observed separately for both animal and human species, followed by variations observed in dielectric properties of cortical bone and trabecular bone. Moreover, a comparative analysis of studies is presented for dielectric properties of bone in low frequency and microwave frequency range. Next, the relationship between bone dielectric properties and bone quality parameters is investigated to assess the correlation, and the potential to monitor disease progression based on dielectric properties. Finally, MWI is introduced as a potential tool for monitoring osteoporosis. Various potential existing MWT algorithms are considered for the application of bone health monitoring and existing studies that considered MWI for bone imaging applications are also discussed for completeness.

2.1 Introduction

This thesis has investigated the dielectric properties of bone for developing a low-cost MWT based medical device for monitoring osteoporosis. Osteoporosis is a major bone disease, caused due to progressive demineralisation of bones that deteriorates the trabecular bone microarchitecture, and hence leads to bone fragility and fractures [1],[2]. Before this investigation, studies have found that the dielectric properties of

bone are influenced by varying bone mineralisation levels. However, no study to date has ever developed a dedicated MWI prototype for bone imaging application. Therefore, the strategic focus of this thesis was to develop a dedicated MWI-based electromagnetic device for bone health monitoring. The structure of this chapter is as follows:

1. Section 2.2 details the anatomy and physiology of normal bone;
2. Section 2.3 describes the clinical need (osteoporosis);
3. Section 2.4 presents an overview of the existing imaging/diagnostic modalities to monitor osteoporosis;
4. Section 2.5 examines the dielectric properties of bone, as follows:
    a. A review of low-frequency properties (2.5.1) for both animal and human bone;
    b. An analysis of the relationship between the bone dielectric properties and bone mineral density in the low-frequency range.
    c. A review of high-frequency properties (2.5.2) for both animal and human bone;
    d. An analysis of the relationship between the bone dielectric properties and bone mineral density in the high-frequency range.
5. Sections 2.6, 2.7, and 2.8 discuss MWI, its feasibility for the bone imaging application and existing experimental prototypes;
6. Finally, conclusions are drawn in Section 2.9.

2.2 Bone Anatomy and Physiology

Bone is composed of bone tissue, bone marrow, blood vessels, epithelium, and nerves. Bone tissue is also referred to as osseous tissue and is one of the major structural and supportive connective tissue of the body. The rigid part of the bone is mainly due to mineralisation of bone tissue. Bone tissue is mainly composed of a mineralised matrix in the form of hydroxyapatite crystals [Ca_{10} $(PO_4)_6$ $(OH)_2$] (50 – 70%) and bone cells. Bone tissue also serves as a storage site for calcium and phosphate. The blood mobilises both calcium and phosphate from bone and maintains their appropriate levels throughout the body. Thus, bone plays a significantly important role in the homeostatic regulation of blood calcium levels throughout the body and provides support and protection of the skeleton [3].

Bone cells are responsible for the development of new bone tissue and help in the continuous bone remodelling process. Bone cells can be classified into two main types: osteoclasts and osteoblasts. Osteoclasts are large multinucleate cells that are responsible for the breakdown of bone tissue. Contrary to this, osteoblasts are small single nucleus cells that are responsible for building new bone tissue [4]. The breakdown of bone caused by osteoclasts plays a vital role during the bone remodelling process. Osteoclasts release enzymes on the bone site which breaks down the bone. On the other hand, osteoblasts allow the bone to be remodelled. Osteoblasts first put the collagen fibres and then deposit calcium phosphate on the bone site. Calcium phosphate is hardened by the hydroxide and bicarbonate ions and helps in the formation of new bone. The new bone developed in the bone remodelling process is called osteoid [5].

The overall human skeleton is composed of cortical bone (also termed compact bone) and trabecular bone (also termed cancellous bone) [24]. The ratio of cortical bone to trabecular bone in a human skeleton varies depending upon the anatomical site of the body [5]. Cortical bone has a dense and solid structure and forms the exterior of the bone. Cortical bone contributes about 80% of human skeleton weight. Moreover, cortical bone supports the whole body, provides support for the movement, and releases a chemical element that mainly includes calcium. Osteon is the primary anatomical and functional unit of cortical bone [4]. Trabecular bone is less dense and has a higher surface area to mass ratio compared to cortical bone. Trabecular bone is softer and weaker that makes it flexible compared to cortical bone. Trabecular bone is typically found at the end of long bones, near to joints, and within the vertebrae. The trabecular bone is highly vascular and is mainly composed of marrow and blood vessels. Trabecula is the primary anatomical and functional unit of trabecular bone [4]. Bones are classified based on their shape and are divided into the following four groups:

1. Long Bones: Long bones are longer in one dimension compared to other bones and consist of shafts at two ends of the bone. Examples of long bones are the tibia and the metacarpals.
2. Short Bones: Short bones are nearly equal in length and diameter. An example of short bones is the carpal bones of the hands.
3. Flat Bones: Flat bones are thin and resemble a plate. An example of flat bones is the bones of the calvaria and the sternum.

4. Irregular Bones: The irregular bones have an irregular shape and do not fit into any of the above categories of bone. Their shape is usually complex. An example of such bones is a vertebra.

The anatomy of the bone is shown in Figure 2.1. In Figure 2.1, the epiphysis (head) and the start of the diaphysis (shaft) of a typical long bone are shown. Trabecular bone with its characteristic honeycomb structure is prevalent in the epiphysis but extends into the diaphysis underneath the cortex and surrounds the medullary (marrow) cavity. The metaphysis is the area between the head and shaft and contains the epiphyseal plate, which is the area where new bone tissues originate early in life with this area later ossifying. It can be seen from Figure 2.1 that the structure of trabecular bone is highly inhomogeneous and anisotropic as compared to cortical bone, and is scattered in bone marrow [3],[4].

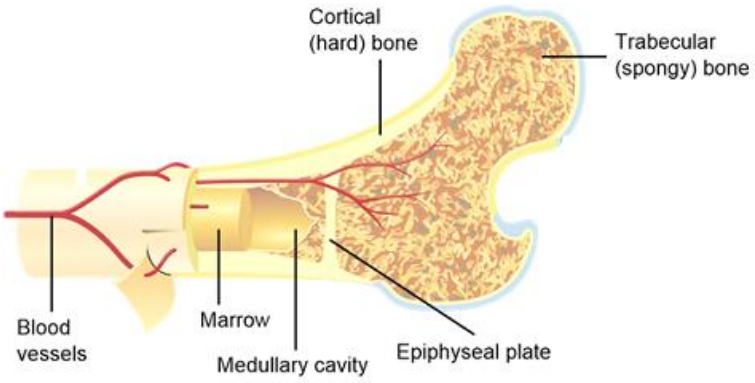

Figure 2.1: Anatomical structure of bone [7].

2.3 Osteoporosis

Osteoporosis is one of the most commonly encountered bone disease worldwide [8]. Osteoporosis is characterised as low bone mass, accompanied by continuous systematic deterioration of the trabecular bone microarchitecture and hence, leads to bone fragility and fractures [1]. Demineralisation of the bones is considered to be the major cause of osteoporosis [3]. On the cellular level, the imbalance between osteoclast-mediated bone resorption and osteoblast-mediated bone deposition results in decreased bone mass [9]. Osteoporosis has a high prevalence among postmenopausal women. Before the postmenopausal stage, the female hormones known as estrogens restrict the activity of osteoclasts, however, in postmenopausal women the estrogen levels are reduced, therefore the secretion of osteoclasts increase, thus resulting in an imbalance between the resorption and formation of bone [10].

Osteoporosis has approximately affected about 75 million people in the United States, Europe, and Japan, including one-third of postmenopausal women and most of the elderly population [3]. Approximately 1.3 million osteoporotic fractures are reported in the United States [3]. Based on the prevalence and cause, osteoporosis is classified into the following three general categories:

1. Type I primary osteoporosis;
2. Type II primary osteoporosis;
3. Secondary osteoporosis.

Type I primary osteoporosis mainly occurs in postmenopausal women. Type I osteoporosis occurs in an earlier stage of life compared to type II osteoporosis. The long-term effects of type I osteoporosis are severe compared to osteoporosis that occurs in the later stage of life. Type II primary osteoporosis mainly occurs in elderly people. The prevalence of type II osteoporosis is mainly for people in the age group of 70 to 80 years and causes serious morbidity. Secondary osteoporosis develops due to drug therapy or due to any disease process that affects the bone remodelling process. Few other major reasons for secondary osteoporosis include malnutrition, immobilisation, and metabolic bone disease [3].

The osteoporotic bone has a normal histologic structure; however, an osteoporotic bone has less tissue mass compared to a non-osteoporotic bone [3]. The comparison between osteoporotic and non-osteoporotic bone is shown in Figure 2.2. It can be observed from Figure 2.2 that normal bone has more compact and dense trabecular microarchitecture compared to osteoporotic bone. Less bone mass causes the weakening of bones that makes the bone fragile and more prone to fractures following minor trauma. The most commonly encountered osteoporotic fractures are hip fractures, wrist fractures, and compressed vertebrae fractures. These fractures result in the disability of elderly people at the expense of loss of their independence. Hip fracture is one of the very common and serious outcomes of osteoporosis, having a mortality rate of 14 – 36% during the first year after fracture. The risk of mortality for patients suffering from osteoporosis is mainly because of hospitalisation complications due to immobilisation, increased risk of pneumonia, pulmonary thrombosis, and embolism [7].

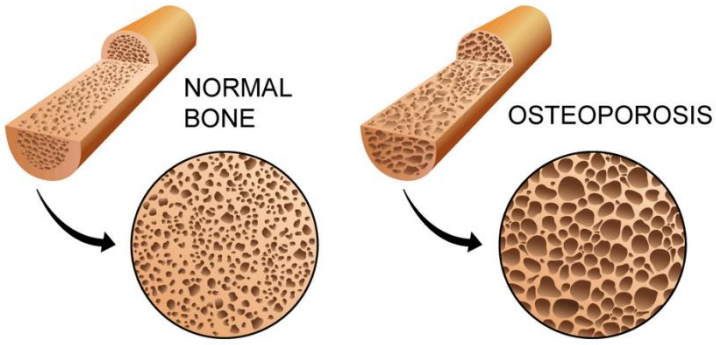

Figure 2.2: Comparison of osteoporotic and non-osteoporotic bone [11].

Traditionally, patients suffering from osteoporosis are advised to improve their diet along with vitamin D and calcium supplements with moderate exercise to prevent further bone loss. Moreover, pharmacologic therapy is directed at slowing down the bone resorption process [3]. Until recently, hormone replacement therapy was one of the preferred treatments for postmenopausal women suffering from osteoporosis. In hormone replacement therapy, the hormones are replaced with estrogen and progesterone. The estrogen helps to slow the bone resorption process and hence diminishes bone loss. However, the Women's Health Initiative has found that hormone replacement therapy reduces the fracture risk, but it causes a greater risk of cardiovascular diseases as well as an increased risk of breast cancer [3].

2.4 Bone Imaging Modalities/Diagnostic Methods

Exponential growth has been observed towards the development of bone imaging modalities, as new imaging modalities and analytic techniques have improved the potential for non-invasive monitoring of bone health [7]. The WHO has adopted BMD, as the key method for diagnosing osteoporosis [11]. The severity of the disease is characterised by the value of BMD in a particular bone area. The history of BMD measurement dates back to the early 1940s [12]. At those time, the bone density was measured on plain radiographs. However, the radiographs did not register the loss of bone density until 40% of the bone loss had occurred. In current clinical practice, the value of BMD for the patient under observation is compared with BMD of the young populations of the same gender. This difference of BMD between patients under observation and BMD of the young population is referred to as T-score. The WHO suggests that a patient with a T-score less than 2.5 should be considered osteoporotic [13]. Many imaging modalities exist in the literature for the assessment of BMD including single-photon absorptiometry (SPA), dual-photon absorptiometry (DPA),

QUS, radiographs and magnetic resonance imaging (MRI), DXA, and QCT [7]. The benefits and limitations of each modality are discussed in the following section.

2.4.1 Single-Photon Absorptiometry

SPA was developed in 1963. This method measured the BMD by sending a single-energy photon beam through the bone and soft tissue. The amount of mineral in the path traversed by the beam was quantified based on the beam received at the detector. The common anatomical site of measuring BMD in this method was the distal radius (wrist) as the distal radius has a minimum amount of soft tissue. The duration of the test in SPA usually takes 10 minutes. The limitation of the SPA is that the radioactive source that emits the photon beam decays gradually and must be replaced after some time [14]. Moreover, due to the presence of soft tissue, the BMD measured by this approach was not considered clinically significant.

2.4.2 Dual-Photon Absorptiometry

DPA uses a photon beam that has two distinct energy peaks. One of the energy peaks was designed to be absorbed by the soft tissue, while the second energy peak designed to be absorbed by the bone. Both the energy peaks of traversed beams were subtracted to determine the BMD. The common anatomical sites for measuring BMD in this method were the spine and proximal femur. The prediction of fracture risk by DPA was more accurate compared to SPA, however, the isotope used to emit photon beam decayed faster compared to SPA, which imposed poorer precision. Moreover, DPA poses limitations to monitor the change of BMD during the follow-up of an individual patient due to factors such as source decay and source change [14].

2.4.3 Quantitative Ultrasound

The QUS method is another diagnostic technique to evaluate fracture risk. The QUS method measures the broadband ultrasound attenuation and the velocity of sound measured at the patient's heel. This method of evaluating fracture risk is non-invasive and does not involve the use of ionising radiations. The cost of the test is comparatively low compared to other methods, but the performance of QUS is less satisfactory than other imaging modalities [13]. Therefore, this technique has not been well adopted by the clinicians because QUS is unable to penetrate through the bone, and hence the bone mass was measured only by considering the outer bone surface.

2.4.4 Radiographs and Magnetic Resonance Imaging

Another similar approach to QUS involves the visual inspection of simple radiographs. In this approach, radiographs of the metacarpal, distal phalanges, and distal forearm are visually inspected to monitor osteoporosis. The risk assessment is based on analysing the cortical width of the second, third, and fourth metacarpals. This method has been used for many years for the assessment of fracture risk due to osteoporosis. Like radiographs, MRI has been also employed to monitor the fracture risk. MRI does not provide any information about the BMD of the bone but provides high-resolution information on the trabecular microarchitecture of the bone [15]. MRI is used in limited clinical setups for investigation procedures due to the high cost and complexity of the tests [13].

2.4.5 Dual Energy X-ray Absorptiometry

DXA works similarly to DPA. The measurement of BMD by DXA has been available for clinical use since 1987. In current clinical practices, DXA is a readily available surrogate marker of bone strength and fracture risk. The DXA addresses the limitations of SPA and DPA by employing an X-ray source instead of the radioactive isotope. Therefore, the energy of the radiation source does not decay in DXA and remains constant over time. Moreover, the scan time of DXA is short compared to DPA and uses low dose radiation compared to DPA. The DXA is used as a standard clinical modality and is considered a “gold standard” for measuring BMD worldwide [1]. DXA calculates the BMD of central bone sites (hip, lumbar spine) and also peripheral sites (heel, distal forearm), and maps to a T-score [16].

The DXA scans are extremely precise having a precision range of 1% to 2%. DXA offers precise monitoring of change in BMD over time for patients suffering from osteoporosis. A pencil beam-type scanner was used in first-generation DXA machines. The second-generation DXA machines used a fan-beam scanner that employs a group of detectors. The second-generation machines are considerably faster and produce higher resolution image compared to first-generation machines. DXA offers certain limitations, firstly, it assesses areal BMD (aBMD, g/cm^2). The aBMD considers the bone area in square centimetres and does not account for the depth of the bone site under consideration [12]. Secondly, DXA is a composite measure of cortical and trabecular bone BMD and hence is prone to overestimation of BMD [12]. Besides this, DXA does not provide information on the structure and biology of the trabecular bone

pattern which is also considered key indicators for diagnosing osteoporosis; hence, using BMD solely for clinical care of overall fracture risk has limitations [17]. Moreover, the DXA scan uses standard X-ray doses up to 0.86 mrem, therefore frequent DXA scans are associated with long-term health risks [18]. Finally, the DXA scans are expensive and the device is not portable.

2.4.6 Quantitative Computed Tomography

QCT was recognized in the late 1970s. The QCT measures vBMD, and measures BMD of trabecular bones separately from cortical bone, and is, therefore, less prone to soft tissue errors [19]. The QCT can separate the surrounding tissues from the tissue of interest, that is the trabecular bone in case of osteoporosis monitoring. QCT can specifically detect metabolic activities of the trabecular bone, which makes it a more sensitive discriminator of BMD changes than DXA. QCT provides a true 3-D image of bone and determines the 3-D BMD of the bone. However, QCT is rarely used in clinical practice settings due to the high-intensity doses of X-rays required. The radiation dose of QCT is about 10 times the radiation dose of the DXA scan. Moreover, QCT is rarely used in clinical setups due to expensive equipment, poor availability, and cost of the test than DXA scans [19].

2.5 Dielectric Properties of Bone

The phenomena of EM wave reflection and propagation through biological tissues can be characterised by dielectric properties namely, the relative permittivity (ε_r) and conductivity (σ) [20]. The interaction of EM waves with biological tissues has been well investigated, starting from early studies by England and Sharples [27],[28] in 1940 - 1950, and by Cook in 1951 [29]. Since then, many studies have been performed to measure the dielectric properties of human tissues. Some of the major applications of the dielectric properties of tissues include determination of the specific absorption rate (SAR), design of EM-based medical devices [30],[31], design validation of wireless communication, and on-body devices [32], [33]. The dielectric properties of the biological tissues have formed the basis for the development of several EM diagnostic and therapeutic medical devices [7],[20]. These types of devices include time-domain microwave radar for breast health monitoring [35], microwave ablation for treating liver, lung, kidney, bone, and adrenal tumours [36], and microwave hyperthermia for breast cancer treatment [37].

The dielectric properties of tissues are both temperature and frequency-dependent [34]. When an external electric field is applied to biological tissue, the randomly oriented molecules of the biological tissue are polarised based on the direction of the applied electric field. The polarisation of molecules due to the applied electric field induces an electric field in the opposite direction of the applied electric field. The magnitude of the induced electric field is smaller compared to the magnitude of the applied electric field [24]. The amount of time taken by the molecules to get polarised is known as relaxation time τ. The amount of resistance offered by the molecules to the applied electric field can be expressed in terms of complex permittivity [25]. For a time-varying field, the complex permittivity of biological tissue can be defined as:

$$\varepsilon(\omega) = \varepsilon'(\omega) - j\varepsilon''(\omega) \qquad (2.1)$$

where $\varepsilon'(\omega)$ is the relative permittivity also termed as dielectric constant, $\varepsilon''(\omega)$ is the dielectric loss, $j = \sqrt{-1}$, and $\omega = 2\pi f$ (rad/s) represents frequency in radians and f denotes the frequency of operation and has SI units of Hz. The relative permittivity represents the ability of a material to store energy and the dielectric loss represents the energy dissipated in the material. The imaginary part of the complex permittivity also termed dielectric loss is used to compute the electrical conductivity and is expressed in terms of Siemens per metre (S/m) [26]. The electrical conductivity can be computed as follows:

$$\sigma(\omega) = \omega\varepsilon_0\varepsilon''(\omega) \qquad (2.2)$$

where ε_0 is the permittivity of free space expressed in Farads per metre (F/m). The value of ε_0 is $8.8541 \times 10^{-12} F/m$.

MWI has been previously used to measure *in vivo* dielectric properties of the breast, and it has been recently proposed to measure the dielectric properties of the calcaneus bone for monitoring osteoporosis [18],[21]–[23]. Studies have found that the dielectric properties of bone are influenced by different mineralisation levels of the bone [7]. Therefore, a quantitative relationship between the dielectric properties of bone and the corresponding mineralisation levels can potentially be exploited to develop an MWI-based imaging device for the monitoring of osteoporosis. However, the development of such a medical device requires reliable data that establishes a definitive correlation between dielectric properties and bone quality. Several studies have reported the dielectric properties of bones at low-frequency range [6], [38]–[44]

and in the microwave frequency range [18], [23], [42], [45]–[49]. Studies have found a significant dielectric contrast between healthy and diseased human trabecular bones [50]. Moreover, the dielectric properties of bones are found to be influenced by the mineralisation level of bones [48],[51],[52]. Therefore, several studies [18],[40],[41],[49],[46] have suggested that bone health can be predicted by the dielectric properties of the bone. The relationship between BMD and the dielectric properties is reported in [52],[53],[39],[46],[53]–[56]. However, the reported relationship is not consistent across the studies. Although, most of the studies have reported *ex vivo* dielectric properties of bone, however, some recent studies [18],[58], [59] have also reported *in vivo* dielectric properties of the bone in the microwave frequency range, including [18] where a non-invasive MWI technique was used to estimate the dielectric properties of human calcaneus bones. There has been significant experimental work in bone dielectric characterisation over the past four decades, but it is still difficult to understand and generalise the relationship between the dielectric properties and biophysical properties of bone. To this end, the next sub-section presents a detailed overview of the dielectric properties of animal and human bone tissues both for low and microwave frequency range.

2.5.1 Dielectric Properties of Bone in Low-Frequency Range

This sub-section reviews the dielectric properties of bone in the low-frequency range and analyses the confounders that may have resulted in variations in the reported data. Fourteen studies have reported the dielectric properties of bone from 1983 – 2018. The reviewed studies have reported the dielectric properties of bones and the relationship between bone dielectric properties and bone quality (in terms of BMD) across the low frequency range (10 Hz – 1 GHz). Across the frequency range of interest, all of the studies investigated *ex vivo* dielectric properties of bones, and no study has reported the *in vivo* dielectric properties of bones. The bone samples were acquired from different species: seven studies reported dielectric properties of human bones; five studies reported the properties of bovine bones; one study reported the properties of porcine bones, and one study reported the rat bone properties. The techniques employed to measure the dielectric properties of bones also varied across different studies. The study reference, study type, frequency range, source of a bone sample, and measurement technique of each reviewed study are tabulated in Table 2.1.

Table 2.1: Comparative description of reported studies.
ε = relative permittivity; σ = conductivity; IA=Impedance Analyser

Reference	Study Type	Frequency Range	Source	Measurement Technique	Dielectric Properties
Kosterich *et al.* [60]	*ex vivo*	10 Hz–100 MHz	rodent cortical bone	Platinum Electrodes, IA, Vector impedance meter	ε = (6.4 ± 2.4)×102, σ(S/m) = 13.3±2.8 (at 10 kHz)
Reddy and Saha [61]	*ex vivo*	1 kHz–1 MHz	bovine cortical bone	Differential technique	ε_{axial} = 688 (at 10 kHz)
Mercato and Garcia [62]	*ex vivo*	1 kHz–1 MHz	bovine cortical bone	Differential technique	$\varepsilon_{distal\ epiphysis}$ = 29400 (at 1 kHz)
De Mercato and Sanchez [63]	*ex vivo*	100 Hz, 10 kHz and 1 MHz	bovine cortical bone	Chlorided silver metal Electrodes, Automatic IA	σ_{axial} = 66 ± 7.3(μS cm^{-1}) to 107±2.5(μS cm^{-1})
Gabriel *et al.* [64]	*ex vivo*	10 Hz–20 GHz	porcine cortical bone	IA, Network analyser OECL probes	ε = 1.0E+3-1.0E+1 σ(S/m)=1.0E-2-1.0E+1
Sierpowska *et al*. [41]	*ex vivo*	100 Hz–10 MHz	bovine trabecular bone	Stainless-steel Electrodes, LCR meter	ε = 290±130, σ(S/m)=3.6±1.4
Unal *et al*. [44]	*ex vivo*	20 Hz–2 MHz	bovine cortical bone	Text fixture, LCR meter	ε = 8; σ(μS m^{-1}) = 0.1
Singh and Beharl [65]	*ex vivo*	0.5–108 MHz	human cortical bone	Q meter, vector impedance meter	ε = 10 (at 10 MHz)
Saha and Williams [66]	*ex vivo*	120 Hz–10 MHz	human trabecular bone	Chlorided silver metal Electrodes, LCR meter	ε = 33.06±8.82 (at 10 MHz), σ(mS cm^{-1})=3.6
Saha and Williams [54]	*ex vivo*	120 Hz–10 MHz	human cortical bone	Chlorided silver metal Electrodes, LCR meter	ε = 308±72, σ (S/m) = 5.26±2.22 (at 10 kHz)
Saha and Williams [67]	*ex vivo*	120 Hz–10 MHz	human trabecular bone	Chlorided silver metal Electrodes, LCR meter	ε = 601±194, σ = 1.96±0.93 (Lateral-medial Direction, at 10 kHz)

Williams and Saha [53]	*ex vivo*	10 kHz, 100 kHz, and 1 MHz	human trabecular and cortical bone	Chlorided silver metal Electrodes, LCR meter	r = 0.4285 between resistivity of human cortical bone and density measures
Sierpowska *et al.* [39]	*ex vivo*	50 Hz–5 MHz	human trabecular bone	Stainless-steel Electrodes, LCR meter	ε = 34.9±4.7 (femur), 31.6±7.7 (Tibia); σ(S/m) = 0.085±0.035 (femur), 0.101±0.034 (Tibia)
Haba *et al*. [68]	*ex vivo*	20 Hz	human trabecular bone	Impedance spectroscopy	ε = $(8.1\times10^6)\pm(5.2\times10^6)$

2.5.1.1 Dielectric Properties of Animal Bone Tissue in Low-Frequency Range

This sub-section reviews studies that have investigated the dielectric properties of animal bone tissue in the low-frequency range (10 Hz – 1 GHz), presented in chronological order.

In 1983, Kosterich *et al*. [60] examined the dielectric properties of freshly excised and formalin-fixed cortical femoral bone samples from rats across the frequency range of 10Hz - 100 MHz. The bone sample size was six. An impedance analyser and a vector impedance meter were used to measure the complex impedance, with the bone samples placed between platinum electrodes. It was observed that the conductivity of fresh bone is 2 – 3 times higher than the conductivity of formalin-fixed bone and that the conductivity for both types of bone samples was independent of frequency below 100 kHz. It was observed in the study that, the conductivity of bone samples increases as a power function of frequency. At 100 Hz, the average conductivity of six bone samples was found to be 12.6 mS/m and 4.8 mS/m for fresh and formalin-fixed bone samples respectively. The average dielectric properties of six bone samples are tabulated in Table 2.2.

TABLE 2.2: Permittivity and conductivity values of rat bones at 37° C.

Frequency	Conductivity mS/m (Fresh Bone)	Conductivity mS/m (Fixed Bone)	Permittivity (Fresh Bone)	Permittivity (Fixed Bone)
100 Hz	12.6 ± 2.6	4.8 ± 0.7	$(3.8 \pm 2.0) \times 10^3$	$(1.6 \pm 0.5) \times 10^3$
1 kHz	12.9 ± 2.7	4.8 ± 0.7	$(1.0 \pm 0.5) \times 10^3$	$(7.7 \pm 1.0) \times 10^2$
10 kHz	13.3 ± 2.8	4.9 ± 0.7	$(6.4 \pm 2.4) \times 10^2$	$(4.2 \pm 0.5) \times 10^2$
100 kHz	14.4 ± 2.9	5.4 ± 0.6	$(2.8 \pm 0.3) \times 10^2$	$(1.9 \pm 0.3) \times 10^2$
1 MHz	17.3 ± 3.2	7.2 ± 1.1	$(8.7 \pm 1.3) \times 10^1$	$(8.1 \pm 1.2) \times 10^1$
10 MHz	23.7 ± 4.4	13.5 ± 2.3	$(3.7 \pm 0.5) \times 10^1$	$(4.0 \pm 0.7) \times 10^1$

Next, in 1984, Reddy and Saha [61] examined the dielectric properties of fluid-saturated cortical bovine bone across the frequency range of 1kHz – 1 MHz. The bone sample size was five and the measurements were performed in all three principal directions (longitudinal, circumferential, and radial) of bone. A differential technique was used for dielectric properties measurement. The impedance was reported to be the lowest in the axial direction, whereas the specific resistivity in the radial direction was higher than that of the circumferential and axial directions. At 10 kHz, the values of specific resistance were found to be 54, 36, and 17 kΩ in radial, circumferential, and axial directions respectively. Similarly, at 10 kHz, the values of specific capacitance were found to be 21.4, 24.74, and 60.87 pF cm^{-1} in radial, circumferential, and axial directions respectively. The relative permittivity was found to be highest in the axial direction compared to radial and circumferential directions, as shown in Table 2.3.

TABLE 2.3: Permittivity values of bovine cortical bones.

Frequency	Axial Direction	Circumferential Direction	Radial Direction
100 MHz	74	30	23

In 1988, Mercato and Garcia [62] presented a comparative analysis between the dielectric properties of the proximal and distal epiphysis (The epiphyses are two extremes of the tibia. The proximal epiphysis of the tibia is near to knee and distal epiphysis is close to the ankle) with diaphysis (the diaphysis is the central portion of the bone between proximal and distal epiphyses) in a frequency range of 1 kHz – 1 MHz. The bone specimens were acquired from a bovine femur. The dielectric properties of bone samples were measured using the differential method. The measurement results indicated that the specific capacitance values in both epiphyses were larger than those obtained in diaphysis at any frequency. The relative permittivity was observed to be highest in the proximal epiphysis compared to distal epiphysis, and diaphysis, as shown in Table 2.4.

TABLE 2.4: Permittivity values of the bovine femur at proximal, distal epiphysis, and diaphysis of bovine cortical bones.

Frequency	**Extreme Proximal Epiphysis**	**Distal Epiphysis**	**Mid Region Proximal Epiphysis**	**Diaphysis**
1 kHz	91049	85268	78948	68958

In 1991, De Mercato and Sanchez [63] examined the longitudinal variability of electric properties in three principal directions (radial, axial and tangential) along the diaphysis of bovine cortical femoral bone samples at three frequencies: 100 Hz, 10 kHz, and 1 MHz. The bone sample size was nine. The dielectric properties were measured using an impedance analyser. It was observed that the conductivity and permittivity show significant variations along the diaphysis. The conductivity and relative permittivity values increased in magnitude near the epiphyses. The conductivity was found to be highest in the axial direction at all three measurement frequencies, intermediate in the tangential direction, and least in the radial direction. In conductivity, a variation of 47%, 53%, and 59% were observed at different positions in axial, tangential, and radial directions respectively. The relative permittivity and conductivity values are tabulated in Table 2.5.

TABLE 2.5: Permittivity and conductivity values of bovine cortical bone in three principal directions.

Frequency	Dielectric Properties	Axial Direction	Radial Direction	Tangential Direction
1 kHz	Relative Permittivity	870	780	730
5 MHz	Conductivity (μS/cm)	73	40.2	54.5

In 1996, Gabriel *et al*. [64] examined the dielectric properties of cortical and trabecular bone samples across the frequency range of 10 Hz – 20 GHz. Multiple measurement techniques were used. Specifically, an impedance analyser, network analyser, and open-ended coaxial probes (OECL) probes were used to measure the dielectric properties of bones. The bone samples were obtained from porcine. It was observed that the dielectric properties of trabecular bone are higher than those of cortical bone over the investigated frequency range. However, this study only measured the dielectric properties of porcine cortical and trabecular bone samples.

In 2003, Sierpowska *et al*. [41] examined the dielectric properties of bovine trabecular bone samples across a frequency range of 100Hz – 10 MHz. Electrical current was employed on samples through two round stainless-steel electrodes placed in a faraday cage with an LCR meter. The bone sample size was forty. This study also investigated the relationship between dielectric properties and vBMD. The vBMD was measured by dividing the aBMD with the sample thickness that was measured with a micrometre, where the aBMD was measured by DXA. A strong positive linear correlation was observed between the vBMD and the dielectric properties ($r = 0.866$). In this study, different sites of the bovine femur were considered and it was observed that at $f = 50\,kHz$ the relative permittivity of femoral caput was highest (381) and the femoral greater trochanter was lowest (85). The corresponding vBMD in these sites were 0.586 gcm^{-3} and 0.198 gcm^{-3}, respectively. At $f = 50\,kHz$, the conductivity of femoral lateral condyle was found to be highest (4.2 Sm^{-1}) and least in the femoral medial condyle.

Most recently, in 2018, Unal *et al*. [44] examined the relationship between the dielectric properties and the mechanical properties (toughness, strength, and elastic modulus) across a frequency range of 20 Hz – 2 MHz. The measurements were

performed on wet and increasingly dehydrated bovine cortical bone samples. The sample size was twenty-four. The dielectric properties of bones were measured using an LCR meter and a test fixture was used to place the bone samples. It was observed that the dielectric properties of bone vary as a result of dehydration of the bone. The authors found that the bound and unbound water components are major determinants of bone dielectric properties. It was observed in this study that the impact of unbound water on the dielectric properties is more significant than that of the bound water. The authors emphasised that their findings strongly suggest that dielectric properties of cortical bone may be used to identify the bone strength and toughness and hence further *in vivo* studies can be carried out.

2.5.1.2 Dielectric Properties of Human Bone Tissue in Low-Frequency Range

This sub-section reviews studies that have investigated the dielectric properties of human bones in the low-frequency range (10 Hz – 108 MHz). The studies are discussed in chronological order.

In 1984, Singh and Beharl [65] examined the dielectric properties of human cortical femur bone across a frequency range of 0.5 – 108 MHz. In this study, the parameters of resistivity, relative permittivity, dissipation factor, impedance, and phase angle were measured in the bone to understand the mechanism of electrical osteogenesis (the process of osteogenesis by using electrical stimulation). A Q-meter and vector impedance meter were used to measure the dielectric properties. The experiments revealed that the resistivity, relative permittivity, and impedance decrease as frequency increases. It was found that the resistivity and relative permittivity variations are least in the collagen, intermediate in the bone, and highest in the apatite. The comparative analysis of relative permittivity variation over the observed frequency range for human bone, apatite, and collagen is shown in Figure 2.3.

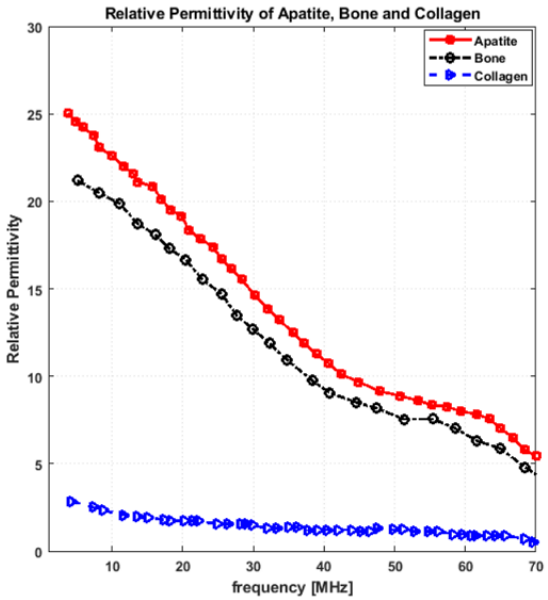

Figure 2.3: Comparison of relative permittivity for human bone, apatite, and collagen [65].

In 1992, Saha and Williams [66] examined the electrical (resistivity and specific capacitance) and dielectric properties of wet human trabecular bone as a function of frequency (120Hz – 10MHz) and direction. The bone samples were acquired from the distal tibia of three patients (two male, one female). To measure the dielectric properties of bone samples in all three principal directions (longitudinal, circumferential, and radial), an LCR meter was used. The bone samples were placed between chlorided-silver electrodes. The mean resistivity of 30 trabecular bone specimens at 100 kHz in the longitudinal, anterior-posterior, and lateral-medial direction was 500 ohm-cm, 613 ohm-cm, and 609 ohm-cm respectively, whereas the mean specific capacitance of these bone samples at 100 kHz in the longitudinal, anterior-posterior, and lateral-medial direction was 8.64 $pFcm^{-1}$, 615.25 $pFcm^{-1}$, and 14.64 $pFcm^{-1}$ respectively. It was observed that the dielectric properties are significantly dependent on frequency; however, resistivity and impedance are not highly frequency dependent. The dielectric properties showed an anisotropic behaviour since the values for the longitudinal direction differ from those obtained in the other two orthogonal directions. However, the values of the properties for the anterior-posterior direction and the lateral-medial direction show a significant correlation.

In 1992, Saha and Williams [54] examined the electrical and dielectric properties of wet human cortical bone. The bone samples were acquired from the distal tibia of

a 54-year-old male. An LCR meter was used to measure the dielectric properties of the bone samples in all three principal directions. The bone samples were placed between chlorided-silver metal electrodes. The mean resistivity value of 10 cortical bone samples at 100 kHz in the axial, circumferential, and radial directions were 1.55 kΩ-cm, 15.79 kΩ-cm, and 21.5 kΩ-cm respectively; whereas the mean specific capacitance of these bone samples at 100 kHz in the axial, circumferential, and radial directions were 33.81 $pFcm^{-1}$, 9.98 $pFcm^{-1}$, and 9.83 $pFcm^{-1}$ respectively. The resistivity was found to be highest in the radial direction and lowest in the longitudinal direction. Conversely, the specific capacitance was found to be highest in the longitudinal direction and lowest in the radial direction. The dielectric properties were measured in the radial direction, and it was reported that the dielectric properties of rat bones measured in [60] have larger values, compared to the dielectric properties of wet human cortical bone measured in this study.

In 1995, Saha and Williams [67] reported a comparative study on the dielectric properties of wet human cortical and trabecular bone samples across the frequency range of 120 Hz – 10 MHz. The study was performed on bone samples acquired from the distal tibia of three patients (two male, one female). The electrical and dielectric properties of cortical and trabecular bones were measured in three principal orientation of bones. An LCR meter was used to measure the dielectric properties of bone samples. The bone samples were placed between chlorided-silver metal electrodes. It was observed that the resistivity of human cortical bone is approximately 3.1 times higher than that of trabecular bone in the longitudinal direction and 25 times higher in the transverse direction. A similar trend was observed in the relative permittivity also. The relative permittivity of cortical bone was found to be approximately 3.9 times higher than that of the trabecular bone in the longitudinal direction, and 0.65 times higher in the transverse direction. The dielectric properties of both cortical and trabecular bone samples in all three directions at 10 kHz are tabulated in Table 2.6.

TABLE 2.6: Relative permittivity and conductivity values of trabecular and cortical bone samples in three orthogonal directions at 10 kHz.

Trabecular Bone		
Direction	**Conductivity (mS/cm)**	**Dielectric Permittivity**
Longitudinal	2.31 ± 1.01	574 ± 371
Anterior-posterior	1.83 ± 0.69	594 ± 154
Lateral-medial	1.96 ± 0.93	601 ± 194
Cortical Bone		
Direction	**Conductivity (mS/cm)**	**Dielectric Permittivity**
Axial	66.2 ± 15.3	1.267 ± 66.3
Circumferential	7.0 ± 2.7	307 ± 61.6
Radial	5.3 ± 2.2	308 ± 111

In 1996, Williams and Saha [53] investigated the relationship of electrical properties of wet cortical and trabecular human bones with the wet, dry, and ash tissue densities. The bone samples were acquired from the human distal tibia. The measurements were performed at the frequencies of 10kHz, 100 kHz, and 1 MHz. As in the previous studies, the properties were measured using an LCR meter with chlorided-silver metal electrodes. To prevent dehydration, the measurements were carried out in a humidity chamber at near 100% relative humidity. A significant positive correlation ($r = 0.617$, at 100 kHz) was reported between the dielectric properties of trabecular bone and density measures (wet, dry, and ash bone tissue densities). Similarly, a positive correlation was observed between the specific capacitance of trabecular bone and density measures, whereas a weak correlation ($r = 0.4285$) was found between the resistivity of human cortical bone and density measures. It was observed that no correlation existed between the resistivity of trabecular bone and density measures.

In 2005, Sierpowska *et al*. [39] examined the effect of dielectric properties variation on human trabecular bones acquired from different anatomical sites, across a frequency range of 50 Hz – 5 MHz. Trabecular bone samples were obtained from the distal femur and proximal tibia from thirteen human knee joints. The dielectric properties were measured by applying an electrical current to samples through two

round stainless-steel electrodes placed in a Faraday cage using an LCR meter. It was observed that the difference between the relative permittivity for femoral and tibial bone samples at 1.2 MHz was 9.5% approximately. However, the difference in conductivity at 1.2 MHz was approximately 16% between femoral and tibial bone samples.

In 2017, Haba *et al*. [68] examined the dielectric properties of trabecular and sub-chondral human femoral head bone of 20 patients who underwent a total hip replacement due to hip osteoarthritis. The dielectric properties of the bone samples were measured over 0.10 Hz – 10 kHz using impedance spectroscopy. The two electrodes were gold plated brass plates. A non-linear correlation between BMD and dielectric properties was reported in this study. It was suggested that electrical impedance spectroscopy can be applied for *in vivo* measurements of dielectric properties.

2.5.1.3 Comparative Analysis of Dielectric Properties of Bones in Low-Frequency Range

Section 2.5.1.1 and 2.5.1.2 detailed the dielectric properties of animal and human bone tissues respectively in a low-frequency range in chronological order. As the target anatomical site to monitor osteoporosis is trabecular bone, therefore, for in-depth analysis, the following section evaluates the variations observed in dielectric properties of cortical bone and trabecular bone separately.

2.5.1.3.1 Variations in Dielectric Properties of Cortical Bone

This sub-section compares the inter and intra-species variation of the dielectric properties of cortical bone reported across different studies. The relative permittivity and conductivity of cortical bone samples in the low-frequency range are plotted in Figure 2.4 (a) and (b) respectively. The data in the literature are reported across different frequencies, therefore, for the comparison, a common frequency point (10 MHz) is chosen to evaluate the variation in the data. Comparative analysis indicates that:

1. There is a significant variation in the relative permittivity of the cortical bone (mean± standard deviation (SD) = 40.93 ± 35.63) across different species (human, porcine, bovine, and rat), which is also in line with the BMD variation reported in [69].
2. The relative permittivity of the bovine cortical bone (52.86 ± 54.59) is

significantly higher than that of the human cortical bone (29.33 ± 8.62). Considering the higher BMD of bovine compared to a human, a positive correlation between the relative permittivity and BMD can be inferred, which is also in line with the findings of [53],[41].

3. The variation in the relative permittivity of human cortical bone (SD = 8.62, 29%) is lower than the variation in bovine cortical bone (SD = 54.59, 103%). The dielectric properties reported by Unal *et al*. [44] are found to be significantly low in comparison to the literature. The underneath reason for this difference may be due to; different measurement procedures, sample preparation, bone composition, the porosity of bone sample, age, and anatomical location of bone.

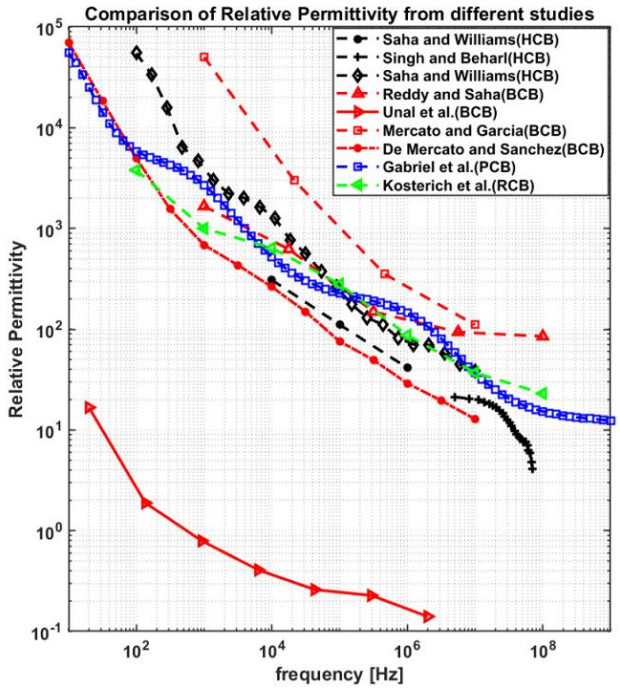

(a)

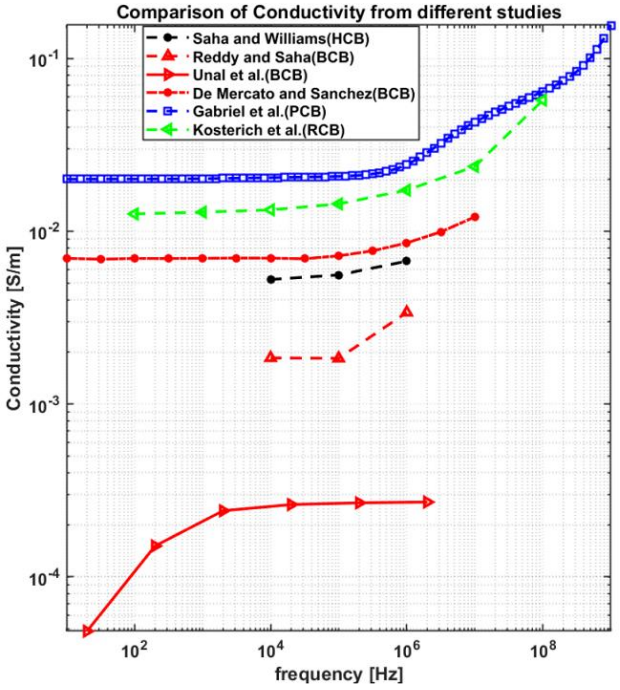

(b)

Figure 2.4: Comparison of dielectric properties of cortical bone from reported studies. The graph shows a comparison between the dielectric properties of bones sourced from different species (human, bovine, porcine, and rat). The dielectric properties reported for Unal *et al.* are for the wet bone samples. HCB = Human Cortical Bone; BCB = Bovine Cortical Bone; PCB = Porcine Cortical Bone; RCB = Rat Cortical Bone.

2.5.1.3.2 Variations in Dielectric Properties of Trabecular Bone

This sub-section compares the inter and intra-species variation of the dielectric properties of trabecular bone reported across different studies. The relative permittivity and conductivity of trabecular bone over the low-frequency range are shown in Figure 2.5 (a) and (b) respectively. The available studies did not allow the same choice of frequency as in the previous section, so for the comparison, 10 kHz is chosen to calculate the variation in the data. The comparative analysis indicates that:

1. There is a significant variation in the relative permittivity of the trabecular bone (mean ± SD = 23904 ± 42180) between different species (human, bovine and porcine).
2. There is a significant variation in the relative permittivity of the human trabecular bone. The mean and standard deviation from different studies is found to be 38777 ± 52238.
3. The relative permittivity values of porcine and bovine trabecular bone samples show less variation, the mean percentage difference between relative permittivity values of porcine and bovine trabecular bone samples is 20%.

It is assumed that the intra-species differences between the bone dielectric properties are mainly due to the type of sample (i.e., the anatomical location), measurement technique, and age of species, however, the inter-species differences between the bone dielectric properties are due to bone samples acquired from different species (bovine, porcine, human, rat).

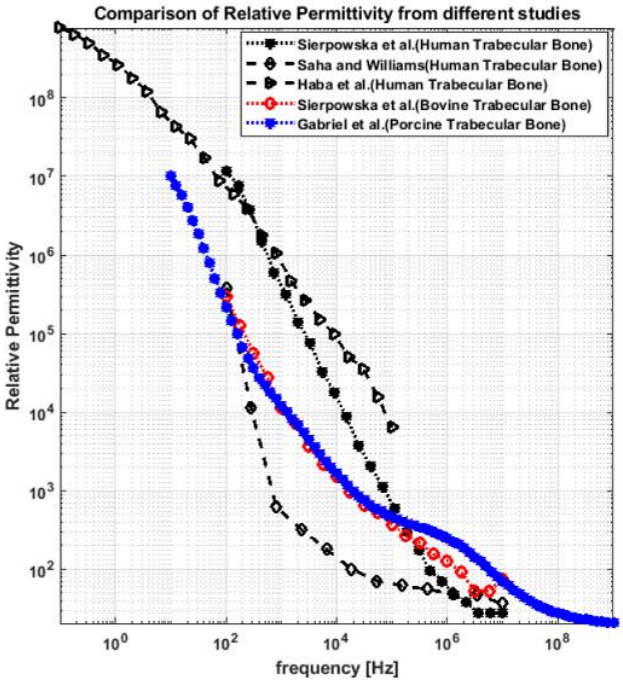

(a)

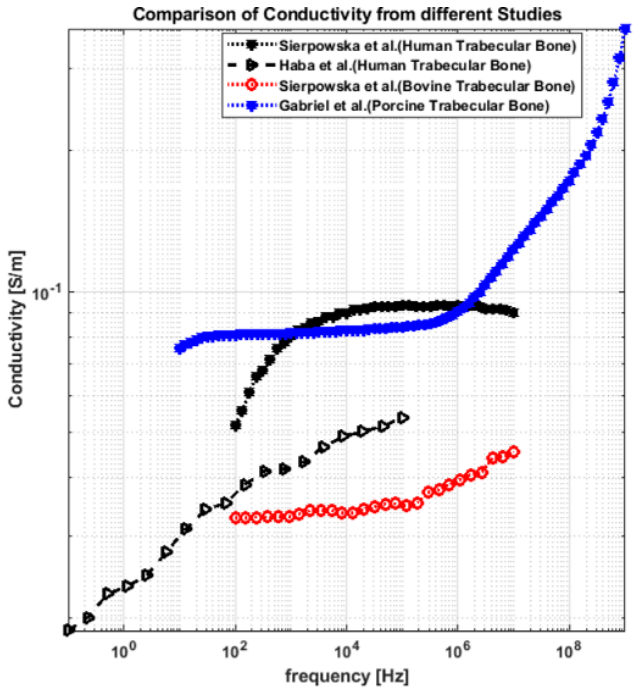

(b)

Figure 2.5: Comparison of dielectric properties of trabecular bone from reported studies. The reported studies exhibit variation in results and the dielectric properties of trabecular bones of human, bovine, porcine, and rat all vary from each other.

2.5.1.4 Relationship between Bone Dielectric Properties and Bone Mineral Density

The dielectric properties of bones are found to be influenced by BMD [7],[18]; hence, the quantitative relationship between dielectric properties of bone and BMD can potentially be exploited to develop an electromagnetic-based imaging device for monitoring of osteoporosis [2],[18]. Therefore, this sub-section compares the relationship between the dielectric properties of bones and BMD reported across different studies. A total of three studies reported on the relationship between BMD and dielectric properties, two of which involved human bones [53] and [38] and one which involved animal bones [41]. The comparative analysis indicates that:

1. Dielectric properties of bone appear to vary monotonically with BMD [41], [18]. It is well reported in the literature that the BMD varies with age [13], [70], thus it can be deduced that the dielectric properties of bones may also vary with age [18].
2. Two of the three studies reported a positive linear correlation between the dielectric properties and the BMD, while one reported a non-linear correlation.

To summarize, Sierpowska *et al*. [41] found a strong positive linear correlation between BMD and dielectric properties ($r = 0.866$) at 50 kHz for bovine trabecular bone samples. Consistent with Sierpowska *et al*. [41], Williams and Saha in [53] found a correlation of $r = 0.617$ between the dielectric properties and BMD at 100 kHz. Both studies are in agreement with each other, however, the difference between the correlation coefficients may be due to the difference in species, as Sierpowska *et al*. [41] investigated the relationship for bovine trabecular bone samples and Williams and Saha in [53] investigated the same for human distal tibia. In contrast to the two above studies, Haba *et al*. [38] found a non-linear correlation between dielectric properties and BMD for human trabecular bone samples. The authors stated that the difference was likely due to the difference of bone samples from osteoarthritis human patients, unlike the above studies that utilised healthy bone samples. BMD values were not reported in this study and the change of dielectric properties was expressed in terms of percentage change of mineralisation.

In summary, the review of low-frequency dielectric properties of bones found a significant inter and intra-species variation in the dielectric properties. The intra-species variation can be associated with the difference in bone type, measurement technique, and sample handling. The studies examining the relationship between BMD

and dielectric properties found contradictory results. Two studies reported a positive linear correlation between BMD and the dielectric properties; however, one study found a non-linear correlation. Hence, the relationship between BMD and the dielectric properties of bones over the low-frequency range is not consistent. The microwave frequency band provides an alternate compared to the low-frequency band for the development of a non-invasive EM-based medical device for bone health monitoring. Further, bone itself has a heterogeneous structure and the distribution of bone mineralisation is not uniform [72]. Therefore, imaging resolution of the bone imaging modality would be an important consideration. To this end, a microwave frequency range of 0.5 – 8.5 GHz, which is similar to the frequency range used in preclinical breast imaging systems, would be a reasonable choice for bone imaging [72]. This frequency range could provide a good compromise between penetration depth and imaging resolution [73]. To this end, the following section summarises all available dielectric data of bone in the microwave frequency range, and analyses the confounders that may have resulted in variations in reported data. Therefore, the bone dielectric properties and the relationship between BMD and bone dielectric properties in the microwave frequency range are investigated in the following section.

2.5.2 Dielectric Properties of Bone in Microwave Frequency Range

This sub-section reviews the dielectric properties of bones in the microwave frequency range and analyses the confounders that may have resulted in variations in the reported data. Several studies have been performed to measure the dielectric properties of bones in the microwave frequency range [18], [23], [42], [45]–[49]. While some of these studies only measured the dielectric properties of bone, some studies also investigated the relationship between bone quality and bone dielectric properties. However, these studies are often limited in terms of the number of bone samples and the range of BMD of bone samples examined and do not provide a definite quantitative relationship between the BMD and the dielectric properties [7],[74]. Additionally, these studies differ in terms of measurement techniques, location of bone sample source, type of bones, and bone sample preparation methods. Each of these factors can influence the measured dielectric properties.

A total of seven studies have reported on the dielectric properties of bone in the microwave frequency range. These studies have evaluated the dielectric properties of bones and the interrelationship between bone dielectric properties and bone quality

across the microwave frequency range. Six of the studies investigated *ex vivo* dielectric properties of bones and one study analysed *in vivo* dielectric properties of bones. The source of bone samples in all studies varied from each other. Two studies reported dielectric properties of bovine bone samples, three studies reported the same for porcine bone samples, and two studies reported these properties for human bone samples. The techniques employed to measure the dielectric properties of bones also varied across the different studies. Three studies used OECL along with a vector network analyser, two studies employed an MWT system, and two studies used thin cell time-domain spectroscopy to acquire dielectric properties. The study reference, study type, frequency range, source of a bone sample, and measurement technique of each reviewed study are tabulated in Table 2.7.

Table 2.7: Comparative description of reported studies.
ε = relative permittivity; σ = conductivity; IA=Impedance Analyser

Reference	Study Type	Frequency Range	Source	Measurement Technique	Dielectric Properties
Ivancich *et al*. [47]	*ex vivo*	10 MHz-1.3 GHz	Adult bovine cortical and trabecular tibial bone	Thin cell time-domain spectroscopy (TDS) HP (1815B) Sampler, HP (1801A) oscilloscope, SNA (HP8711A)	ε = 9.64 (demineralised bone, 238.49 MHz), ε = 17.75 (native bone, 414.85 MHz)
Gabriel *et al*. [42]	*ex vivo*	10 Hz–20 GHz	Porcine cortical bone	OECL, IA (HP4192A), IA(HP 8753C), IA(HP8720)	ε = 1.0E+3-1.0E+1 σ (Sm^{-1}) = 1.0E-2-1.0E+1
Peyman *et al*. [24]	*ex vivo*	50 MHz–20 GHz	Porcine cortical bone	OECL, Network Analyser (Agilent 8720D)	ε = 28.1 ± 2.0, σ (Sm^{-1}) = 0.34 ± 0.04 (10 Kg, 450 Hz)
Irastorza *et al*. [9]	*ex vivo*	80 MHz–1 GHz	Bovine diaphysis femur cortical bone	OECL, HP (1815B) TDR/Sampler, HP (1801A) oscilloscope, SNA (HP8711A)	ε = 14.8 (natural bone) ε = 27.5 (demineralised bone) (80 MHz)
Meaney *et al*. [18]	*ex vivo*	900-1300 MHz	Porcine trabecular femoral bone	MWT	ε = 48, σ = 1.9 (1100 MHz)

Meaney *et al*. [17]	*in vivo*	900-1700 MHz	Human trabecular calcaneus bone	MWT	ε = 13.6, σ =0.84 (1300 MHz)
Irastorza *et al*. [46]	*ex vivo*	100-1300 MHz	Human trabecular femoral head bone	OECL, HP (1815B) TDR/Sampler, HP (1801A) oscilloscope, SNA (HP8711A)	ε = 46.85 , σ = 0.578 (400 MHz)

2.5.2.1 Dielectric Properties of Animal Bone Tissue in Microwave Frequency Range

This sub-section reviews all studies that have investigated the dielectric properties of animal bone tissue in chronological order, along with studies that have examined the relationship between the dielectric properties of animal bone tissue and the bone quality (in terms of both BMD and bone volume fraction (BVF)) in the microwave frequency range.

In 1992, Ivancich *et al*. [47] examined the (*ex vivo*) dielectric properties of water-saturated cortical bone in both a natural (untreated) and demineralised state across the frequency range of 10 MHz - 1.3 GHz using time-domain spectroscopy. The bone sample was taken from an adult bovine tibia and only one tibia was used for measurements. This study found that the relative permittivity for demineralised cortical bones is significantly higher than the relative permittivity of natural bones. Since the BMD of demineralised bone is less than that of natural bone, the study suggests a negative correlation between BMD and relative permittivity. The relative permittivity values are shown in Figure 2.6. This study did not report conductivity results and demineralisation levels were not quantified in terms of the BMD.

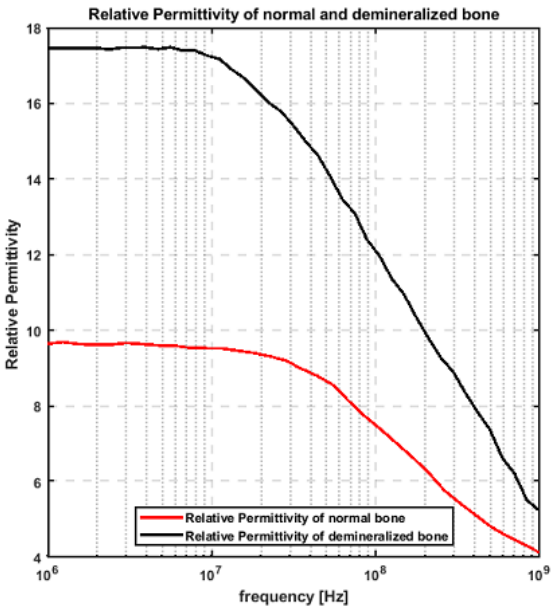

Figure 2.6: Permittivity for normal and demineralised bone samples [47].

Next, in 1996, Gabriel *et al*. [42] examined the (*ex vivo*) dielectric properties of cortical and trabecular bone across the frequency range of 10 Hz – 20 GHz, with impedance and network analysers and OECL probes. The bone samples were porcine in origin and the sample size was not specified in the paper. The permittivity and conductivity values are shown in Figure 2.7. It was observed in this study that the dielectric properties of trabecular bone are higher than those of cortical bone over the observed frequency range. This study only measured the dielectric properties of porcine cortical and trabecular bone samples and did not investigate the relationship between dielectric properties and BMD.

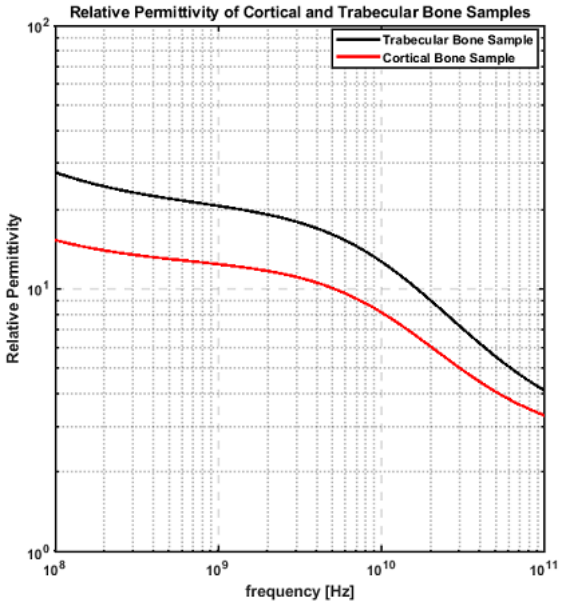

(a)

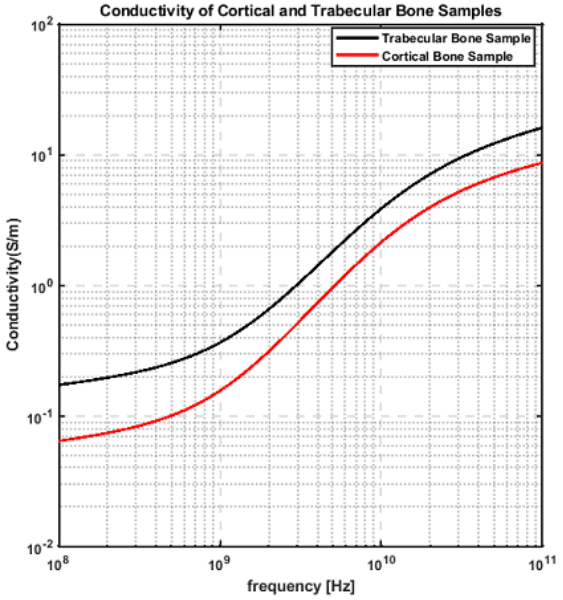

(b)

Figure 2.7: Permittivity and Conductivity for porcine cortical bone sample [42]. The dielectric properties of trabecular bone samples are higher than cortical bone samples.

In 2009, Peyman *et al*. [49] examined the (*ex vivo*) dielectric properties of cortical bone samples across the frequency range of 50 MHz – 20 GHz, using OECL probes and a network analyser. The bones were acquired from porcine models of three different ages (and therefore had an animal sample size of 3). This study aimed to examine the variation of dielectric properties of the tissue with age. The dielectric properties were reported for only four frequency points (450 MHz, 900 MHz, 1800 MHz, and 2400 MHz) and are shown in Figure 2.8. Variations in dielectric properties

with age were observed over the microwave frequency range, due to the reduction of water content in tissues [49]. The dielectric properties of porcine cortical bone decreased significantly as a function of animals' age.

This result suggests a negative correlation between dielectric properties and ageing. As BMD also decreases as a function of age, a positive correlation between BMD and dielectric properties is suggested by this study. Limitations of this study included that measurements were performed for only four frequency points, and the BMD of bone samples was not explicitly quantified within the study. The dielectric properties were reported against the normal demineralisation process of ageing; hence no quantitative relationship can be established between dielectric properties and BMD levels.

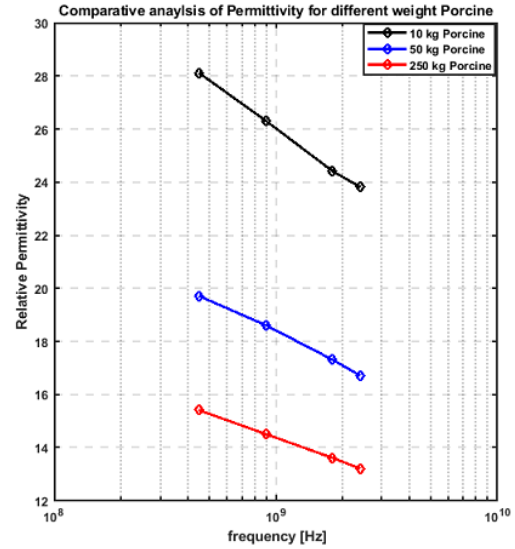

(a)

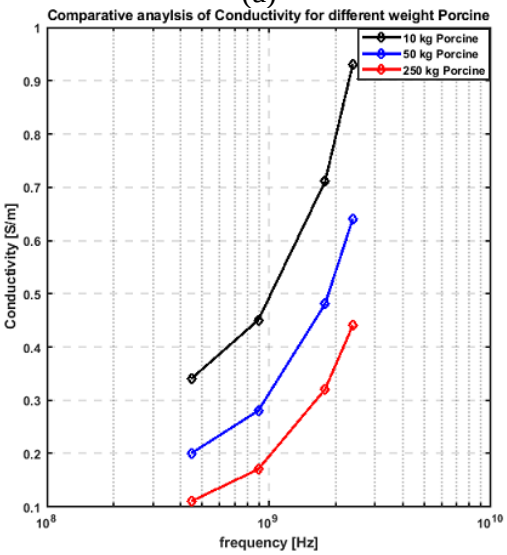

(b)

Figure 2.8: Permittivity and conductivity of ageing porcine tissues at selected frequencies [49]. The dielectric properties reduce as age increases.

In 2011, Irastorza *et al*. [48] examined the (*ex vivo*) dielectric properties of fluid saturated trabecular and cortical bone from bovine animal models across the frequency range of 80 MHz – 1 GHz, using time-domain spectroscopy. The trabecular bone samples were acquired from the femoral condyle and femoral groove, whereas the cortical samples were acquired from the diaphysis of the femur. The number of samples examined was two. The study was performed on natural and demineralised bone samples. It was observed from these measurements that the relative permittivity for both trabecular and cortical bone samples was lower for natural bone samples compared to demineralised samples, as shown in Table 2.8.

Echoing the results of Ivancich *et al*. [47] this study suggests a negative correlation between BMD and relative permittivity. The authors in this study did not report the exact BMD values of both natural and demineralised bone samples. The relative permittivity values for each sample in their natural and demineralised state are expressed at different frequencies also. No result was reported for the conductivity values of demineralised bone samples.

Table 2.8: Measurements on cortical and trabecular bone discs [48].

Parameters	**Sample 1 (Natural)**	**Sample 1 (Demineralised)**	**Sample 2 (Natural)**	**Sample 2 (Demineralised)**
ε_{mf}	14.8	27.5	16.0	42.6
$\Delta\varepsilon_{mf}$	2.1	1.8	1.8	2.3
f_r	452 MHz	247 MHz	580 MHz	264 MHz

More recently, in 2012 Meaney *et al*. [23] examined the (*ex vivo*) dielectric properties of trabecular bone submerged in a 0.9% saline solution over the frequency range of 900-1300 MHz, using an MWT system. The bone sample was taken from a single porcine femur. The study investigated the effect of bone demineralisation on dielectric properties. The bone sample was demineralised between successive microwave scans using acid treatment. The dielectric properties of the demineralised bones after each microwave scan were acquired from two-dimensional (2-D) reconstructed microwave images, as shown in Figure 2.9. A decreasing trend of values was observed in both permittivity and conductivity plotted against BVF as shown in Figure 2.14. Once again, a negative correlation between bone mineralisation and dielectric properties was observed, as shown in Figure 2.10. However, the study suggested that such experiments should be performed on *in vivo* or fresh bones to investigate the effect of blood vessels and marrow on dielectric properties that are found in the pores of bones. In this study, the variation in dielectric properties against

the percentage change of mineralisation level was presented, but again the BMD was not measured. Secondly, only one bone sample was considered for dielectric property measurement; hence the sample size was insufficient to draw any definite relationship between the mineralisation level of the bone sample and dielectric properties.

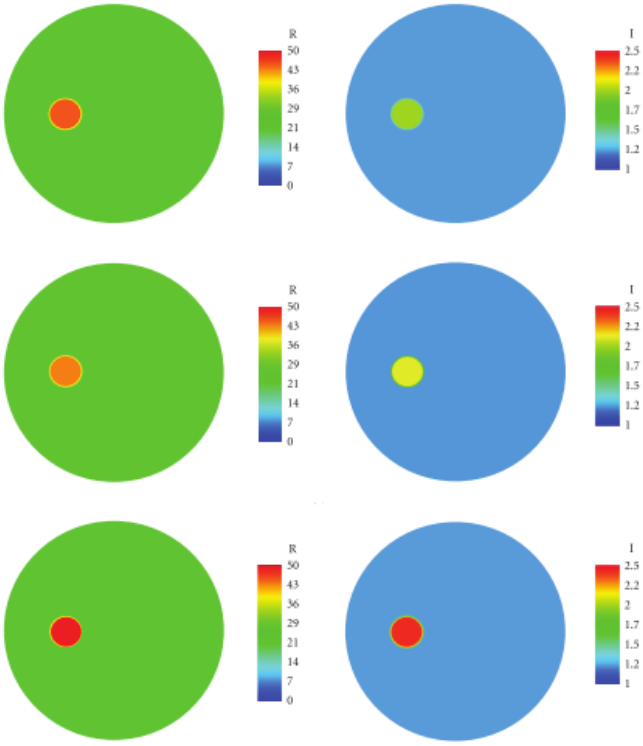

Figure 2.9: Reconstructed permittivity images (left) of the (a) 1st, (b) 2nd, and (c) 5th microwave scan of a saline-saturated bone specimen in a test tube at 1100 MHz, respectively. The images on the right are the corresponding conductivity images (from [23]). The dielectric properties are increasing as the mineralisation level of bones is decreasing after each microwave scan.

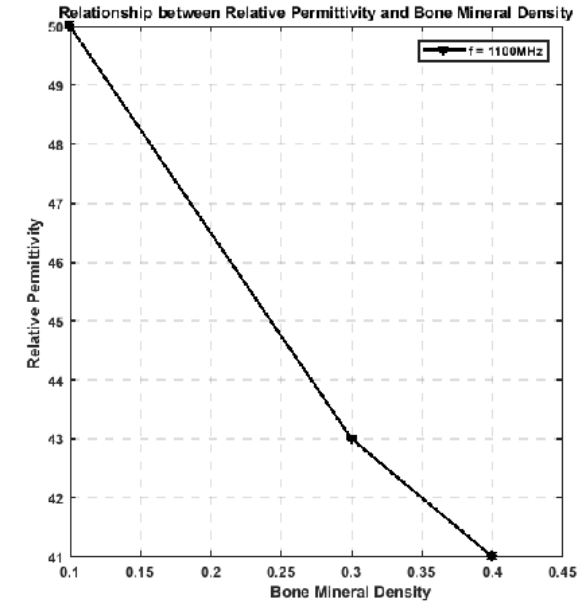

(a)

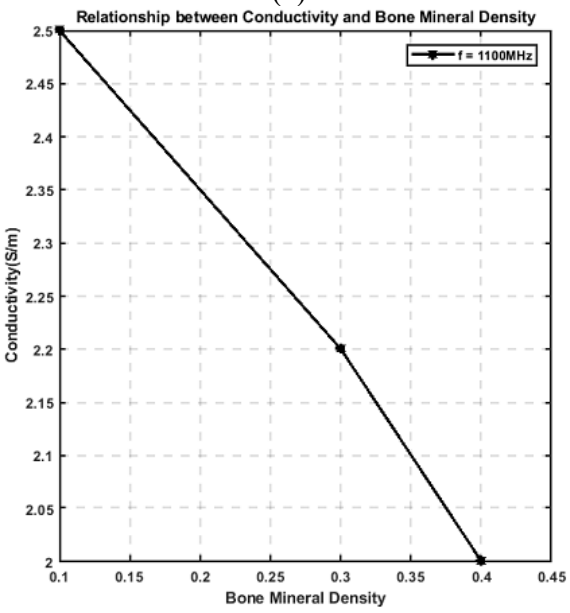

(b)

Figure 2.10: Relationship between the relative permittivity (top) and conductivity (bottom) with bone mineral density [23]. The negative correlation between dielectric properties and BMD.

2.5.2.2 Dielectric Properties of Human Bone Tissue in Microwave Frequency Range

This sub-section reviews all studies that have investigated the dielectric properties of human bone tissue in chronological order, along with studies that have examined the relationship between the dielectric properties of human bone tissue and the bone quality (in terms of both BMD and BVF) in the microwave frequency range.

In 2012, Meaney *et al*. [18] also examined the (*in vivo*) dielectric properties of the human calcaneus (heel) bone across the frequency range of 900-1700 MHz with a step size of 200 MHz, using the MWT system. The study was performed using two patients. Figure 2.11 (a) and (b) represent the soft-prior permittivity (top) and conductivity (bottom) reconstructed images for the first plane of the left and right heels of Patient 1 and Patient 2 respectively at 1300 MHz. The BMD values were acquired from QUS. It can be observed from Figures 2.11 (a) and (b) that the dielectric properties of the normal heel bone have lower values compared to the values of the affected heel bone.

Since the affected heel bone (with a low level of mineralisation) has high dielectric properties relative to those of the normal heel bone (which has a high level of mineralisation), a negative correlation between bone mineralisation and dielectric properties was once again observed. The dielectric properties against BMD are tabulated in Table 2.9. The study only considered two patients and measurements were performed at only one frequency. Therefore, while it reinforces the results of several historical dielectric studies, again no definite correlation between dielectric properties and BMD can be established from these results and further studies are required.

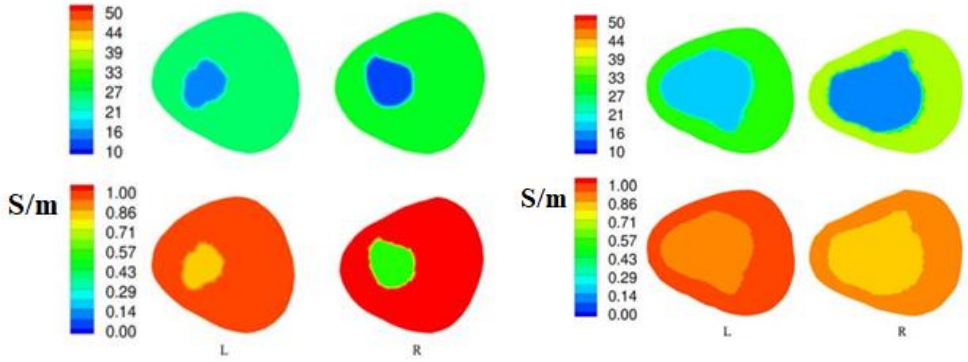

Figure 2.11: (a) 1300 MHz relative permittivity (top) and conductivity (bottom) soft-prior images for the first plane of the left and right heels of patient 1, respectively, (b) 1300 MHz permittivity (top) and conductivity (bottom) soft-prior images for the first plane of the left and right heels of patient 2, respectively (from [18]). Affected heel bone has higher dielectric properties compared to the normal heel bone. For Fig. 7, IEEE LICENSE received. License Number 4294280048384.

Table 2.9: Dielectric Properties against BMD values of two patients [18]

Patient	Foot	Ultrasound BMD	Relative Permittivity	% difference	Conductivity (S/m)	% difference
1	Affected	0.699	13.6	8.4%	0.84	45.2%
	Normal	0.773	12.5		0.53	
2	Affected	0.354	16.7	21.1%	0.92	13.9%
	Normal	0.311	13.5		0.80	

The % difference is between affected and normal feet values of relative permittivity and conductivity.

Irastorza *et al*. [46] in 2014, examined the (*ex vivo*) dielectric properties of trabecular bone across the frequency range of 100-1300 MHz, using OECL probes, a network analyser, and a time-domain reflectometer. The bone samples were taken from the femoral heads of patients that had undergone a total hip replacement, with the mean patient age being 80.7 years. The sample size was six, and therefore six femoral heads were obtained from surgeries. In this study, the authors found a negative correlation between BVF and the dielectric properties. Figure 2.12 represents permittivity and conductivity profiles for the trabecular bone samples. The results obtained both from experiments and simulations showed a significant linear negative correlation between BVF and dielectric properties. The higher the BVF, the lower the dielectric properties. However, the authors did not report any relationship between dielectric properties and BMD.

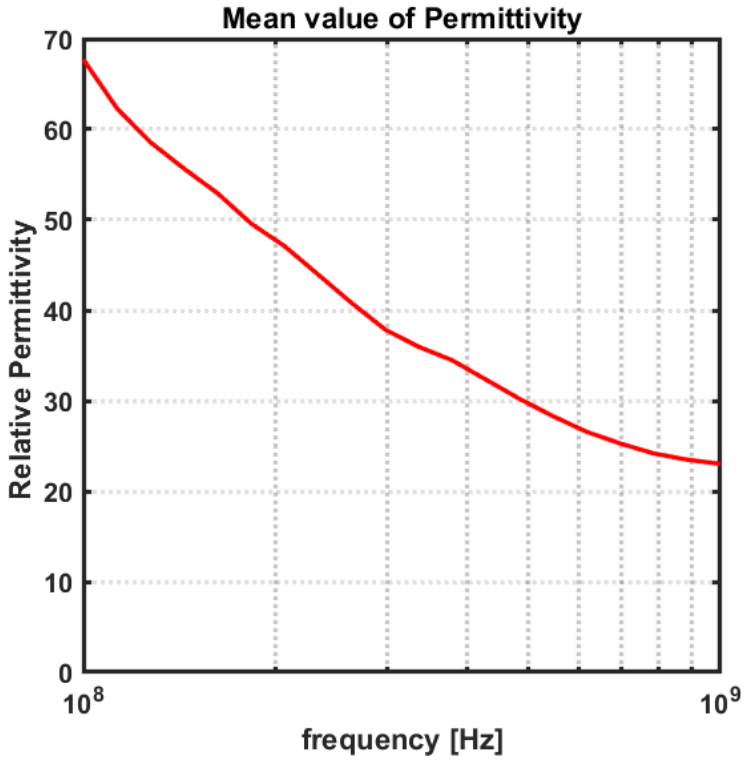

(a)

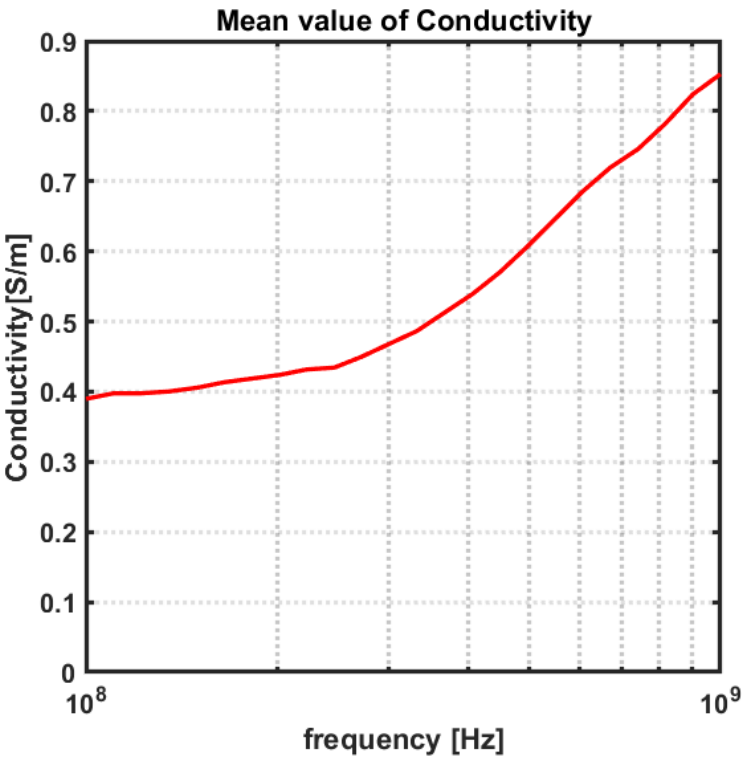

(b)

Figure 2.12: Mean value of relative permittivity and conductivity [46].

2.5.2.3 Comparative Analysis of Dielectric Properties of Bones in Microwave Frequency Range

Section 2.5.2.1 and 2.5.2.2 details the dielectric properties of animal and human bone tissues respectively in chronological order. For more in-depth analysis this section compares the dielectric properties of cortical bone and trabecular bone separately.

2.5.2.3.1 Variations in Dielectric Properties of Cortical Bone

This sub-section compares the inter and intra-species variation of the dielectric properties of cortical bone reported across different studies. One of the studies has reported dielectric properties of bovine cortical bone samples and two for porcine cortical bone samples. A comparison of the relative permittivity and conductivity of cortical bone samples in the microwave frequency range is shown in Figure 2.13 (a) and (b) respectively. The comparative analysis suggests:

1. There is a significant variation in the dielectric properties of bovine and porcine cortical bone. However, this difference may be due to the bovine bone samples being saturated in water during measurements. The mean percentage difference of relative permittivity values between bovine and porcine tissue is 17.46%.
2. Variations exist between the dielectric properties of porcine cortical bone reported in two different studies. The variation in dielectric properties of porcine cortical bones between [42] and [49] is likely due to the age difference of the porcine samples. The mean percentage difference of relative permittivity between both studies is 32.59%.

2.5.2.3.2 Variations in Dielectric Properties of Trabecular Bone

This sub-section compares the inter and intra-species variation of the dielectric properties of trabecular bone reported across different studies. The source of bone samples in all studies varied from each other [7]. Irastorza *et al*. [9] reported dielectric properties of bovine trabecular bone samples, Gabriel *et al*. [42] reported dielectric properties of porcine trabecular bone samples, and Irastorza *et al*. [46] reported dielectric properties of human trabecular bone samples. The techniques employed to measure the dielectric properties of bones also varied across the studies. A comparison of the relative permittivity and conductivity of trabecular bone samples in the

microwave frequency range is shown in Figure 2.13 (a) and (b) respectively. The comparative analysis indicates that:

1. The dielectric properties of trabecular bone are of higher magnitude than those of cortical bone.
2. The dielectric properties of trabecular bone from human femoral heads are much higher than those of other species. The mean percentage difference of relative permittivity between human and bovine trabecular bone is 51.57%.
3. Variations in dielectric properties are observed for bone samples acquired from different species: porcine, bovine, and human.
4. The conductivity profile of bones in the microwave frequency range also shows significant differences between values reported for samples of porcine, bovine, and human origin.

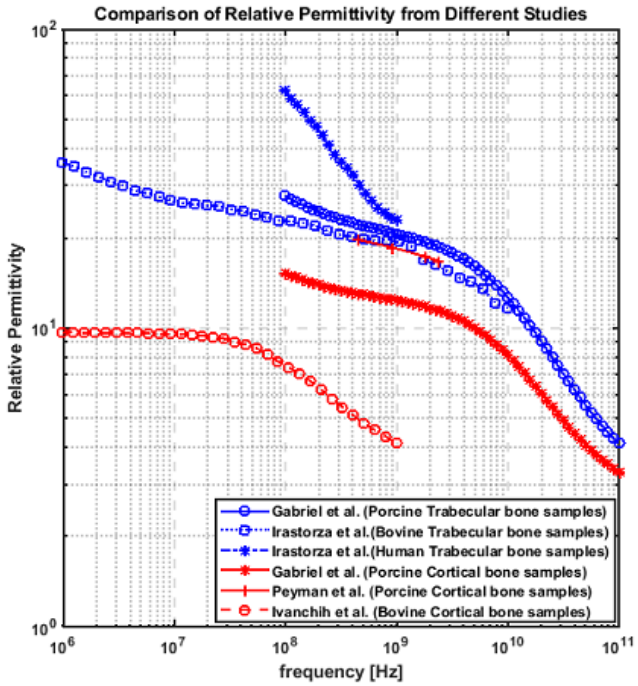

(a)

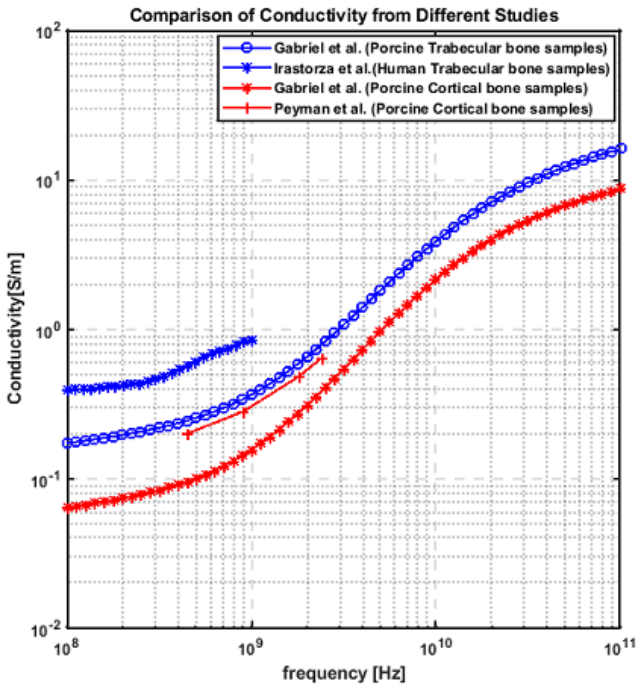

(b)

Figure 2.13: Comparison of relative permittivity and conductivity from reported studies. The reported studies exhibit variation in results; dielectric properties of trabecular bones are higher as compare to dielectric properties of cortical bones.

The differences observed in the dielectric properties are attributed to the source of bone location which is associated with inherent variability in bone composition and microstructure, measurement techniques, and sample preparation. Moreover, based on

the literature review no study has ever measured diseased human bone samples, which is of paramount importance for the development of EM-based diagnostic and therapeutic medical devices for bone diseases.

2.5.2.4 Relationship between Bone Dielectric Properties and Bone Mineral Density

Many studies that have examined the relationship between BMD and dielectric properties in low-frequency found contradictory results. Similarly, a contradictory relationship has been observed between BMD and dielectric properties in the microwave frequency range as well. The quantitative relationship between dielectric properties of bone and BMD can potentially be exploited to develop an MWT-based imaging device for the monitoring of osteoporosis [2],[18]. Therefore, this sub-section compares the relationship between the dielectric properties of bones and BMD reported across different studies. A total of five studies reported the relationship of BMD and dielectric properties, three of which involved animal bones and two involving human bones [18], [23], [47]–[49]. The comparative analysis indicates the following:

1. Dielectric properties of bone appear to vary consistently with BMD.
2. Since it is widely known that BMD varies with age, based on point 1 above, dielectric properties are also expected to vary with age.
3. Four of the five studies examined in this review reported a negative correlation between dielectric properties and BMD, while one reported a positive correlation.

To summarize, Peyman *et al*. [49] found that the dielectric properties reduce as a function of age for porcine cortical bone samples. Since BMD also reduces as a function of age, a positive correlation between BMD and dielectric properties can be inferred. Peyman's study did not report the absolute BMD values, and hence no definite conclusion can be drawn. Irastorza *et al*. [48] found that the dielectric properties for both natural trabecular and cortical bone have lower values compared to the demineralised state; hence a negative correlation is suggested. Meaney *et al*. [23] found a negative correlation between mineralisation levels and dielectric properties for a trabecular bone sample from a porcine femur (lower the mineralisation level higher the dielectric properties). BMD values were not reported in this study and the change of dielectric properties was expressed in terms of percentage change of

mineralisation. In a separate study, Meaney *et al*. [18] found a negative correlation between BMD and dielectric properties for two human patients. The evidence of the relationship between BMD and dielectric properties is inconsistent across the studies. Moreover, the sample size was small, a more comprehensive study is required over a large frequency range to quantify this relationship. The relationship between BMD and dielectric properties is of paramount importance for the characterisation of osteoporosis.

2.5.2.5 Relationship between Bone Dielectric Properties and Bone Volume Fraction

Apart from BMD, the quality of bone and fracture risk can also be well characterised by BVF (BVF = Bone Volume/Total Sample Volume) [7]. BVF is considered as one of the key parameters that explains the microstructure of bone and its relationship to the biomechanic response [46]. Since the strength of the trabecular bone pattern is significantly affected by osteoporosis, BVF can be used to analyse changes in bone strength [7]. Although BVF is clinically not considered for osteoporosis monitoring, several studies have suggested that BVF should be considered as a potential indicator of osteoporosis [46]. Therefore, this sub-section compares the relationship between the dielectric properties of bones and BVF reported across different studies. The variation of dielectric properties concerning BVF is reported only by Meaney *et al*. [23] and Irastorza *et al*. [46]. An analysis of these studies suggests the following:

1. There exists a negative correlation between BVF and dielectric properties (i.e., the higher the BVF, the lower the dielectric properties).
2. The relative permittivity values of human trabecular bones [46] across different levels of BVF are on average 38.25% higher than porcine trabecular bones [23].
3. In contrast to the relative permittivity, the conductivity values of porcine trabecular bones [23] across BVF are higher (at 900 MHz and 1100 MHz) when compared to human trabecular bones [46]. However, the trend is not consistent at 900 MHz, as the conductivity values of porcine trabecular bone dropped closer to conductivity values of human trabecular bones.

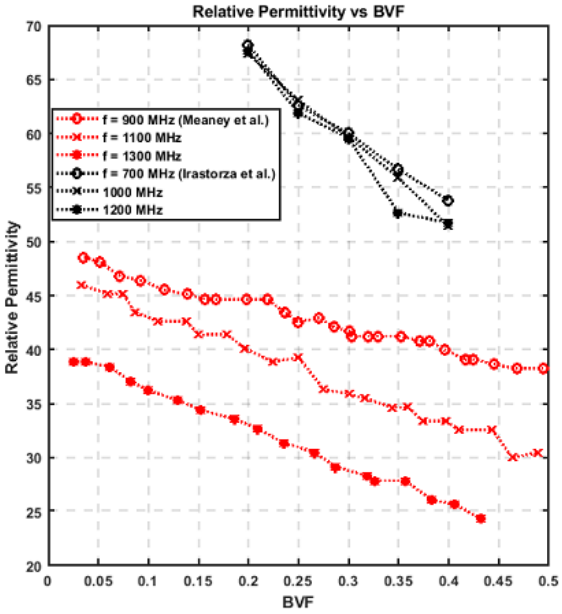

(a)

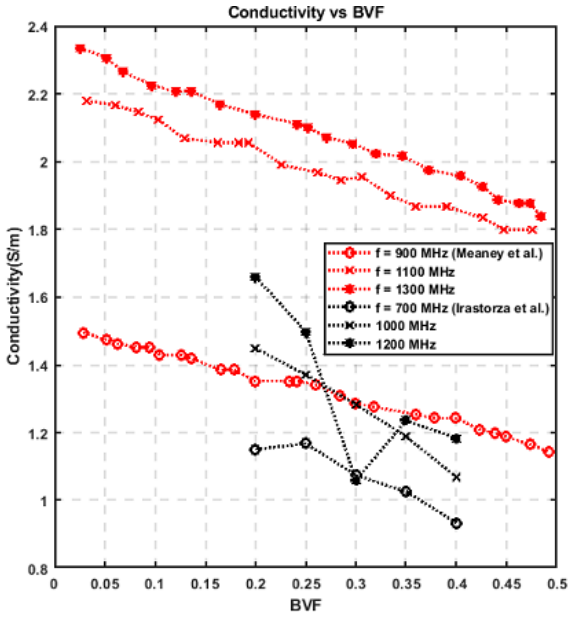

(b)

Figure 2.14: Relationship between relative permittivity and conductivity against BVF [23],[46]. The black curves indicate the dielectric properties of humans and red curves indicate the same for porcine trabecular bones.

In summary, based on the review of all studies, the dielectric properties of trabecular bone samples are found to be higher than those of cortical bone samples. Variations are observed in the dielectric properties across all studies. All studies explaining the variation of BVF against dielectric properties are in agreement with each other in that there is a negative correlation between them. However, the magnitude of the variation between BVF and dielectric properties varies among these

studies. In contrast, the studies examining the relationship between BMD and dielectric properties found contradictory results. Four studies have reported a negative correlation between BMD and the dielectric properties; however, one study found a positive correlation. However, studies have found a significant dielectric contrast between healthy and diseased trabecular human bone samples in the microwave frequency range [72],[18]. Moreover, the dielectric properties of bones are found to be influenced by different mineralisation levels of bones in the microwave frequency range [75]. Therefore, MWI can likely be employed to exploit the dielectric contrast between dielectric properties of healthy and diseased human bones, and hence, to develop an EM-based medical device to monitor osteoporosis. The following section overviews the potential of MWI for monitoring bone health.

2.6 Microwave Imaging

MWI is one of the promising diagnostic technologies being investigated for a range of medical applications. The use of microwaves for imaging human biological tissues dates back to 1979 when Jacobi and Larsen imaged canine kidneys [76]. Since then, MWI has been investigated as a promising emerging imaging modality. One of the notable applications of MWI is towards breast cancer detection [77]–[79], with four clinical systems being tested in clinical trials [79]. The detection of breast cancer relies on the inherent dielectric contrast between normal and malignant breast tissues [30],[77],[78]. Besides breast cancer detection, various studies have employed MWI for the diagnosis of stroke by exploiting the dielectric contrast between ischemic and healthy tissues [82]. Recent studies have investigated the feasibility of using MWI for osteoporosis monitoring [7],[18] based on the assumed contrast between dielectric properties of healthy and diseased bones [50]. The associated clinical advantages and the contrast between dielectric properties of healthy and diseased bones make MWI a potential imaging modality for monitoring bone health in comparison to the existing bone imaging modalities [83],[84]. The key advantages of MWI for diagnosing and monitoring various diseases compared to existing imaging modalities are non-ionising radiations, portability, and low-cost equipment [1],[2].

MWI techniques can be broadly classified into passive, hybrid, and active techniques [86]. In the passive technique, a microwave signal is used to excite the biological tissue. The highly vascular tumour regions absorb relatively higher energy compared to healthy regions that increase the temperature of the tumour region. The

thermal variations are observed through radiometry and hence the tumour regions are separated from healthy regions based on their temperature difference [87]. In the hybrid technique, the thermoacoustic approach is employed along with MWI to achieve better resolution and sensitivity of the tissue to be imaged. The active MWI human tissue involves the illumination of target tissue with an EM field. The EM fields are scattered based on their interaction with human tissue. The dielectric properties of the scattering object dictate the characteristics of the scattered field [26]. The received scattered waves are processed to reconstruct the image of the scattering object. The reconstruction of the scattering object in MWI can be classified into two main categories: radar-based and tomographic MWI [88].

In radar-based MWI techniques, images are constructed based on the scattered waves that arise due to the contrast between normal and malignant tissues [35]. The radar-based techniques are mainly used to localise any strong scatterer/pathology in the biological tissues without reconstructing the full image of biological tissues [71]. The radar-based MWI locates the dielectric contrast areas by exploiting the phase of the scattered microwave signals. The radar-based MWI provides the location, shape, and size of the pathology present in the imaging region [77].

Contrary to radar-based MWI, the tomographic MWI techniques aim at retrieving the spatial distribution of dielectric properties of the biological tissues by processing measured scattered EM field data [86]. The interaction of EM waves with the scattering object results in a non-linear and ill-posed set of measured fields. Therefore, non-linear inversion approaches are required to reconstruct the spatial distribution of the dielectric properties. The tomographic based MWI techniques are computationally expensive compared to radar-based MWI techniques [86]. However, with the development of fast parallel tomography solutions, the computational cost of MWT approaches has reduced significantly [89]. The tomographic-based MWI is computationally complex and takes a long time for image reconstruction compared to radar-based MWI [77]. However, the application of bone imaging involves the characterisation of the spatial distribution of dielectric properties of bone, contrary to breast cancer detection where the objective of MWI is to locate the presence/detection of tumour tissue. Therefore, the objective of this thesis is to investigate MWT to characterise the dielectric properties of healthy and diseased bones. Further details on MWT are provided in the next section.

2.7 Microwave Tomography Imaging

The MWT aims to reconstruct the dielectric properties of the target biological tissue by solving the inverse scattering problem by using the scattered EM energy [2]. In MWT the target anatomical site (in this case human bone) to be imaged is illuminated by an array of microwave antennas operating at microwave frequency range (0.3 – 10 GHz). Each antenna in the array illuminates the anatomical site with a low power microwave signal (single/multi-frequency pulse or broadband pulse). The scattered EM energy is received and sampled at multiple antennas. Based on the application, the aim of MWT involves reconstructing the quantitative or qualitative properties of the target tissue. The qualitative properties aim to retrieve the shape, size, and location of the unknown target, however, the quantitative properties aim to retrieve the 2-D or 3-D spatial distribution of dielectric properties of the unknown target. The qualitative properties of the unknown target can be retrieved by employing linear methods [87]. The linear approximation methods such as Born and Rytov approximations are employed to reconstruct the qualitative properties of the unknown target [90]–[92]. These linear approximation methods help in reconstructing the dielectric profile of targets that have lower dielectric contrast and small size [86]. Moreover, contrast source inversion (CSI) and global optimisation techniques are employed to retrieve the qualitative properties of the target [87]. These approaches are well investigated for the application of breast imaging. To retrieve the quantitative properties (spatial distribution of dielectric properties of the bone) of the unknown target the inversion of the non-linear and ill-posed measured EM scattered fields is performed [93]. Therefore, non-linear inversion techniques are required to solve the EM inverse scattering problem.

Various non-linear iterative techniques [18],[94],[95],[96],[95],[96] have been proposed in the literature to retrieve the quantitative spatial distribution of the dielectric properties of the unknown target. These techniques are classified either as time-domain or frequency-domain techniques. The frequency-domain techniques involve single frequency or multi-frequency measurements to solve non-linear and ill-posed EM inverse scattering problems. Meaney *et al*. [99] in 2000 developed the first MWT system for breast imaging applications. In this study, the authors proposed a frequency domain MWT method known as the log-magnitude unwrapped-phase technique to reconstruct the dielectric properties of the breast. The log-magnitude unwrapped-phase technique is based on the Gauss-Newton optimisation approach

[18],[95] and has successfully reconstructed the dielectric properties of experimental phantoms [86], [87], and *in vivo* dielectric properties of the breast. To improve the estimation of dielectric properties of the breast, this technique has been used in conjunction with MRI. Meaney *et al.* [18] used their breast imaging prototype to measure *in vivo* dielectric properties of the human calcaneus bone by using MWT for a frequency range of 900 - 1700 MHz. In this study, the authors have imaged the human calcaneus of two patients suffering from lower leg injury [18]. Similarly, Meaney *et al.* in [23] reported *ex vivo* dielectric properties of porcine bone samples by using MWT for a frequency of 1100 MHz. The Gauss-Newton approaches are sensitive to the "initial guess", which makes this approach less favourable in scenarios where less *a priori* information is available [100]. In EM inverse scattering problems, an "initial guess" provides the starting point of the convex optimisation problem, hence, an inaccurate "initial guess" would lead to a solution that has no significance to the solution of the problem [100].

The DBIM is another well-known frequency-domain technique for solving the EM inverse scattering problem [97], [98]. The DBIM is an extension of the Born and Rytov approximation and reconstructs the two-dimensional imaging domain where Born and Rytov approximations break down [101]. In the Born approximation technique, the Green's function is not updated at each iteration. However, in the DBIM approach, the Green's function is updated at each iteration making the algorithm more robust towards two dimensional problem solving [101]. The DBIM uses a succession of linear approximations to estimate the spatial distribution of dielectric properties of the reconstruction domain [102]. Like Born and Rytov approximations, the DBIM approach helps in reconstructing the dielectric profile of targets that have lower dielectric contrast and small size [86]. In bone imaging applications, the dielectric contrast between cortical bone and trabecular bone is less [103], therefore the amount of energy penetrating trabecular bone is considerably high than the reflected energy. Therefore, the contribution of measured scattered EM signals due to the trabecular bone would dominate the behaviour of the objective function in the minimisation problem. Other notable frequency domain techniques include variations of the Gauss-Newton optimisation approach and the iterative CSI technique [86].

Contrary to frequency domain techniques, time-domain MWT techniques employ ultra-wideband (UWB) microwave measurements to iteratively solve the EM inverse scattering problem [104]. The conjugate gradient (CG) based approach is employed to

update the dielectric properties during the iterative process. The dielectric properties are updated until the convergence of the EM inverse scattering problem is achieved. Takenaka *et al*. [94] proposed a time-domain MWT approach known as the forward-backward time-stepping (FBTS) method to reconstruct the dielectric properties of breast tissues. Like the CG approach, the FBTS method also involves UWB measurements [104]. Fhager *et al*. [105] employed a similar approach to reconstruct experimental and numerical phantoms [95]. The authors used their experimental prototype for the assessment of experimental phantoms. In most of the time domain MWT techniques, the unknown target to be imaged is modelled by a simplified conductivity model. The conductivity model does not account for dispersion in biological tissues, which poses the limitation and deterioration of performance when using the conductivity model for dispersive biological tissues. However, the conductivity model simplifies the EM inverse scattering problem. Fhager *et al*. [95] estimated the Debye parameters by modifying the time domain MWT technique. The reconstruction of Debye parameters compared to the conductivity model provides a better solution. The computational cost of these algorithms primarily depends upon the forward solver and the regularisation techniques for stabilisation of the inversion method [86]. The fact that only a few studies have been conducted on MWT of human bone motivates further studies on the characterisation of human bone dielectric properties by using MWT. Therefore, this study builds upon the frequency domain MWT method to estimate the dielectric properties of the human numerical bone phantoms. Moreover, no study to date has ever investigated the dielectric properties of different diseased human bones by employing MWT. The characterisation of different diseased bones has paramount importance for the development of EM-based diagnostic and therapeutic medical devices for bone diseases. Despite the promising initial evidence that dielectric properties can be potentially used for osteoporosis diagnosis, no dedicated MWI system exists to measure *in vivo* dielectric properties of human bone in the microwave frequency range. Therefore, one of the objectives of this thesis is to develop a dedicated MWI prototype for bone imaging applications. The next section details about the MWI prototypes that have been employed for bone imaging application.

2.8 Experimental Prototypes

A comprehensive review of MWI experimental prototypes has been presented by O'Loughlin *et al*. [106]. The authors found that several experimental prototypes have been developed that employ a radar-based MWI technique for breast imaging. A small number of these prototypes have been used in patient studies in clinical environments [26],[106]. While the focus of this work is on MWT for bone imaging applications, therefore, this section will provide a brief overview of experimental prototypes that employ MWT for bone imaging applications.

A comprehensive review on bone dielectric properties in microwave frequency range by Amin *et al*. [7] reported that only one study has measured *in vivo* dielectric properties of human trabecular bones. This study was conducted by Meaney *et al*. [18]. The authors have reported *in vivo* dielectric properties of human calcaneus bone by using MWT for a frequency range of 900 - 1700 MHz. In this study, the authors have adapted their breast imaging prototype for imaging the human calcaneus of two patients suffering from lower leg injury [18]. This experimental prototype was designed for breast imaging applications at Dartmouth College, USA (DC) that has been used in several clinical trials beginning in 2000 [99]. Due to the limited sample size, no definite conclusion regarding the dielectric properties of human bones can be drawn from these results. The experimental setup of this study is shown in Figure 2.15.

(a)

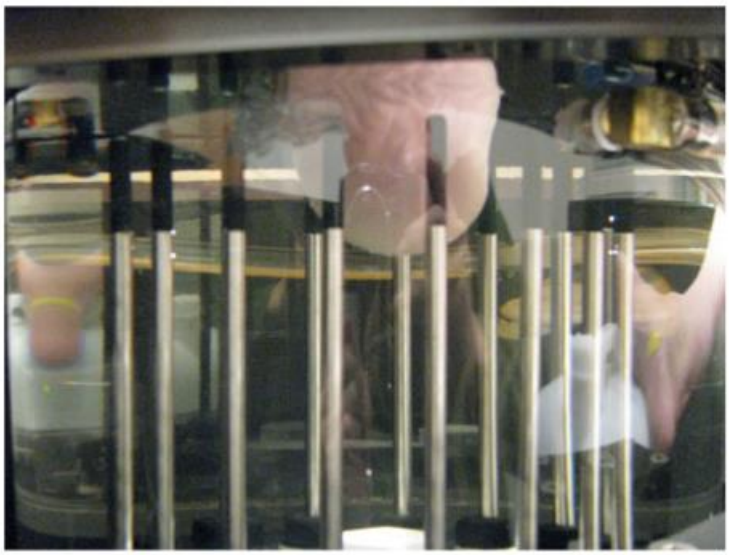

(b)

Figure 2.15: The experimental prototype used by Meaney *et al.* in [18] for human bone imaging.

Similarly, Gilmore *et al*. [107], reported *in vivo* dielectric properties of the human forearms by MWT. In this study, the human forearms of 5 adult male and female volunteers between the ages of 30 and 48 were imaged. Microwave scattering data were collected at 0.8 to 1.2 GHz with 24 transmitting and receiving antennas. Inversion of the microwave data was performed with a balanced version of the multiplicative-regularized contrast source inversion algorithm formulated using the finite-element method (FEM-CSI). Optimal results were found at 0.8 GHz and 1 GHz. The authors found that without the use of prior information a thicker adipose tissue layer leads to a poorer image reconstruction quality. However, the image reconstruction quality has notable improvement when prior information is incorporated as an inhomogeneous background in the inversion algorithm. Moreover,

the two bones can be identified for all volunteers having low subcutaneous adipose layer. However, the authors have not reported the *in vivo* dielectric properties of forearm bones therefore, no definite conclusion regarding the dielectric properties of human bones can be drawn from these results. The experimental setup of this study is shown in Figure 2.16.

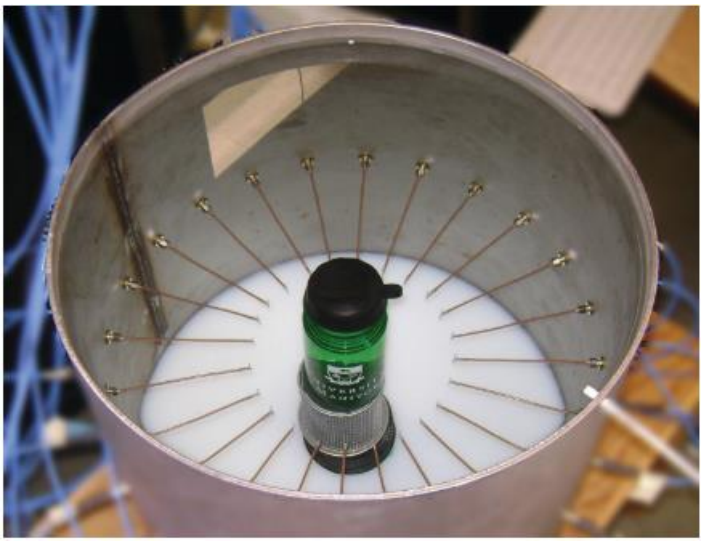

(a)

(b)

Figure 2.16: The experimental prototype used by Gilmore *et al*. [107] for human forearm imaging.

Despite the promising initial evidence that dielectric properties can be potentially used for osteoporosis diagnosis, no dedicated MWI system exists to measure *in vivo* dielectric properties of human bone in the microwave frequency range. Moreover, limited work has been done towards the *in vivo* and *ex vivo* dielectric characterisation of human trabecular bones. Similarly, no study has ever reported the experimental

validation of MWT and corresponding MWI prototype for characterising the diseased human bones, which is of paramount importance for the development of EM-based diagnostic and therapeutic medical devices for bone diseases.

2.9 Conclusion

In this chapter, a brief overview of bone anatomy and physiology is presented. The clinical overview of osteoporosis is presented along with an overview and description of each imaging modality used to diagnose osteoporosis. The dielectric properties of bones are investigated both for low-frequency range and microwave frequency range. For both frequency ranges, the relationship between bone dielectric properties and bone quality parameters is investigated. More specifically, the variation of dielectric properties of cortical bone and trabecular bone is observed both for animal and human bones. The comparison of studies that have reported the dielectric properties of bones is presented as well. The potential of MWI for monitoring osteoporosis is reviewed. The studies that have employed MWT for estimating the spatial distribution of dielectric properties of bones are reviewed. Finally, a brief overview of MWT based clinical prototypes for bone imaging applications is presented.

Experimental work has been performed over the last four decades to characterise bone dielectric properties. Numerous studies were performed to measure the dielectric properties of bone, both in the low-frequency range and in the microwave frequency range. Comparative analysis of these studies found a significant difference between dielectric properties of trabecular and cortical animal bone samples. The differences in the dielectric properties were attributed to the source of bone location which is associated with inherent variability in bone composition and microstructure, measurement techniques, and sample preparation. There were only two studies that have measured the dielectric properties of human bone samples. One of the studies reported *in vivo* dielectric properties of human bone by using MWT. However, the second study has presented *ex vivo* dielectric properties of human trabecular bones by using OECL probes. The fact that only two studies have been conducted on the human bone with a limited sample size motivates further studies on the characterisation of human bone dielectric properties. No study has ever measured the dielectric properties of diseased human bone samples, which is of paramount importance for the development of EM-based diagnostic and therapeutic medical devices for bone diseases. Moreover, the review of studies in the literature to investigate the

relationship between bone dielectric properties and bone health is found to be contradictory. Therefore, further investigation is required to study the relationship between bone mineralisation and bone dielectric properties over a wide frequency range and on larger sample size. This relationship is of paramount importance for characterising bone dielectric properties in osteoporosis.

Based on the contrast between dielectric properties of healthy and diseased human trabecular bones, the MWI based EM device can be proposed to monitor osteoporosis. Moreover, only one study has reported the *in vivo* dielectric properties of human trabecular bones and has employed their breast imaging prototype to image human calcaneus. Despite the promising initial evidence that dielectric properties can be potentially used for osteoporosis diagnosis, no dedicated MWI system exists to measure *in vivo* dielectric properties of human bone in the microwave frequency range.

The fact that only a few studies have been conducted on MWT of human bone; motivates further studies on the characterisation of human bone dielectric properties by using MWT. Moreover, no study has ever reported MWT of diseased human bone samples, which is of paramount importance for the development of EM-based diagnostic and therapeutic medical devices for bone diseases. The rest of the thesis addresses these questions.

2.9 References

[1] US Department of Health and Human Services, "Bone health and osteoporosis: a report of the Surgeon General," *US Heal. Hum. Serv.*, p. 437, 2004.

[2] B. Amin *et al.*, "A feasibility study on microwave imaging of bone for osteoporosis monitoring," *Med. Biol. Eng. Comput.*, 2021.

[3] B. Krier, *Histology A Text and Atlas*, vol. 39, no. 1. 2005.

[4] J. E. Hall, *Guyton and Hall textbook of medical physiology e-Book*. Elsevier Health Sciences, 2010.

[5] B. Clarke, "Normal bone anatomy and physiology.," *Clin. J. Am. Soc. Nephrol.*, vol. 3 Suppl 3, no. Suppl 3, pp. 1–16, 2008.

[6] J. Sierpowska, M. J. Lammi, M. A. Hakulinen, J. S. Jurvelin, R. Lappalainen,

and J. Töyräs, “Effect of human trabecular bone composition on its electrical properties,” *Med. Eng. Phys.*, vol. 29, no. 8, pp. 845–852, 2007.

[7] B. Amin, M. A. Elahi, A. Shahzad, E. Porter, B. McDermott, and M. O’Halloran, “Dielectric properties of bones for the monitoring of osteoporosis,” *Med. Biol. Eng. Comput.*, Aug. 2018.

[8] D. H. Barlow, “Osteoporosis guidelines,” *Climacteric*, vol. 10, no. SUPPL. 2, pp. 79–82, 2007.

[9] M. H. Ross and W. Pawlina, *Histology*. Lippincott Williams & Wilkins, 2006.

[10] G. Y. Tang *et al.*, “Evaluation of MR spectroscopy and diffusion-weighted MRI in detecting bone marrow changes in postmenopausal women with osteoporosis,” *Clin. Radiol.*, vol. 65, no. 5, pp. 377–381, 2010.

[11] W. H. O. S. G. on Prevention, M. of Osteoporosis, and W. H. Organization, *Prevention and management of osteoporosis: report of a WHO scientific group*, no. 921. World Health Organization, 2003.

[12] J. F. Griffith and H. K. Genant, “New imaging modalities in bone,” *Curr. Rheumatol. Rep.*, vol. 13, no. 3, pp. 241–250, 2011.

[13] A. S. Cruz, H. C. Lins, R. V. A. Medeiros, J. M. F. Filho, and S. G. da Silva, “Artificial intelligence on the identification of risk groups for osteoporosis, a general review,” *Biomed. Eng. Online*, vol. 17, no. 1, p. 12, 2018.

[14] C. Background, “Single- and Dual-Photon Absorptiometry Techniques for Bone Mineral Analysis,” *J. Nucl. Med. Technol.*, vol. 14, no. 3, pp. 163–171, 1986.

[15] T. Lang, P. Augat, S. Majumdar, X. Ouyang, and H. K. Genant, “Noninvasive assessment of bone density and structure using computed tomography and magnetic resonance,” *Bone*, vol. 22, no. 5, pp. 149S--153S, 1998.

[16] F. Cosman *et al.*, “Clinician’s Guide to Prevention and Treatment of Osteoporosis,” *Osteoporos. Int.*, vol. 25, no. 10, pp. 2359–2381, 2014.

[17] J. R. Wilkie *et al.*, “Comparison of radiographic texture analysis from computed radiography and bone densitometry systems.,” *Med. Phys.*, vol. 31, no. 4, pp. 882–891, 2004.

[18] P. M. Meaney *et al.*, “Clinical microwave tomographic imaging of the calcaneus: A first-in-human case study of two subjects,” *IEEE Trans. Biomed. Eng.*, vol. 59, no. 12, pp. 3304–3313, 2012.

[19] E.-M. Lochmüller, R. Müller, V. Kuhn, C. A. Lill, and F. Eckstein, “Can Novel Clinical Densitometric Techniques Replace or Improve DXA in Predicting Bone Strength in Osteoporosis at the Hip and Other Skeletal Sites?,” *J. Bone Miner. Res.*, vol. 18, no. 5, pp. 906–912, 2003.

[20] S. Salahuddin, E. Porter, F. Krewer, and M. O’ Halloran, “Optimised analytical models of the dielectric properties of biological tissue,” *Med. Eng. Phys.*, vol. 43, pp. 103–111, 2017.

[21] R. M. Irastorza, C. M. Carlevaro, and F. Vericat, “Is there any information on micro-structure in microwave tomography of bone tissue?,” *Med. Eng. Phys.*, vol. 35, no. 8, pp. 1173–1180, 2013.

[22] A. H. Golnabi, P. M. Meaney, S. Geimer, T. Zhou, and K. D. Paulsen, “Microwave tomography for bone imaging,” *Proc. - Int. Symp. Biomed. Imaging*, vol. 9, pp. 956–959, 2011.

[23] P. M. Meaney, T. Zhou, D. Goodwin, A. Golnabi, E. A. Attardo, and K. D. Paulsen, “Bone dielectric property variation as a function of mineralization at microwave frequencies,” *Int. J. Biomed. Imaging*, vol. 2012, 2012.

[24] A. Vander Vorst, A. Rosen, and Y. Kotsuka, *RF/microwave interaction with*

biological tissues, vol. 181. Wiley Online Library, 2006.

[25] C. Gabriel, S. Gabriel, and E. Corthout, “The dielectric properties of biological tissues: I. Literature survey,” *Phys. Med. Biol. Phys. Med. Biol*, vol. 41, no. 41, pp. 2231–2249, 1996.

[26] M. A. Elahi, “Confocal Microwave Imaging and Artifact Removal Algorithms for the Early Detection of Breast Cancer,” 2018.

[27] T. S. England and N. A. Sharples, “Dielectric properties of the human body in the microwave region of the spectrum,” *Nature*, vol. 163, no. 4143, pp. 487–488, 1949.

[28] T. S. England, “Dielectric properties of the human body for wave-lengths in the 1--10 cm. range,” *Nature*, vol. 166, no. 4220, pp. 480–481, 1950.

[29] H. F. Cook, “The dielectric behaviour of some types of human tissues at microwave frequencies,” *Br. J. Appl. Phys.*, vol. 2, no. 10, p. 295, 1951.

[30] H. Fallahi, A. Shahzad, D. Clausing, M. O. Halloran, M. C. Dennedy, and P. Prakash, “Technological Requirements for Microwave Ablation of Adrenal Masses,” pp. 3724–3727, 2017.

[31] A. Shahzad, D. Clausing, P. Prakash, M. C. Dennedy, and M. O’halloran, “Broadband dielectric properties of adrenal gland for accurate anatomical modelling in medical applications,” in *Electromagnetics in Advanced Applications (ICEAA), 2017 International Conference on*, 2017, pp. 1465–1468.

[32] A. Shahzad, K. Sonja, M. Jones, R. M. Dwyer, and M. O’Halloran, “Investigation of the effect of dehydration on tissue dielectric properties in ex vivo measurements,” *Biomed. Phys. Eng. Express*, vol. 3, no. 4, pp. 1–9, 2017.

[33] E. Porter and M. O’Halloran, “Investigation of Histology Region in Dielectric

Measurements of Heterogeneous Tissues," *IEEE Trans. Antennas Propag.*, vol. 65, no. 10, pp. 5541–5552, 2017.

[34] M. Lazebnik, M. C. Converse, J. H. Booske, and S. C. Hagness, "Ultrawideband temperature-dependent dielectric properties of animal liver tissue in the microwave frequency range," *Phys. Med. Biol.*, vol. 51, no. 7, pp. 1941–1955, 2006.

[35] E. Porter, M. Coates, and M. Popović, "An Early Clinical Study of Time-Domain Microwave Radar for Breast Health Monitoring," *IEEE Trans. Biomed. Eng.*, vol. 63, no. 3, pp. 530–539, 2016.

[36] C. L. Brace, "Radiofrequency and Microwave Ablation of the Liver, Lung, Kidney, and Bone: What Are the Differences?," *Curr. Probl. Diagn. Radiol.*, vol. 38, no. 3, pp. 135–143, 2009.

[37] P. T. Nguyen, A. Abbosh, and S. Crozier, "Microwave hyperthermia for breast cancer treatment using electromagnetic and thermal focusing tested on realistic breast models and antenna arrays," *IEEE Trans. Antennas Propag.*, vol. 63, no. 10, pp. 4426–4434, 2015.

[38] Y. Haba, A. Wurm, M. Köckerling, C. Schick, W. Mittelmeier, and R. Bader, "Characterization of human cancellous and subchondral bone with respect to electro physical properties and bone mineral density by means of impedance spectroscopy," *Med. Eng. Phys.*, vol. 45, pp. 34–41, 2017.

[39] J. Sierpowska *et al.*, "Prediction of mechanical properties of human trabecular bone by electrical measurements.," *Physiol. Meas.*, vol. 26, no. 2, pp. S119–S131, 2005.

[40] J. Sierpowska *et al.*, "Interrelationships between electrical properties and microstructure of human trabecular bone.," *Phys. Med. Biol.*, vol. 51, no. 20,

pp. 5289–303, 2006.

[41] J. Sierpow[1] J. Sierpowska, J. Töyräs, M. A. Hakulinen, S. S., J. S. Jurvelin, and R. Lappalainen, “Electrical and dielectric properties of bovine trabecular bone -- relationships with mechanical properties and mineral density,” Phys.\ Med.\ Biol., vol. 48, J. Töyräs, M. A. Hakulinen, S. S., J. S. Jurvelin, and R. Lappalainen, “Electrical and dielectric properties of bovine trabecular bone -- relationships with mechanical properties and mineral density,” *Phys.\ Med.\ Biol.*, vol. 48, pp. 775–786, 2003.

[42] S. Gabriel, R. W. Lau, and C. Gabriel, “The dielectric properties of biological tissues .2. Measurements in the frequency range 10 Hz to 20 GHz,” *Phys. Med. Biol.*, vol. 41, no. 11, pp. 2251–2269, 1996.

[43] J. D. Kosterich, K. R. Foster, and S. R. Pollack, “Dielectric-Properties Of Fluid-Saturated Bone - The Effect Of Variation In Conductivity Of Immersion Fluid,” *IEEE Trans. Biomed. Eng.*, vol. 31, no. 4, pp. 369–374, 1984.

[44] M. Unal, F. Cingoz, C. Bagcioglu, Y. Sozer, and O. Akkus, “Interrelationships between electrical, mechanical and hydration properties of cortical bone,” *J. Mech. Behav. Biomed. Mater.*, vol. 77, no. September, pp. 12–23, 2018.

[45] A. R. Liboff, R. A. Rinaldi, L. S. Lavine, and M. H. Shamos, “On Electrical Conduction in Living Bone.,” *Clin. Orthop. Relat. Res.*, vol. 106, pp. 330–335, 1975.

[46] R. M. Irastorza, E. Blangino, C. M. Carlevaro, and F. Vericat, “Modeling of the dielectric properties of trabecular bone samples at microwave frequency,” *Med. Biol. Eng. Comput.*, vol. 52, no. 5, pp. 439–447, 2014.

[47] A. Ivancich, J. R. Grigera, and C. Muravchik, “Electric behaviour of natural and demineralized bones. Dielectric properties up to 1 GHz,” *J. Biol. Phys.*, vol.

18, no. 4, pp. 281–295, 1992.

[48] R. Irastorza, M. Mayosky, R. Grigera, and F. Vericat, “Dielectric properties of natural and demineralized collagen bone matrix,” *IEEE Trans. Dielectr. Electr. Insul.*, vol. 18, no. 1, pp. 320–328, 2011.

[49] a. Peyman, C. Gabriel, E. H. Grant, G. Vermeeren, and L. Martens, “Variation of the dielectric properties of tissues with age: the effect on the values of SAR in children when exposed to walkie-talkie devices.,” *Phys. Med. Biol.*, vol. 54, no. 2, pp. 227–241, 2009.

[50] B. Amin *et al.*, “Dielectric characterization of diseased human trabecular bones at microwave frequency,” in *2020 Medical Engineering and Physics*, 2020, pp. 1–8.

[51] P. M. Meaney *et al.*, “Clinical microwave tomographic imaging of the calcaneus: A first-in-human case study of two subjects,” *IEEE Trans. Biomed. Eng.*, vol. 59, no. 12, pp. 3304–3313, 2012.

[52] C. T. Brighton, J. Black, Z. B. Friedenberg, J. L. Esterhai, L. J. Day, and J. F. Connolly, “A multicenter study of the treatment of non-union with constant direct current.,” *JBJS*, vol. 63, no. 1, pp. 2–13, 1981.

[53] P. A. Williams and S. Saha, “The electrical and dielectric properties of human bone tissue and their relationship with density and bone mineral content,” *Ann. Biomed. Eng.*, vol. 24, no. 2, pp. 222–233, Mar. 1996.

[54] S. Saha and P. A. Williams, “Electrical and dielectric properties of Wet Human Cortical Bone as a Function of Frequency,” *IEEE Trans. Biomed. Eng.*, vol. 39, no. 12, pp. 1298–1304, 1992.

[55] M. H. Shamos and L. S. Lavine, “Piezoelectricity as a fundamental property of biological tissues,” *Nature*, vol. 213, no. 5073, pp. 267–269, 1967.

[56] C. A. L. Bassett and R. O. Becker, “Generation of electric potentials by bone in response to mechanical stress,” *Science (80-.).*, vol. 137, no. 3535, pp. 1063–1064, 1962.

[57] A. R. Liboff, R. A. Rinaldi, L. S. Lavine, and M. H. Shamos, “On electrical condution in living bone.,” *Clin. Orthop. Relat. Res.*, no. 106, pp. 330–335, 1975.

[58] A. Rubinacci and L. Brigatti, “A new method for measuring electrical resistance of bone’in vivo’,” *Acta Orthop. Belg.*, vol. 50, no. 5, pp. 686–691, 1984.

[59] A. Tzukert, E. Leviner, Y. Mahler, and S. Shoshan, “Electroconductivity of bone in vitro and in vivo.,” *Clin. Orthop. Relat. Res.*, vol. 179, pp. 270–274, 1983.

[60] J. D. Kosterich, K. R. Foster, and S. R. Pollack, “Dielectric permittivity and electrical conductivity of fluid saturated bone.,” *IEEE Trans. Biomed. Eng.*, vol. 30, no. 2, pp. 81–86, 1983.

[61] G. N. Reddy and S. Saha, “Electrical and Dielectric Properties of Wet Bone as a Function of Frequency,” *IEEE Trans. Biomed. Eng.*, vol. BME-31, no. 3, pp. 296–303, Mar. 1984.

[62] G. De Mercato and F. J. Garcia-Sanchez, “Dielectric properties of fluid-saturated bone: A comparison between diaphysis and epiphysis,” *Med. Biol. Eng. Comput.*, vol. 26, no. 3, pp. 313–316, 1988.

[63] G. De Mercato and F. J. G. Sanchez, “Variation of the electric properties along the diaphysis of bovine femoral bone,” *Med. Biol. Eng. Comput.*, vol. 29, no. 4, pp. 441–446, 1991.

[64] S. Gabriel, R. W. Lau, and C. Gabriel, “The dielectric properties of biological tissues: II. Measurements in the frequency range 10 Hz to 20 GHz,” *Phys. Med.*

Biol., vol. 41, no. 11, p. 2251, 1996.

[65] S. Singh and J. Beharl, "Frequency Dependence of Electrical Properties of Human Bone," *J. Bioelectr.*, vol. 3, no. 1–2, pp. 347–356, 1984.

[66] S. Saha and P. A. Williams, "Electrical and dielectric properties of Wet Human Cancellous Bone as a Function of Frequency," *IEEE Trans. Biomed. Eng.*, vol. 39, no. 12, pp. 1298–1304, 1992.

[67] S. Saha and P. A. Williams, "Comparison of the electrical and dielectric behavior of wet human cortical and cancellous bone tissue from the distal tibia.," *J. Orthop. Res.*, vol. 13, no. 4, pp. 524–32, 1995.

[68] Y. Haba, A. Wurm, M. Köckerling, C. Schick, W. Mittelmeier, and R. Bader, "Characterization of human cancellous and subchondral bone with respect to electro physical properties and bone mineral density by means of impedance spectroscopy," *Med. Eng. Phys.*, vol. 45, pp. 34–41, 2017.

[69] J. Aerssens, S. Boonen, G. Lowet, and J. Dequeker, "Interspecies differences in bone composition, density, and quality: potential implications for in vivo bone research," *Endocrinology*, vol. 139, no. 2, pp. 663–670, 1998.

[70] J. J. Carey and M. F. Delaney, "T-scores and Z-scores," *Clin. Rev. Bone Miner. Metab.*, vol. 8, no. 3, pp. 113–121, 2010.

[71] B. L. Oliveira and M. O. Halloran, "Microwave Breast Imaging : Experimental tumour phantoms for the evaluation of new breast cancer diagnosis systems Biomedical Physics & Engineering Related content Microwave Breast Imaging : experimental tumour phantoms for the evaluation of new breast can," no. January, 2018.

[72] B. Amin *et al.*, "Dielectric characterization of diseased human trabecular bones at microwave frequency," *Med. Eng. Phys.*, vol. 78, 2020.

[73] V. Zhurbenko, “Challenges in the design of microwave imaging systems for breast cancer detection,” *Adv. Electr. Comput. Eng.*, vol. 11, no. 1, pp. 91–96, 2011.

[74] R. M. Irastorza, E. Blangino, C. M. Carlevaro, and F. Vericat, “Modeling of the dielectric properties of trabecular bone samples at microwave frequency,” *Med. Biol. Eng. Comput.*, vol. 52, no. 5, pp. 439–447, 2014.

[75] P. M. Meaney, T. Zhou, D. Goodwin, A. Golnabi, E. A. Attardo, and K. D. Paulsen, “Bone dielectric property variation as a function of mineralization at microwave frequencies,” *J. Biomed. Imaging*, vol. 2012, p. 7, 2012.

[76] L. E. Larsen and J. H. Jacobi, “Microwave scattering parameter imagery of an isolated canine kidney,” *Med. Phys.*, vol. 6, no. 5, pp. 394–403, 1979.

[77] M. A. Elahi *et al.*, “Evaluation of image reconstruction algorithms for confocal microwave imaging: Application to patient data,” *Sensors (Switzerland)*, vol. 18, no. 6, 2018.

[78] D. O. Loughlin *et al.*, “Sensitivity and Specificity Estimation Using Patient-Specific Microwave Imaging in Diverse Experimental Breast Phantoms,” vol. 38, no. 1, pp. 303–311, 2019.

[79] D. O’Loughlin, M. O’Halloran, B. M. Moloney, M. Glavin, E. Jones, and M. A. Elahi, “Microwave Breast Imaging: Clinical Advances and Remaining Challenges,” *IEEE Trans. Biomed. Eng.*, vol. 65, no. 11, pp. 2580–2590, 2018.

[80] M. Lazebnik *et al.*, “A large-scale study of the ultrawideband microwave dielectric properties of normal, benign and malignant breast tissues obtained from cancer surgeries,” *Phys. Med. Biol.*, vol. 52, no. 20, pp. 6093–6115, 2007.

[81] J. Bourqui and E. C. Fear, “System for Bulk Dielectric Permittivity Estimation of Breast Tissues at Microwave Frequencies,” *IEEE Trans. Microw. Theory*

Tech., vol. 64, no. 9, pp. 3001–3009, 2016.

[82] R. Scapaticci, L. Di Donato, I. Catapano, and L. Crocco, "A feasibility study on microwave imaging for brain stroke monitoring," *Prog. Electromagn. Res.*, vol. 40, pp. 305–324, 2012.

[83] B. Amin, M. A. Elahi, A. Shahzad, E. Parle, L. McNamara, and M. Orhalloran, "An insight into bone dielectric properties variation: A foundation for electromagnetic medical devices," *EMF-Med 2018 - 1st EMF-Med World Conf. Biomed. Appl. Electromagn. Fields COST EMF-MED Final Event with 6th MCM*, pp. 3–4, 2018.

[84] S. N. Makarov, G. M. Noetscher, S. Arum, R. Rabiner, and A. Nazarian, "Concept of a Radiofrequency Device for Osteopenia / Osteoporosis Screening," pp. 1–15, 2020.

[85] R. Scapaticci, P. Kosmas, and L. Crocco, "Wavelet-Based Regularization for Robust Microwave Imaging in Medical Applications," *IEEE Trans. Biomed. Eng.*, vol. 62, no. 4, pp. 1195–1202, 2015.

[86] A. Shahzad, M. O'Halloran, E. Jones, and M. Glavin, "A multistage selective weighting method for improved microwave breast tomography," *Comput. Med. Imaging Graph.*, vol. 54, pp. 6–15, 2016.

[87] O. Halloran and O. Halloran, "Title A multistage selective weighting method for improved microwave breast tomography Link to A Multistage Selective Weighting Method for Improved Microwave Breast Tomography," 2016.

[88] J. Bourqui, J. M. Sill, and E. C. Fear, "A prototype system for measuring microwave frequency reflections from the breast," *Int. J. Biomed. Imaging*, vol. 2012, 2012.

[89] A. Shahzad, M. O'Halloran, M. Glavin, and E. Jones, "A novel optimized

parallelization strategy to accelerate microwave tomography for breast cancer screening," in *2014 36th Annual International Conference of the IEEE Engineering in Medicine and Biology Society*, 2014, pp. 2456–2459.

[90] J. C. Bolomey, A. Izadnegahdar, L. Jofre Roca, C. PICHOT DU MEZERAY, and G. Peronnet, "Microwave diffraction tomography for biomedical applications," *IEEE Trans. Microw. Theory Tech.*, vol. 30, no. 11, pp. 1998–2000, 1982.

[91] N. H. Farhat, "Microwave holography and coherent tomography," *Med. Appl. Microw. Imaging*, pp. 66–81, 1986.

[92] L. Jofre, M. S. Hawley, A. Broquetas, E. de los Reyes, M. Ferrando, and A. R. Elias-Fuste, "Medical imaging with a microwave tomographic scanner," *IEEE Trans. Biomed. Eng.*, vol. 37, no. 3, pp. 303–312, Mar. 1990.

[93] J. D. Shea, P. Kosmas, S. C. Hagness, and B. D. Van Veen, "Three-dimensional microwave imaging of realistic numerical breast phantoms via a multiple-frequency inverse scattering technique," *Med. Phys.*, vol. 37, no. 8, pp. 4210–4226, 2010.

[94] T. Takenaka, H. Jia, and T. Tanaka, "Journal of Electromagnetic Waves Microwave Imaging of Electrical Property Distributions By a Method," no. January 2015, pp. 37–41.

[95] A. Fhager, M. Gustafsson, S. Nordebo, and S. Member, "Image Reconstruction in Microwave Tomography Using a Dielectric Debye Model," *IEEE Trans. Biomed. Eng.*, vol. 59, no. 1, pp. 156–166, 2012.

[96] A. Fhager, M. Gustafsson, and S. Nordebo, "Image Reconstruction in Microwave Tomography Using a Dielectric Debye Model," *IEEE Trans. Biomed. Eng.*, vol. 59, no. 1, pp. 156–166, Jan. 2012.

[97] Z. Miao and P. Kosmas, “Multiple-Frequency DBIM-TwIST Algorithm for Microwave Breast Imaging,” *IEEE Trans. Antennas Propag.*, vol. 65, no. 5, pp. 2507–2516, 2017.

[98] L. M. Neira, B. D. Van Veen, and S. C. Hagness, “High-resolution microwave breast imaging using a 3-D inverse scattering algorithm with a variable-strength spatial prior constraint,” *IEEE Trans. Antennas Propag.*, vol. 65, no. 11, pp. 6002–6014, 2017.

[99] P. M. Meaney, M. W. Fanning, D. Li, S. P. Poplack, and K. D. Paulsen, “A clinical prototype for active microwave imaging of the breast,” *IEEE Trans. Microw. Theory Tech.*, vol. 48, no. 11, pp. 1841–1853, 2000.

[100] R. Scapaticci, P. Kosmas, and S. Member, “Wavelet-Based Regularization for Robust Microwave Imaging in Medical Applications,” *IEEE Trans. Biomed. Eng.*, vol. 62, no. 4, pp. 1195–1202, 2015.

[101] Y. M. Wang, “Reconstruction of Two-Dimensional Permittivity Distribution Using the Distorted Born Iterative Method,” vol. 9, no. 2, 1990.

[102] M. Ambrosanio, P. Kosmas, S. Member, V. Pascazio, and S. Member, “A Multithreshold Iterative DBIM-Based Algorithm for the Imaging of Heterogeneous Breast Tissues,” *IEEE Trans. Biomed. Eng.*, vol. 66, no. 2, pp. 509–520, 2019.

[103] B. Amin, M. A. Elahi, A. Shahzad, E. Porter, and M. O’Halloran, “A review of the dielectric properties of the bone for low frequency medical technologies,” *Biomed. Phys. Eng. Express*, vol. 5, no. 2, p. 022001, 2019.

[104] A. Shahzad, “Fast Ultra Wideband Microwave Imaging for Early Stage Breast Cancer Detection by,” no. July, 2017.

[105] A. Fhager, S. K. Padhi, and J. Howard, “3D image reconstruction in microwave

tomography using an efficient FDTD model," *IEEE Antennas Wirel. Propag. Lett.*, vol. 8, pp. 1353–1356, 2009.

[106] D. O'Loughlin, M. O'Halloran, B. M. Moloney, M. Glavin, E. Jones, and M. A. Elahi, "Microwave breast imaging: Clinical advances and remaining challenges," *IEEE Trans. Biomed. Eng.*, vol. 65, no. 11, pp. 2580–2590, 2018.

[107] C. Gilmore, A. Zakaria, S. Pistorius, and J. Lovetri, "Microwave imaging of human forearms: Pilot study and image enhancement," *Int. J. Biomed. Imaging*, vol. 2013, 2013.

Chapter 3

Dielectric Characterisation of Diseased Human Trabecular Bones at Microwave Frequency

Article overview

This work presents the *ex vivo* dielectric characterisation of human trabecular bones from osteoporotic and osteoarthritis patients. The trabecular bone samples are obtained from human femoral heads from patients that were undergoing total hip replacement surgeries. The total sample size for the dielectric characterisation analysis was forty-five from twelve patients. Twenty-three bone samples are obtained from osteoporotic patients and twenty-two bone samples are obtained from osteoarthritis patients. The trabecular bone microarchitecture of osteoarthritis patients is compact and dense compared to osteoporotic patients. Therefore, the bone samples from these two sets of patients allow establishing the variation in bone dielectric properties due to variation in microarchitecture between two diseased bones. The trabecular microarchitecture of osteoarthritis patients is much more compact and dense compared to osteoporotic patient's trabecular microarchitecture. The dense trabecular microarchitecture of bone indicates a higher degree of mineralisation due to the increased amount of bone present, therefore, the bone samples from osteoarthritis patients can be considered as healthy bone samples in comparison to osteoporotic bone samples. The dielectric properties of the bone samples are measured by employing an open-ended coaxial probe measurement technique. The comparison of dielectric properties from both sets of patients is presented in this study. A comparative analysis is presented between trabecular bone microarchitecture for osteoporotic and osteoarthritis patients. Moreover, a comparison between the dielectric properties of the current study and the dielectric properties of human trabecular bone in the literature is presented. Finally, a regression analysis is performed between the bone dielectric properties and bone volume fraction to relate bone dielectric properties with bone microarchitecture parameter.

This work has been published in the journal of *Medical Engineering & Physics (2020)*. I am the first lead author in the paper, which is co-authored with my supervisors. The bone samples were processed by Eoin Parle and Laoise McNamara. The measurement of dielectric properties of the bone samples, the processing of dielectric properties data, the measurement and processing of trabecular bone microarchitecture of the bone samples, and finally, the regression analysis between bone dielectric properties and trabecular bone microarchitecture was led by me. I led all parts of the work with the support of my supervisors.

Abstract

The objective of this study is to determine whether *in vitro* dielectric properties of human trabecular bones, can distinguish between osteoporotic and osteoarthritis patients' bone samples. Specifically, this study enlightens intra-patient variation of trabecular bone microarchitecture and dielectric properties, inter-disease comparison of bone dielectric properties, and finally establishes the correlation to traditional bone histomorphometry parameter (bone volume fraction) for diseased bone tissue. Bone cores were obtained from osteoporotic and osteoarthritis patients ($n = 12$). These were scanned using microCT to examine bone volume fraction. An open-ended coaxial probe measurement technique was employed to measure dielectric properties over the 0.5 – 8.5 GHz frequency range. The dielectric properties of osteoarthritis patients are significantly higher than osteoporotic patients; with an increase of 41% and 45% for relative permittivity and conductivity respectively. The dielectric properties within each patient vary significantly, variation in relative permittivity and conductivity was found to be greater than 25% and 1.4% respectively. A weak correlation ($r = 0.5$) is observed between relative permittivity and bone volume fraction. Osteoporotic and osteoarthritis bones can be differentiated based on the difference in dielectric properties. Although these do not correlate strongly to bone volume fraction, it should be noted that bone volume fraction is a poor predictor of fracture risk. The dielectric properties of bones are found to be influenced by the mineralisation levels of bones. Therefore, the dielectric properties of bones may have the potential as a diagnostic measure of osteoporosis.

Chapter 3. Dielectric Characterisation of Diseased Human Trabecular Bones at Microwave Frequency

3.1 Introduction

The phenomena of electromagnetic (EM) wave reflection and propagation through biological tissues can be characterised by dielectric properties namely, the relative permittivity and conductivity [1]. Dielectric properties of biological tissues have formed the basis for the development of a number of EM diagnostic and therapeutic medical devices [2],[3]. Some applications of dielectric properties of biological tissues include microwave hyperthermia for breast cancer treatment [4], microwave imaging (MWI) for breast health monitoring [5] and microwave ablation for treating liver, lung, kidney and adrenal tumours [6],[7]. MWI has been used to measure *in vivo* dielectric properties of the breast, and recently to measure the dielectric properties of calcaneus bone [5],[8]. It has been proposed that the dielectric properties of bones can be used to monitor osteoporosis [9],[10]. Bone dielectric properties are influenced by mineralisation and it was proposed that a dielectric property based medical device could diagnose osteoporosis [8], albeit that this has never been established.

Osteoporosis is characterised by continuous progressive loss of bone density and systematic deterioration of trabecular bone microarchitecture, which leads to bone fragility and fracture [11]. Annually, osteoporosis results in 8.9 million fractures worldwide [12]. Almost 50% of women and 25% of men aged above 50 years in the US experience an osteoporotic fracture, and approximately 43.6 million suffer from osteopenia, a term used to describe low bone density [8],[13],[14]. In the EU a hip fracture is reported after every 30 seconds, and about 1700 fractures are reported per day [15]. Due to an ageing population, these fractures are expected to double by 2050 and by 2025 the economic burden will be $25.3billion [16].

Dual-energy X-ray absorptiometry (DXA) is the standard modality for the clinical diagnosis of osteoporosis [17],[18]. DXA calculates the bone mass from the Bone mineral density (BMD, g/cm^2) of central (hip, lumbar spine) and peripheral sites (heel, distal forearm) [18]. Bone volume fraction (BV/TV) encompasses changes in the trabecular bone volume [9],[10] and can also inform the detection of osteoporosis [10]. DXA scan uses ionising radiation, and therefore frequent DXA scans are associated with long term health risks [8]. Further, DXA systems are expensive and not portable. Therefore, a low cost, portable and non-ionising diagnostic device is required for monitoring osteoporosis [19]. Most importantly, BMD commonly fails to identify individuals that are likely to experience fracture [20], because it does not

capture bone quality which is dictated by tissue microarchitecture, composition and the degree of microdamage, each of which contributes to different degrees to fracture risk. An MWI device could potentially be used for the diagnosis of osteoporosis to overcome the limitations of existing approaches [21]. However, the development of such a device requires detailed knowledge of the dielectric properties of diseased and normal human bones and quantification of their relationship to bone mineralisation.

Experimental work has been performed over the last four decades to characterise bone dielectric properties [10]. Numerous studies were performed to measure the dielectric properties of bone, both in the low-frequency range [22–30,30,30–32] and in the microwave frequency range [8–10,19,33–36]. A comprehensive review of bone dielectric properties in the microwave frequency range was reported by Amin *et al.* [15]. The authors reported that most studies measured dielectric properties of trabecular and cortical bone samples from porcine or bovine animals. Comparative analysis of these studies found significant differences between the dielectric properties of trabecular and cortical animal bone samples. The differences in the dielectric properties were attributed to the source of bone location which is associated with inherent variability in bone composition and microstructure, measurement techniques, and sample preparation. There were only two studies that measured the dielectric properties of human bone samples. Meaney *et al.* [8] reported *in vivo* dielectric properties of human bone by using microwave tomography (MWT) imaging for a frequency range of 900-1700 MHz. However, this study only considered two patients suffering from a lower leg injury and dielectric properties were reported at a single frequency of 1300 MHz. Therefore, due to the limited sample size, no definite conclusion regarding the dielectric properties of human bones can be drawn from these results. Irastorza *et al.* [10], measured *in vitro* dielectric properties of human trabecular bones using open-ended coaxial line (OECL) probes in the frequency range of 100-1300 MHz. In this study, bulk dielectric properties of human trabecular bone samples were estimated from bone samples submerged in phosphate-buffered saline (PBS). The patients were going through total hip replacement surgery. The dielectric properties of human trabecular bone were observed to be significantly high compared to the dielectric properties of animal trabecular bone samples [15]. The fact that only two studies have been conducted on the human bone with a limited sample size ($n = 2, 6$) motivates further studies on the characterisation of human bone dielectric

properties. Indeed, no study has ever measured diseased human bone samples, which is of paramount importance for the development of EM-based diagnostic and therapeutic medical devices for bone diseases.

The variation in bone dielectric properties with respect to bone mass parameters (BMD and BV/TV) has been reported in previous work by Meaney *et al*. [9] and Irastorza *et al.* [10]. Those studies found a negative relationship between BV/TV and dielectric properties. Three studies have reported variation of dielectric properties of bone with respect to bone mineralisation levels [9],[8],[35]. Peyman *et al*. [35] found a positive correlation between bone mineralisation levels and dielectric properties of porcine cortical bone. In contrast, Meaney *et al*. [9] reported a negative correlation between mineralisation and dielectric properties of porcine trabecular bone from the femur. Similarly, Meaney *et al.* [8] found a negative correlation between BMD and dielectric properties for two patients. Based on these contradictory results, further investigation is required to study the relationship between bone mineralisation and bone dielectric properties over a wide frequency range and on a larger sample size. This relationship is of paramount importance for characterising bone dielectric properties in osteoporosis.

This study focuses on the measurement of diseased human bone samples. A total of forty-five trabecular bone samples were acquired from osteoporotic and osteoarthritis patient populations. Osteoarthritis patients have compact and dense trabecular bone microarchitecture compared to osteoporotic patients [37]. These two populations provide bone samples to allow us to establish the variation in bone dielectric properties due to disease states.

Microarchitecture of these bone samples was obtained from microCT scans and then dielectric properties were measured *in vitro* using an OECL across the microwave frequency range of 0.5-8.5 GHz. MWI is a modality of choice for imaging heterogeneous organs such as the human breast due to better imaging resolution that can be achieved at microwave frequencies [38]. The bone itself has a heterogeneous structure and the distribution of bone mineralisation is not uniform [39]. Therefore, imaging resolution of any future bone imaging modality would be an important consideration. This study chose a microwave frequency range of 0.5 – 8.5 GHz, which is similar to the frequency range used in preclinical breast imaging systems [40]. This

frequency range could provide a good compromise between penetration depth and imaging resolution [41].

Bone is a heterogeneous structure and in human anatomy, many layers proceed before the bone. Both microarchitectural parameters and dielectric properties were compared between osteoarthritis and osteoporotic patient populations. Finally, the relationship between dielectric properties and bone quality in terms of BV/TV was investigated.

3.2 Methodology

3.2.1 Experimental Design

Twelve patients were considered (osteoporotic $n = 7$ patients, osteoarthritis $n = 5$ patients) in this study, which were obtained from a separate study examining the bone composition of human osteoarthritis and osteoporosis patients [42]. For that study, human femoral heads were obtained from patients that were undergoing total hip replacement surgeries under ethical approval and informed written patient consent. The ethical approval was granted by the Clinical Research Ethics Committee, Galway University Hospitals, Galway, Ireland. The mean age of osteoporotic patients was 70.5 ± 8 years and the mean age of osteoarthritis patients was 73.4 ± 1 years. During surgery, upon removal from the patient, femoral heads were wrapped in PBS soaked gauze and stored in a sterile container prior to freezing at -20^{o} C. After thawing, cores of approximately 13mm × 5mm × 5mm were sectioned from the femoral head using a Buehler Isomet Low Speed Saw fitted with a 5-inch diamond watering blade at speeds of approximately 40rpm.

For this study, we investigated multiple trabecular bone samples (12.7 ± 1.4 mm × 5 ± 0.5 mm × 5 ± 1 mm) from each patient resulting in samples sizes for osteoporotic ($n = 23$) and osteoarthritis ($n = 22$). The temperature of bone samples was recorded before each sample was measured (21 ± 0.1°C).

3.2.2 CT Scanning

Immediately after cutting, each core was scanned by microCT at 17.2 μm voxel size (Scanco μCT100, Energy Intensity: 70kVp, 114 μA, 8 W, using 0.1mm aluminium filter to minimize beam hardening, integration time: 500msec) while submerged in PBS to keep samples hydrated. For trabecular microarchitecture analysis, volumes of interest (VOIs) were contoured manually from each bone core and thresholded (using a single global threshold of 355 mgHA/cm^3 for all cores). The contoured images were

segmented to create a binary image, isolating bone tissue. Weekly calibration of the microCT machine using hydroxyapatite phantoms ensured consistency between scans. Manufacturer supplied evaluation scripts were run on segmented VOIs to quantify BV/TV.

3.2.3 Dielectric Measurements

The OECL technique was employed to measure bone dielectric properties. The measurements were recorded in the frequency range of 0.5-8.5 GHz over 101 linearly spaced frequency points. To avoid uncertainty in measurements due to probe movement and repositioning, the Keysight slim form probe 85070E was connected directly to the Keysight E5063A vector network analyser (VNA) [1]. To avoid movement of the sample, the bone sample was placed on a lifting stand for solid contact with the probe. The temperature of each bone sample was measured by using a digital infrared thermometer with dual-laser targeting (N85FR). The temperature of liquids for calibration and validation was measured using a digital thermometer (HI98509). The VNA was used to measure reflection coefficient (S_{11}) at 101 linearly spaced frequency points, and a commercially available software suite (Keysight N1500A) was used to convert the S_{11} parameters to real (ε') and imaginary (ε'') parts of complex permittivity [2]. The complex permittivity is defined as:

$$\varepsilon(\omega) = \varepsilon'(\omega) - j\varepsilon''(\omega) \qquad (3.1)$$

where $\varepsilon'(\omega)$ is the relative permittivity also termed as dielectric constant, $\varepsilon''(\omega)$ is the dielectric loss, and ω represents frequency in radians. The relative permittivity represents the ability of a material to store energy and the dielectric loss represents the energy dissipated in the material. The imaginary part of the complex permittivity also termed dielectric loss is used to compute electrical conductivity as follows:

$$\sigma(\omega) = \omega\varepsilon_0\varepsilon''(\omega) \qquad (3.2)$$

where ε_0 is the permittivity of free space.

3.2.4 Measurement Protocol & System Uncertainty Analysis

Before measuring the dielectric properties of bone samples, the measurement equipment was calibrated. The equipment was calibrated by using Air/Short/Deionised water calibration procedure. Deionised water was used as standard load material during the calibration procedure. A validation measurement

was carried by verifying the dielectric properties of 0.1 M NaCl (saline) at 22 ^{o}C [4]. A total of 9 validation measurements were performed. The uncertainty of the equipment's accuracy is reported in Table 3.1. The uncertainty in accuracy in terms of percentage is defined as:

$$UC_{ACC}(f) = \left(\frac{x_{meas}(f) - x_{ref}(f)}{x_{ref}(f)}\right) \times 100 \quad (3.3)$$

where x_{meas} represents measured dielectric properties of 0.1 M NaCl and x_{ref} represents standard dielectric properties of 0.1 M NaCl [43] at the measured temperature. The uncertainty in the repeatability of measurements is also reported in Table 3.1. The uncertainty in repeatability of measurements in terms of percentage is defined as:

$$UC_{REP}(f) = \left(\frac{x_{meas}(f) - x_{mean}(f)}{x_{mean}(f)}\right) \times 100 \quad (3.4)$$

where x_{mean} represents the mean of the measured dielectric properties. The total combined uncertainty is reported in Table 3.1.

Table 3.1: Percent uncertainty in accuracy and repeatability of measurements.

Parameter	$\boldsymbol{\varepsilon_r}$ (%)	**σ (%)**
$\boldsymbol{UC_{ACC}}$	0.41	2.5
$\boldsymbol{UC_{REP}}$	0.2	0.04
Combined	0.61	2.54

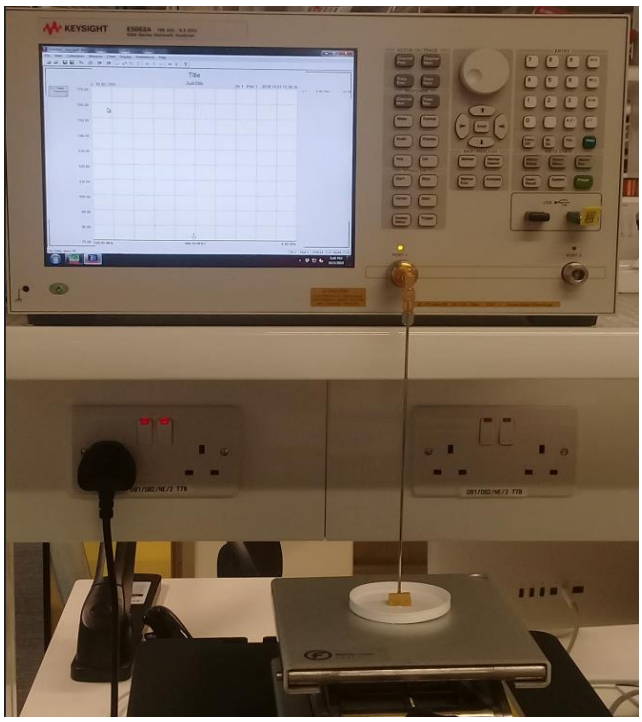

Figure 3.1: Photograph of the experimental setup.

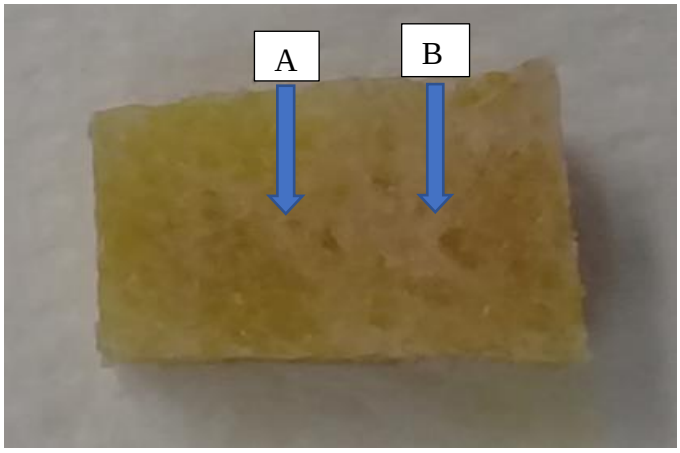

Figure 3.2: Photograph of the bone sample. The arrows show the measurement points. Approximately similar locations were selected as measurement points on the other side of the sample.

3.3 Results and Discussion

3.3.1 Trabecular Microarchitecture of Bone Samples

To analyse the microarchitecture of bone samples, BV/TV was measured using micro-CT. Firstly, the intra-patient variation of BV/TV was analysed for four osteoporotic patients. Four samples were obtained from patient 1 and 2, while, six samples were obtained from patient 3 and 4. From the microCT scan data, it was confirmed that

BV/TV varies within each patient's femoral head as shown in Figure 3.3. Figure 3.3 represents the mean and standard deviation of BV/TV for four osteoporotic patients. These intra-patient variations confirmed that the bone has a heterogeneous structure and its microarchitecture varies within each human's femoral head.

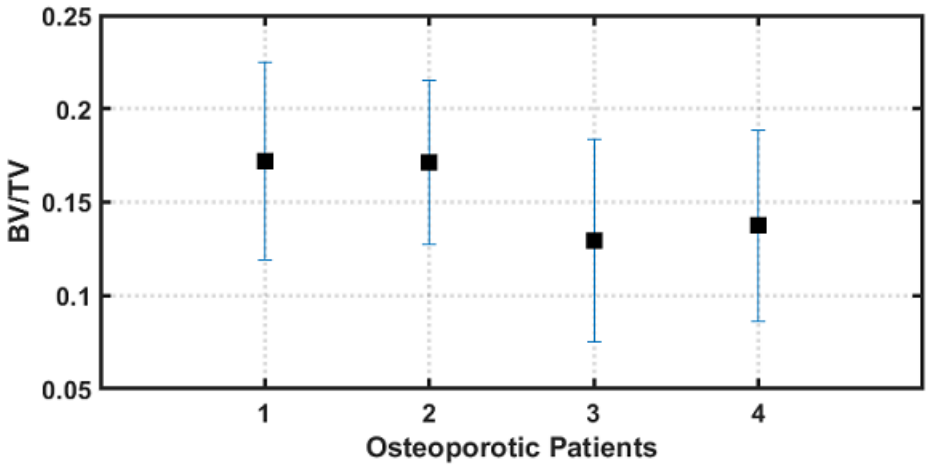

Figure 3.3: Intra-patient variation of BV/TV for osteoporotic patients.

To examine the inter-disease variation between osteoporotic and osteoarthritis patients in terms of BV/TV, BV/TV of bone samples obtained from both sets of patients is shown in Figure 3.4. The mean BV/TV of osteoarthritis patients is 69% higher than osteoporotic patients. The mean ± SD of BV/TV of osteoporotic patients is found to be 0.1451 ± 0.0538 and for osteoarthritis patients is 0.2979 ± 0.0910. The difference in means of BV/TV confirms that osteoarthritis patients have compact and dense trabecular microarchitecture as compared to osteoporotic patients. The osteoporotic patients have more porous trabecular bone microarchitecture.

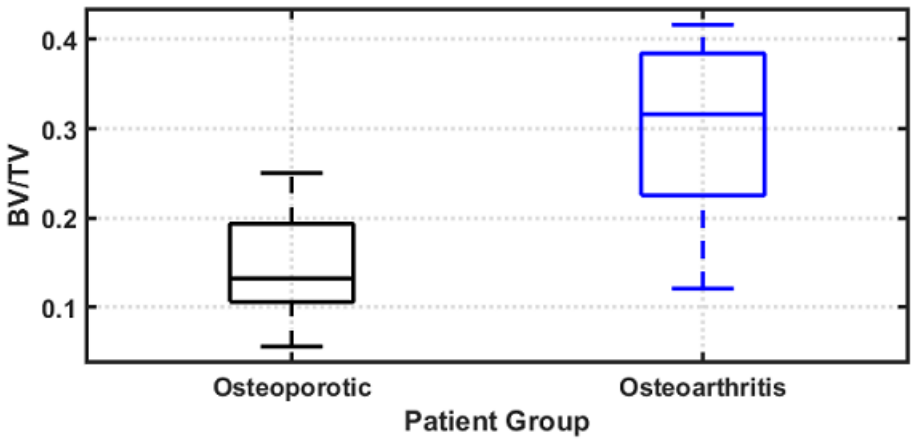

Figure 3.4: Comparison of BV/TV between osteoporotic and osteoarthritis bone samples.

3.3.2 Dielectric Properties of Trabecular Bone Samples

3.3.2.1 Intra-patient Variation of Dielectric Properties

To examine intra-patient variation in terms of bone dielectric properties, two osteoporotic patients were considered. Four bone samples were obtained from both patient's femoral head and their dielectric properties were examined. The mean and standard deviation of dielectric properties are shown in Figure 3.5. The solid curve in Figure 3.5 represents mean dielectric properties from one patient's femoral head and the error bars on each curve indicate the variation of dielectric properties from each patient's femoral head. The intra-patient variation of bone dielectric properties in terms of mean percentage difference of relative permittivity and conductivity values for the 63-year male is 25% and 1.4% respectively. Similarly, the intra-patient variation in terms of mean percentage difference of relative permittivity and conductivity values of the 71-year female is 28% and 1.6% respectively. The intra-patient variation in dielectric properties is mainly due to heterogeneous trabecular microarchitecture of the femoral head, which varies within each patient as can be seen in Figure 3.3.

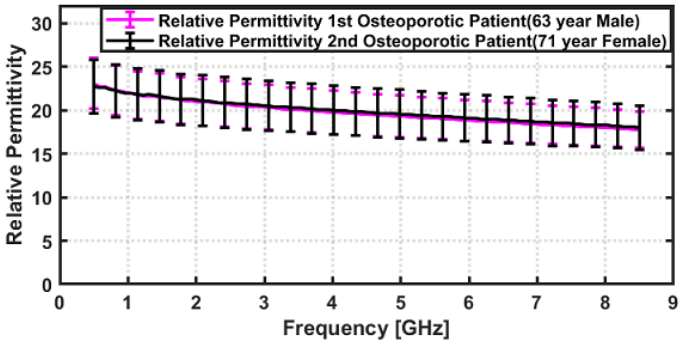

(a)

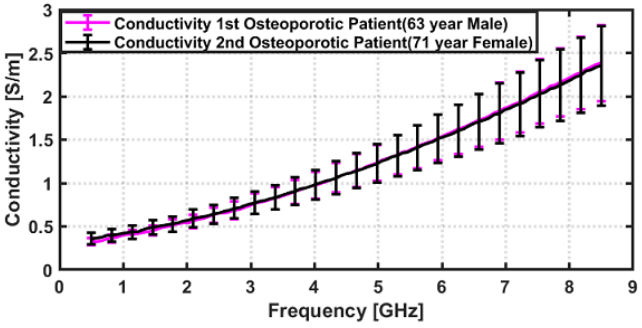

(b)

Figure 3.5: Intra-patient variation of (a) Relative Permittivity (b) Conductivity in 2 osteoporotic patients.

3.3.2.2 Dielectric properties of Osteoporotic and Osteoarthritis Patient's Bones

The dielectric properties of osteoporotic and osteoarthritis patients' bone samples are shown in Figure 3.6. The solid curve represents mean dielectric properties from each patients' population and error bars on each curve indicate standard error of dielectric properties. The mean dielectric properties of osteoarthritis patients' bone samples are higher in magnitude than osteoporotic patients' bone samples with an overall mean percentage difference of 41% and 45% for relative permittivity and conductivity values respectively. The difference in dielectric properties between two sets of patients' bone samples can be due to the fact that the microarchitecture of the trabecular bone pattern of osteoarthritis patients is much more compact and dense compared to osteoporotic patients. Clinically, it is examined that the porous regions of osteoporotic bones have more fat than normal bones, these porous regions are occupied with yellow marrow during the ageing process [44],[45]. Since the dielectric properties of fats are lower than the dielectric properties of bones, it would be expected that this contributes to the lower dielectric properties of osteoporotic bone compared to those of osteoarthritis samples [45],[46].

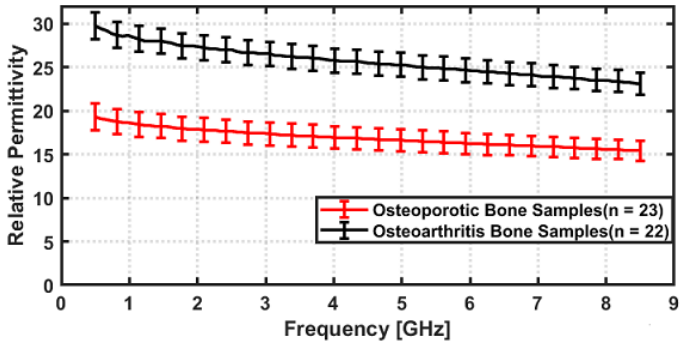

(a)

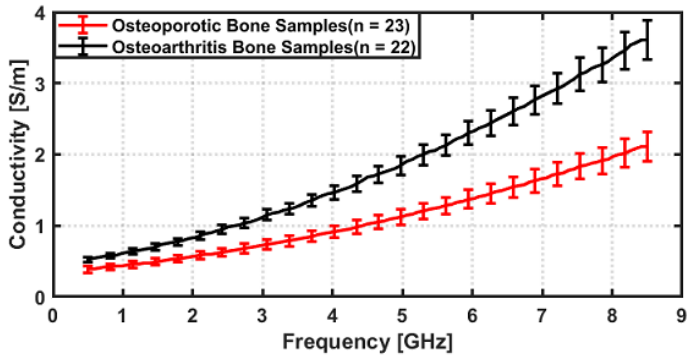

(b)

Figure 3.6: Comparison of osteoporotic and osteoarthritis bone samples in terms of (a) Relative Permittivity (b) Conductivity.

A comparison between osteoporotic and osteoarthritis patients in terms of relative permittivity and conductivity at discrete frequency points is presented in Figure 3.7. The boxes represent the corresponding dielectric properties of each patient population. It is evident from Figure 3.7 that the difference between the dielectric properties of osteoporotic and osteoarthritis patients is significant over the observed frequency points. A maximum percentage difference of 42.5% is found at 500 MHz in relative permittivity and 52.3% at 8.5 GHz in conductivity.

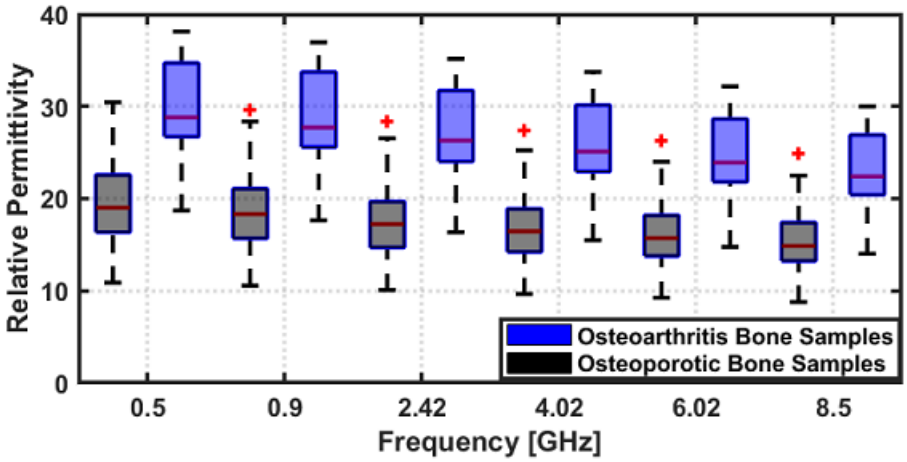

(a)

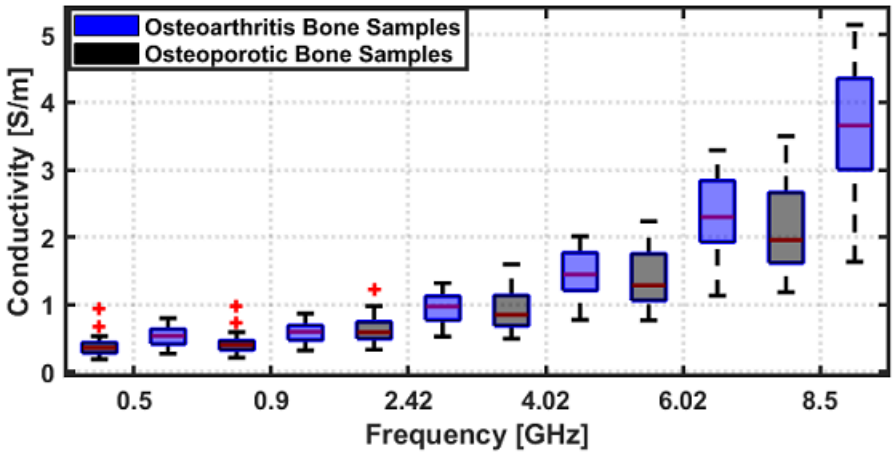

(b)

Figure 3.7: Comparison of osteoporotic and osteoarthritis bone samples in terms of (a) Relative Permittivity (b) Conductivity at 0.5 GHz, 0.9 GHz, 2.42 GHz, 4.02 GHz, 6.02 GHz and 8.5 GHz. The red markers in plots represent the outliers in data.

The mean percentage difference between osteoporotic and osteoarthritis patients in terms of relative permittivity and conductivity is tabulated in Table 3.2.

Table 3.2: Mean percentage difference between osteoporotic and osteoarthritis bone samples.

Frequency	**0.5 GHz**	**0.9 GHz**	**2.42 GHz**	**4.02 GHz**	**6.02 GHz**	**8.5 GHz**
$\boldsymbol{\varepsilon_r}$ (% **diff**)	42.5*	42.1*	41.8*	41.3*	40.9*	39.8*
$\boldsymbol{\sigma}$ (% **diff**)	30.1**	31.5**	40.7*	46.4*	50.8*	52.3*

The values of ε_r and σ marked * have *p*-value < 0.00001and the values marked ** have *p*-value < 0.01.

To investigate the significance of the difference of dielectric properties of osteoporotic and osteoarthritis patient's bone samples, a statistical two-tail *t-test* was performed on dielectric properties of both sets of patients. A *p-value* < 0.01 was obtained at frequencies 500 MHz, 900 MHz, 2.42 GHz, 4.02 GHz, 6.02 GHz, and 8.5 GHz. The two-tail *t-test* at all above-mentioned frequencies showed there exists a statistical difference between dielectric properties of osteoporotic and osteoarthritis bone samples. This significant difference between two populations for both relative permittivity and conductivity suggests that a single frequency MWI device can be used to classify osteoporotic and osteoarthritis patients bone samples.

3.3.2.3 Comparison of Dielectric Properties with Literature

A comparative analysis of the dielectric properties of human trabecular bone samples from the literature is presented in Figure 3.8. Since the dielectric properties are highly species-dependent [15], the results are compared only with measurements of Irastorza *et al.* [10] who reported *in vitro* dielectric properties of human trabecular bones ($n = 6$) in frequency range of 100-1300 MHz by employing OECL probes on bone samples submerged in PBS solution. Since PBS has high dielectric properties as compared to bone [47], the dielectric properties of bone samples would be impacted. In this study, we have measured the dielectric properties of bones without immersing the bone samples in PBS during measurement. We found that dielectric properties of osteoarthritis bone samples are lower in magnitude in comparison to dielectric properties of trabecular human bone samples reported by Irastorza *et al.* [10].

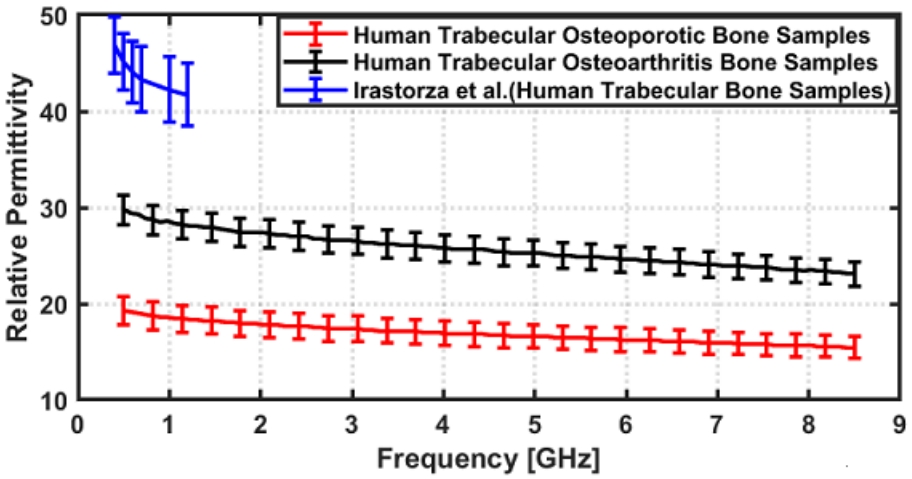

(a)

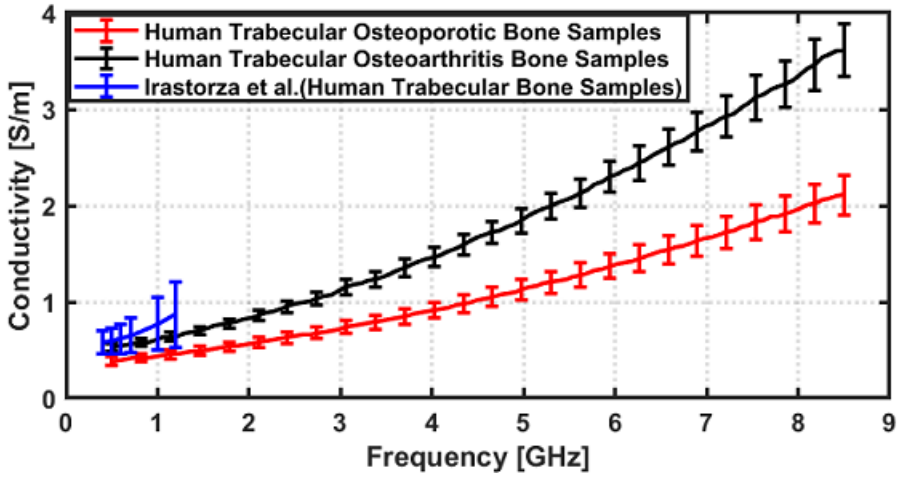

(b)

Figure 3.8: Comparative analysis of trabecular bone dielectric properties with current study and literature (a) Relative Permittivity (b) Conductivity.

3.3.3 Relationship between dielectric properties and BV/TV of trabecular bone samples

Based on results reported by Irastorza *et al.* [10] for the relationship between BV/TV and bone dielectric properties, we have performed a linear regression analysis to analyse the relationship between BV/TV and diseased bone dielectric properties. The analysis was performed at 500 MHz, 900 MHz, 2.42 GHz, 4.02 GHz, and 6.02 GHz, shown in Figure 3.9. Among selected frequencies, a relatively strong relationship was observed at 900 MHz. The linear regression analysis showed a weak positive relationship between BV/TV and relative permittivity with an R^2 value of 0.256 and a correlation coefficient r of 0.50 at 900 MHz. The R^2 value of 0.045 and a correlation coefficient r of 0.22 was found between BV/TV and conductivity of bone samples at

900 MHz. Irastorza *et al.* [10] reported a negative correlation between BV/TV and dielectric properties, with a maximum R^2 value of 0.77 and 0.60 for relative permittivity and conductivity respectively at 700 MHz.

Bone is a mineralised matrix composed of hydroxyapatite crystals ($[Ca_{10}(PO_4)_6(OH)_2]$) (50 – 70%), organic matrix (20 – 40%), water (5 – 10%) and lipids (<3%) [48]. The weak linear regression model suggests that BV/TV alone cannot predict the dielectric properties, since it only quantifies the bone volume in the overall sample volume. Since a major part of the bone constitutes the mineral matrix, BMD would play a significant role in characterising bone dielectric properties. Thus, BMD along with BV/TV may be more suitable to correlate to the dielectric profiles in osteoporotic and osteoarthritis bone.

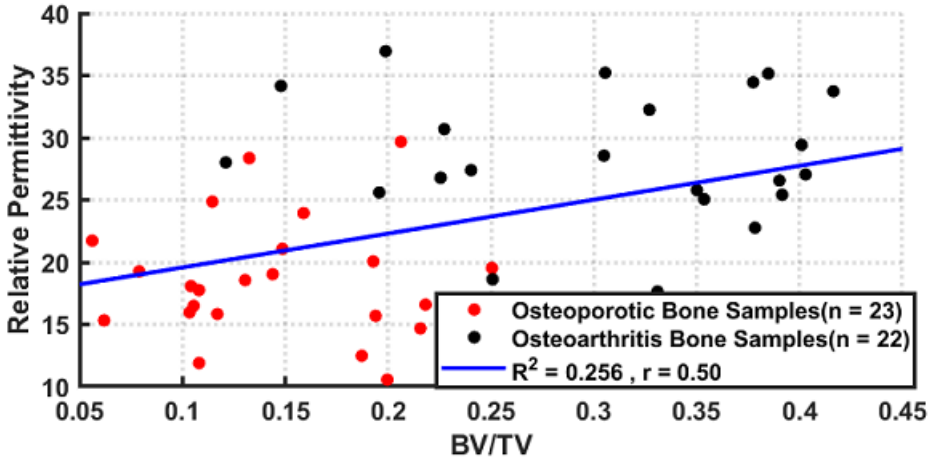

(a)

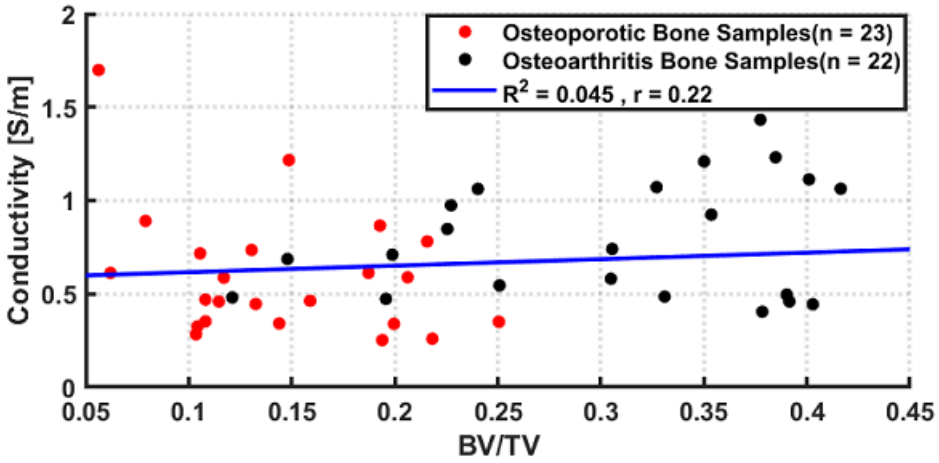

(b)

Figure 3.9: Scatter plot between BV/TV and (a) Relative Permittivity (b) Conductivity at 900 MHz.

3.3.4 Effect of PBS on Bone Samples

Since the bone samples were preserved in PBS after surgical extraction, the impact of PBS on the dielectric properties of bone samples was examined. To examine this effect, one bone sample was separately measured over time. The sample was taken out of the PBS and kept in the open air for a period of 5 hours so that the PBS evaporates thoroughly. During the drying process, dielectric measurements were recorded every hour. A total of four measurements were recorded on the bone sample at each time instant. The overall mean percentage standard deviation of multiple measurements over time was found to be 0.6% and 0.03% for relative permittivity and conductivity values, respectively. These measurements indicate that PBS did not impact the bone dielectric properties.

3.4 Conclusion

In this study, the dielectric properties of diseased human trabecular bone samples were measured. The bone sample size was forty-five from twelve patients. Twenty-three bone samples were obtained from osteoporotic patients and twenty-two bone samples were obtained from osteoarthritis patients. In this paper, we have presented the analysis on BV/TV of osteoporotic and osteoarthritis bone samples, an analysis on the intra-patient variation of bone dielectric properties, dielectric properties of osteoporotic and osteoarthritis bone samples, the relationship between dielectric properties and BV/TV, and a comparison of the current study's findings with the literature.

The study showed an overall mean percentage difference of 41% and 45% for relative permittivity and conductivity values respectively between osteoarthritis and osteoporotic patients bone samples. The variation within the femoral head for both observed osteoporotic patients in terms of relative permittivity and conductivity was found to be greater than 25% and 1.4% respectively. The analysis of microarchitecture parameters of bone suggests a significant difference between BV/TV of osteoarthritis and osteoporotic patients. The percentage difference between mean BV/TV of osteoarthritis and osteoporotic patients is 69%. Finally, the regression analysis suggests a weak positive relationship between BV/TV and relative permittivity (r = 0.50) and conductivity (r = 0.22) at 900 MHz. However, these preliminary findings have shown that there is a statistically significant difference between dielectric properties of osteoporotic and osteoarthritis bone samples. These findings provide a

foundation for the development of microwave-frequency based bone imaging device to diagnose and monitor osteoporosis.

It should be noted that this study only investigated the correlation between dielectric properties and BV/TV. The results show that the BV/TV, which quantifies trabecular bone microarchitecture does not solely account for dielectric properties. Dielectric properties are known to be influenced by mineralisation and are also expected to be influenced by other bone constituents, including organic matrix, water, and lipids. Therefore, considering other major constituents of bone particularly bone mineralisation (BMD) along with the BV/TV will allow for the development of a more realistic model that can predict bone quality based on dielectric properties.

Acknowledgements

This work was supported by the European Research Council under the European Union's Horizon 2020 Programme/ERC Grant Agreement BioElecPro n. 637780. MicroCT scanning research was conducted with financial support from the Irish Research Council Government of Ireland Postdoctoral Fellowship (GOIPD/2016/493) and Science Foundation Ireland (SFI) and was co-funded under the European Regional Development fund under grant number 14/IA/2884.

Conflict of Interest: The authors declare that there is no conflict of interest regarding the publication of this article.

Competing interests: None declared

Funding: This work was supported by the European Research Council under the European Union's Horizon 2020 Programme/ERC Grant Agreement BioElecPro n. 637780. MicroCT scanning research was conducted with financial support from the Irish Research Council Government of Ireland Postdoctoral Fellowship (GOIPD/2016/493) and Science Foundation Ireland (SFI) and was co-funded under the European Regional Development fund under grant number 14/IA/2884.

Ethical approval: Granted By Clinical Research Ethics Committee, Galway University Hospitals, Galway, Ireland.

3.5 References

[1] Salahuddin S, Porter E, Krewer F, O' Halloran M. Optimised analytical models of the dielectric properties of biological tissue. Med Eng Phys 2017;43:103–11. doi:10.1016/j.medengphy.2017.01.017.

[2] Shahzad A, Sonja K, Jones M, Dwyer RM, O'Halloran M. Investigation of the effect of dehydration on tissue dielectric properties in ex vivo measurements. Biomed Phys Eng Express 2017;3:1–9. doi: 10.1088/2057-1976/aa74c4.

[3] Porter E, OHalloran M. Investigation of Histology Region in Dielectric Measurements of Heterogeneous Tissues. IEEE Trans Antennas Propag 2017:1–1. doi:10.1109/TAP.2017.2741026.

[4] Nguyen PT, Abbosh A, Crozier S. Microwave hyperthermia for breast cancer treatment using electromagnetic and thermal focusing tested on realistic breast models and antenna arrays. IEEE Trans Antennas Propag 2015;63:4426–34. doi:10.1109/TAP.2015.2463681.

[5] Porter E, Coates M, Popović M. An Early Clinical Study of Time-Domain Microwave Radar for Breast Health Monitoring. IEEE Trans Biomed Eng 2016;63:530–9. doi:10.1109/TBME.2015.2465867.

[6] Brace CL. Radiofrequency and Microwave Ablation of the Liver, Lung, Kidney, and Bone: What Are the Differences? Curr Probl Diagn Radiol 2009;38:135–43. doi:10.1067/j.cpradiol.2007.10.001.

[7] Fallahi H, Shahzad A, Clausing D, Halloran MO, Dennedy MC, Prakash P. Technological Requirements for Microwave Ablation of Adrenal Masses. *11th European Conference on Antennas and Propagation (EUCAP)* 2017:3724–7. doi:10.23919/EuCAP.2017.7928268.

[8] Meaney PM, Goodwin D, Golnabi AH, Zhou T, Pallone M, Geimer SD, et al. Clinical microwave tomographic imaging of the calcaneus: A first-in-human case study of two subjects. IEEE Trans Biomed Eng 2012;59:3304–13. doi:10.1109/TBME.2012.2209202.

[9] Meaney PM, Zhou T, Goodwin D, Golnabi A, Attardo EA, Paulsen KD. Bone dielectric property variation as a function of mineralization at microwave frequencies. Int J Biomed Imaging 2012;2012. doi:10.1155/2012/649612.

[10] Irastorza RM, Blangino E, Carlevaro CM, Vericat F. Modeling of the dielectric properties of trabecular bone samples at microwave frequency. Med Biol Eng Comput 2014;52:439–47. doi:10.1007/s11517-014-1145-y.

[11] Cruz AS, Lins HC, Medeiros RVA, Filho JMF, da Silva SG. Artificial intelligence on the identification of risk groups for osteoporosis, a general review. Biomed Eng Online 2018;17:12. doi:10.1186/s12938-018-0436-1.

[12] Cosman F, de Beur SJ, LeBoff MS, Lewiecki EM, Tanner B, Randall S, et al. Clinician's Guide to Prevention and Treatment of Osteoporosis. Osteoporos Int 2014;25:2359–81. doi:10.1007/s00198-014-2794-2.

[13] Laster AJ. Dual-Energy X-Ray Absorptiometry: 2014;75:132–6.

[14] Manuscript A. NIH Public Access. Sci York 2006;283:345–56. doi:10.1146/annurev-pathol-011110-130203.Disorders.

[15] Amin B, Elahi MA, Shahzad A, Porter E, McDermott B, O'Halloran M. Dielectric properties of bones for the monitoring of osteoporosis. Med Biol Eng Comput 2018. doi:10.1007/s11517-018-1887-z.

[16] Burge R, Dawson-Hughes B, Solomon DH, Wong JB, King A, Tosteson A. Incidence and Economic Burden of Osteoporosis-Related Fractures in the United States, 2005-2025. J Bone Miner Res 2007;22:465–75. doi:10.1359/jbmr.061113.

[17] Organization WH. WHO SCIENTIFIC GROUP ON THE ASSESSMENT OF OSTEOPOROSIS AT PRIMARY HEALTH Care Level. World Heal Organ 2004;May:5–7. doi:10.1016/S0140-6736(02)08761-5.

[18] Lochmüller E-M, Müller R, Kuhn V, Lill CA, Eckstein F. Can Novel Clinical Densitometric Techniques Replace or Improve DXA in Predicting Bone Strength in Osteoporosis at the Hip and Other Skeletal Sites? J Bone Miner Res 2003;18:906–12. doi:10.1359/jbmr.2003.18.5.906.

[19] Golnabi AH, Meaney PM, Geimer S, Zhou T, Paulsen KD. Microwave tomography for bone imaging. Proc - Int Symp Biomed Imaging 2011;9:956–9. doi:10.1109/ISBI.2011.5872561.

[20] Hillier TA, Cauley JA, Rizzo JH, Pedula KL, Ensrud KE, Bauer DC, et al. Risk Factors Improve Fracture Prediction in Older Women 2013;26:1774–82. doi:10.1002/jbmr.372.The.

[21] Amin B, Elahi MA, Shahzad A, Parle E, McNamara L, Orhalloran M. An insight into bone dielectric properties variation: A foundation for electromagnetic medical devices. EMF-Med 2018 - 1st EMF-Med World Conf Biomed Appl Electromagn Fields COST EMF-MED Final Event with 6th MCM 2018:3–4. doi:10.23919/EMF-MED.2018.8526050.

[22] Haba Y, Wurm A, Köckerling M, Schick C, Mittelmeier W, Bader R. Characterization of human cancellous and subchondral bone with respect to electro physical properties and bone mineral density by means of impedance spectroscopy. Med Eng Phys 2017;45:34–41. doi:10.1016/j.medengphy.2017.04.002.

[23] Sierpowska J, Lammi MJ, Hakulinen MA, Jurvelin JS, Lappalainen R, Töyräs J. Effect of human trabecular bone composition on its electrical properties. Med Eng Phys 2007;29:845–52. doi:10.1016/j.medengphy.2006.09.007.

[24] Saha S, Williams PA. Electrical and dielectric properties of Wet Human Cancellous Bone as a Function of Frequency. IEEE Trans Biomed Eng 1992;39:1298–304. doi:10.1109/TBME.1984.325268.

[25] Unal M, Cingoz F, Bagcioglu C, Sozer Y, Akkus O. Interrelationships between electrical, mechanical and hydration properties of cortical bone. J Mech Behav Biomed Mater 2018;77:12–23. doi:10.1016/j.jmbbm.2017.08.033.

[26] Unal M, Cingoz F, Bagcioglu C, Sozer Y, Akkus O. Interrelationships between electrical, mechanical and hydration properties of cortical bone. J Mech Behav Biomed Mater 2018;77:12–23. doi:10.1016/j.jmbbm.2017.08.033.

[27] Sierpowska J, Hakulinen M a, Töyräs J, Day JS, Weinans H, Jurvelin JS, et al. Prediction of mechanical properties of human trabecular bone by electrical measurements. Physiol Meas 2005;26:S119–31. doi:10.1088/0967-3334/26/2/012.

[28] Sierpowska J, Töyräs J, Hakulinen MA, Saarakkala S, Jurvelin JS, Lappalainen R. Electrical and dielectric properties of bovine trabecular bone -- relationships with mechanical properties and mineral density. Phys Med Biol 2003; 48:775–86. doi:10.1088/0031-9155/48/6/306.

[29] Chakkalakal DA, Johnson MW, Harper RA, Katz JL. Dielectric Properties of Fluid-Saturated Bone. IEEE Trans Biomed Eng 1980;BME-27:95–100. doi:10.1109/TBME.1980.326713.

[30] Saha S, Williams PA. Electrical and dielectric properties of Wet Human Cortical Bone as a Function of Frequency. IEEE Trans Biomed Eng 1992;39:1298–304. doi:10.1109/TBME.1984.325268.

[31] Williams PA, Saha S. The electrical and dielectric properties of human bone tissue and their relationship with density and bone mineral content. Ann Biomed Eng 1996;24:222–33. doi:10.1007/BF02667351.

[32] Saha S, Williams PA. Comparison of the electrical and dielectric behavior of wet human cortical and cancellous bone tissue from the distal tibia. J Orthop Res 1995;13:524–32. doi:10.1002/jor.1100130407.

[33] Ivancich A, Grigera JR, Muravchik C. Electric behaviour of natural and demineralized bones. Dielectric properties up to 1 GHz. J Biol Phys 1992;18:281–95. doi:10.1007/BF00419425.

[34] Gabriel C, Chan TY, Grant EH, Burdette E, Cain F, Seals J, et al. measurement of the Dielectric Properties of Tissues at Microwave Frequencies. Phys Med Biol 1996;41:2251–69. doi:10.1088/0031-9155/41/11/001.

[35] Peyman a., Gabriel C, Grant EH, Vermeeren G, Martens L. Variation of the dielectric properties of tissues with age: the effect on the values of SAR in children when exposed to walkie-talkie devices. Phys Med Biol 2009;54:227–41. doi:10.1088/0031-9155/55/17/5249.

[36] Gabriel S, Lau RW, Gabriel C. The dielectric properties of biological tissues .2. Measurements in the frequency range 10 Hz to 20 GHz. Phys Med Biol 1996;41:2251–69. doi:10.1088/0031-9155/41/11/002.

[37] Topoliński T, Mazurkiewicz A, Jung S, Cichański A, Nowicki K. Microarchitecture parameters describe bone structure and its strength better than BMD. Sci World J 2012;2012. doi:10.1100/2012/502781.

[38] Oliveira BL, Halloran MO. Microwave Breast Imaging : Experimental tumour phantoms for the evaluation of new breast cancer diagnosis systems. Biomed

Phys Eng Express 2018;4: 025036. doi:10.1088/2057-1976/aaaaff.

[39] Allen MR, Burr DB. Chapter 5 - Bone Growth, Modeling, and Remodeling. In: Burr DB, Allen MRBT-B and ABB (Second E, editors., Academic Press; 2019, p. 85–100. doi:https://doi.org/10.1016/B978-0-12-813259-3.00005-1.

[40] O'Loughlin D, O'Halloran M, Moloney BM, Glavin M, Jones E, Elahi MA. Microwave Breast Imaging: Clinical Advances and Remaining Challenges. IEEE Trans Biomed Eng 2018;65:2580–90. doi:10.1109/TBME.2018.2809541.

[41] Zhurbenko V. Challenges in the design of microwave imaging systems for breast cancer detection. Adv Electr Comput Eng 2011;11:91–6. doi:10.4316/aece.2011.01015.

[42] Parle E, Tio S, Behre A, Carey JJ, Murphy CG, O'Brien TF, et al. Bone Mineral Is More Heterogeneously Distributed in the Femoral Heads of Osteoporotic and Diabetic Patients: A Pilot Study. JBMR Plus 2019;n/a:e10253. doi:10.1002/jbm4.10253.

[43] Gabriel C, Peyman A. Dielectric measurement: Error analysis and assessment of uncertainty. Phys Med Biol 2006;51:6033–46. doi:10.1088/0031-9155/51/23/006.

[44] Tang GY, Lv ZW, Tang RB, Liu Y, Peng YF, Li W, et al. Evaluation of MR spectroscopy and diffusion-weighted MRI in detecting bone marrow changes in postmenopausal women with osteoporosis. Clin Radiol 2010;65:377–81. doi:10.1016/j.crad.2009.12.011.

[45] Balmer TW, Vesztergom S, Broekmann P, Stahel A, Büchler P. Characterization of the electrical conductivity of bone and its correlation to osseous structure. Sci Rep 2018;8:1–8. doi:10.1038/s41598-018-26836-0.

[46] Peyman A, Gabriel C. Cole-Cole parameters for the dielectric properties of porcine tissues as a function of age at microwave frequencies. Phys Med Biol 2010;55. doi:10.1088/0031-9155/55/15/N02.

[47] Sierpowska J, Hakulinen MA, Töyräs J, Day JS, Weinans H, Kiviranta I, et al. Interrelationships between electrical properties and microstructure of human

trabecular bone. Phys Med Biol 2006;51:5289–303. doi:10.1088/0031-9155/51/20/014.

[48] Palmer LC, Newcomb CJ, Kaltz SR, Spoerke ED, Samuel I. NIH Public Access 2009;108:4754–83. doi:10.1021/cr8004422.

Chapter 4

A Feasibility Study on Microwave Imaging of Bone for Osteoporosis Monitoring

Article overview

This work presents the initial feasibility analysis for developing a microwave imaging (MWI) device for monitoring osteoporosis. The dielectric contrast of tissues present in the calcaneus is investigated and a transmission line (TL) formalism approach is adopted to investigate the feasible frequency band for the operation of the MWI device. An analysis is presented to find the optimal matching medium for maximum electromagnetic (EM) waves penetration into the calcaneus. The numerical modelling of the human calcaneus is presented and the finite difference time domain (FDTD) simulations are performed to analyse the electric field (E-field) penetration in the five-layered human calcaneus. Firstly, the contrast of dielectric properties of tissues present in the human calcaneus is investigated. Secondly, the TL formalism approach is adopted for finding the optimal selection of frequency band and the corresponding matching medium. Finally, the numerical modelling of human calcaneus bone is performed. Based on FDTD simulations performed the E-field penetration, received signal strength, and power loss in the five-layered calcaneus model is then analysed, and the received signal strength between the two ports is analysed. The initial feasibility analysis suggests that the proposed guidelines can be considered as a useful tool before designing of MWI system. These findings support the idea for the development of an MWI device for bone health monitoring.

This work has been published in the journal of *Medical & Biological Engineering & Computing (2021)*. I am the first lead author in the paper, which is co-authored with my supervisors. I performed the literature review to investigate the dielectric properties of calcaneus tissues. The TL formalism approach for finding a feasible frequency band and the numerical modelling of bone was performed by me. I led all parts of the work with support from my supervisors.

Chapter 4. A Feasibility Study on Microwave Imaging of Bone for Osteoporosis Monitoring

Abstract

The dielectric properties of bones are found to be influenced by the demineralisation of bones. Therefore, microwave imaging (MWI) can be used to monitor *in vivo* dielectric properties of human bones and hence aid in the monitoring of osteoporosis. This paper presents the feasibility analysis of the MWI device for monitoring osteoporosis. Firstly, the dielectric properties of tissues present in the human heel are analysed. Secondly, a transmission line (TL) formalism approach is adopted to examine the feasible frequency band and the matching medium for MWI of trabecular bone. Finally, simplified numerical modelling of the human heel was set to monitor the penetration of E-field, the received signal strength, and the power loss in a numerical model of the human heel. Based on the TL formalism approach, 0.6 – 1.9 GHz frequency band is found to feasible for bone imaging purpose. The relative permittivity of the matching medium can be chosen between 15 – 40. The average percentage difference between the received signal for feasible and inconvenient frequency band was found to be 82%. The findings based on the dielectric contrast of tissues in the heel, the feasible frequency band, and the finite difference time domain simulations support the development of an MWI prototype for monitoring osteoporosis.

4.1 Introduction

Osteoporosis is a major bone disease, caused due to progressive demineralisation of bones that deteriorates the trabecular bone microarchitecture, and hence leads to bone fragility and fractures [23],[11]. Annually, 8.9 million fractures are reported worldwide due to osteoporosis [10]. Osteoporosis is considered the most commonly encountered bone disease in the US, as it almost affects 50% of American women and 25% of men over the age of 50 years [26]. Due to the ageing population in the EU, osteoporotic fractures are expected to be doubled by 2050 and hence will overall impact the economic burden to $25.3 billion [8]. Bone mineral density (BMD) is considered a key clinical indicator to monitor osteoporosis and is widely accepted in clinics for its diagnosis [29]. Currently, a dual-energy X-ray absorptiometry (DXA) scan is employed to measure the BMD of the trabecular bone [29],[20]. However, DXA is not cost-effective, as the scan is time-consuming and the device is not portable. Moreover, DXA uses ionising radiations, and therefore frequent DXA scans are associated with long term health risks [22]. Therefore, alternative imaging

technologies such as microwave imaging (MWI) have targeted trabecular bone evaluation to replace DXA in the overall diagnosis of osteoporosis [16].

MWI is an emerging diagnostic technology being investigated for a range of medical applications such as breast cancer detection and diagnosing brain stroke [33],[25],[32]. The key advantages of MWI for diagnosing and monitoring various diseases compared to existing imaging modalities are non-ionising radiations, portability, and low cost [3]. Recent studies have investigated the feasibility of using MWI for osteoporosis monitoring [1],[22],[12] based on the notable difference between dielectric properties of healthy and diseased human trabecular bones [2],[5],[6]. The associated clinical advantages and the difference of dielectric properties between healthy and diseased human trabecular bones make MWI a potential imaging modality for monitoring bone health in comparison to the DXA [5],[21]. MWI can be classified into two main categories: radar-based and tomographic MWI [7]. In radar-based MWI techniques, images are constructed based on the scattered waves that arise due to the dielectric contrast between normal and malignant tissues [30]. The radar-based techniques are mainly used to localize any strong scatterer/pathology in the biological tissues without reconstructing the full image of biological tissues [27]. Contrary to this, the tomographic MWI techniques aim at retrieving the spatial distribution of dielectric properties (relative permittivity (ε_r) and conductivity ($\sigma(S/m)$)) of biological tissues by processing measured scattered electromagnetic (EM) field data [33].

A comprehensive review of bone dielectric properties in the microwave frequency range was reported by Amin *et al.* [1]. This review reported that only two studies to date have measured the dielectric properties of human trabecular bones, which suggests that limited work has been done on this topic. Meaney *et al.* [22] reported *in vivo* dielectric properties of human calcaneus bone by using microwave tomography (MWT) for a frequency range of 900 - 1700 MHz. In this study, the authors have used their breast imaging prototype for imaging the human heel of two patients suffering from a lower leg injury and achieved promising results [22]. However, a dedicated MWI system for bone imaging application would further improve their results for monitoring osteoporosis. The second study was performed by Irastorza *et al.* [18], in which the authors have measured *in vitro* dielectric properties of normal human trabecular bones extracted from patients undergoing total hip replacement surgeries

by using open-ended coaxial line (OECL) probes in the frequency range of 100 - 1300 MHz. In another study, Amin *et al.* [5] reported *in vitro* dielectric properties of diseased human trabecular bones extracted also from patients undergoing total hip replacement surgeries by using OECL probes in a frequency range of 0.5 - 8.5 GHz. Amin *et al*. [5] also performed a comparison between diseased human trabecular bones with different bone volume fraction finding a significant dielectric variation between osteoporotic and osteoarthritis human trabecular bone samples.

Despite the promising initial evidence that dielectric properties can be potentially used for osteoporosis diagnosis, no dedicated MWI system exists to measure *in vivo* dielectric properties of human bone in the microwave frequency range. Some of the important initial steps towards the development of an MWI system for bone imaging require the knowledge of the optimal frequency band, the appropriate matching medium for maximum EM field penetration, and the development of numerical bone models to be adopted in the validation. Therefore, this study aims to investigate these issues to assess the feasibility of MWI for imaging bones and monitoring osteoporosis and osteoarthritis and will accelerate the development of prototype systems and algorithms to image the dielectric properties of bone for diagnostic purposes.

The application of MWI for the reconstruction of dielectric properties of target tissue primarily depends upon the dielectric contrast between the target and its surrounding tissues. The target tissue for bone imaging application to monitor osteoporosis is trabecular bone, as osteoporosis continuously deteriorates the trabecular bone microarchitecture, which makes the bone fragile causing fractures [10]. Moreover, the trabecular bones (inner part of the bone) have a spongier pattern than the cortical bones (hard exterior part of the bone), thus trabecular bones are more prone to osteoporotic fractures [26]. Therefore, firstly, this study has collated and analysed the dielectric properties of various human heel tissues from the literature. The human heel is composed of skin, fat, muscle, cortical bone, and trabecular bone. The dielectric contrast of heel tissues will determine whether the trabecular bone can be distinguished based on the dielectric properties from other tissues present in the heel. Once the dielectric contrast of heel tissues was established, a transmission line (TL) formalism approach as the one adopted in [32] for MWI applied to cerebrovascular diseases was adopted for finding feasible frequency band for bone imaging applications as well as a proper matching medium. The electric field (E-field)

penetration, the received signal strength, and the power loss were analysed for this feasible frequency band and the proposed matching medium. In this analysis, simplified numerical modelling of the human heel was exploited.

The finite difference time domain (FDTD) simulations were performed using numerical models of the heel, which was modelled as a five-layered cylinder composed of: skin, fat, muscle, cortical bone, and trabecular bone. Further, to analyse the feasible frequency band for osteoporotic and osteoarthritis bone samples, the dielectric properties of the trabecular bone layer in the five-layered cylindrical model were modified based on the dielectric properties of osteoporotic and osteoarthritis bone samples as reported by Amin *et al.* [5]. The trabecular bone microarchitecture of osteoarthritis patients is compact and dense compared to osteoporotic patients [35]. The dense trabecular microarchitecture of bone indicates a higher degree of mineralisation due to the greater amount of bone present [22],[23]. Therefore, the bone samples from osteoarthritis and osteoporotic patients allows establishing the variation in bone dielectric properties due to variation in mineralisation content and microarchitecture between two diseased bones [4]. Once an optimal frequency band was determined, the matching medium dielectric properties were selected based on the feasible frequency band. An optimum choice for matching medium helps to improve the coupling between the incident wave and the tissues. In summary, this study has investigated: the dielectric contrast of human heel tissues; suitable frequency band for bone imaging; appropriate matching medium for maximum EM field penetration in the heel; numerical model of the human heel, and validation of selected frequency band in terms of E-field penetration in the trabecular bone, received signal strength across the numerical model of the heel, and power loss across simple but realistic human heel imaging scenario. The findings of this study support the development of an MWI prototype for monitoring osteoporosis.

4.2 Methods

4.2.1 Dielectric properties contrast of tissues present in the heel

The application of MWI for reconstructing the dielectric properties of biological tissues primarily depends upon the dielectric contrast between the tissues of the target anatomical site. Therefore, to diagnose osteoporosis the trabecular bone should exhibit a dielectric contrast to other tissues present in the heel and their contrast between different heel tissues was investigated. The tissues considered for modelling the

human heel were skin, fat, muscle, cortical bone, and trabecular bone. The dielectric measurement data of considered tissues was acquired from Gabriel *et al*. [15] for a frequency range of 0.5 – 5 GHz. Gabriel *et al*. [15]'s study is the most comprehensive study widely used for characterising the dielectric properties of tissue measured under a similar experimental setup. Moreover, to analyse the penetration depth of EM waves as a function of frequency, the skin depth of considered tissues is analysed. The skin depth data of considered tissues were acquired from Gabriel *et al*. [14] for a frequency range of 0.5 – 5 GHz. Gabriel *et al*. [14] have presented the skin depth of various biological tissues as a function of frequency. The data acquired from Gabriel *et al*. [14] was plotted in MATLAB (The MathWorks, Natick, MA, USA). The anatomical structure of the human heel and the structure of bone is shown in Figure 4.1 (a) and (b) respectively.

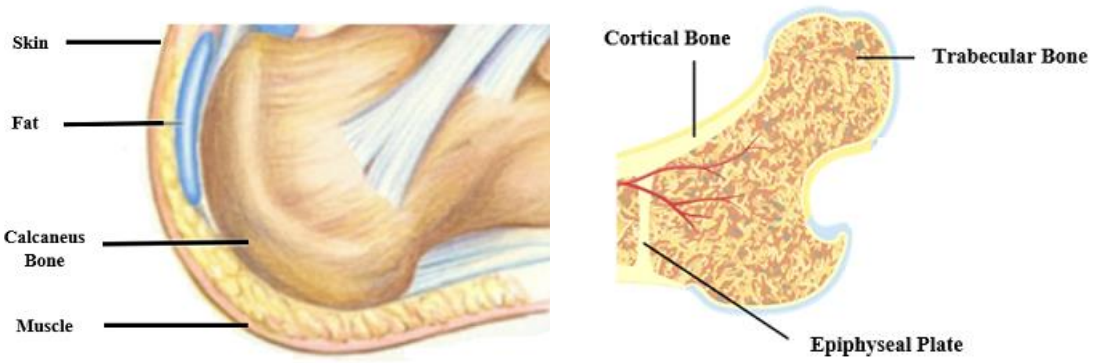

(a) (b)

Figure 4.1: (a) Anatomical structure of human heel (© 2014 WebMD, LLC. All rights reserved) (b) Anatomical structure of bone.

4.2.2 On the choice of frequency range and the matching medium

The choice of frequency range and matching medium's relative permittivity suitable for the design of an MWI device for bone health monitoring is performed by adopting the TL formalism approach as in [32]. These two parameters represent the degrees of freedom of the MWI device [31], the choice of these parameters should be performed to impact the following two objectives:

1. Maximum incident power should penetrate the target tissue (in our case the trabecular bone)
2. The spatial resolution should be maximum to detect the small variations in the target tissue

The frequency range and the matching medium properties dictate the wavelength of the EM wave and hence the spatial resolution achieved by MWI [34]. Moreover, the choice of the relative permittivity of the matching medium determines, from each frequency, the EM wave penetration into the medium under investigation, the higher the matching between electrical discontinuities, the higher the EM penetration would be.

To address these choices, a planar layered model and a cylindrical layered model were investigated. The planar layered model allows for the use of the TL formalism approach and it is therefore convenient for a first-order analysis which is then validated numerically with the cylindrical layered model [31]. The TL formalism approach helps to identify the feasible frequency band based on the transmission coefficient (T). In TL formalism approach, the anatomical site to be imaged is modelled as one-dimensional (1-D) planar layered model, where each layer is assigned with an equivalent impedance (Z) [32]. The penetration of EM waves into trabecular bone can be assessed from the strength of the transmission coefficient. Moreover, the choice of matching medium's relative permittivity is dictated based on the feasible frequency band.

4.2.2.1 Planar layered model

The planar layered model approach models the heel as a 1-D layered structure. The probing wave (E_{inc}) which impacts the 1-D structure is modelled as a plane wave with normal incidence. The 1-D heel structure of the human heel is composed of five layers: skin, fat, muscle, cortical bone, and trabecular bone as shown in Figure 4.2. Based on the empirical studies and average statistics of the thickness of human biological tissues the thickness of skin, fat, and cortical bone was taken equal to 3.5 mm [28], 5 mm [32], and 3 mm [13] respectively. While the thickness of other layers is based on the values reported in the literature, the thickness of the muscle is assumed to be 6 mm (slightly greater than the fat). The trabecular bone was modelled as half-space to ensure maximum penetration of the EM field. Each layer was assigned the dielectric properties of the corresponding tissue layer. The 1-D numerical modelling and FDTD simulations were performed with MATLAB (The MathWorks, Natick, MA, USA).

Figure 4.2: The 1-D planar layered model of the human heel, which is composed of five layers: skin, fat, muscle, cortical bone, and trabecular bone. E_{inc} is the probing wave.

To investigate the propagation of the EM wave using the TL formalism, each tissue layer is modelled as impedance as shown in Figure 4.3. The impedances $Z_{mm}, Z_s, Z_f, Z_m, Z_{CB}$, and Z_{TB} represent impedance of matching medium, skin, fat, muscle, cortical bone, and trabecular bone respectively. The trabecular bone represents the load of the TL circuit. The impedance of any specific tissue layer (Z_n) is modelled as:

$$Z_n = \sqrt{\frac{\mu_o}{\varepsilon_o \varepsilon_n}} \qquad (4.1)$$

where ε_n denotes the complex permittivity of the tissue layer under consideration, μ_o and ε_o denote permeability and relative permittivity of free space respectively. The amount of incident power captured by the heel can be modelled by using the transmission coefficient and is given as:

$$T = 1 - \Gamma \ , \qquad (4.2)$$

where Γ denotes the reflection coefficient at plane HH' (interface between the matching medium and the heel). The reflection coefficient is given as:

$$\Gamma = \frac{Z_{HH'} - Z_{mm}}{Z_{HH'} + Z_{mm}} \qquad (4.3)$$

where Z_{mm} denotes the impedance of matching medium and $Z_{HH'}$ denotes the impedance of the plane HH'.

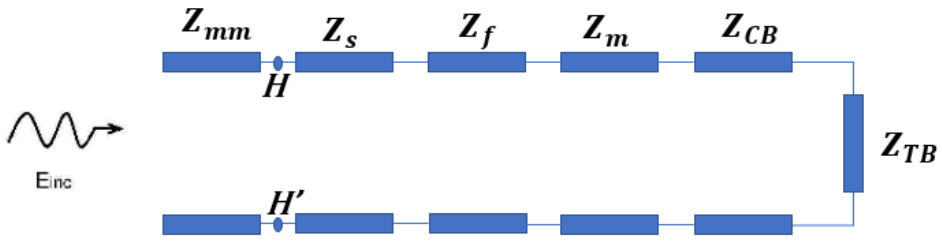

Figure 4.3: The transmission line model of 1-D heel structure. The $Z_{mm}, Z_{HH'}, Z_s, Z_f, Z_m, Z_{CB}$, and Z_{TB} represent impedance of matching medium, plane HH', skin, fat, muscle, cortical bone, and trabecular bone respectively.

4.2.2.2 Cylindrical layered model

To assess the validity of the outcomes (feasible frequency band and matching medium permittivity) of the TL analysis with a more realistic (while still simple) model, a five-layered cylindrical heel model was designed as shown in Figure 4.4. The choice of cylindrical layered model is used because the shape of the human heel resembles closely a cylinder. The validity was assessed in terms of E-field penetration into trabecular bone, the amplitudes of the received signal, and the power loss in the five-layered heel structure. The objective of the numerical modelling was to assess the validity of the feasible frequency band obtained by the TL analysis. Therefore, a single frequency of 1.3 GHz was selected from the feasible frequency band (0.6 – 1.9 GHz) and FDTD simulations were then performed at the selected frequency of 1.3 GHz. Therefore, each layer of the model was assigned with a relative permittivity and conductivity of the corresponding tissue of the human heel at 1.3 GHz as acquired from Gabriel *et al*. [15]. The thickness and dielectric properties of each layer are tabulated in Table 4.1.

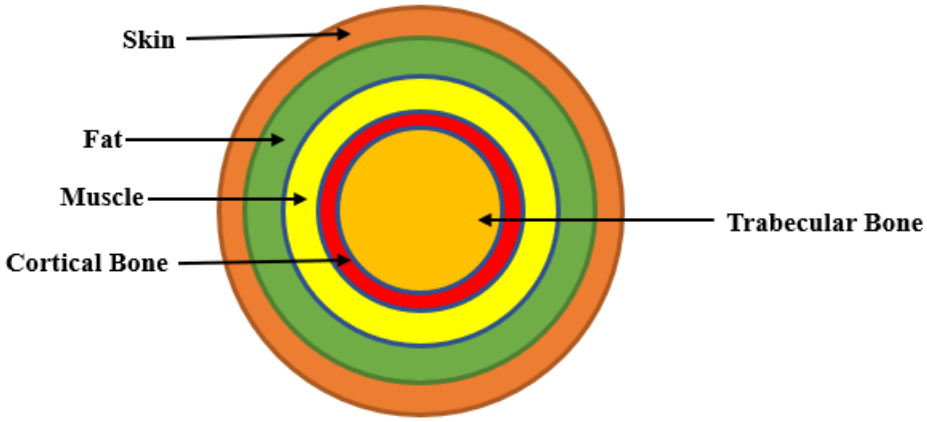

Figure 4.4: A five-layered human heel model.

Table 4.1: Dielectric properties and thickness of considered tissues of the human heel. The dielectric properties are reported at 1.3 GHz. The values are taken from Gabriel *et al*. [15].

Tissue	**Relative Permittivity**	**Conductivity** $[S/m]$	**Thickness[mm]**
Skin	39.917	1.0009	3.5
Fat	5.4073	0.061787	5
Muscle	54.268	1.0973	6
Cortical Bone	12.124	0.19638	3
Trabecular Bone	20.06	0.44158	15

To assess the E-field penetration for osteoporotic and osteoarthritis bones, the dielectric properties of the trabecular bone layer for the five-layered cylindrical model were modified. The values of relative permittivity and conductivity for osteoporotic and osteoarthritis bones were acquired from Amin *et al*. [5]. The values of relative permittivity and conductivity for osteoporotic and osteoarthritis bones at 1.3 GHz are tabulated in Table 4.2. The numerical modelling and FDTD simulations were performed in computer simulation technology software (CST MWS Suite 2018, Dassault Systemes, France).

Table 4.2: Dielectric Properties of osteoporotic and osteoarthritis human trabecular bone samples at 1.3 GHz.

Bone Sample	**Relative Permittivity**	**Conductivity** $[S/m]$
Osteoporotic	18.2981	0.4746
Osteoarthritis	28.0299	0.6705

To validate the feasible frequency band, the five-layered cylindrical model was excited by using four waveguide ports having transverse magnetic (TM) propagation. These waveguide ports sequentially illuminated the cylindrical model with a modulated wideband Gaussian pulse. The waveguide ports were placed circularly at equidistant from each other around the cylindrical model. The simulation box had a size of 125 mm × 50 mm × 125 mm and a total of 370,881 mesh cells. The minimum and maximum mesh cell sizes are 1 mm and 1.86045 mm respectively. The perfectly matched layer (PML) boundary conditions were used in the simulation. The minimum distance of PML to the simulating structure is 4 fractions wavelength. The FDTD simulation was performed in CST and the received signal strength between two

waveguide ports placed around the five-layered cylindrical model was analyzed.

4.3 Results and Discussion

This section firstly presents an analysis of the comparison of dielectric properties of considered tissues in the heel. Then, the TL formalism approach is presented to investigate the feasible frequency band of the MWI system for bone imaging application considering the human heel as our target anatomical site. The peripheral location of the human calcaneus bone and a similar ratio of cortical to the trabecular bone as found in the femoral head and lumbar spine makes it suitable for bone health monitoring [22],[36],[24]. The femoral head and lumbar spine are primary targets for standard osteoporosis monitoring technologies [36].

4.3.1 Dielectric properties contrast of tissues present in the heel

Figure 4.5 shows the dielectric properties of all considered tissues present in the heel. The dielectric data is acquired from Gabriel *et al*. [15]'s database for the 0.5 – 5 GHz frequency band. The dielectric profile of tissues suggests that a significant amount of contrast exists in terms of relative permittivity and conductivity among all tissues present in the heel. More precisely, as it can be observed from Figure 4.5 that the dielectric properties of trabecular bone can be well distinguished from the dielectric properties of other tissues present in the heel. The average percentage difference between the relative permittivity and conductivity of the skin and trabecular bone is found to be 70% and 56% respectively, whereas the average percentage difference between the relative permittivity and conductivity of trabecular bone and cortical bone is found to 48% and 65% respectively, across 0.5 – 5 GHz. The presence of enough dielectric contrast between heel tissues assures that MWI can be employed to distinguish and to reconstruct the dielectric properties of trabecular bone.

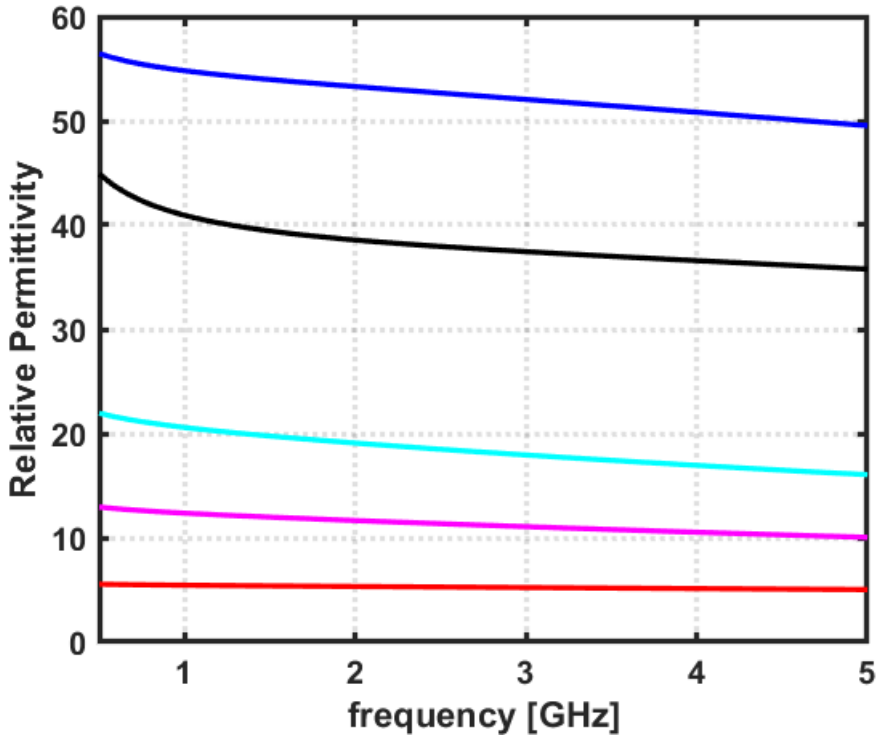

(a)

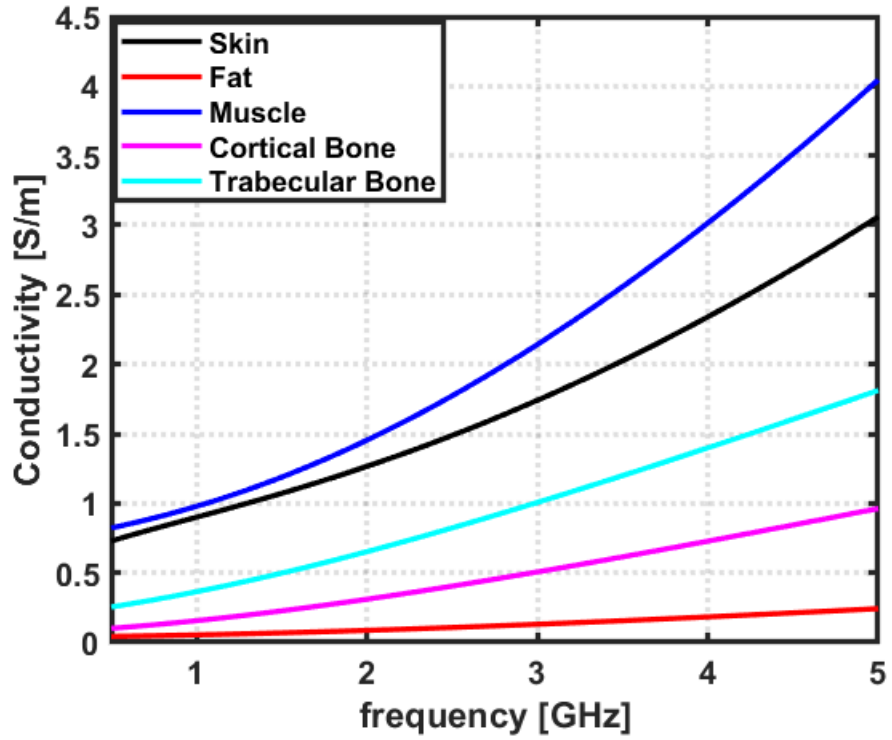

(b)

Figure 4.5: Dielectric properties of considered tissues in human heel: (a) Relative Permittivity; (b) Conductivity. The values are taken from Gabriel *et al*. [15].

4.3.2 On the Choice of Frequency Range and the Matching Medium

4.3.2.1 Planar Layered Model

To determine the feasible frequency band and relative permittivity of the matching medium, the transmission coefficient is evaluated as a function of frequency (0.5 – 5 GHz) as shown in Figure 4.6. It can be observed from Figure 4.6, that a frequency band exists between 2 – 3.5 GHz, where the transmission coefficient is significantly less. The magnitude of the transmission coefficient in the 2 – 3.5 GHz range is comparatively lower compared to 0.6 – 1.9 GHz, hence the operating conditions of the MWI device does not seem favourable in this frequency range.

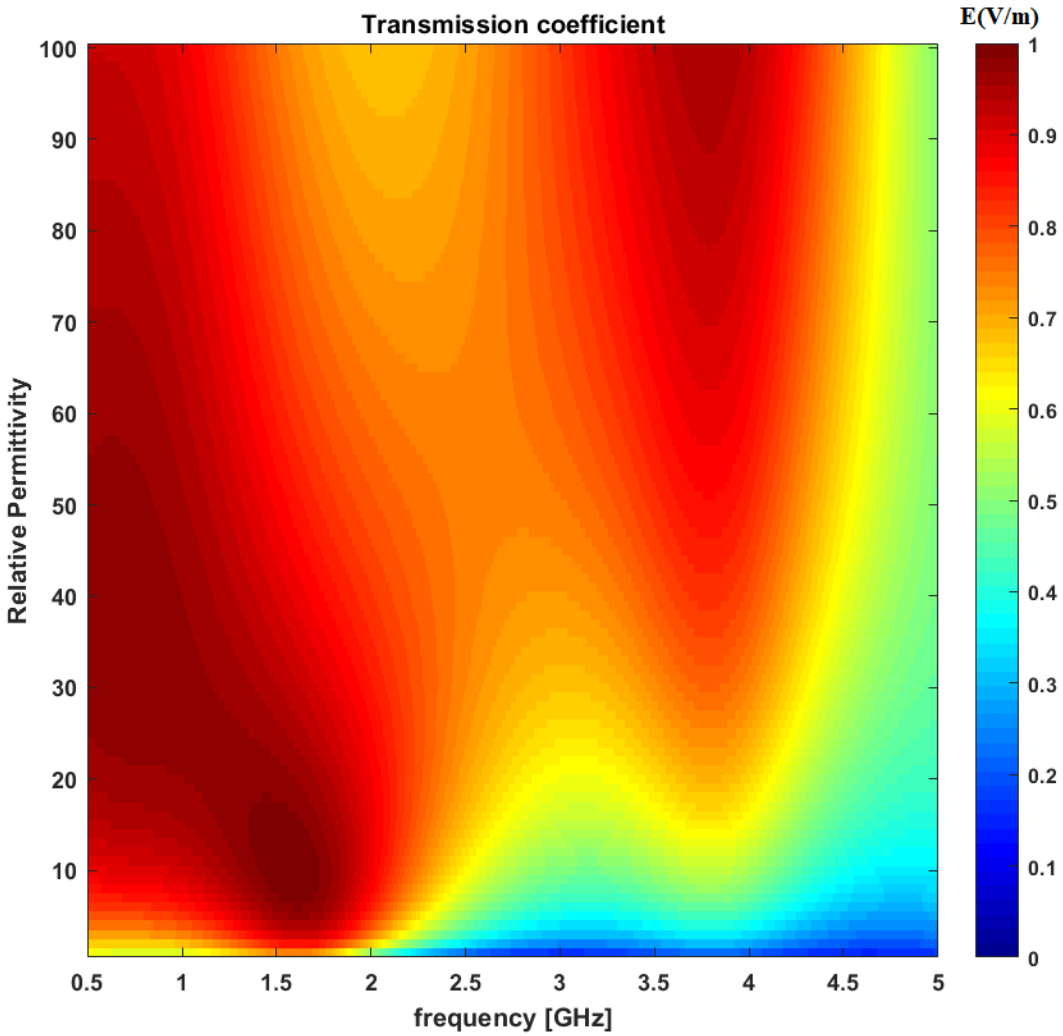

Figure 4.6: The transmission coefficient as a function of frequency and relative permittivity of the matching medium.

The 2 – 3.5 GHz frequency range is less convenient for the MWI device. The value of the transmission coefficient is less in the 2 – 3.5 GHz frequency range, this is because a noticeable difference exists in terms of dielectric properties of each layer

considered in the five-layered heel model. In addition to this, the electrical length of low permittivity tissue layers such as fat and cortical bone causes a strong mismatch. It can be observed that the magnitude of the transmission coefficient is strong beyond 3 GHz. However, the low penetration depth of all considered tissues beyond 2.5 GHz makes 3 GHz less favourable for the MWI device. Taking all these considerations, 0.6 – 1.9 GHz would be the most appropriate frequency range for MWI of the human heel for bone health monitoring. Regarding the choice of relative permittivity for matching medium, it can be observed from Figure 4.6 that any value of relative permittivity can be chosen between 15 – 40 for a frequency range of 0.6 – 1.9 GHz. The value of relative permittivity greater than 40 results in a higher frequency range. As the spatial resolution depends upon the wavelength in the background medium, therefore, a matching medium having a large value of relative permittivity will be preferable [34]. The choice of matching medium primarily depends upon factors such as conductive loss, relative permittivity, antenna matching, and ease of use [17]. Therefore, an oil/water emulsion can be prepared to achieve a conductivity of 0.05 S/m and relative permittivity of 23 [17]. Other fluids including safflower oil, glycerin, and acetone can also be used as a matching medium to achieve similar relative permittivity and conductivity [17].

The penetration of EM waves in human biological tissues reduces as a function of frequency. To investigate the feasible frequency band based on the penetration of EM waves, data is acquired from Gabriel *et al*. [14] for considered tissues present in the heel. Figure 4.7 depicts the penetration of EM fields for the observed frequency band (0.5 – 5 GHz). It can be observed from Figure 4.7 that the penetration of EM fields reduces above 3 GHz in all considered tissues of the heel. Therefore, considering frequencies above 3 GHz for designing an MWI system would not be feasible for bone imaging applications due to the low penetration of EM waves.

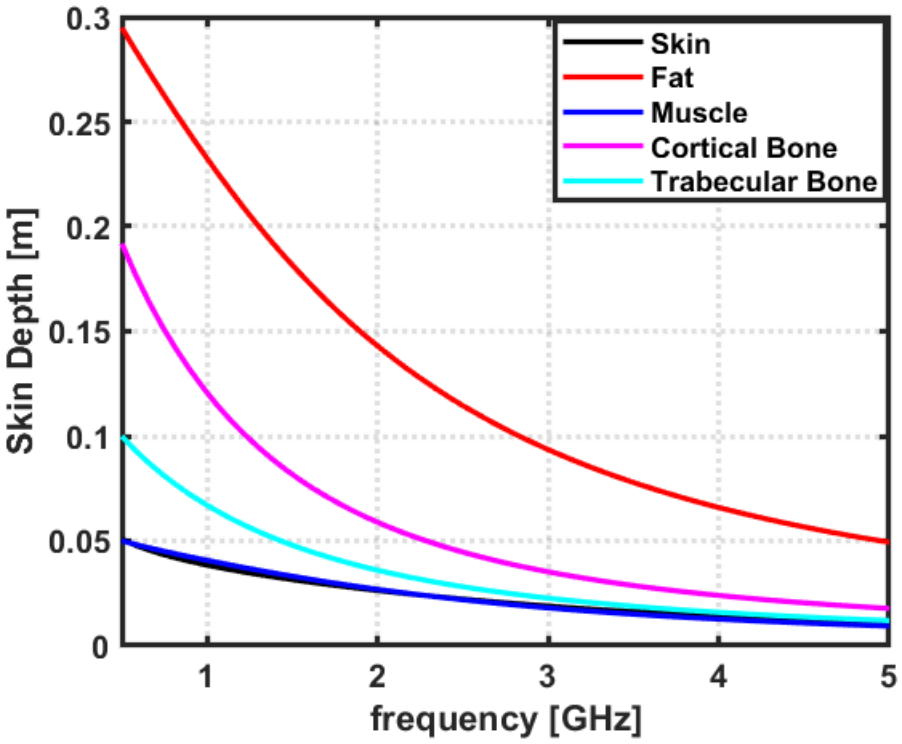

Figure 4.7: Skin depth of considered tissues in the human heel. The values are taken from Gabriel *et al*. [14].

4.3.2.2 Cylindrical Layered Model

The waveguide port 1 was excited and the received signal strength at port 2 was analyzed. Both port 1 and port 2 were placed opposite each other, ensuring maximum distance between the ports. Two simulations in CST were performed. The first simulation was performed for a 0.6 – 1.9 GHz frequency band, while, the second simulation was performed for a 2.4 – 3.5 GHz frequency band. The coupling medium used in the simulations has a relative permittivity of 23 and conductivity of 0.005 S/m. Figure 4.8 shows the comparative analysis of the received signal at port 2 when port 1 was excited. It can be observed from Figure 4.8, that the received signal at port 2 is significantly high for the frequency band of 0.6 – 1.9 GHz (feasible frequency band) compared to the received signal for the frequency band of 2.4 – 3.5 GHz (inconvenience frequency band). The average percentage difference between the maximum signal for the two cases is found to be 82%, however, the average percentage difference between the minimum signal for the two cases is found to be 88%. As the received signal for the 0.6 – 1.9 GHz frequency band is found to be more compared to the 2.4 – 3.5 GHz frequency band, therefore, our feasibility analysis based on transmission coefficient is validated. Therefore, the upper-frequency range of MWI should be kept below 2 GHz for the maximum received signal.

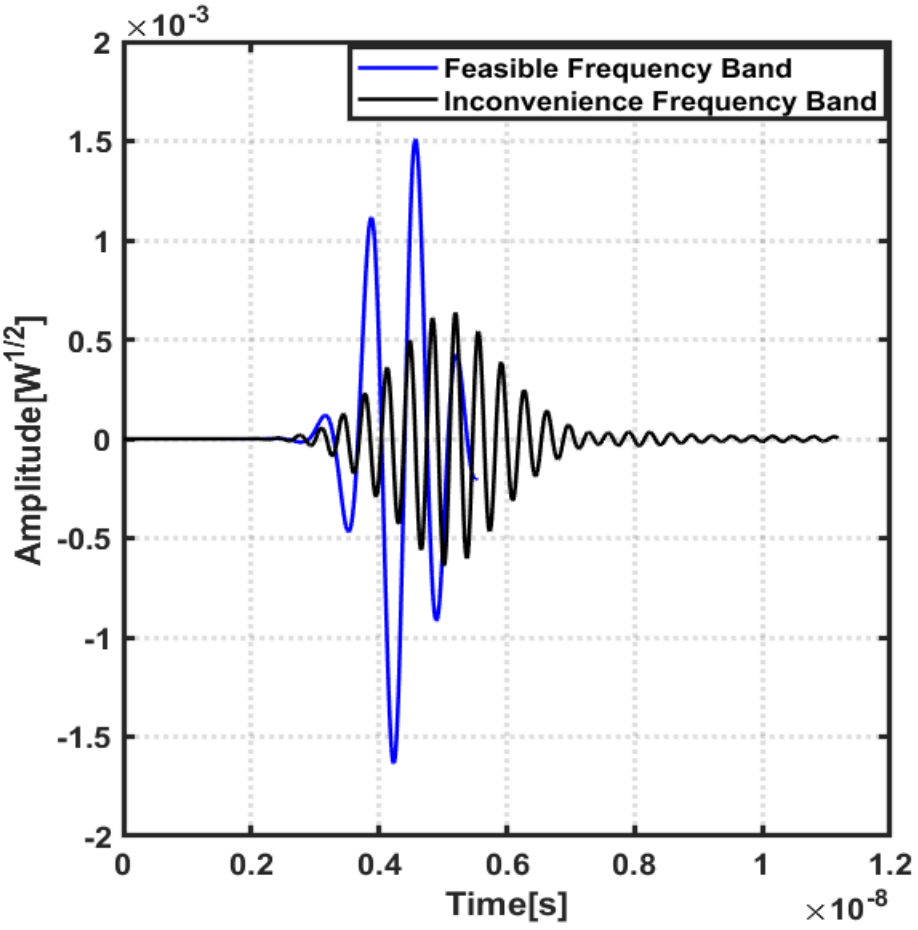

Figure 4.8: Port signals for feasible and inconvenience frequency band.

An analysis was performed in CST, to analyze the power loss across five-layered medium as a function of frequency. The result of power loss across the five-layered cylindrical model is shown in Figure 4.9. It can be observed from Figure 4.9 that the power loss increases in the five-layered cylindrical model as the frequency increases. Thus, for maximum power penetration and minimum power loss for the trabecular bone layer, the operational frequency of the MWI device should be restricted to the lower frequency band.

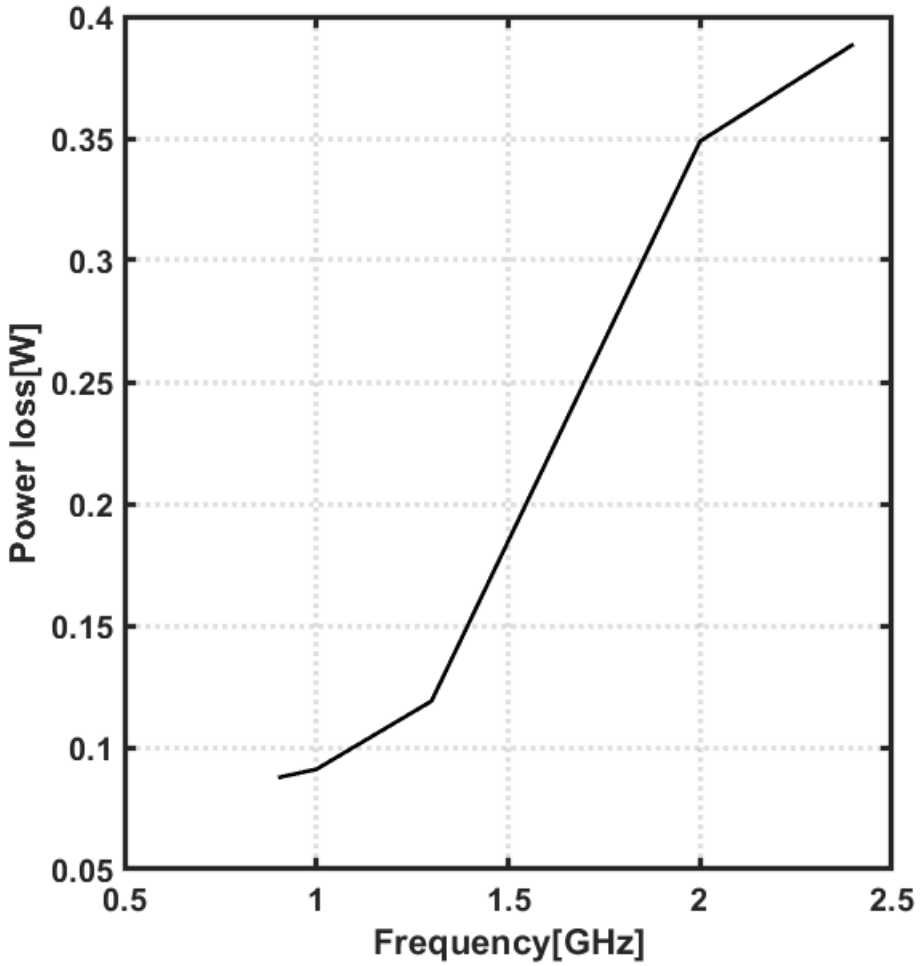

Figure 4.9: Power loss in dielectrics for five-layered medium.

4.3.2.3 E-field Distribution in Numerical Bone Models

Figure 4.10(a) shows the z-component of E-field distribution at 1.3 GHz for an osteoporotic numerical bone model. It can be observed from Figure 4.10(a) that a noticeable amount of E-field penetrates trabecular bone for a five-layered cylindrical model. The penetration of E-field to trabecular bone layer, and hence, the dielectric contrast of the five-layered model suggests enough initial evidence that a dielectric properties map can be generated by applying MWT imaging algorithms on measured EM scattered fields. Moreover, it can also be observed from Figure 4.10(a) that the skin and muscle layers have higher E-field intensity compared to the trabecular bone layer. This is because these layers have high dielectric properties compared to other layers, therefore, most of the E-field is dissipated in these layers.

Figure 4.10(b) shows the z-component of E-field distribution at 1.3 GHz for the osteoarthritis numerical bone model. Like the osteoporotic numerical bone model, it can be observed from Figure 4.10(b) that enough E-field penetrates trabecular bone

for the osteoarthritis numerical bone model. Therefore, based on enough E-field penetration both for osteoporotic and osteoarthritis numerical bone models, it can be concluded that the MWT algorithm would be able to classify the numerical bone models based on reconstructed dielectric properties. Similar findings were obtained for the numerical bone model developed by using dielectric properties of trabecular bone acquired from Gabriel *et al*. [15] as shown in Figure 4.10(c).

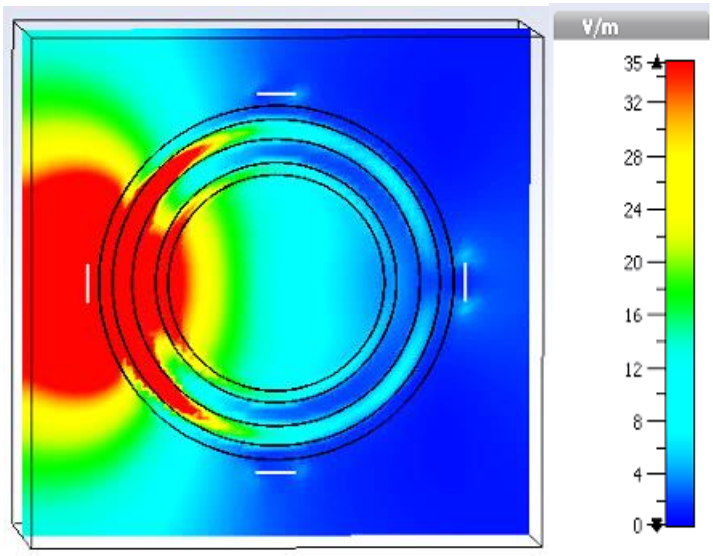

(a)

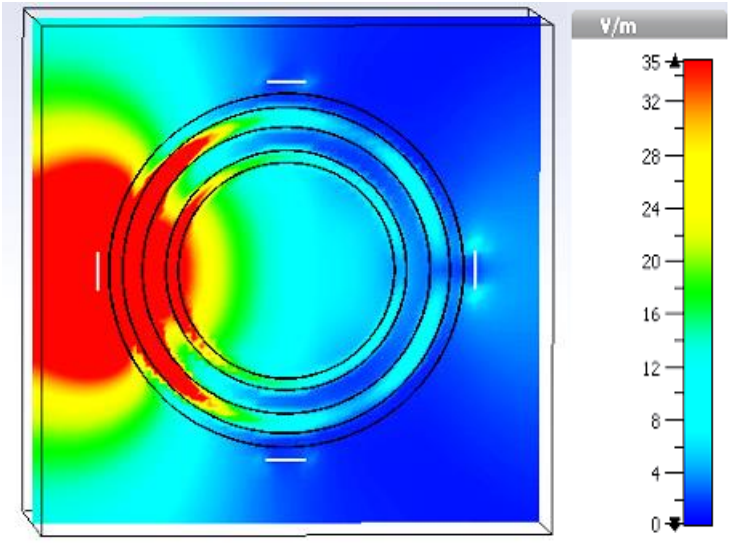

(b)

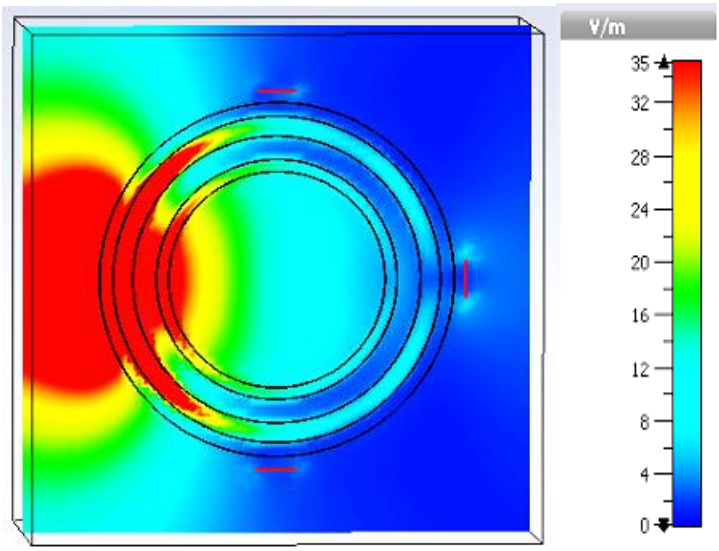

(c)

Figure 4.10: Average E-field distribution at 1.3 GHz; (a) for Osteoporotic Bone (b) for Osteoarthritis Bone (c) for Gabriel *et al*. [15]'s Trabecular Bone.

4.4 Conclusion

The application of MWI for reconstructing the dielectric properties primarily depends upon the dielectric contrast between tissues of the target anatomical site. Moreover, the spatial resolution of reconstructed images and maximum penetration of EM fields to target tissue primarily depends upon the operational frequency range of the MWI device. This study has made the first attempt towards the investigation of aforementioned constraints before designing of MWI device for monitoring osteoporosis. Firstly, the contrast of dielectric properties of tissues present in the human heel was investigated. Secondly, the TL formalism approach is adopted for finding an optimal selection of frequency band and the corresponding matching medium. Finally, the numerical modelling of the human heel is performed. Based on FDTD simulations performed, the E-field penetration, the received signal strength, and the power loss in the five-layered heel model were analysed. The initial findings from CST simulations on E-field penetration supported the choice of the frequency band by the TL formalism approach. The initial feasibility analysis suggests that the dielectric contrast of the target anatomical site along with the TL formalism approach can be considered as useful tools before designing of MWI system.

These findings support the idea for the development of the MWI device for bone health monitoring. The future work will be based on the development of an MWI prototype for bone imaging. Initially, the MWI system will be tested on bone

phantoms. The dielectric properties of bone phantoms will be reconstructed by employing the MWT algorithm. The development of such an MWI device for *in vivo* dielectric properties assessment of bones will help in monitoring the bone quality and hence will provide a low cost, non-invasive, and portable solution for monitoring bone health.

Acknowledgements

The research leading to these results has received funding from the European Research Council under the European Union's Horizon 2020 Programme/ERC Grant Agreement BioElecPro n. 637780 and from the EMERALD project funded from the European Union's Horizon 2020 research and innovation program under the Marie Skłodowska-Curie grant agreement No. 764479. This work is also supported by COST Action MyWAVE CA17115 with an STSM grant entitled "European network for advancing Electromagnetic hyperthermic medical technologies".

Conflict of Interest: The authors declare that they have no conflict of interest.

References

1. Amin B, Elahi MA, Shahzad A et al (2018) Dielectric properties of bones for the monitoring of osteoporosis. Med Biol Eng Comput. https://doi.org/10.1007/s11517-018-1887-z
2. Amin B, Elahi MA, Shahzad A et al (2019) A review of the dielectric properties of the bone for low frequency medical technologies. Biomed Phys Eng Express 5:022001. https://doi.org/10.1088/2057-1976/aaf210
3. Amin B, Kelly D, Shahzad A et al (2020) Microwave calcaneus phantom for bone imaging applications. In: 2020 14th Eur. Conf. Antennas Propag. S 1–5
4. Amin B, Shahzad A, Farina L et al (2019) Investigating human bone microarchitecture and dielectric properties in microwave frequency range. In: 2019 13th Eur. Conf. Antennas Propag. IEEE, S 1–5
5. Amin B, Shahzad A, Farina L et al (2020) Dielectric characterization of diseased human trabecular bones at microwave frequency. In: 2020 Med. Eng. Phys. S 1–8
6. Amin B, Shahzad A, O'halloran M, Elahi MA (2020) Microwave bone imaging: A preliminary investigation on numerical bone phantoms for bone health monitoring. Sensors (Switzerland) 20:1–21.

https://doi.org/10.3390/s20216320

7. Bourqui J, Sill JM, Fear EC (2012) A prototype system for measuring microwave frequency reflections from the breast. Int J Biomed Imaging. https://doi.org/10.1155/2012/851234
8. Burge R, Dawson-Hughes B, Solomon DH et al (2007) Incidence and Economic Burden of Osteoporosis-Related Fractures in the United States, 2005-2025. J Bone Miner Res 22:465–475. https://doi.org/10.1359/jbmr.061113
9. Chen H, Zhou X, Fujita H et al (2013) Age-related changes in trabecular and cortical bone microstructure. Int J Endocrinol 2013:213234. https://doi.org/10.1155/2013/213234
10. Cosman F, de Beur SJ, LeBoff MS et al (2014) Clinician's Guide to Prevention and Treatment of Osteoporosis. Osteoporos Int 25:2359–2381. https://doi.org/10.1007/s00198-014-2794-2
11. Cruz AS, Lins HC, Medeiros RVA et al (2018) Artificial intelligence on the identification of risk groups for osteoporosis, a general review. Biomed Eng Online 17:12. https://doi.org/10.1186/s12938-018-0436-1
12. Fajardo JE, Lotto FP, Vericat F et al (2020) Microwave tomography with phaseless data on the calcaneus by means of artificial neural networks. Med Biol Eng Comput 58:433–442
13. Fajardo JE, Vericat F, Irastorza G et al (2019) Sensitivity analysis on imaging the calcaneus using microwaves. Biomed Phys Eng Express. https://doi.org/10.1088/2057-1976/ab3330
14. Gabriel C (2010) Dielectric properties of body tissues in the frequency range 10Hz–100GHz. IFAC (L'Istituto di Fis. Appl. "Nello Carrara") Website
15. Gabriel C, Gabriel S, Corthout E et al (1996) The dielectric properties of biological tissues : III . Parametric models for the dielectric spectrum of tissues The dielectric properties of biological tissues : III . Parametric models for the dielectric spectrum of tissues.
16. Golnabi AH, Meaney PM, Geimer S et al (2011) Microwave tomography for bone imaging. Proc - Int Symp Biomed Imaging 9:956–959. https://doi.org/10.1109/ISBI.2011.5872561
17. Haynes M, Stang J, Moghaddam M (2014) Real-time microwave imaging of

differential temperature for thermal therapy monitoring. IEEE Trans Biomed Eng 61:1787–1797. https://doi.org/10.1109/TBME.2014.2307072

18. Irastorza RM, Blangino E, Carlevaro CM, Vericat F (2014) Modeling of the dielectric properties of trabecular bone samples at microwave frequency. Med Biol Eng Comput 52:439–447. https://doi.org/10.1007/s11517-014-1145-y
19. Van Der Linden JC, Weinans H (2007) Effects of microarchitecture on bone strength. Curr Osteoporos Rep 5:56–61. https://doi.org/10.1007/s11914-007-0003-3
20. Lochmüller E-M, Müller R, Kuhn V et al (2003) Can Novel Clinical Densitometric Techniques Replace or Improve DXA in Predicting Bone Strength in Osteoporosis at the Hip and Other Skeletal Sites? J Bone Miner Res 18:906–912. https://doi.org/10.1359/jbmr.2003.18.5.906
21. Makarov SN, Noetscher GM, Arum S et al (2020) Concept of a Radiofrequency Device for Osteopenia / Osteoporosis Screening. :1–15. https://doi.org/10.1038/s41598-020-60173-5
22. Meaney PM, Goodwin D, Golnabi AH et al (2012) Clinical microwave tomographic imaging of the calcaneus: A first-in-human case study of two subjects. IEEE Trans Biomed Eng 59:3304–3313. https://doi.org/10.1109/TBME.2012.2209202
23. Miller PD, Zapalowski C, Kulak CAM, Bilezikian JP (1999) Bone densitometry: The best way to detect osteoporosis and to monitor therapy. J Clin Endocrinol Metab 84:1867–1871. https://doi.org/10.1210/jc.84.6.1867
24. Njeh CF, Langton CM (1997) The effect of cortical endplates on ultrasound velocity through the calcaneus: an in vitro study. Br J Radiol 70:504–510
25. O'Loughlin D, O'Halloran M, Moloney BM et al (2018) Microwave Breast Imaging: Clinical Advances and Remaining Challenges. IEEE Trans Biomed Eng 65:2580–2590. https://doi.org/10.1109/TBME.2018.2809541
26. Office of the Surgeon General (2004) Bone Health and Osteoporosis - NCBI Bookshelf.
27. Oliveira BL, Halloran MO (2018) Microwave Breast Imaging : Experimental tumour phantoms for the evaluation of new breast cancer diagnosis systems Biomedical Physics & Engineering Related content Microwave Breast Imaging : experimental tumour phantoms for the evaluation of new breast can.

https://doi.org/10.1088/2057-1976/aaaaff

28. Oltulu P, Ince B, Kökbudak N et al (2018) Measurement of epidermis, dermis, and total skin thicknesses from six different body regions with a new ethical histometric technique. Turk Plast Rekonstruktif ve Estet Cerrahi Derg 26:56–61. https://doi.org/10.4103/tjps.tjps_2_17
29. Organization WH (2004) WHO SCIENTIFIC GROUP ON THE ASSESSMENT OF OSTEOPOROSIS AT PRIMARY HEALTH Care Level. World Heal Organ May:5–7. https://doi.org/10.1016/S0140-6736(02)08761-5
30. Porter E, Coates M, Popović M (2016) An Early Clinical Study of Time-Domain Microwave Radar for Breast Health Monitoring. IEEE Trans Biomed Eng 63:530–539. https://doi.org/10.1109/TBME.2015.2465867
31. Scapaticci R, Bjelogrlic M, Vasquez JAT et al (2018) Microwave technology for brain imaging and monitoring: physical foundations, potential and limitations. In: Emerg. Electromagn. Technol. Brain Dis. Diagnostics, Monit. Ther. Springer, S 7–35
32. Scapaticci R, Di Donato L, Catapano I, Crocco L (2012) A feasibility study on microwave imaging for brain stroke monitoring. Prog Electromagn Res 40:305–324
33. Shahzad A, O'Halloran M, Jones E, Glavin M (2016) A multistage selective weighting method for improved microwave breast tomography. Comput Med Imaging Graph 54:6–15. https://doi.org/10.1016/j.compmedimag.2016.08.007
34. Slaney M, Kak AC, Larsen LE (1984) Limitations of Imaging with First-Order Diffraction Tomography. IEEE Trans Microw Theory Tech 32:860–874. https://doi.org/10.1109/TMTT.1984.1132783
35. Topoliński T, Mazurkiewicz A, Jung S et al (2012) Microarchitecture parameters describe bone structure and its strength better than BMD. Sci World J. https://doi.org/10.1100/2012/502781
36. Vogel JM, Wasnich RD, Ross PD (1988) The clinical relevance of calcaneus bone mineral measurements: a review. Bone Miner 5:35–58. https://doi.org/10.1016/0169-6009(88)90005-0.

Chapter 5

Microwave Bone Imaging: A Preliminary Investigation on Numerical Bone Phantoms for Bone Health Monitoring

Article overview

This work presents the reconstruction of dielectric properties of the numerical bone phantoms. The bone phantoms are developed based on the dielectric properties of the cortical bone and the trabecular bone. A two-layered circular model of bone is developed. The outer layer represents the cortical bone and the inner layer represents the trabecular bone. To assess the robustness of the developed microwave tomography (MWT) imaging method, a set of diverse bone phantoms are developed. The outer layer in all phantoms represents the cortical bone. The inner layer that represents the trabecular bone was varied to mimic the natural variation of dielectric properties for various clinical conditions. To this end, the bone phantoms for osteoporotic and osteoarthritis patients are developed based on their trabecular bone dielectric properties presented in Chapter 3. The bone phantoms are developed based on the single-pole Debye parameters. The performance of the distorted Born iterative method (DBIM) algorithm along with the compressed sensing-based iterative method for linear inversion of electromagnetic (EM) waves is evaluated for the reconstruction of dielectric properties of the bone phantoms. A linear inversion approach referred to as the iterative method with adaptive thresholding for compressed sensing (IMATCS) has been employed for solving the underdetermined set of linear equations at each DBIM iteration. The EM inverse scattering problem is solved on dielectrically accurate two-dimensional bone phantoms. The bone phantoms are assessed for different settings of the signal-to-noise ratio. To overcome the challenges posed by the ill-posedness of the EM inverse scattering problem, the L_2-based regularisation approach has been adopted in the amalgamation of the IMATCS approach. The

quantitative comparison between the reconstructed and corresponding reference bone dielectric properties is performed by using the normalised root mean square error and the structural similarity index. The objective is to evaluate MWT for the assessment and the reconstruction of different diseased bone phantoms for bone health monitoring. The evaluation of MWT methods on numerical phantoms before clinical testing of the MWT system helps to evaluate the robustness of the adopted approach for the reconstruction of dielectric properties under a realistic imaging scenario.

This work has been published in the journal of *Sensors (2020)*. I am the first lead author in the paper, which is co-authored with my supervisors. I developed the DBIM algorithm in the amalgamation of the IMATCS approach for solving the underdetermined set of linear equations. I led all parts of the work with the support of my supervisors.

Abstract

Microwave tomography (MWT) can be used as an alternative modality for monitoring human bone health. Studies have found a significant dielectric contrast between healthy and diseased human trabecular bones. A set of diverse bone phantoms were developed based on single-pole Debye parameters of osteoporotic and osteoarthritis human trabecular bones. The bone phantoms were designed as a two-layered circular structure, where the outer layer mimics the dielectric properties of the cortical bone and the inner layer mimics the dielectric properties of the trabecular bone. The electromagnetic (EM) inverse scattering problem was solved using a distorted Born iterative method (DBIM). A compressed sensing-based linear inversion approach referred to as the iterative method with adaptive thresholding for compressed sensing (IMATCS) has been employed for solving the underdetermined set of linear equations at each DBIM iteration. To overcome the challenges posed by the ill-posedness of the EM inverse scattering problem, the L_2-based regularisation approach was adopted in the amalgamation of the IMATCS approach. The simulation results showed that osteoporotic and osteoarthritis bones can be differentiated based on the reconstructed dielectric properties even for low values of the signal-to-noise ratio. These results show that the adopted approach can be used to monitor bone health based on the reconstructed dielectric properties.

Chapter 5. Microwave Bone Imaging: A Preliminary Investigation on Numerical Bone Phantoms for Bone Health Monitoring

5.1 Introduction

Microwave imaging (MWI) is an emerging diagnostic technology being investigated for a range of medical applications. The key advantages of MWI for diagnosing and monitoring various diseases compared to existing imaging modalities are non-ionising radiations, portability, and low cost [1,2]. One of the notable applications of MWI is towards breast cancer detection [3–5], with four clinical systems being tested in clinical trials [5]. The detection of breast cancer relies on the inherent dielectric contrast between normal and malignant breast tissues [6–9]. Besides breast cancer detection, various studies have employed MWI for the diagnosis of brain stroke, exploiting the dielectric contrast between ischemic and healthy tissues [10,11]. Recent studies have investigated the feasibility of using MWI for osteoporosis monitoring [2,12] based on the notable dielectric contrast between healthy and diseased human trabecular bones [13]. The dual-energy X-ray absorptiometry (DXA) is widely employed in clinical practices for bone health monitoring. However, DXA poses long-term health risks to the patients as it uses ionising radiations up to 0.86 mrem [14]. Similarly, three-dimensional quantitative computed tomography (QCT) and high-resolution peripheral quantitative computed tomography (HR-pQCT) are rarely used in clinical practices due to the high-intensity ionising radiations, expensive equipment, and cost of the test [15]. These imaging modalities provide high-resolution images and are clinically accepted. Contrary to this, MWI provides low-resolution images with the advantages of non-ionising radiations, portability, and low cost, these clinical advantages and the dielectric contrast between healthy and diseased human trabecular bones make MWI a potential imaging modality for monitoring bone health in comparison to the DXA, QCT, and HR-pQCT [14,16].

MWI can be classified into two main categories: radar-based and tomographic MWI [17]. In radar-based MWI techniques, images are constructed based on the scattered waves that arise due to the dielectric contrast between normal and malignant tissues [6]. The radar-based techniques are mainly used to localise any strong scatterer/pathology in the biological tissues without reconstructing the full image of the biological tissues [18]. Contrary to this, the tomographic MWI techniques aim at retrieving the spatial distribution of dielectric properties (relative permittivity (ε_r) and conductivity ($\sigma\ (S/m)$)) of biological tissues by processing the measured scattered electromagnetic (EM) field data [19]. The tomographic-based MWI techniques are

computationally expensive compared to the radar-based MWI techniques [19]. However, with the development of fast parallel tomography solutions, the computational cost of microwave tomography (MWT) approaches has reduced significantly [20].

The EM inverse scattering problem is inherently ill-posed and non-linear [1]. The regularisation and linearisation techniques are applied to deal with the non-linearity and ill-posedness of the EM inverse scattering problem [19,21]. To this end, various non-linear iterative techniques have been proposed in the literature, such as the forward-backward time-stepping method [22], Gauss-Newton optimisation approach [12,23], and microwave tomography using the dielectric Debye model [24]. The computational cost of these algorithms primarily depends upon the forward solver and the regularisation techniques for the stabilisation of the inversion method [19]. Moreover, the Gauss-Newton approaches are sensitive to the "initial guess", which makes this approach less favourable in scenarios where less *a priori* information is available [25]. In EM inverse scattering problems, an "initial guess" provides the starting point of the convex optimisation problem; hence, an inaccurate "initial guess" would lead to a solution that has no significance to the solution of the problem [1]. Besides non-linear iterative techniques, few linear approximation methods also exist, such as Born and Rytov approximations. These linear approximation methods help in reconstructing the dielectric properties of the targets that have lower dielectric contrast and small size [19]. In bone imaging applications, the dielectric contrast between cortical bone and trabecular bone is less [26]; therefore, the amount of energy penetrating trabecular bone is considerably higher than the reflected energy. Therefore, the contribution of measured scattered EM signals due to the trabecular bone would dominate the behaviour of the objective function in the minimisation problem.

The distorted Born iterative method (DBIM) is a well-known linear approximation technique for solving the EM inverse scattering problem [27,28]. The DBIM is an extension of Born and Rytov approximation and reconstructs the two-dimensional (2-D) and relatively high contrast imaging domain. The Born and Rytov approximations break down when the contrast of the imaging domain is relatively high, such as in the case of biological tissues [29]. In the Born approximation technique, Green's function is not updated at each iteration. However, in the DBIM approach, Green's function is

updated at each iteration that makes it robust towards high contrast non-linear reconstruction problems [29]. The DBIM uses a succession of linear approximations to estimate the spatial distribution of dielectric properties of the reconstruction domain [30]. In this study, the underdetermined set of linear equations are solved by using an iterative method with adaptive thresholding for compressed sensing (IMATCS) during each DBIM iteration [31]. The IMATCS approach belongs to the family of compressed sensing (CS) methods, where the sparse signal is recovered from a lower-dimensional measurement vector, i.e., the number of measurements are much less than the number of signal entries [31]. Hence, CS techniques are suitable for determining the solution of an underdetermined system of linear equations based on the measurement matrix at each DBIM iteration [31].

Various other thresholding techniques exist for solving an underdetermined set of linear equations, such as iterative hard thresholding (IHT) [32], *K*-sparse algorithms, and iterative shrinkage thresholding algorithm (ISTA) [33]. The performance of these techniques primarily depends upon the threshold value and sparsity number as *a priori* information for signal recovery [31]. Similarly, the ISTA approaches are computationally expensive as they involve the selection of coefficients that maximise the correlation between propagation and scattering matrix at each iteration [30]. The IMATCS approach addresses the limitations of these techniques by picking the most significant signal entries at each iteration. In the IMATCS approach, a crude reconstruction is successively applied to the linear measurements of the signal. The recovered signal is then sparsed by employing an adaptive thresholding function [31]. The non-linearity and ill-posedness of the EM inverse scattering problem may cause unstable reconstructions of the target domain. Regularisation techniques are applied to increase the robustness and to overcome the non-linearity of the EM inverse scattering problem [30]. Since the EM inverse scattering problem is approximated as linear in medical imaging applications; therefore, the IMATCS algorithm may diverge after some iterations. To address this limitation, an L_2-regularisation strategy is employed that leads to stable signal recovery. The L_2-IMATCS performs better in scenarios where the IMATCS algorithm becomes unstable [31].

A comprehensive review of bone dielectric properties in the microwave frequency range by Amin *et al.* [2] reported that very few studies have measured dielectric properties of the human trabecular bones. Meaney *et al*. [12] reported *in vivo* dielectric

properties of human calcaneus bone by using MWT for a frequency range of 900–1700 MHz for two patients suffering from lower leg injury [12]. Due to the limited sample size, no definite conclusion regarding the dielectric properties of human bones can be drawn from these results. Similarly, Meaney *et al.* [34] reported *in vitro* dielectric properties of porcine bone samples by using MWT for a frequency of 1100 MHz. In this study, the optimal results for the reconstruction of bone phantoms were found at 1 GHz. This frequency provided a good compromise between penetration depth and imaging resolution [35,36]. Furthermore, considering frequencies above 3 GHz for microwave bone imaging application would not be feasible due to the low penetration of EM waves [10]. Moreover, the fact that only a few studies have been conducted on the MWT of human bone motivates further studies on the characterisation of human bone dielectric properties by using MWT. Moreover, no study has ever reported MWT of diseased human bone samples, which is of paramount importance for the development of EM-based diagnostic and therapeutic medical devices for bone diseases.

Two previous studies have performed the reconstruction of bone dielectric properties and both of these studies have reconstructed bone as a homogeneous tissue [12,37]. However, bone has a cortical and trabecular layer with significantly different dielectric properties [38]. No previous study has reported the reconstruction of the cortical and trabecular layer of the bone. This study aimed to assess whether the dielectric contrast between the cortical bone and trabecular bone is maintained in a simplistic imaging scenario and whether diseased trabecular bones can be differentiated based on the reconstruction of dielectric properties using MWT. Therefore, this work has considered a simplistic scenario of reconstructing a two-layered bone structure, where the outer layer mimics the dielectric properties of cortical bone and the inner layer mimics the dielectric properties of trabecular bone. This paper presents the implementation of the DBIM algorithm for the reconstruction of dielectrically accurate numerical bone phantoms. A total of seven bone phantoms were developed based on the single-pole Debye parameters of cortical bone and trabecular bone. A two-stage genetic algorithm (GA) [39] was used to fit the single-pole Debye model to the dielectric data of the cortical bone and trabecular bone obtained from Gabriel *et al*. [40]. Gabriel *et al*. [40] examined the (*in vitro*) dielectric properties of cortical bone and trabecular bone samples from porcine. This study has

developed osteoporotic and osteoarthritis bone phantoms based on single-pole Debye parameters obtained from the dielectric measurements reported by Amin *et al*. [13]. The trabecular bone microarchitecture of osteoarthritis patients is compact and dense compared to osteoporotic patients [41]. The dense trabecular microarchitecture of bone indicates a higher degree of mineralisation due to an increased amount of bone present [42,43]. Therefore, the bone samples from these two sets of patients allow the establishment of the variation in bone dielectric properties due to variation in the mineralisation content and microarchitecture between two diseased bones. The L_2-IMATCS approach reported by Azghani *et al*. [31] is employed as a linear solver in each DBIM iteration. The L_2-IMATCS approach for reconstruction has shown promising results for a diverse range of dielectrically informed numerical bone phantoms. The initial findings on numerical tissue-mimicking phantoms have demonstrated that the osteoporotic and osteoarthritis human trabecular bones can be differentiated based on the spatial distribution of their reconstructed dielectric properties.

5.2 Mathematical Formulation

The multiple scattering interactions in the heterogeneous target region cause non-linearity and the fact that the number of measurements is too small compared to the number of unknowns in the microwave inverse problem results in an ill-posed EM inverse scattering problem [44]. Therefore, non-linear optimisation methods are used to estimate the dielectric properties of the target region from the measured EM scattered fields [44]. This involves an EM simulation along with the inversion of linear approximation of the EM field during each iteration of the algorithm. The unknown dielectric properties are estimated by using a parametric model of complex permittivity over the desired frequency band. To this end, this study implemented the DBIM approximation method, which linearises the EM scattering wave equation by replacing the total field with a known incident field [21]. The incident field is estimated at each iteration of the DBIM algorithm in the presence of known background.

5.2.1 DBIM Formulation

In an EM inverse scattering problem, a set of EM scattered fields are obtained from an unknown target region Ω as shown in Figure 5.1. A known EM source illuminates

the imaging region V with the EM field. The resulting scattered field from the target region Ω is measured at one or more observation points outside the imaging region V as shown in Figure 5.1. The unknown complex permittivity ε in the imaging region V is estimated based on the measured scattered field and the complex permittivity of the background region. The integral equation of EM field at measurement point r and frequency ω can be expressed as:

$$\Delta E_s(r,\omega) = E_t(r,\omega) - E_i(r,\omega), \tag{5.1}$$

$$= \omega^2\mu \int_V G_b(r,r',\omega)\,\delta(r',\omega)E_t(r',\omega)\,dr', \tag{5.2}$$

where ΔE_s is the EM scattered field, E_t is the total field, E_i is the incident field in the presence of known background, G_b is the dyadic Green's function for the background, and δ is the contrast function between the complex permittivity of the unknown region $(\varepsilon(r,\omega))$ and the dielectric profile of background $(\varepsilon_b(r,\omega))$. Thus, equation 5.2 represents the set of field measurements of the target region. The unknown of the objective function in equation 5.2 is the contrast function $(\delta(r',\omega) = \varepsilon(r',\omega) - \varepsilon_b(r',\omega))$. The number of unknowns in the imaging region V are often greater than the number of measurements, which results in an undetermined system having no unique solution. Similarly, Green's function may not be available analytically when the background is not homogenous space [44]. Moreover, the total field within the imaging region V is unknown, which is a function of the complex permittivity of the unknown region, thus making the system non-linear in the unknown contrast function.

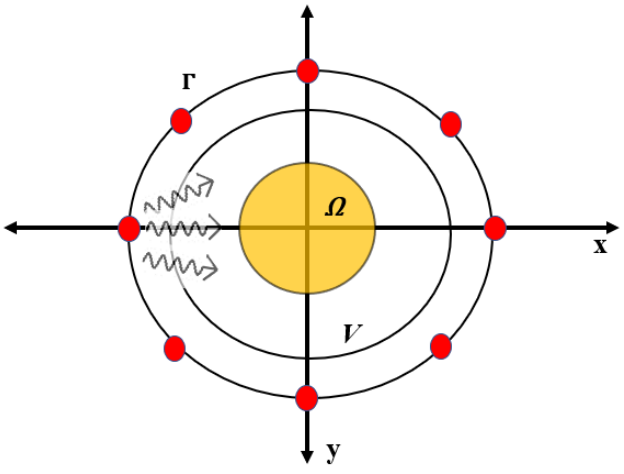

Figure 5.1: Microwave imaging scenario. Γ denotes the contour with all EM sources, V denotes the overall imaging region, and Ω denotes the target to be imaged.

The DBIM method performs a succession of linear approximations to tackle the non-linearity of the EM inverse scattering problem given in equation 5.2. At each DBIM iteration, the total field within the target region is approximated by the incident field, i.e., E_t is replaced by E_i in equation 5.2. Each DBIM iteration involves the computation of the background field and Green's function at the antennas and inside the imaging region *V*, which can be numerically computed by a *forward solution* of the EM scattering equation. During each DBIM iteration, the system of EM scattered equations obtained from the *forward solution* is inverted to obtain an approximate solution of the contrast between the target region and the current estimate of the background profile referred to as an *inverse solution*. The DBIM algorithm updates the background dielectric profile by iterating between *forward* and *inverse solutions* until convergence is reached in the minimisation of residual scattering [44].

5.2.2 IMATCS Algorithm

In CS methods, the successful recovery of the signal primarily depends upon the measurement matrix. Various matrix transformation approaches are adopted, such as Toeplitz, Gaussian, and Bernoulli matrices, to transform the measurement matrix [31]. However, in the EM inverse scattering problem, the manipulation of the measurement matrix is not straightforward [31]. Moreover, the unknown complex permittivity vector is not sparse at each DBIM iteration. Finding a transformation matrix to induce sparsity in a complex permittivity vector is a challenging task. Furthermore, the EM equations are inherently non-linear and are approximated as linear as shown in equation 5.2. To find the *inverse solution* in each DBIM iteration, this study employed the IMATCS method [31]. The IMATCS method belongs to the family of thresholding techniques. As discussed earlier, the threshold techniques need to be finely tuned based on *a priori* information of the underlying signal. However, many medical applications lack *a priori* information of the unknown signal. The IMATCS method addresses this limitation by using an adaptive threshold approach. The threshold value is exponentially decreased at each iteration of the IMATCS algorithm. The linear approximation of the EM integral equation given in equation 5.1 can be expressed as:

$$y = Mx, \qquad (5.3)$$

where y represents the residual measurement data vector, M represents the measurement matrix having dimensions $m \times n$ ($m < n$), and x represents the

unknown contrast function ($\delta(r', \omega) = \varepsilon(r', \omega) - \varepsilon_b(r', \omega)$) in terms of single-pole Debye parameters. The measurement matrix M is constructed by the incident field and the dyadic Green's function for the background and is updated at each DBIM iteration. The aim in equation 5.3 is to find x from y, subject to the condition that the number of measurements m are less than the number of unknowns n. The considered problem expressed in equation 5.3 can be solved by using the IMATCS method and can be expressed as:

$$\min_x \| y - Mx \|_2^2 + \beta \| x \|_0. \tag{5.4}$$

The solution of equation 5.4 for the adaptive IMATCS approach can be written as:

$$x_{j+1} = A_0 e^{-\alpha i}\big(x_k + \beta M^* (y - M x_k)\big), \tag{5.5}$$

where M^* is the conjugate transpose of M, β controls the convergence of the algorithm, A_0 is the threshold value, x_k is the unknown coefficient vector, α is the threshold step size, and j is the iteration number. The algorithm given in equation 5.5 starts with a null initial value, i.e., $x_0 = 0$. The x_j is recovered after the specified number of IMATCS iterations. The adaptive threshold enables the recovery of x_j from the linear measurements without any *a priori* information of the signal [31].

The IMATCS method finds x_j from the set of measurements shown in equation 5.2. However, these measurements are not linear and are approximated as linear in MWI applications. Therefore, this assumption may lead to instability and divergence of some IMATCS iterations. To address this limitation, an L_2-regularised L_0-minimisation approach is adopted as reported by Azghani *et al*. [31]. The optimisation problem given in equation 5.4 can be re-casted as:

$$\min_x \| y - Mx \|_2^2 + \beta_1 \| x \|_0 + \beta_2 \| x \|_2^2 . \tag{5.6}$$

The solution of equation 5.6 for the adaptive IMATCS approach can be written as:

$$x_{j+1} = \frac{1}{1+\beta_2} A_0 e^{-\alpha i}\big(x_k + \beta_1 M^* (y - M x_k)\big). \tag{5.7}$$

The instability caused in the IMATCS approach due to the linear assumption of measurements in equation 5.2 is addressed by the L_0/L_2, minimisation/regularisation approach. The L_2-regularisation approach is derived from the L_2-IHT method. The L_2-IHT method is extremely sensitive towards the proper selection of the threshold value

and therefore does not result in convergence of an acceptable solution [31]. However, the L_2-IMATCS approach provides a stable and better recovery of x_j from the linear measurements given in equation 5.2. The L_2-IMATCS approach for the *inverse solution* in each DBIM iteration is given in Algorithm 1.

Algorithm 1 L_2-IMATCS

1: The measurement matrix M updates at each DBIM iteration

2: **Input**: The measurement matrix M

The residual measurement data vector y

3: **Output**: The contrast function δ

4: **Method:** L_2-IMATCS

$$x_0 \leftarrow 0$$

for j = 1: *itrmax*

$$Thresh \leftarrow A_0 e^{-\alpha j}$$

$$x_j \leftarrow \frac{1}{1+\beta_2} Thresh\left(x_{j-1} + \beta_1 M^* \left(y - M x_{j-1}\right)\right)$$

end for

End method

5: Update the contrast function δ based on x_j

6: Return to **1**

5.2.3 Parameter Selection of IMATCS Algorithm

The optimal solution of x_j from the L_2-IMATCS approach primarily depends upon the choice of regularisation parameters β_1 and β_2, the threshold value A_0, the threshold step size α, and the maximum iterations of the IMATCS algorithm [31]. The parameter β_1 controls the convergence of the algorithm and is subject to the following condition:

$$0 \leq \beta_1 \leq \frac{2}{\gamma_{max}(MM^*)}, \tag{5.8}$$

where $\gamma_{max}(MM^*)$ is the maximum value of eigenvalues of the product of M and its conjugate. The measurement matrix M updates in each DBIM iteration. For the reconstruction of dielectric properties of bone in the following section, the value of β_1 is set as:

$$\beta_1 = \frac{1.9}{\gamma_{max}(MM^*)}. \quad (5.9)$$

The choice of the threshold value and maximum iterations of the IMATCS algorithm influence the quality and resolution of the reconstructed image. The selection of the threshold value and maximum iterations of the IMATCS algorithm was performed empirically for the case of reconstruction of bone dielectric properties. The results are reported in the following section. Similarly, the value of the threshold step size was set to equal 0.01 for the reconstruction of all considered bone phantoms. The value of the threshold step size was found empirically. The small step size of the threshold step size allows a slow decrease in the threshold value for each IMATCS iteration, thus capturing almost all significant components of the signal.

5.2.4 Numerical Bone Phantoms

A two-layered circular model of bone was developed. The outer layer represents the cortical bone and the inner layer represents the trabecular bone. This study considered a total of seven bone phantoms. The outer layer in all phantoms represents the cortical bone. The inner layer that represents the trabecular bone was varied to mimic the natural variation of dielectric properties reported in the literature for various clinical conditions. The sequence of bone tissues for outer and inner layers with their corresponding labels are tabulated in Table 5.1.

Table 5.1: Numerical bone phantoms for simulations.

PL	OBTL	IBTL
P1	Cortical Bone	Trabecular Bone
P2	Cortical Bone	Osteoporotic Bone Mean
P3	Cortical Bone	Osteoporotic Bone Lower Bound
P4	Cortical Bone	Osteoporotic Bone Upper Bound
P5	Cortical Bone	Osteoarthritis Bone Mean
P6	Cortical Bone	Osteoarthritis Bone Lower Bound
P7	Cortical Bone	Osteoarthritis Bone Upper Bound

PL = Phantom Label, OBTL = Outer Bone Tissue Layer, IBTL = Inner Bone Tissue Layer.

The two-layered circular model was transformed into an electromagnetic model based on the single-pole Debye parameters of each layer. The frequency dependence of complex permittivity of biological tissues can be modelled by using a single-pole

Debye model over the frequency range of interest (0.5–8.5 GHz). The single-pole Debye model can be expressed as:

$$\varepsilon_r(\omega) = \varepsilon_\infty + \frac{\Delta\varepsilon}{1+j\omega\tau} + \frac{\sigma_s}{j\omega\varepsilon_0}, \tag{5.10}$$

where ε_∞ is the permittivity value at the highest frequency under consideration, $\Delta\varepsilon$ is the difference between the permittivity value at the highest and lowest frequency values under consideration, σ_s is the conductivity, and τ is the relaxation time constant. The parametric values of the Debye parameters for the considered bone tissues are tabulated in Table 5.2 for the frequency range of 0.5–8.5 GHz. Moreover, the values of relative permittivity and conductivity are listed in Table 5.2 for the frequency of 1 GHz. To simplify the FDTD simulation, the relaxation time constant was considered spatially invariant with a constant value of 0.5 ps. A two-stage genetic algorithm (GA) was used to fit the single-pole Debye model to the measured data obtained from Gabriel *et al*. [40] for bone phantom P1. Moreover, the single-pole Debye parameters were determined for osteoporotic and osteoarthritis human trabecular bones based on the dielectric properties reported by Amin *et al*. [13]. Lazebnik *et al*. [45] proposed single-pole Debye parameters for breast tissues at the microwave frequency range. These parameters are widely employed for microwave breast imaging. However, no study to date has ever proposed single-pole Debye parameters for cortical bone and trabecular bone. To this end, this study determined single-pole Debye parameters for the evaluation of bone phantoms.

Table 5.2: Single-pole Debye parameters of bone tissues. The values of ε_r and σ are given for 1 GHz.

Tissue	$\boldsymbol{\varepsilon_\infty}$	$\boldsymbol{\Delta\varepsilon}$	$\boldsymbol{\sigma_s(S/m)}$	$\boldsymbol{\varepsilon_r}$	$\boldsymbol{\sigma(S/m)}$
Cortical Bone	8.75	4	0.01	12.39	0.0736
Trabecular Bone	14	7	0.1	20.43	0.2125
Osteoporotic Bone Mean	16	3	0.12	18.73	0.1677
Osteoporotic Bone Lower Bound	14	3	0.12	16.73	0.1677
Osteoporotic Bone Upper Bound	17	3	0.12	19.73	0.1677
Osteoarthritis Bone Mean	24	5	0.1	28.55	0.1795
Osteoarthritis Bone Lower Bound	22	5	0.1	26.55	0.1795
Osteoarthritis Bone Upper Bound	25	5	0.1	29.55	0.1795

5.3 Results and Discussion

This section presents the results obtained by the L_2-IMATCS approach for bone dielectric properties' reconstruction using dielectrically informed numerical models.

5.3.1 Simulation Testbed

The measured data were collected by simulating the model of the imaging system using the finite difference time domain (FDTD) method with a uniform grid cell size of 1 mm. The FDTD simulation was also used as a forward solver for the inversion process as commonly used in previous studies that investigated the breast numerical phantoms [1,19,30,31,44]. In all our simulation testbeds, the bone phantoms were assumed to be immersed in a lossless non-dispersive matching medium whose single-pole Debye parameters are $\varepsilon_\infty = 2.848, \Delta\varepsilon = 1.104, \sigma_s = 0.005\, S/m$. The evaluated bone phantoms, simulations, and reconstructions are performed for 2-D imaging scenarios. To gain maximum coverage and optimal resolution, a total of nine ideal dipole antennas were placed in a circular array across the bone phantoms as shown in Figure 5.2. For the 2-D geometry, the Hertzian dipole antennas correspond to point sources. These point sources were equally spaced around the bone phantom in a circular array of a radius of 12 cm. These point sources sequentially illuminated the bone phantoms with a modulated wideband Gaussian pulse with a centre frequency of 1 GHz and −3-dB bandwidth. The scattered EM signals from bone phantoms were recorded, and unique measurements for each transmit-receive antenna pair were recorded. All the redundant data from reciprocal channels and monostatic channels were not recorded. The L_2-IMATCS approach reconstructs the single-pole Debye parameters, which were then converted into a complex permittivity profile of bone. To avoid "inverse crime", the simulated data were corrupted with additive Gaussian noise (AWGN) [1].

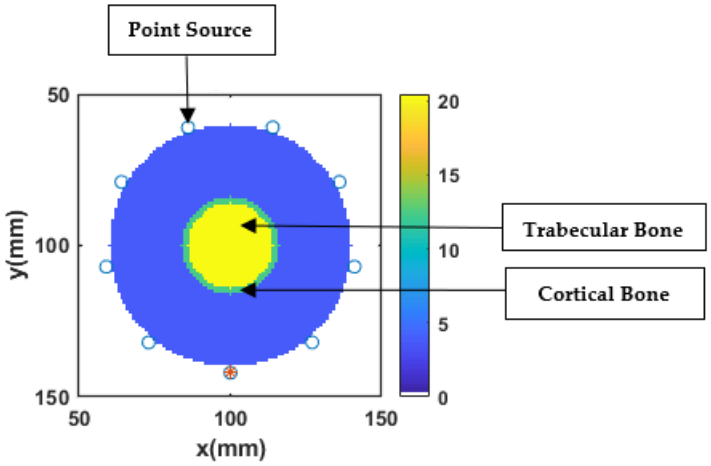

Figure 5.2: Simulation testbed.

5.3.2 Performance Metrics

Two scalar metrics are considered in this study to perform a quantitative comparison between the reconstructed and corresponding reference bone dielectric properties. The first scalar metric measures the error based on the normalised root mean square error (NRMSE) between the complex permittivity of reference bone phantom and reconstructed bone phantom. The NRMSE is defined as:

$$\text{NRMSE} = \| \varepsilon_r(f) - \hat{\varepsilon}_r(f) \|_{L^2}^2 \Big/ \| \varepsilon_r(f) \|_{L^2}^2, \tag{5.11}$$

where $\varepsilon_r(f)$ is the complex permittivity profile of reference bone dielectric properties, and $\hat{\varepsilon}_r(f)$ is the complex permittivity profile of reconstructed bone dielectric properties. The NRMSE is separately calculated for both the real (ε') and imaginary (ε'') parts of the complex permittivity profile for all bone phantoms. The results of NRMSE for the real and imaginary parts of complex permittivity for all reconstructed bone phantoms are tabulated in Table 5.3. For a fair comparison, the NRMSE is calculated for the two-layered circular bone phantom inside the imaging domain *V*. The application of the regularisation approach resulted in smooth reconstructed complex permittivity profiles, thus resulting in lower error values between the reference and reconstructed bone phantoms. Similar values of NRMSE were reported by Ambrosanio *et al.* [30] for the reconstruction of 2-D numerical heterogeneous breast phantoms. The authors proposed an adaptive multi-threshold ISTA (AMTISTA) approach for the reconstruction of breast phantoms.

Table 5.3: NRMSE between original and reconstructed bone phantoms.

Phantom	NRMSE	
	ε'	ε''
P1	0.212	0.253
P2	0.239	0.228
P3	0.249	0.228
P4	0.226	0.222
P5	0.246	0.252
P6	0.228	0.242
P7	0.242	0.245

The second performance metric, the structural similarity index (SSIM), intends to correlate the structural similarity between the reconstructed and reference bone dielectric properties [46]. To this end, SSIM compares two images at a time. The SSIM considers the luminance, contrast, and structure to produce a similarity value between the two images [6]. The SSIM values range between 0 and 1, a value of 0 indicates that no structural similarity exists between the two images under comparison; however, a value of 1 indicates maximum similarity between the two images under comparison. The results of SSIM between the real and imaginary parts of the reference and reconstructed complex permittivity profiles are tabulated in Table 5.4. Based on the SSIM values in Table 5.4, it can be observed that the reference and reconstructed bone dielectric properties have high similarity in terms of the real and imaginary parts of complex permittivity for each considered bone phantom.

Table 5.4: SSIM between original and reconstructed bone phantoms.

Phantom	SSIM	
	ε'	ε''
P1	0.973	0.995
P2	0.968	0.997
P3	0.959	0.997
P4	0.971	0.997
P5	0.959	0.993
P6	0.966	0.994
P7	0.9532	0.992

5.3.3 Choice of Number of IMATCS iterations, Number of DBIM iterations, and Threshold (A_0)

The choice of the number of IMATCS iterations, number of DBIM iterations, and threshold (A_0) has a significant impact on the resolution and quality of the reconstructed complex permittivity profile of bone. For the optimal selection of these parameters, a numerical analysis was performed on bone phantom P1. The complex permittivity profile of bone phantom P1 was reconstructed for the different number of IMATCS iterations while keeping a fixed number of DBIM iterations. The NRMSE values were calculated for the real part of the complex permittivity of reconstructed bone phantom P1 for each simulation as shown in Figure 5.3 (a). The minimum value of NRMSE was obtained for five IMATCS iterations. It can be observed from Figure 5.3 (a) that the NRMSE increases as the number of IMATCS iterations increase; similarly, a higher trend of NRMSE values was observed for IMATCS iterations less than five. Therefore, for the reconstruction of all bone phantoms, five IMATCS iterations were used. Similarly, for the optimal number of DBIM iterations, the bone phantom 1 was simulated for the different number of DBIM iterations for a fixed number of IMATCS iterations (five). The NRMSE values were calculated for the real part of the complex permittivity of the reconstructed bone phantom P1 as shown in Figure 5.3 (b). It can be observed from Figure 5.3 (b) that the NRMSE increases as the number of DBIM iterations increases. This is because no constraint on the upper limit of values was incorporated on the Debye parameters after each DBIM iteration, which results in saturation of the estimated Debye parameters. Moreover, the value of

the threshold remains fixed in the IMATCS approach for solving an underdetermined set of linear equations, which results in the saturation of most of the components of the updating contrast function. Therefore, the value of NRMSE increases significantly after the first DBIM iteration. The minimum value of NRMSE was found for the first DBIM iteration. Therefore, the reconstruction of all bone phantoms in this study was obtained for the first DBIM iteration.

To find the optimal value for the threshold value A_0, the bone phantom P1 was simulated for different values of the threshold for a fixed number of IMATCS (five) and DBIM iterations (one). The NRMSE values were calculated for the real part of the reconstructed complex permittivity profile as shown in Figure 5.3 (c). Based on the NRMSE values, it can be observed from Figure 5.3 (c) that the minimum values of NRMSE resulted in a threshold in the range of 90–100. Moreover, it can be observed that the values of NRMSE increase for a threshold greater than 100. Similarly, for thresholds less than 90, the values of NRMSE are found on the higher side. Therefore, for the reconstruction of all considered bone phantoms in this study, the value of the threshold was kept in the range of 90–100.

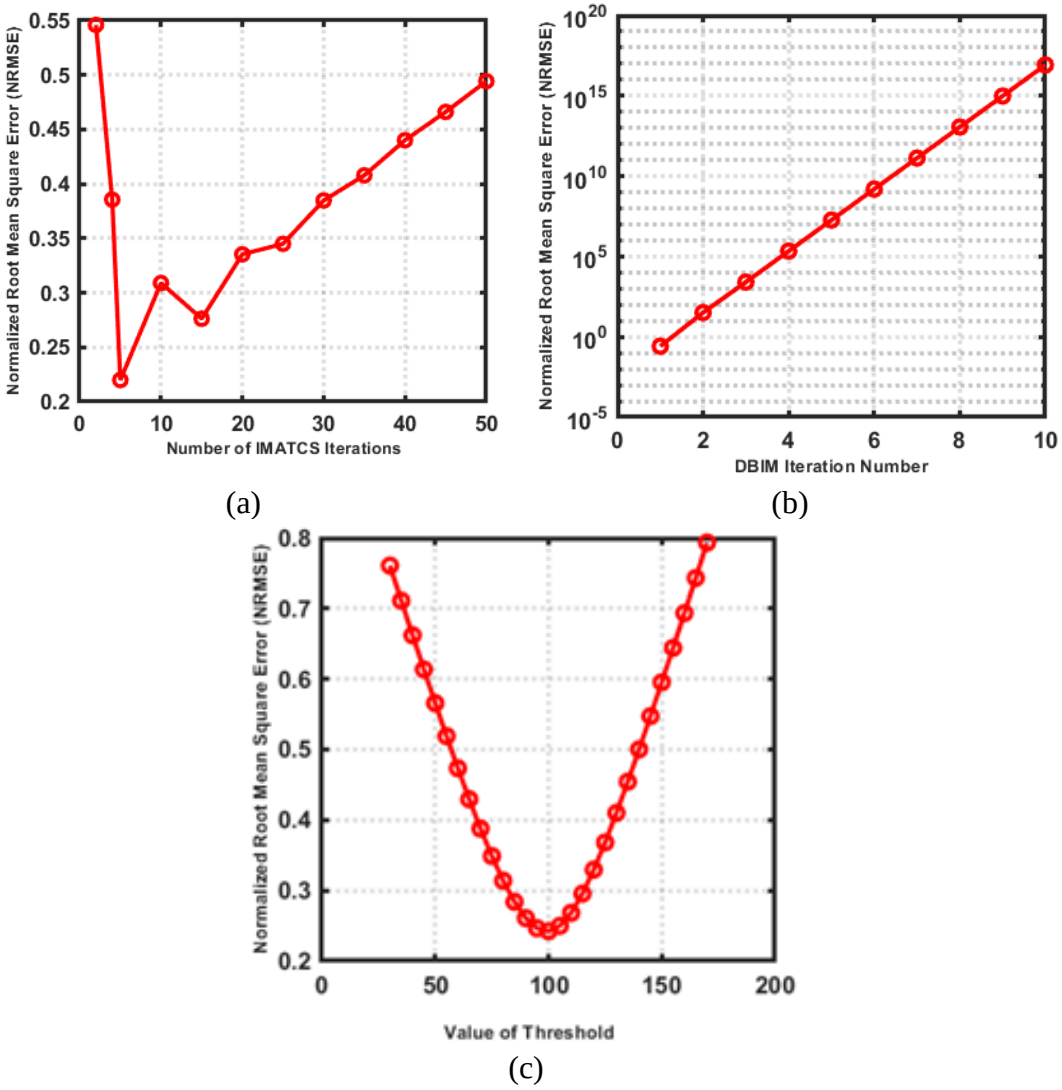

Figure 5.3: Relationship between NRMSE and (a) number of IMATCS iterations, (b) number of DBIM iterations, and (c) value of threshold (A_0).

5.3.4 Reconstruction of Numerical Bone Phantom 1 (P1)

As discussed, a two-layered circular model of bone was developed as shown in Figure 5.4 (a) and (b), representing the reference real and imaginary parts of the complex permittivity of bone phantom P1, respectively. The outer green layer is assigned the dielectric properties of the cortical bone and the inner yellow layer is assigned the dielectric properties of the trabecular bone. The point sources were directly in contact with the imaging region *V*. For all bone phantoms, initially, the single-pole Debye parameters were reconstructed at 1 GHz. The reconstructed Debye parameters were then transformed into the complex permittivity profile. The value of β_2 was set to 0.005 for the reconstruction of bone dielectric properties. No *a priori* information was used for the L_2-IMATCS approach for the reconstruction of bone dielectric properties.

The reconstructed real and imaginary parts of the complex permittivity of bone phantom P1 are shown in Figure 5.4 (c) and (d) respectively. Comparing the reference and reconstructed real and imaginary parts of complex permittivity, it can be observed that the shape and size of bone phantom P1 remain intact after the reconstruction. Moreover, the reconstructed real and imaginary part of the complex permittivity of bone phantom P1 suggests that good reconstructions of bone dielectric properties can be achieved by using the L_2-IMATCS approach, resulting in lower values of NRMSE for the real and imaginary parts of the complex permittivity as tabulated in Table 5.3.

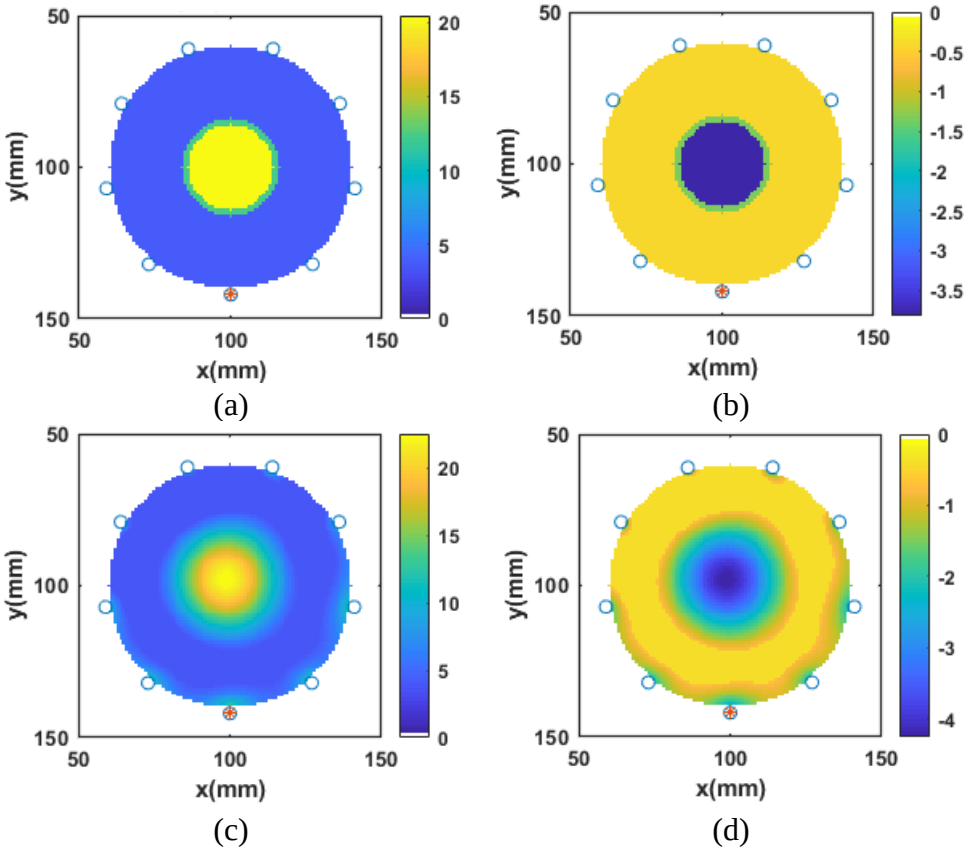

Figure 5.4: Real and imaginary parts of complex permittivity of (a) and (b) reference P1, (c) and (d) reconstructed P1 at 1 GHz.

5.3.5 Reconstruction of Numerical Bone Phantom 2, 3, and 4 (P2, P3, P4)

The bone phantoms P2, P3, and P4 were categorised as osteoporotic bone phantoms. Like P1; P2, P3, and P4 were designed as two-layered circular bone models. The outer layer was assigned the dielectric properties of the cortical bone, whereas the dielectric properties of the inner trabecular bone layer were varied to account for the natural variation of dielectric properties of osteoporotic bones reported by Amin *et al.* [13]. The bone phantom P2 was designed to mimic the mean dielectric properties of

osteoporotic bones, bone phantom P3 was assigned the lower-bound dielectric properties of osteoporotic bones, and bone phantom P4 was assigned the upper-bound dielectric properties of osteoporotic bones. The lower- and upper-bound dielectric properties of osteoporotic bones were considered to investigate the robustness of the L_2-IMATCS approach for the reconstruction of dielectric properties of diverse bone phantoms. Moreover, to investigate the fact that the reconstruction of complex permittivity profiles of bone phantoms P2, P3, and P4 do not overlap with each other, the reconstructed complex permittivity profiles kept the natural variation of dielectric properties of osteoporotic bones intact. The visual images for reconstructed complex permittivity profiles for bone phantoms P2, P3, and P4 are similar; therefore, only the reconstructed images of bone phantom P2 are shown here. Figure 5.5 (a) and (b), represents the reference real and imaginary part of the complex permittivity of bone phantom P2, respectively. The simulation setup was kept the same for the reconstruction of all bone phantoms as described for P1. The reconstructed real and imaginary parts of the complex permittivity of P2 are shown in Figure 5.5 (c) and (d) respectively. Comparing the reference and reconstructed real and imaginary parts of the complex permittivity of bone phantom P2, it can be observed that good reconstructions of bone dielectric properties are achieved by using the L_2-IMATCS approach. The values of NRMSE and SSIM for the bone phantoms P2, P3, and P4 were calculated for the real and imaginary parts of the complex permittivity and are tabulated in Tables 5.4 and 5.5, respectively.

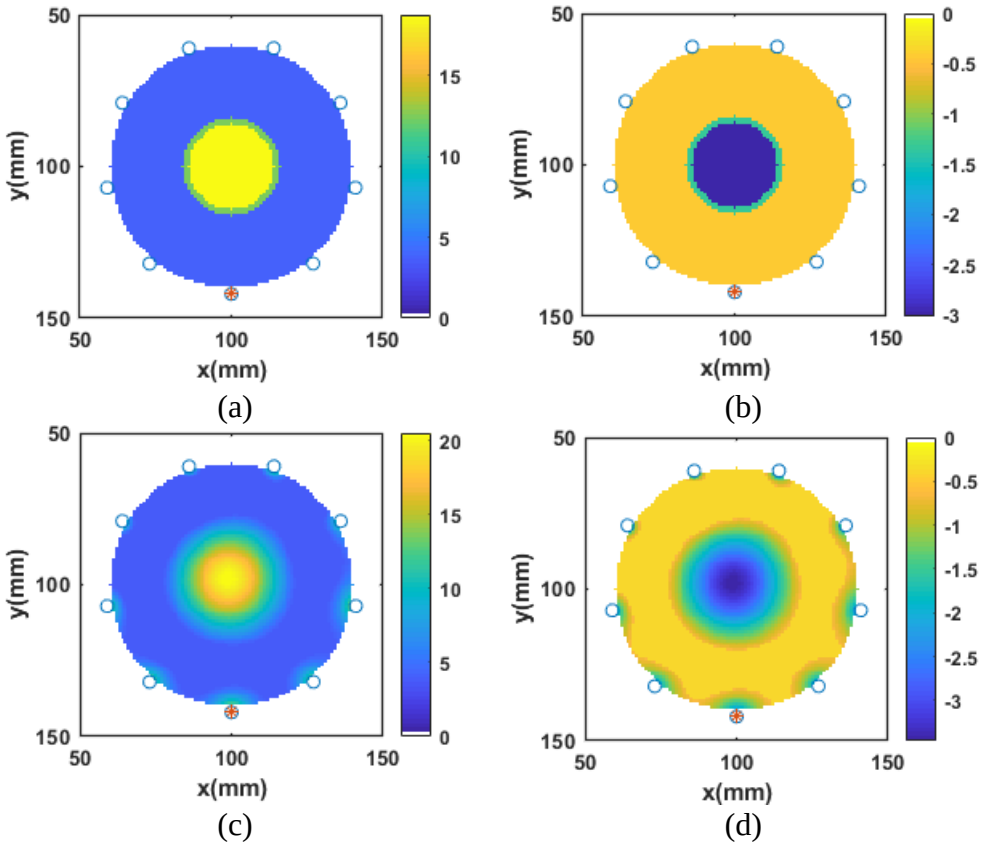

Figure 5.5: Real and imaginary parts of complex permittivity of (a) and (b) reference P2, (c) and (d) reconstructed P2 at 1 GHz.

5.3.6 Reconstruction of Numerical Bone Phantom 5, 6, and 7 (P5, P6, P7)

The bone phantoms P5, P6, and P7 were categorised as osteoarthritis bone phantoms. Like P1, P5, P6, and P7 were designed as two-layered circular bone models. The outer layer was assigned the dielectric properties of the cortical bone, whereas the dielectric properties of the inner trabecular bone layer were varied to account for the natural variation of dielectric properties of osteoarthritis bones reported by Amin *et al*. [13]. The bone phantom P5 was designed to mimic the mean dielectric properties of osteoarthritis bones, bone phantom P6 was assigned the lower-bound dielectric properties of osteoarthritis bones, and bone phantom P7 was assigned the upper-bound dielectric properties of osteoarthritis bones. As for the case of osteoporotic bone phantoms, the L_2-IMATCS approach provides robustness for the reconstruction of the complex permittivity profile of bone phantoms P5, P6, and P7. Moreover, the reconstruction of complex permittivity profiles of bone phantoms P5, P6, and P7 do not overlap with each other and the reconstructed complex permittivity profiles keep the natural variation of dielectric properties of osteoarthritis bones intact. The mean

values of single-pole Debye parameters for osteoarthritis bones, as tabulated in Table 5.2, are higher as compared to osteoporotic bones. The contrast between single-pole Debye parameters between outer and inner layers of bone phantoms P5, P6, and P7, is higher compared to the bone phantoms P2, P3, and P4. The visual images for reconstructed complex permittivity profiles for the bone phantoms P5, P6, and P7 are similar; therefore, only the reconstructed images of bone phantom P5 are shown here. Figure 5.6 (a) and (b), represents the reference real and imaginary parts of the complex permittivity of bone phantom P5, respectively. The reconstructed real and imaginary parts of the complex permittivity of bone phantom P5 are shown in Figure 5.6 (c) and (d) respectively. Comparing the reference and reconstructed real and imaginary parts of the complex permittivity parts of bone phantom P5, it can be observed that good reconstruction of numerical bone phantoms can be achieved by using the L_2-IMATCS approach, even for higher contrast two-layered bone phantoms. The values of NRMSE and SSIM for bone phantoms P5, P6, and P7 were calculated for the real and imaginary parts of the complex permittivity and are tabulated in Tables 5.4 and 5.5, respectively.

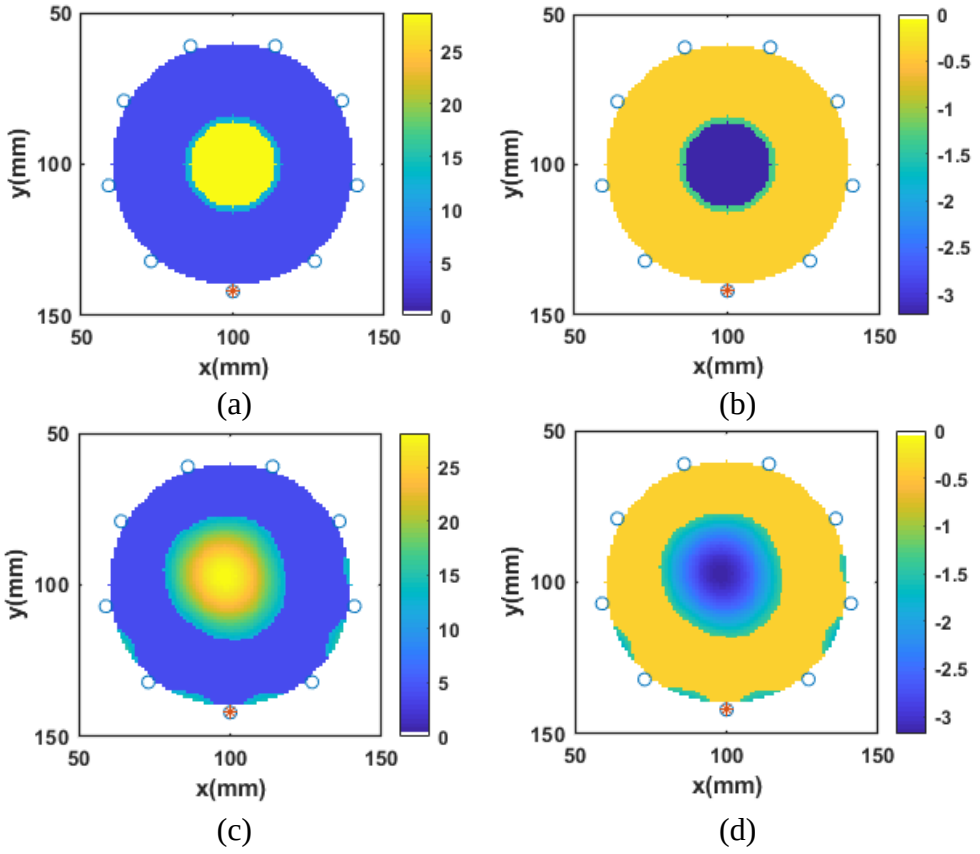

Figure 5.6: Real and imaginary parts of complex permittivity of (a) and (b) reference P5, (c) and (d) reconstructed P5 at 1 GHz.

5.3.7 Robustness of L_2-IMATCS for Reconstruction of Bone Phantoms P1, P2, P3, P4, P5, P6, and P7

To investigate the robustness of the L_2-IMATCS approach for all considered bone phantoms, an analysis was performed to compare the peak values of the complex permittivity profile of reference and reconstructed bone phantoms. Figure 5.7 (a) and (b) represents the comparison of the peak value of real and imaginary parts of the complex permittivity of all considered bone phantoms, respectively. The red-filled dots in the scatter plot represent the peak value of the complex permittivity of the reference bone phantom, whereas the black-filled dots represent the peak value of the reconstructed complex permittivity for each bone phantom. It can be observed from Figure 5.7 (a) and (b) that the differentiation between the different diseased bones is possible using the real part of the reconstructed complex permittivity of bone phantoms. The reconstructed peak values of the complex permittivity of each bone phantom compared to the reference profile ensures the robustness of the L_2-IMATCS approach for the reconstruction of diverse bone phantoms. Hence, the adopted approach for the differentiation of osteoporotic and osteoarthritis bone phantoms can be employed for bone health monitoring. The next step involves investigating the robustness of the L_2-IMATCS approach for the experimental data, where the measurements will be performed on anatomically realistic bone phantoms.

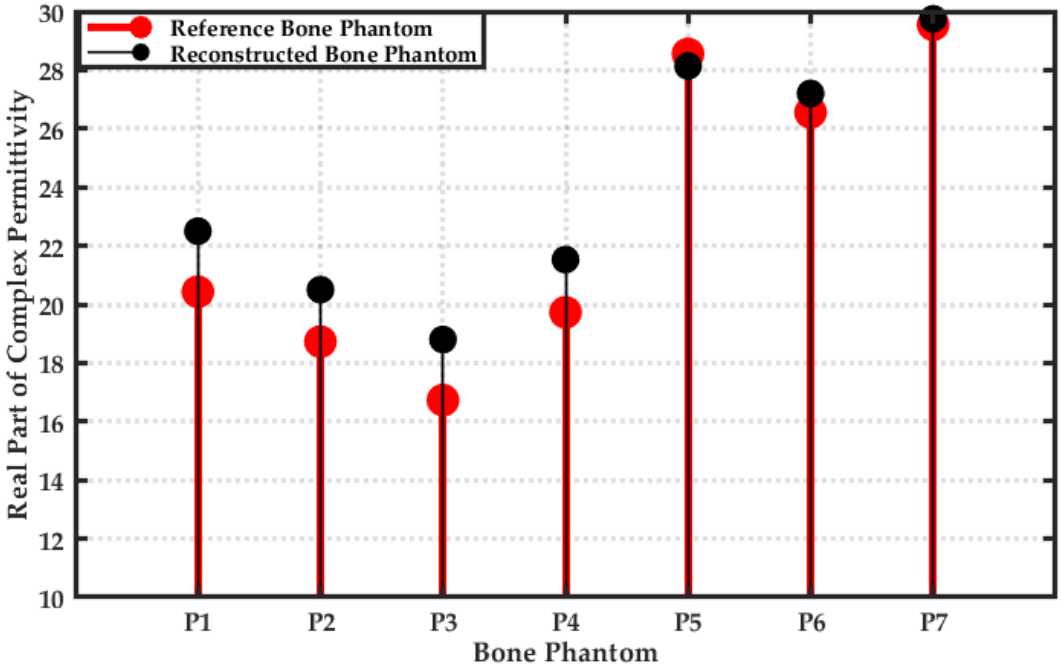

(a)

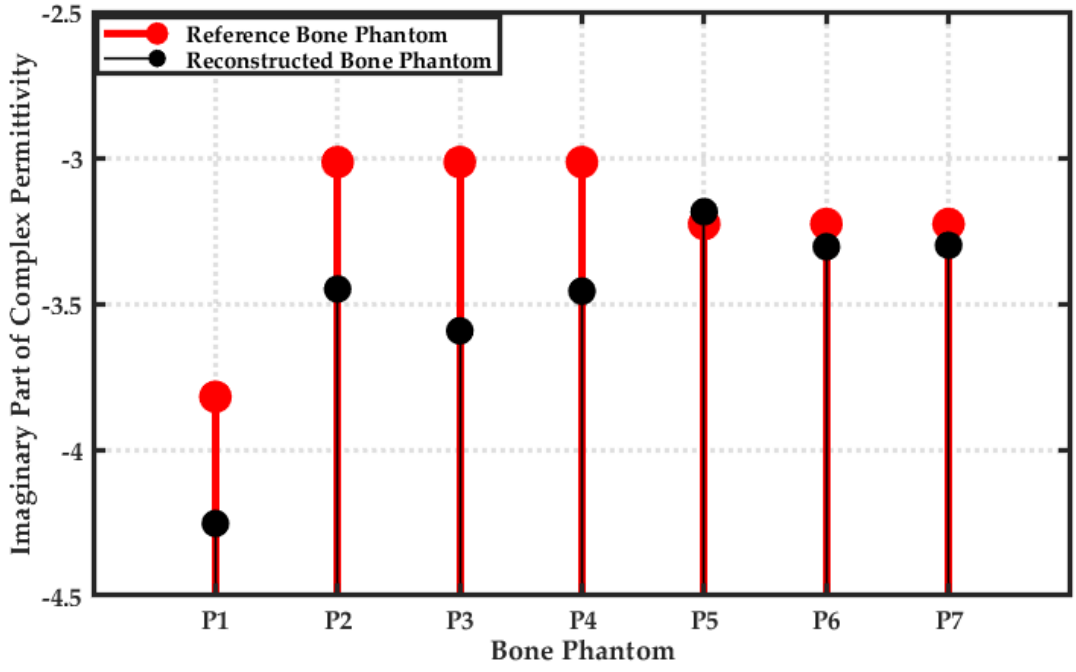

(b)

Figure 5.7: (a) Peak values of the real part of complex permittivity of reconstructed and reference bone phantoms (b) Peak values of the imaginary part of complex permittivity of reconstructed and reference bone phantoms at 1 GHz.

5.3.8 Relative Error between Reference and Reconstructed Numerical Bone Phantoms

Figure 5.8 (a) and (b) represents the relative error map for the real and imaginary parts of the complex permittivity of bone phantom P1, respectively. The reference and reconstructed real and imaginary parts of the complex permittivity of bone phantom P1 are shown in Figure 5.4. It can be observed from Figure 5.8 (a) and (b) that the relative error between the reference and reconstructed real and imaginary parts of the complex permittivity is low in general. However, as expected, the error is larger at the edges of the bone phantom. There are two reasons for observing large relative error at the edges or boundary areas: the first reason is the expected large EM field perturbation at the boundaries of two mediums with different dielectric properties, and the second reason is due to a small localization error in the reconstructed dielectric profile. Moreover, the error is small for the real part of complex permittivity compared to the imaginary part of complex permittivity. The lower error values suggest that the reconstructed real and imaginary parts of the complex permittivity of bone phantom P1 can be achieved by using the L_2-IMATCS approach. A similar effect on the boundaries was found for all seven bone phantoms.

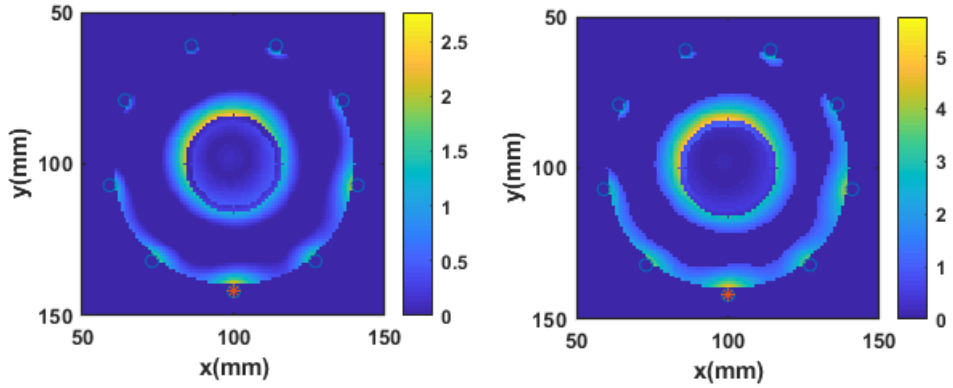

Figure 5.8: Relative error maps for (a) Real part of complex permittivity (b) Imaginary part of complex permittivity for bone phantom P1 at 1 GHz.

To investigate the relative error for all considered bone phantoms, an analysis was performed to calculate the relative error between peak values of the real and imaginary parts of the complex permittivity of the reference and reconstructed bone phantoms. Figure 5.9 represents the relative error between the peak values of the real and imaginary part of the complex permittivity of all considered bone phantoms. The red-

filled dots represent the relative error between the peak values of the real part of complex permittivity, whereas the black-filled dots represent the relative error between the peak values of the imaginary part of the complex permittivity for each bone phantom. It can be observed from Figure 5.9 that the relative error is found to be less for the real part compared to the imaginary part of the complex permittivity.

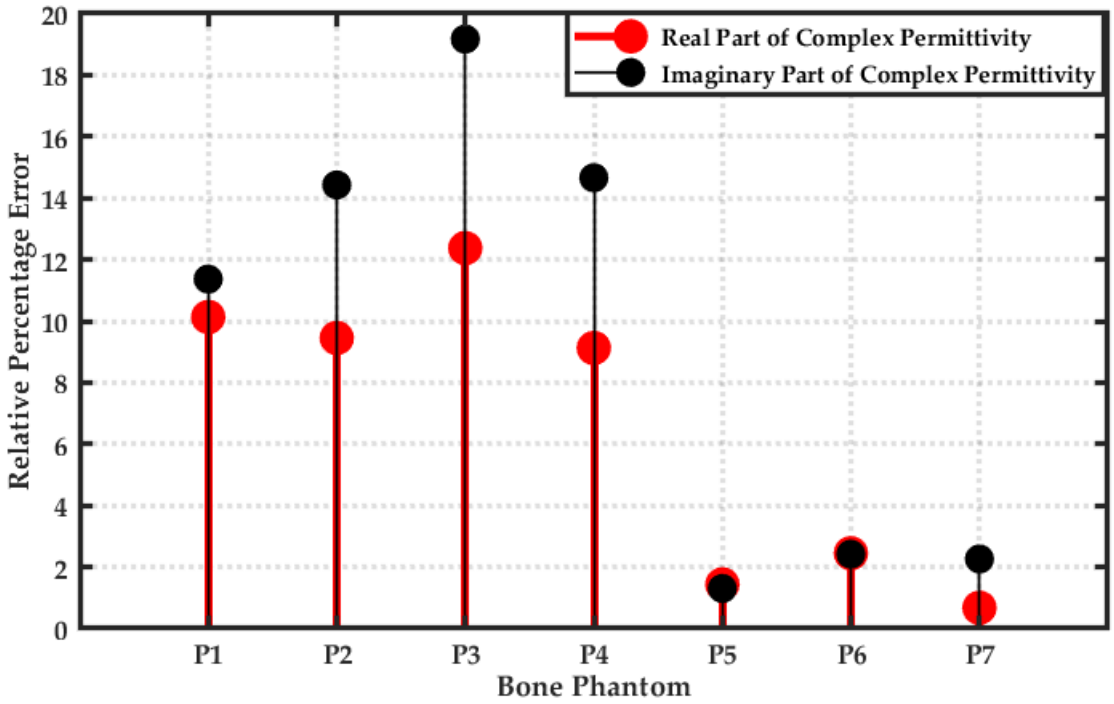

Figure 5.9: Relative percentage error between peak values of reference and reconstructed real and imaginary parts of complex permittivity at 1 GHz for all bone phantoms.

5.3.9 Impact of Signal-to-Noise Ratio (SNR) on Reconstructed Numerical Bone Phantoms

To evaluate the robustness of the L_2-IMATCS approach in noisy scenarios, and to avoid "inverse crime", the total field calculated from bone phantom simulations was corrupted with AWGN [1]. The variation of NRMSE on the reconstructed complex permittivity profile is observed for a range of SNR values. The values of SNR range from 20 to 60 dB with a step size of 10 dB. An individual experiment was performed for each considered bone phantom for a specific value of SNR. The total field calculated from each bone phantom was corrupted with the corresponding value of SNR relative to the energy of the total field. To this end, a total of 35 numerical experiments (7 numerical phantoms × 5 SNR levels) were performed. The procedure adopted for the assessment of SNR on reconstructed numerical bone phantoms is the

same as that reported in the literature [1,19,30,31,44]. The NRMSE was calculated between the reference and reconstructed complex permittivity profiles for all bone phantoms in the presence of SNR. The results are tabulated in Tables 5.5 and 5.6. It can be observed from Tables 5.5 and 5.6, where even for low SNR values of 20 dB relative to the total received signal, the reconstruction errors are quite low both for the real and imaginary parts of the complex permittivity profile. The low reconstruction error values ensure the robustness of the L_2-IMATCS approach in the presence of AWGN.

Table 5.5: NRMSE between original and reconstructed bone phantoms for the real part of complex permittivity.

SNR (dB)	P1	P2	P3	P4	P5	P6	P7
20	0.224	0.239	0.249	0.228	0.247	0.228	0.244
30	0.220	0.238	0.249	0.226	0.245	0.229	0.243
40	0.220	0.239	0.249	0.226	0.245	0.229	0.242
50	0.220	0.239	0.249	0.226	0.247	0.228	0.243
60	0.220	0.239	0.249	0.226	0.246	0.228	0.243

Table 5.6: NRMSE between original and reconstructed bone phantoms for the imaginary part of complex permittivity.

SNR (dB)	P1	P2	P3	P4	P5	P6	P7
20	0.256	0.229	0.228	0.223	0.253	0.241	0.247
30	0.254	0.229	0.229	0.222	0.252	0.243	0.246
40	0.253	0.228	0.228	0.221	0.252	0.242	0.245
50	0.253	0.228	0.228	0.222	0.252	0.242	0.245
60	0.253	0.228	0.228	0.222	0.252	0.242	0.245

5.4. Conclusions

The evaluation of MWI methods on numerical phantoms before clinical testing of the MWI system provides a controlled realistic imaging scenario. Moreover, it helps to evaluate the robustness of the adopted approach for the reconstruction of dielectric properties under realistic imaging scenarios. This study considered seven diverse numerical bone phantoms with accurate dielectric properties of different diseased

human bones. To reconstruct the dielectric properties, a DBIM-based MWT approach was adopted in conjunction with the L_2-IMATCS approach.

The results of reconstructed bone dielectric properties showed that the adopted approach for linear inversion provides good reconstruction in comparison to the reference bone dielectric properties even for low SNR values. The results showed that the osteoporotic and osteoarthritis bones can be differentiated based on reconstructed complex permittivity profiles. The objective of this study was to evaluate MWT for the assessment of different diseased bone phantoms for bone health monitoring. The reported NRMSE between reference and reconstructed bone dielectric properties is in agreement with the literature reporting the L_2-IMATCS approach for reconstruction of numerical breast phantoms.

This study reconstructed the dielectric properties of simplified 2-D bone phantoms. While the considered scenario is rather simplistic, it demonstrates the feasibility of reconstruction of bone dielectric properties using the proposed method. Future studies will extend the adopted approach to more realistic three-dimensional imaging scenarios in addition to the evaluation of the proposed methods on experimental data obtained from anatomically realistic bone phantoms measured with the MWI system. Further, a more proper decomposition basis will be investigated for enforcing sparsity to reduce the ill-posedness of the EM inverse scattering problem.

Funding: The research leading to these results has received funding from the European Research Council under the European Union's Horizon 2020 Programme (H2020)/ERC grant agreement BioElecPro n. 637780.

Conflicts of Interest: The authors declare no conflict of interest. The funders had no role in the design of the study; in the collection, analyses, or interpretation of data; in the writing of the manuscript, or in the decision to publish the results.

References

1. Scapaticci, R.; Kosmas, P.; Crocco, L. Wavelet-based regularization for robust microwave imaging in medical applications. *IEEE Trans. Biomed. Eng.* **2015**, *62*, 1195–1202, doi:10.1109/TBME.2014.2381270.
2. Amin, B.; Elahi, M.A.; Shahzad, A.; Porter, E.; McDermott, B.; O'Halloran, M. Dielectric properties of bones for the monitoring of osteoporosis. *Med. Biol. Eng. Comput.* **2018**, doi:10.1007/s11517-018-1887-z.

3. Elahi, M.A.; O'Loughlin, D.; Lavoie, B.R.; Glavin, M.; Jones, E.; Fear, E.C.; O'Halloran, M. Evaluation of image reconstruction algorithms for confocal microwave imaging: Application to patient data. *Sensors (Switzerland)* **2018**, *18*, doi:10.3390/s18061678.
4. Loughlin, D.O.; Oliveira, B.L.; Santorelli, A.; Porter, E.; Glavin, M.; Jones, E.; Popovi, M.; Halloran, M.O. Sensitivity and specificity estimation using patient-specific microwave imaging in diverse experimental breast phantoms. *IEEE Trans. Med. Imaging* **2019**, *38*, 303–311, doi:10.1109/TMI.2018.2864150.
5. O'Loughlin, D.; O'Halloran, M.; Moloney, B.M.; Glavin, M.; Jones, E.; Elahi, M.A. Microwave breast imaging: Clinical advances and remaining challenges. *IEEE Trans. Biomed. Eng.* **2018**, *65*, 2580–2590, doi:10.1109/TBME.2018.2809541.
6. Porter, E.; Coates, M.; Popović, M. An early clinical study of time-domain microwave radar for breast health monitoring. *IEEE Trans. Biomed. Eng.* **2016**, *63*, 530–539, doi:10.1109/TBME.2015.2465867.
7. Lazebnik, M.; Popovic, D.; McCartney, L.; Watkins, C.B.; Lindstrom, M.J.; Harter, J.; Sewall, S.; Ogilvie, T.; Magliocco, A.; Breslin, T.M.; et al. A large-scale study of the ultrawideband microwave dielectric properties of normal, benign and malignant breast tissues obtained from cancer surgeries. *Phys. Med. Biol.* **2007**, *52*, 6093–6115, doi:10.1088/0031-9155/52/20/002.
8. Bourqui, J.; Fear, E.C. System for bulk dielectric permittivity estimation of breast tissues at microwave frequencies. *IEEE Trans. Microw. Theory Tech.* **2016**, *64*, 3001–3009, doi:10.1109/TMTT.2016.2586486.
9. O'Loughlin, D.; Oliveira, B.L.; Adnan Elahi, M.; Glavin, M.; Jones, E.; Popović, M.; Halloran, M.O. Parameter search algorithms for microwave radar-based breast imaging: Focal quality metrics as fitness functions. *Sensors (Switzerland)* **2017**, *17*, 1–20, doi:10.3390/s17122823.
10. Scapaticci, R.; Di Donato, L.; Catapano, I.; Crocco, L. A feasibility study on microwave imaging for brain stroke monitoring. *Prog. Electromagn. Res.* **2012**, *40*, 305–324.
11. Vasquez, J.A.T.; Scapaticci, R.; Turvani, G.; Bellizzi, G.; Rodriguez-Duarte, D.O.; Joachimowicz, N.; Duchêne, B.; Tedeschi, E.; Casu, M.R.; Crocco, L.; et

al. A prototype microwave system for 3d brain stroke imaging. *Sensors (Switzerland)* **2020**, *20*, 1–16, doi:10.3390/s20092607.

12. Meaney, P.M.; Goodwin, D.; Golnabi, A.H.; Zhou, T.; Pallone, M.; Geimer, S.D.; Burke, G.; Paulsen, K.D. Clinical microwave tomographic imaging of the calcaneus: A first-in-human case study of two subjects. *IEEE Trans. Biomed. Eng.* **2012**, *59*, 3304–3313, doi:10.1109/TBME.2012.2209202.
13. Amin, B.; Shahzad, A.; Farina, L.; Parle, E.; McNamara, L.; O'Halloran, M.; Elahi, M.A. Dielectric characterization of diseased human trabecular bones at microwave frequency. *Med Eng. Phys.* **2020**, *78*, 21–28, doi:10.1016/j.medengphy.2020.01.014.
14. Makarov, S.N.; Noetscher, G.M.; Arum, S.; Rabiner, R.; Nazarian, A. Concept of a radiofrequency device for osteopenia / osteoporosis screening. *Sci. Rep.* **2020**, 1–15, doi:10.1038/s41598-020-60173-5.
15. Lochmüller, E.-M.; Müller, R.; Kuhn, V.; Lill, C.A.; Eckstein, F. Can novel clinical densitometric techniques replace or improve Dxa in predicting bone strength in osteoporosis at the hip and other skeletal sites? *J. Bone Miner. Res.* **2003**, *18*, 906–912, doi:10.1359/jbmr.2003.18.5.906.
16. Amin, B.; Elahi, M.A.; Shahzad, A.; Parle, E.; McNamara, L.; Orhalloran, M. An insight into bone dielectric properties variation: A foundation for electromagnetic medical devices. In Proceedings of the EMF-Med 2018—1st EMF-Med World Conference on Biomedical Applications of Electromagnetic Fields. COST EMF-MED Final Event with 6th MCM, Split, Croatia, 10–13 September 2018; pp. 3–4, doi:10.23919/EMF-MED.2018.8526050.
17. Bourqui, J.; Sill, J.M.; Fear, E.C. A prototype system for measuring microwave frequency reflections from the breast. *Int. J. Biomed. Imaging* **2012**, *2012*, doi:10.1155/2012/851234.
18. Oliveira, B.L.; Halloran, M.O. Microwave breast imaging : Experimental tumour phantoms for the evaluation of new breast cancer diagnosis systems biomedical physics & engineering related content microwave breast imaging : Experimental tumour phantoms for the evaluation of new breast can. *Biomed. Phys. Eng. Express* **2018**, doi:10.1088/2057-1976/aaaaff.

19. Shahzad, A.; O'Halloran, M.; Jones, E.; Glavin, M. A multistage selective weighting method for improved microwave breast tomography. *Comput. Med. Imaging Graph.* **2016**, *54*, 6–15, doi:10.1016/j.compmedimag.2016.08.007.
20. Shahzad, A.; O'Halloran, M.; Glavin, M.; Jones, E. A novel optimized parallelization strategy to accelerate microwave tomography for breast cancer screening. In Proceedings of the 2014 36th Annual International Conference of the IEEE Engineering in Medicine and Biology Society, Chicago, IL, USA, 26–30 August 2014; pp. 2456–2459.
21. Scapaticci, R.; Bjelogrlic, M.; Vasquez, J.A.T.; Vipiana, F.; Mattes, M.; Crocco, L. Microwave technology for brain imaging and monitoring: Physical foundations, potential and limitations. In *Emerging Electromagnetic Technologies for Brain Diseases Diagnostics, Monitoring and Therapy*; Crocco, L., Karanasiou, I., James, M., Conceição, R. Eds.; Springer: Cham, Switzerland, 2018; pp. 7–35.
22. Takenaka, T.; Jia, H.; Tanaka, T. Microwave image reconstruction of tissue property dispersion characteristics utilizing multiple-frequency information. *IEEE Trans. Microw. Theory Tech.* **2004**, *52*(8), pp.1866-1875, doi:10.1163/156939300X00383.
23. Fang, Q.; Meaney, P.M.; Paulsen, K.D. Microwave image reconstruction of tissue property dispersion characteristics utilizing multiple-frequency information. IEEE Trans. Microw. Theory Techn. **2004**, 52, 1866–1875.
24. Fhager, A.; Gustafsson, M.; Nordebo, S. Image reconstruction in microwave tomography using a dielectric debye model. IEEE Trans. Biomed. Eng. **2012**, 59, 156–166.
25. Gilmore, C.; Mojabi, P; LoVetri, J. Comparison of an enhanced distorted born iterative method and the multiplicative-regularized contrast source inversion method. *IEEE Trans. Antennas Propag*. **2009**, *57*(8), pp.2341-2351., doi:10.1109/TAP.2009.2024478.
26. Amin, B.; Elahi, M.A.; Shahzad, A.; Porter, E.; O'Halloran, M. A review of the dielectric properties of the bone for low frequency medical technologies. *Biomed. Phys. Eng. Express* **2019**, *5*, 022001, doi:10.1088/2057-1976/aaf210.

27. Miao, Z.; Kosmas, P. Multiple-Frequency DBIM-TwIST algorithm for microwave breast imaging. *IEEE Trans. Antennas Propag.* **2017**, *65*, 2507–2516, doi:10.1109/TAP.2017.2679067.
28. Neira, L.M.; Van Veen, B.D.; Hagness, S.C. High-resolution microwave breast imaging using a 3-D inverse scattering algorithm with a variable-strength spatial prior constraint. *IEEE Trans. Antennas Propag.* **2017**, *65*, 6002–6014, doi:10.1109/TAP.2017.2751668.
29. Wang, Y.M. Reconstruction of two-dimensional permittivity distribution using the distorted born iterative method. *IEEE Trans. Med. Imaging* **1990**, *9*, 218–225.
30. Ambrosanio, M.; Kosmas, P.; Member, S.; Pascazio, V.; Member, S. A multithreshold iterative DBIM-based algorithm for the imaging of heterogeneous breast tissues. *IEEE Trans. Biomed. Eng.* **2019**, *66*, 509–520, doi:10.1109/TBME.2018.2849648.
31. Azghani, M.; Kosmas, P.; Marvasti, F. Microwave medical imaging based on sparsity and an iterative method with adaptive thresholding. *IEEE Trans. Med. Imaging* **2014**, *34*, 357–365.
32. Blumensath, T.; Davies, M.E. Iterative thresholding for saparse approximations. *J. Fourier Anal. Appl.* **2008**, *14*, 629–654, doi:10.1007/s00041-008-9035-z.
33. Beck, A.; Teboulle, M. A fast iterative shrinkage-thresholding algorithm. *Soc. Ind. Appl. Math. J. Imaging Sci.* **2009**, *2*, 183–202, doi:10.1137/080716542.
34. Meaney, P.M.; Zhou, T.; Goodwin, D.; Golnabi, A.; Attardo, E.A.; Paulsen, K.D. Bone dielectric property variation as a function of mineralization at microwave frequencies. *Int. J. Biomed. Imaging* **2012**, *2012*, doi:10.1155/2012/649612.
35. Zhurbenko, V. Challenges in the design of microwave imaging systems for breast cancer detection. *Adv. Electr. Comput. Eng.* **2011**, *11*, 91–96, doi:10.4316/aece.2011.01015.
36. Catapano, I.; Di Donato, L.; Crocco, L.; Bucci, O.M.; Morabito, A.F.; Isernia, T.; Massa, R. On quantitative microwave tomography of female breast. *Prog. Electromagn. Res.* **2009**, *97*, 75–93, doi:10.2528/PIER09080604.
37. Gilmore, C.; Zakaria, A.; Pistorius, S.; Lovetri, J. Microwave imaging of human forearms: Pilot study and image enhancement. *Int. J. Biomed. Imaging* **2013**, *2013*, doi:10.1155/2013/673027.

38. Amin, B.; Kelly, D.; Shahzad, A.; O'Halloran, M.; Elahi, M.A. Microwave calcaneus phantom for bone imaging applications. In Proceedings of the 2020 14th European Conference on Antennas and Propagation (EuCAP), Copenhagen, Denmark, 15–20 March 2020; pp. 1–5.
39. Salahuddin, S.; Porter, E.; Krewer, F.; O'Halloran, M. Optimised analytical models of the dielectric properties of biological tissue. *Med. Eng. Phys.* **2017**, *43*, 103–111.
40. Gabriel, S.; Lau, R.W.; Gabriel, C. The dielectric properties of biological tissues : III. Parametric models for the dielectric spectrum of tissues. *Phys. Med. Biol.* **1996**, *41*, 2271.
41. Topoliński, T.; Mazurkiewicz, A.; Jung, S.; Cichański, A.; Nowicki, K. Microarchitecture parameters describe bone structure and its strength better than BMD. *Sci. World J.* **2012**, *2012*, doi:10.1100/2012/502781.
42. Chen, H.; Zhou, X.; Fujita, H.; Onozuka, M.; Kubo, K.Y. Age-related changes in trabecular and cortical bone microstructure. *Int. J. Endocrinol.* **2013**, *2013*, 213234, doi:10.1155/2013/213234.
43. Van Der Linden, J.C.; Weinans, H. Effects of microarchitecture on bone strength. *Curr. Osteoporos. Rep.* **2007**, *5*, 56–61, doi:10.1007/s11914-007-0003-3.
44. Shea, J.D.; Kosmas, P.; Hagness, S.C.; van Veen, B.D. Three-dimensional microwave imaging of realistic numerical breast phantoms via a multiple-frequency inverse scattering technique. *Med. Phys.* **2010**, *37*, 4210–4226, doi:10.1118/1.3443569.
45. Lazebnik, M.; Okoniewski, M.; Booske, J.H.; Hagness, S.C. Highly accurate debye models for normal and malignant breast tissue dielectric properties at microwave frequencies. *IEEE Microw. Wirel. Compon. Lett.* **2007**, *17*, 822–824.
46. Wang, Z.; Bovik, A.C.; Sheikh, H.R.; Simoncelli, E.P. Image quality assessment: From error visibility to structural similarity. *IEEE Trans. Image Process.* **2004**, *13*, 600–612.

Chapter 6

Anthropomorphic Calcaneus Phantom for Microwave Bone Imaging Applications

Article overview

This work presents the preparation and dielectric characterisation of liquid and solid based tissue-mimicking mixtures (TMMs) to mimic the dielectric properties of human calcaneus tissues. The polylactic acid-based three-dimensional (3-D) printed and carbon black-based cylindrical bone and realistic human calcaneus structures are developed. The liquid-based TMMs provide the flexibility of varying dielectric properties to mimic the tissue behaviours such as degradation of bone tissue. However, the solid TMMs provide more realistic, stable, and anatomically accurate phantoms. The liquid TMMs for skin, muscle, cortical bone, and trabecular bone are developed using a mixture of Triton X-100, water, and salt. These liquid TMMs can be used with 3-D printed structures to mimic the anatomical calcaneus for bone imaging applications. The solid TMMs for skin, cortical bone, and trabecular bone are developed using carbon black, graphite, polyurethane, and isopropanol. The dielectric properties of the TMMs are measured using an open-ended coaxial probe measurement technique across 0.5 – 8.5 GHz. The dielectric properties of TMMs developed aligns well with the reference dielectric data. The objective is to propose liquid and solid based TMMs within the acceptable error range of dielectric properties and hence to maintain a contrast between target tissues of the considered anatomical site. The variations observed in the dielectric properties of TMMs are in agreement with the literature reporting TMMs for human biological tissues.

This work has been published in the journal of the IEEE Journal of Electromagnetics, RF and Microwaves in Medicine and Biology *(2020).* I am the first lead author in the paper, which is co-authored with my supervisors. I designed and printed the 3-D printed structures and developed the liquid and solid based TMMs. The measurement of dielectric properties of the TMMs and the processing of dielectric

properties data was led by me. I led all parts of the work with support from my supervisors.

Abstract

Recent studies have found a significant dielectric contrast between healthy and osteoporotic human trabecular bones. This dielectric contrast can be exploited by microwave imaging for monitoring human bone health. The tissue-mimicking phantoms play a vital role in preclinical testing of the microwave imaging system. This paper presents an anatomically realistic multi-layered 3-D printed and carbon black-based human calcaneus structure. The liquid and solid based tissue-mimicking mixtures are also proposed to mimic the dielectric properties of skin, muscle, cortical bone, and trabecular bone. The liquid tissue-mimicking mixtures are composed of Triton X-100, water, and salt, whereas the solid tissue-mimicking mixtures are composed of carbon black, graphite, polyurethane, and isopropanol. The dielectric properties of the tissue-mimicking mixtures were measured using an open-ended coaxial probe measurement technique across 0.5 – 8.5 GHz. The average percentage difference between the relative permittivity and conductivity of reference data and proposed liquid tissue-mimicking mixtures was found to be 7.8% and 9.6% for skin, 0.38% and 14% for muscle, 9.6% and 5% for cortical bone, and 3.4% and 2.4 % for trabecular bone, respectively, across 0.5 – 8.5 GHz. For solid tissue-mimicking mixtures, this difference was found to be 3.93% and 0.64% for skin, 6.13% and 9.21% for cortical bone, and 10.66% and 41.82% for trabecular bone, respectively for relative permittivity and conductivity. The proposed tissue-mimicking mixtures along with 3-D printed structures can be used as a valuable test platform for microwave bone imaging system development.

6.1 Introduction

Microwave imaging (MWI) is an emerging diagnostic technology being investigated for a range of medical applications. MWI relies on the contrast of dielectric properties of biological tissues, namely relative permittivity (ε_r) and conductivity (σ (S/m)), of target anatomical site in the human body [1]. The key advantages of MWI over the other clinical imaging modalities are safety (non-ionising radiations), portability, and low cost [2]. These advantages make MWI a safe alternative to existing imaging technologies for diagnosing and monitoring various diseases such as breast cancer

detection and diagnosing brain stroke [3],[4],[5]. Several recent studies have investigated the feasibility of using MWI for osteoporosis monitoring [6],[11], which are based on a notable contrast between the dielectric properties of different diseased bones [10]. The current standard modalities for osteoporosis diagnosis and monitoring are dual-energy X-ray absorptiometry (DXA) and computed tomography (CT). Both DXA and CT use ionising radiations, therefore, these are not suitable for frequent scans [6],[9]. The associated clinical advantages of MWI and contrast of dielectric properties between healthy and diseased bones make MWI a potential routine imaging modality for monitoring bone health in comparison to the DXA and CT [11].

The experimental evaluation of the MWI prototype helps to examine the prototype in a controlled real-world scenario. To this end, tissue-mimicking phantoms play a vital role in the evaluation of repeatability, stability, imaging quality, and imaging resolution of an MWI system. Moreover, the performance of the imaging algorithms in the presence of external noise and system interference can be well assessed from experimental evaluation [12]. The tissue-mimicking phantoms emulate the dielectric properties and anatomy of various human body parts. Ideally, the reference phantoms should be anatomically and dielectrically accurate whilst being mechanically and dielectrically stable over time and easily produced [13]. The tissue-mimicking mixtures (TMMs) used in phantoms can be either liquid-based, such as oil-in-gelatin and Triton X-100 mixtures, or solid based, such as polyurethane-based TMMs [14]. Oil-in-gelatin TMMs have been widely used to emulate breast tissues and are attractive due to their ease of fabrication and their ability to simulate the dielectric properties of a wide range of tissues [15]. One major limitation of oil-in-gelatin TMMs is their sensitivity to environmental exposure, which causes desiccation over time [13]. Among liquid-based TMMs, Triton X-100 appears to be an excellent candidate due to its better relative heat stability (allowing performance of experiments at room temperature and human body temperature) and because its dielectric properties are stable for up to a year [13]. The liquid nature of Triton X-100 solutions ensures that complex three-dimensional (3-D) structures can be filled by avoiding air bubbles in these structures. Various studies have used this approach to mimic the dielectric properties of head and breast tissues [13],[25]. The limitation in this approach is that the 3-D printed shells have not been dielectrically characterised and this can potentially affect the quality of reconstructed images [18]. Alternatively, polyurethane

can be used as a potential solid TMM. In the polyurethane TMMs, the dielectric properties are controlled by adding carbon black and graphite powders to the rubber mixture [19]. Due to flexibility, dielectric stability, and mechanical strength, the polyurethane mixtures outperform the liquid TMMs [20]. Moreover, the solid TMMs does not involve any additional and unwanted 3-D printed structures, thus minimising the effect in reconstructed microwave images [19]. However, these TMMs are hard to reconfigure to account for changes associated with the shape of the anatomical lesion when compared to liquid-based TMMs [13]. There has been limited development on bone mimicking phantoms with only simplified homogeneous structures reported for head models [13],[21]. However, to the best of the author's knowledge, no study has ever reported TMMs for cortical and trabecular bones separately for the application of bone imaging.

Recent advancements in manufacturing technologies have enabled building complex and relatively easily reproducible 3-D printed structures for use in solid phantom development. One drawback of 3-D printed moulds is the limited choice of fabrication substrates. Acrylonitrile butadiene styrene (ABS) is a commonly used substrate for 3-D printed phantom moulds, despite its electrical permittivity and conductivity being far from the dielectric properties of the biological tissues. At a frequency of 2.45 GHz, the dielectric contrast in terms of the average percentage difference between ABS and trabecular bone is 144% and 195% for ε_r and σ, respectively. This significant dielectric contrast creates a mismatch between the biological tissues and the ABS layers in the 3-D printed structures referred to as "electrical perturbance". The previous studies have experimentally [18] shown that due to the high dielectric contrast with respect to the various biological tissues, the ABS walls perturb the field significantly even with wall thickness as low as 1.5mm [13].

This paper presents an anthropomorphic multi-layered human calcaneus phantom for MWI system evaluation. A full 3-D model of a human foot was altered to obtain a multi-layered human calcaneus structure. The major tissue layers considered for developing the calcaneus phantom are skin, muscle, cortical bone, and trabecular bone. The human calcaneus bone is shown in Figure 6.1. The peripheral location of human calcaneus bone as can be seen in Figure 6.1, makes it the most suitable location for MWI. Our preliminary study has reported Triton X-100 based TMMs to mimic the

dielectric properties of skin, muscle, cortical bone, and trabecular bone over 0.5 – 8.5 GHz frequency range [14]. These TMMs are used in 3-D printed structures that hold the liquid TMMs. While phantoms based on these TMMs and 3-D printed structures are useful for preliminary experiments, there is significant unwanted electromagnetic (EM) field perturbance due to the presence of 3-D printed substrate [13]. To avoid this unwanted EM field perturbance, this study proposes carbon black-based anatomical phantoms that mimic the dielectric properties of skin, cortical bone, and trabecular bone over the 0.5 – 8.5 GHz frequency range. Most of the microwave tomography (MWT) imaging systems operate below 3 GHz [8]. Gilmore *et al*. [22] has reconstructed the human forearms bones by MWT. The optimal results were found at 0.8 GHz and 1 GHz. Scapaticci *et al*. [5] found that the penetration of electromagnetic (EM) waves in human biological tissues reduce as a function of frequency. Therefore, considering frequencies above 3 GHz for microwave bone imaging application would not be feasible due to the low penetration of EM waves. However, the wideband imaging systems particularly the radar-based imaging techniques use higher frequencies [4]. Therefore, the liquid and carbon black-based TMMs are characterised over a wide frequency range (0.5 – 8.5 GHz). These TMMs can be used for both tomographic and radar-based imaging techniques. The 3-D printed moulds and counter-moulds were designed to develop the realistic carbon black-based calcaneus phantom. The outer layer of the calcaneus phantom mimics the dielectric properties of the skin. The interior of the calcaneus phantom mimics the calcaneus bone. The calcaneus bone has a carbon black-based layer mimicking dielectric properties of the cortical bone, and a cavity to contain the trabecular bone mimicking material. This trabecular bone cavity is filled with trabecular bone mimicking liquid. The flexibility of using liquid TMM for trabecular bone in the proposed phantom allows for mimicking a natural variation of trabecular bone dielectric properties. Moreover, the trabecular bone cavity can be filled with TMM of diseased trabecular bone. The carbon black-based phantoms will reduce the artefacts in images that would be otherwise present in the plastic phantoms. However, the liquid TMMs based phantoms are still useful for preliminary experiments for evaluation of the prototype and imaging algorithms due to ease of preparation.

Figure 6.1: Human calcaneus bone.

6.2 Methodology

6.2.1 3-D Printed Structures

The design and fabrication complexity of the anatomical structure primarily depends upon the corresponding details of the anatomical site. Moreover, the accuracy and precision to replicate any anatomical site in the human body is highly dependent upon the application to be investigated [23]. In this study two types of human bone structures were modelled: 1) a two-layered hollow cylinder was designed to represent the cortical and trabecular bones, and 2) a 3-D model of the human foot was used to develop an anatomically realistic human calcaneus phantom. The model was designed as a three-layered human calcaneus structure. These three layers were filled with liquid TMMs for skin, cortical bone, and trabecular bone. The human calcaneus was chosen as the target anatomical site due to the proximity of the calcaneus bone to the skin, and the ratio of cortical to the trabecular bone is also similar to that found in the femoral head and lumbar spine [24],[25], which are primary targets for standard osteoporosis monitoring technologies. A 3-D modelling software (Autodesk Fusion 3D) was used to produce all 3-D models. These models were then printed with Ultimaker 2+ Extended 3-D printer at 200 °C using a polylactic acid (PLA) filament. The thickness of walls was kept to 2mm to prevent leakage of liquid TMMs and to avoid potential low field perturbation. Finally, these 3-D printed structures were filled with liquid TMMs for Triton X-100 based phantoms. Moreover, similar 3-D models were developed as moulds for carbon black-based phantoms.

6.2.2 Liquid Tissue Mimicking Mixtures Preparation

The liquid TMMs were composed of Triton X-100, water, and salt (NaCl). The preparation of TMMs was based on the guidelines outlined in [13],[26]. The solution of Triton X-100, water, and salt was put in a glass beaker and was thoroughly mixed until the disappearance of air bubbles. The percentage of salt was varied following the difference between the conductivity of reference tissue and the conductivity of the

proposed TMM. The higher concentrations of salt were used for tissues having high conductivity values, however, higher concentrations of Triton X-100 were used to lower both the conductivity and permittivity of the solutions. As described in [13], TMM solutions that contain 45-55% of Triton X-100 become highly viscous, however, none of the Triton X-100 solutions except skin fell in that range. In this study, we have proposed liquid TMMs for skin, cortical bone, and trabecular bone. The composition of constituents was adjusted until the dielectric properties of TMMs were close to the reference values reported by Gabriel *et al*. [27].

6.2.3 Solid Tissue Mimicking Mixtures Preparation

The solid TMMs were composed of carbon black, graphite, polyurethane, and isopropanol. Since this TMM provides enough flexibility for recreating the target dielectric properties of various biological tissues [28]. A similar procedure has been adopted for the preparation of TMMs as outlined in [23]. Firstly, a polyurethane base was prepared by mixing equal masses of two liquid precursors to polyurethane as per the manufacturer's instructions (VytaFlex 20, Smooth-On, Easton, PA, USA). Once the polyurethane base was ready, the graphite powder and carbon black powder were mixed. To get the desired dielectric properties of TMMs, the mixture of carbon black, graphite, and polyurethane was thoroughly mixed. It has been observed in [16] that polyurethane provides a mechanically strong base while the relative permittivity and conductivity of various biological tissues can be achieved by varying proportions of graphite and carbon black. It was observed that the values of dielectric properties increase as the mass percentage of carbon black and graphite powder increases. However, the blended mixture gets thicker and extremely difficult to mix as the mass percentage of carbon black and graphite powder is increased. To achieve the uniformity of mixture and higher dielectric properties, a small amount of isopropanol was added as a thinning agent. For optimal dielectric properties of the final phantom, rectangular cuboids $50 \times 20 \times 20$ mm^3 were designed as reference samples and their dielectric properties were measured. The 3-D printed moulds were developed to shape the solid TMMs into anatomically realistic carbon black based phantoms. This study has proposed the composition of solid TMMs for skin, cortical bone, and trabecular bone.

6.2.4 Dielectric Properties Measurement

The dielectric properties of liquid and solid TMMs were measured by employing an open-ended coaxial probe (OECL) technique. The measurements were recorded in the frequency range of 0.5 – 8.5 GHz over 101 linearly spaced frequency points. The dielectric measurements were performed by Keysight slim form probe 85070E connected directly to the Keysight E5063A vector network analyzer (VNA) [29]. The temperature of liquids for calibration and validation was measured using a digital thermometer (HI98509-1) from Hanna Instruments. The VNA was used to measure the reflection coefficient (S_{11}) at 101 linearly spaced frequency points, and a commercially available software suite (Keysight N1500A) was used to convert the S_{11} parameters to real (ε') and imaginary (ε'') parts of complex permittivity [1].

A standard three-load one-port calibration (Air, Short, and Deionised water) was used to calibrate the measurement equipment before the measurement of dielectric properties. The calibration of the measurement equipment was verified by measuring the dielectric properties of the 0.1 M NaCl solution (saline) at 22 ºC [30]. A total of 6 validation measurements were performed. The uncertainty of the equipment's accuracy is reported in Table 6.1. The uncertainty in accuracy in terms of percentage is defined as:

$$UC_{ACC}(f) = \left(\frac{x_{meas}(f) - x_{ref}(f)}{x_{ref}(f)}\right) \times 100 \qquad (6.1)$$

where x_{meas} represents measured dielectric properties of 0.1 M NaCl and x_{ref} represents standard dielectric properties of 0.1 M NaCl [30] at the measured temperature. The repeatability of measurements is also reported in Table 6.1, and defined as:

$$UC_{REP}(f) = \left(\frac{x_{meas}(f) - x_{mean}(f)}{x_{mean}(f)}\right) \times 100 \qquad (6.2)$$

where x_{mean} represents the mean of the measured dielectric properties. To compute the uncertainties, the measurements were recorded in the frequency range of 0.5-8.5 GHz over 101 linearly spaced frequency points. The reported values of UC_{ACC} and UC_{REP} are averaged over the measured frequency range (0.5-8.5 GHz). The combined uncertainty is the sum of UC_{ACC} and UC_{REP} both for relative permittivity and conductivity. The uncertainty analysis was based on previous studies [1],[30]. The total combined uncertainty is reported in Table 6.1.

Table 6.1: Percent uncertainty in accuracy and repeatability of measurements.

Parameter	$\boldsymbol{\varepsilon_r}$ **(%)**	$\boldsymbol{\sigma}$ $\boldsymbol{(S/m)}$ **(%)**
UC_{ACC}	0.04	2.75
UC_{REP}	0.07	0.75
Combined	0.11	3.50

The reported values of UC_{ACC} and UC_{REP} are averaged over the measured frequency range (0.5-8.5 GHz).

6.3 Results and Discussion

6.3.1 3-D Printed Structures

The 3-D printed structures were developed to hold the liquid TMMs for each tissue. Figure 6.2 (a) and (b) shows the two-layered cylindrical bone phantom, and Figure 6.2 (c) and (d) shows the anatomically realistic three-layered calcaneus phantom. The cylindrical structure only incorporates the cortical bone and trabecular bone. The cylindrical structure was printed as an initial simplistic test case for the MWI system. As the calcaneus bone, in general, resembles an irregular shaped cylinder, therefore for initial imaging purposes, the cylindrical structure can be used. The anatomically realistic 3-D calcaneus structure was designed to simulate a more realistic imaging scenario. To avoid problems such as leakage, trapped air, and weakness of the structure, the thickness of the walls was chosen to be 2mm, which is a compromise between mechanical stability and electrical perturbance. The authors have tested ABS structures of 1.5 mm thickness and 2 mm thickness. The thickness of 2 mm for ABS structures ensured that the liquid TMMs do not leak to adjacent layers in a multi-layered 3-D printed structure and provides good mechanical stability.

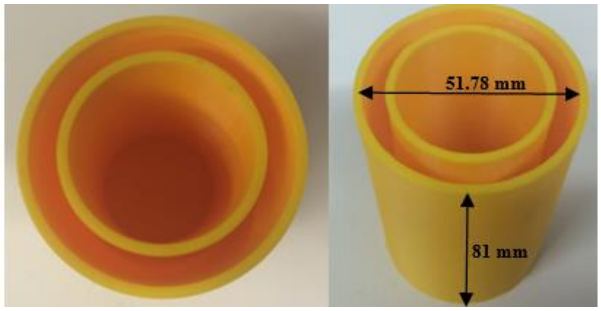

(a) (b)

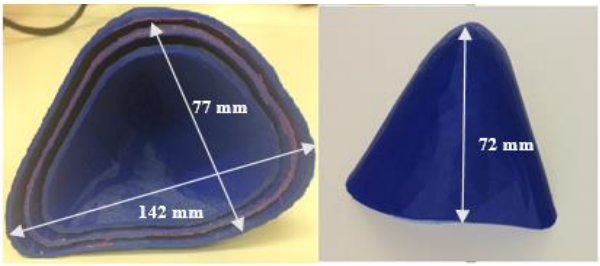

(c) (d)

Figure 6.2: 3-D printed two-layered cylindrical bone phantom (a) Top View (b) Side View and anatomically accurate human calcaneus structure (c) Interior View (d) Exterior View.

6.3.2 Liquid Tissue Mimicking Mixtures

To mimic the dielectric properties of skin, muscle, cortical bone, and trabecular bone, several TMMs containing Triton X-100, water, and salt were made. The percentage of Triton X-100 was varied from 90% to 24%, whereas, the percentage of water was varied from 10% to 76%. The dielectric properties of all TMMs were analysed and the composition of each TMM was varied to match the target tissue. Among all TMMs, four solutions were selected that mimic the dielectric properties of skin, muscle, cortical bone, and trabecular bone. The recipe for muscle tissue-mimicking material was obtained from [13], whereas the dielectric properties of skin, cortical bone, and trabecular bone were achieved by varying the composition of TMMs. The composition of TMMs that mimic the dielectric properties of each target tissue is given in Table 6.2.

Table 6.2: Composition of liquid TMMs.

Target Tissue	Triton X-100 (vol %)	Deionized water (vol %)	NaCl (g/L)
Skin	40	60	5.2
Muscle [13]	24	76	5
Cortical Bone	77	23	0.8
Trabecular Bone	69.5	30.5	0.8

While the recipe of muscle is taken from [13], the recipes for skin, cortical bone, and trabecular bone are proposed in this study. NaCl is expressed in terms of grams/liter(g/L).

The measured dielectric properties of liquid TMMs of target tissues (solid plots) and the reference dielectric data (dashed plots) are shown in Figure 6.3. Each solid curve in Figure 6.3 indicates the mean value of six measurements taken at 101 linearly spaced frequency points between 0.5 – 8.5 GHz. The measurements were obtained at multiple sites in the liquid. The dashed plots represent the corresponding tissue's reference dielectric data taken from a large scale study conducted by Gabriel *et al*. [27]. It can be observed from Figure 6.3 (a) and (b), that the mean dielectric properties of TMMs are well aligned with the reference dielectric properties of modelled tissues. The average percentage difference was calculated between relative permittivity and conductivity values of reference tissues from Gabriel *et al*. [27] and the relative permittivity and conductivity values of proposed TMMs over 0.5 – 8.5 GHz and is presented in Table 6.3. This difference was found to be less at lower frequencies compared to higher frequencies. The average percentage difference between the dielectric properties of TMM and its respective tissue is found to be less than ± 10%, which is within the expected variance in biological tissue [31]. The variations observed in the results are in agreement with the literature reporting TMMs for human biological tissues [13],[23],[32].

Table 6.3: Average percentage difference between TMM and reference tissue dielectric data.

Target Tissue	ε_r (%)	$\sigma(S/m)$ (%)
Skin	7.8	9.6
Muscle	0.38	14
Cortical Bone	9.6	5
Trabecular Bone	3.4	2.4

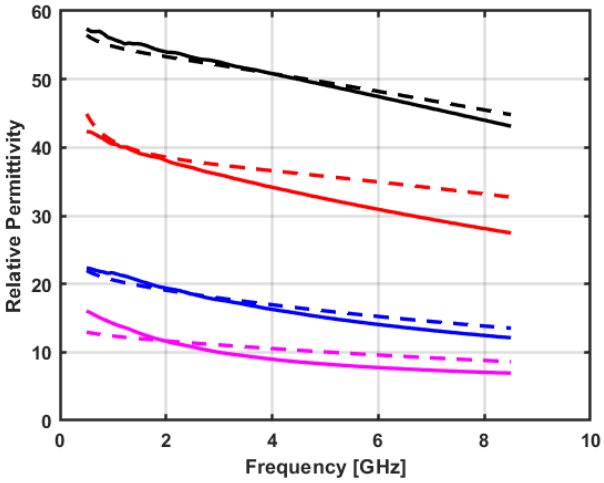

(a)

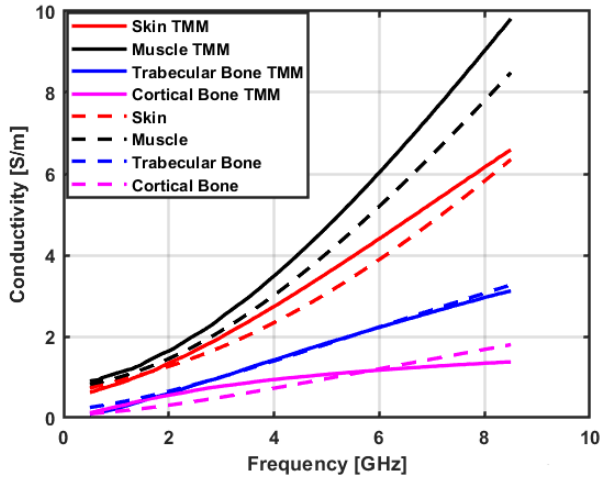

(b)

Figure 6.3: Dielectric properties of liquid tissue-mimicking mixtures over 0.5 – 8.5 GHz frequency band: (a) Relative Permittivity (b) Conductivity. The measured dielectric data of TMMs (solid lines) are compared with reference data (dotted lines) from Gabriel *et al*. [27].

6.3.3 Solid Tissue Mimicking Mixtures

This study has made a first attempt to develop solid TMMs for cortical bone and trabecular bone. Also, a solid TMM for skin is developed for a fully anatomical and dielectrically accurate calcaneus phantom. Several TMMs containing carbon black, graphite, urethane, and isopropanol were made for each tissue. The composition of TMMs that mimic the dielectric properties of investigated tissues is given in Table 6.4.

Table 6.4: Composition of solid TMMS.

Target Tissue	cb (sv%)	Graphite (sv%)	Urethane (sv%)	Isopropanol (mL/100g)
Skin	5	28	67	3
CB	4	0	96	3
TB	5	0	95	3

CB = Cortical Bone, TB = Trabecular Bone, cb = carbon black, sv = solid volume, mL/100g = milliliter/100 gram. Recipes for skin, cortical bone, and trabecular bone are proposed in this study.

The mixture of carbon black, graphite, urethane, and isopropanol was thoroughly mixed and left for 24 hours before the dielectric measurements were performed. Figure 6.4 shows the dielectric properties of the TMMs and the reference values of the respective tissues. Each solid curve in Figure 6.4 indicates the mean value of six measurements taken at 101 linearly spaced frequency points between 0.5 – 8.5 GHz. The measurements were obtained at multiple sites on the solid TMM. It can be observed from Figure 6.4 (a) and (b), that the mean dielectric properties of TMMs are well aligned with the dielectric properties of respective tissues, particularly the relative permittivity. However, there is a relatively large deviation between the conductivity of TMMs and reference data. The large deviation in conductivity is mainly observed due to the absence of water in solid TMMs. The solid TMMs are composed of isopropanol as a liquid constituent. Since, the conductivity of water is higher and has an exponential behaviour compared to isopropanol, which has lower conductivity and non-exponential behaviour within the 0.5 – 8.5 GHz frequency range, therefore, the conductivity profile of proposed TMMs have lower values at higher frequencies compared to reference data. However, the proposed TMMs maintain a realistic

contrast between the conductivities of target tissues of the considered anatomical site. This contrast can be well observed below 3 GHz, where most of the MWT imaging systems operate [8]. The variations observed in conductivity profiles of solid TMMs are in agreement with literature reporting the conductivity of solid TMMs for human biological tissues [22],[28],[32]. The average percentage difference was calculated between relative permittivity and conductivity values of reference tissues from Gabriel *et al*. [27] and the relative permittivity and conductivity values of proposed TMMs over 0.5 – 8.5 GHz and is presented in Table 6.5.

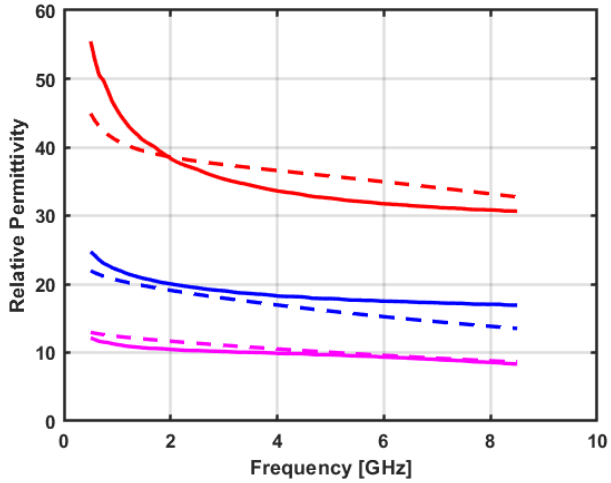

(a)

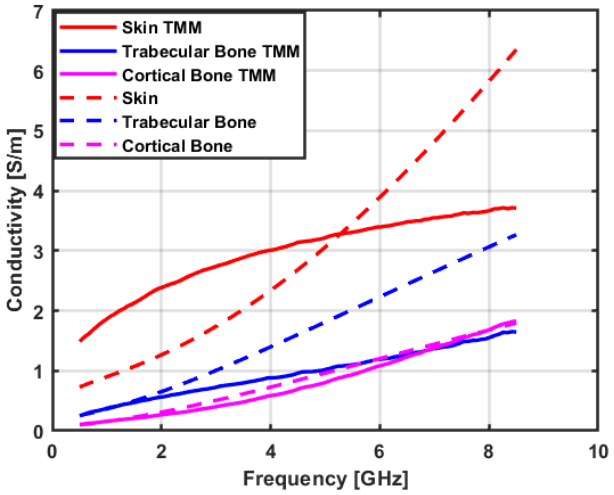

(b)

Figure 6.4: Dielectric properties of solid tissue-mimicking mixtures over 0.5 – 8.5 GHz frequency band: (a) Relative Permittivity (b) Conductivity. The measured dielectric data of TMMs (solid lines) are compared with reference data (dotted lines) from Gabriel *et al*. [27].

Table 6.5: Average percentage difference between TMM and reference tissue dielectric data.

Target Tissue	$\boldsymbol{\varepsilon_r}$ **(%)**	$\boldsymbol{\sigma}$ $\boldsymbol{(S/m)}$ **(%)**
Skin	3.93	0.64
Cortical Bone	6.13	9.21
Trabecular Bone	10.66	41.82

The average percentage difference between the dielectric properties of each TMM and corresponding reference values was found to be less for lower frequencies compared to higher frequencies for solid TMMs as observed in liquid TMMs. The average percentage difference in relative permittivity profiles of the bone TMMs and corresponding tissues are smaller compared to the average percentage difference in conductivity profiles.

Figure 6.5 (a) and (b) show side and top views of cylindrical shaped solid calcaneus phantom. As discussed earlier the cylindrical-shaped phantoms were designed as initial test cases for the MWI system. The outer layer of the phantom mimics the dielectric properties of cortical bone and the inner layer was filled with trabecular bone's liquid TMM.

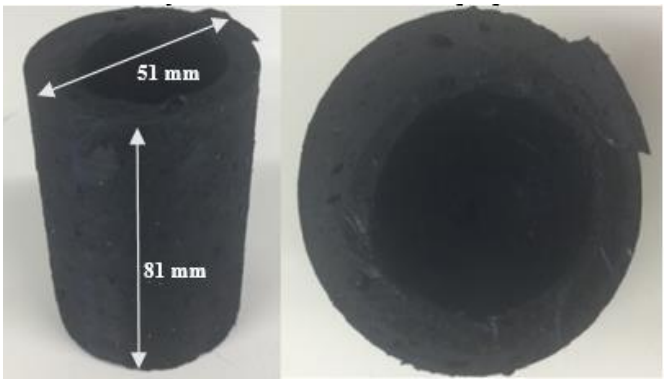

(a) (b)

Figure 6.5: Cylindrical shaped calcaneus bone phantom (a) Side view (b) Top View.

An anatomically realistic solid calcaneus phantom was also developed as shown in Figure 6.6 (a) and (b). Figure 6.6 (a) and (b) shows the interior and exterior views of a realistic calcaneus phantom. The phantom is composed of a solid single layer having an interior cavity, where the external and internal layers mimic the dielectric properties of the skin.

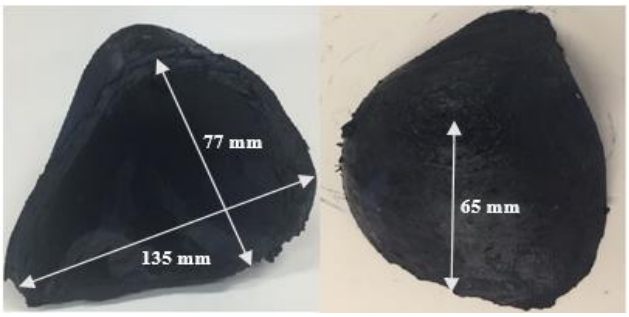

(a) (b)

Figure 6.6: Anatomically realistic calcaneus phantom (a) Interior view (b) Exterior View.

Figure 6.7 (a) and (b) shows the exterior and interior views of a realistic calcaneus bone phantom. The outer layer mimics the dielectric properties of cortical bone and the inner layer constitutes the liquid TMM of trabecular bone. The calcaneus bone phantom was then placed into the calcaneus phantom. The empty spaces left between the skin layer and the outer layer of calcaneus bone phantom were filled with liquid TMM of muscle.

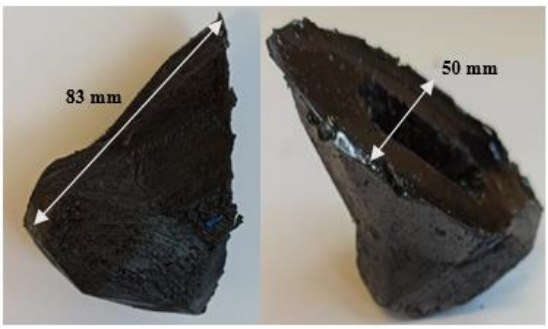

(a) (b)

Figure 6.7: Anatomically realistic calcaneus bone phantom (a) Exterior View (b) Interior view.

6.4 Conclusion

Phantoms play a vital role in assessing the data acquisition, pre-processing signal evaluation, and repeatability of measurements in a controlled realistic scenario for an MWI system. In this study, two types of MWI phantoms were developed: 1) liquid-based TMMs to provide the flexibility of varying dielectric properties to mimic the tissue behaviours such as the growth of cancer or degradation of bone tissue; 2) solid TMMs for more realistic, stable and anatomically accurate phantoms. The liquid TMMs for skin, muscle, cortical bone, and trabecular bone were developed using mixtures of Triton X-100, water, and salt. These liquid TMMs can be used with 3-D

printed structures to mimic anatomical calcaneus bone for imaging applications. The solid TMMs for skin, cortical bone, and trabecular bone were developed using carbon black, graphite, polyurethane, and isopropanol. The solid TMMs are easily mouldable, relatively inexpensive, mechanically, and dielectrically stable over time. The dielectric properties of TMMs developed in this study aligns well with the reference dielectric data. The combined average percentage difference between dielectric properties of liquid TMMs and the reference data is found to be less than 10% for target tissues. Similar findings are observed for solid TMMs, except for the conductivity of trabecular bone that significantly deviated from reference data at higher frequencies. The objective of the study was to propose liquid and solid based TMMs within an acceptable error range of dielectric properties and hence to maintain a contrast between target tissues of the considered anatomical site. The variations observed in dielectric properties of TMMs are in agreement with the literature reporting TMMs for human biological tissues. Future studies will focus on developing a more realistic replication of human calcaneus that should also involve trabecular bone microarchitecture along with bone marrow for experimental investigation of bone models for monitoring bone health.

Funding: The research leading to these results has received funding from the European Research Council under the European Union's Horizon 2020 Programme (H2020)/ERC grant agreement BioElecPro n. 637780.

Conflicts of Interest: The authors declare no conflict of interest. The funders had no role in the design of the study; in the collection, analyses, or interpretation of data; in the writing of the manuscript, or in the decision to publish the results.

References

1. A. Shahzad, K. Sonja, M. Jones, R. M. Dwyer, and M. O'Halloran, "Investigation of the effect of dehydration on tissue dielectric properties in ex vivo measurements," *Biomed. Phys. Eng. Express*, vol. 3, no. 4, pp. 1–9, 2017.
2. R. Scapaticci, P. Kosmas, and L. Crocco, "Wavelet-Based Regularization for Robust Microwave Imaging in Medical Applications," *IEEE Trans. Biomed. Eng.*, vol. 62, no. 4, pp. 1195–1202, 2015.
3. A. Shahzad, M. O'Halloran, E. Jones, and M. Glavin, "A multistage selective weighting method for improved microwave breast tomography," *Comput. Med. Imaging Graph.*, vol. 54, pp. 6–15, 2016.

4. D. O'Loughlin, M. O'Halloran, B. M. Moloney, M. Glavin, E. Jones, and M. A. Elahi, "Microwave Breast Imaging: Clinical Advances and Remaining Challenges," *IEEE Trans. Biomed. Eng.*, vol. 65, no. 11, pp. 2580–2590, 2018.
5. R. Scapaticci, L. Di Donato, I. Catapano, and L. Crocco, "A feasibility study on microwave imaging for brain stroke monitoring," *Prog. Electromagn. Res.*, vol. 40, pp. 305–324, 2012.
6. B. Amin, M. A. Elahi, A. Shahzad, E. Porter, B. McDermott, and M. O'Halloran, "Dielectric properties of bones for the monitoring of osteoporosis," *Med. Biol. Eng. Comput.*, Aug. 2018.
7. B. Amin, M. A. Elahi, A. Shahzad, E. Porter, and M. O'Halloran, "A review of the dielectric properties of the bone for low frequency medical technologies," *Biomed. Phys. Eng. Express*, vol. 5, no. 2, p. 022001, 2019.
8. P. M. Meaney, T. Zhou, D. Goodwin, A. Golnabi, E. A. Attardo, and K. D. Paulsen, "Bone dielectric property variation as a function of mineralization at microwave frequencies," *Int. J. Biomed. Imaging*, vol. 2012, 2012.
9. P. M. Meaney *et al.*, "Clinical microwave tomographic imaging of the calcaneus: A first-in-human case study of two subjects," *IEEE Trans. Biomed. Eng.*, vol. 59, no. 12, pp. 3304–3313, 2012.
10. B. Amin *et al.*, "Dielectric characterization of diseased human trabecular bones at microwave frequency," in *2020 Medical Engineering and Physics*, 2020, pp. 1–8.
11. B. Amin, M. A. Elahi, A. Shahzad, E. Parle, L. McNamara, and M. Orhalloran, "An insight into bone dielectric properties variation: A foundation for electromagnetic medical devices," *EMF-Med 2018 - 1st EMF-Med World Conf. Biomed. Appl. Electromagn. Fields COST EMF-MED Final Event with 6th MCM*, pp. 3–4, 2018.
12. M. A. Elahi *et al.*, "Evaluation of image reconstruction algorithms for confocal microwave imaging: Application to patient data," *Sensors (Switzerland)*, vol. 18, no. 6, 2018.
13. N. Joachimowicz, B. Duchêne, C. Conessa, and O. Meyer, "Anthropomorphic Breast and Head Phantoms for Microwave Imaging," *Diagnostics*, vol. 8, no. 4, p. 85, 2018.
14. B. Amin, D. Kelly, A. Shahzad, M. O'Halloran, and M. A. Elahi, "Microwave calcaneus phantom for bone imaging applications," in *2020 14th European*

Conference on Antennas and Propagation (EuCAP), 2020, pp. 1–5.

15. M. Lazebnik, E. L. Madsen, G. R. Frank, and S. C. Hagness, "Tissue-mimicking phantom materials for narrowband and ultrawideband microwave applications," *Phys. Med. Biol.*, vol. 50, no. 18, p. 4245, 2005.
16. J. Garrett and E. Fear, "Stable and flexible materials to mimic the dielectric properties of human soft tissues," *IEEE Antennas Wirel. Propag. Lett.*, vol. 13, no. c, pp. 599–602, 2014.
17. N. Joachimowicz, C. Conessa, T. Henriksson, and B. Duchêne, "Breast phantoms for microwave imaging," *IEEE Antennas Wirel. Propag. Lett.*, vol. 13, pp. 1333–1336, 2014.
18. T. Rydholm, A. Fhager, M. Persson, S. Geimer, and P. Meaney, "Effects of the Plastic of the Realistic GeePS-L2S-Breast Phantom," *Diagnostics*, vol. 8, no. 3, p. 61, 2018.
19. J. Garrett and E. Fear, "A New Breast Phantom With a Durable Skin Layer for Microwave Breast Imaging," *IEEE Trans. Antennas Propag.*, vol. 63, no. 4, pp. 1693–1700, 2015.
20. T. Hikage, Y. Sakaguchi, T. Nojima, and Y. Koyamashita, "Development of lightweight solid phantom composed of silicone rubber and carbon nanotubes," in *2007 IEEE International Symposium on Electromagnetic Compatibility*, 2007, pp. 1–4.
21. R. Scapaticci, M. Bjelogrlic, J. A. T. Vasquez, F. Vipiana, M. Mattes, and L. Crocco, "Microwave technology for brain imaging and monitoring: physical foundations, potential and limitations," in *Emerging Electromagnetic Technologies for Brain Diseases Diagnostics, Monitoring and Therapy*, Springer, 2018, pp. 7–35.
22. C. Gilmore, A. Zakaria, S. Pistorius, and J. Lovetri, "Microwave imaging of human forearms: Pilot study and image enhancement," *Int. J. Biomed. Imaging*, vol. 2013, 2013.
23. B. McDermott *et al.*, "Anatomically and dielectrically realistic microwave head phantom with circulation and reconfigurable lesions," *Prog. Electromagn. Res. B*, vol. 78, pp. 47–60, 2017.
24. J. M. Vogel, R. D. Wasnich, and P. D. Ross, "The clinical relevance of calcaneus bone mineral measurements: a review," *Bone Miner.*, vol. 5, no. 1, pp. 35–58, 1988.

25. B. Clarke, “Normal bone anatomy and physiology.,” *Clin. J. Am. Soc. Nephrol.*, vol. 3 Suppl 3, no. Suppl 3, pp. 1–16, 2008.
26. D. A. Pollacco, M. C. Conti, L. Farrugia, P. S. Wismayer, L. Farina, and C. V Sammut, “Dielectric properties of muscle and adipose tissue-mimicking solutions for microwave medical imaging applications,” *Phys. Med. Biol.*, vol. 64, no. 9, p. 95009, 2019.
27. C. Gabriel *et al.*, “The dielectric properties of biological tissues : III . Parametric models for the dielectric spectrum of tissues The dielectric properties of biological tissues : III . Parametric models for the dielectric spectrum of tissues,” 1996.
28. B. L. Oliveira, D. O’Loughlin, M. O’Halloran, E. Porter, M. Glavin, and E. Jones, “Microwave Breast Imaging: Experimental tumour phantoms for the evaluation of new breast cancer diagnosis systems,” *Biomed. Phys. Eng. Express*, vol. 4, no. 2, p. 25036, 2018.
29. S. Salahuddin, E. Porter, F. Krewer, and M. O’ Halloran, “Optimised analytical models of the dielectric properties of biological tissue,” *Med. Eng. Phys.*, vol. 43, pp. 103–111, 2017.
30. C. Gabriel and A. Peyman, “Dielectric measurement: Error analysis and assessment of uncertainty,” *Phys. Med. Biol.*, vol. 51, no. 23, pp. 6033–6046, 2006.
31. C. Gabriel, “Dielectric properties of biological tissue: Variation with age,” *Bioelectromagnetics*, vol. 26, no. SUPPL. 7, pp. 12–18, 2005.
32. J. Garrett and E. Fear, “Stable and flexible materials to mimic the dielectric properties of human soft tissues,” *IEEE Antennas Wirel. Propag. Lett.*, vol. 13, pp. 599–602, 2014.

Chapter 7

Experimental Validation of Microwave Imaging Prototype and DBIM-IMATCS Algorithm for Bone Health Monitoring

Article overview

This work presents the experimental data and hardware acquisition system developed to image the bone phantoms presented in Chapter 6. A dedicated microwave imaging (MWI) prototype is developed to reconstruct the spatial distribution of dielectric properties of the human calcaneus phantoms for bone imaging application. The spatial distribution of dielectric properties of the experimental phantoms is reconstructed by employing the distorted Born iterative method (DBIM) algorithm along with compressed sensing (CS) based iterative method for linear inversion of electromagnetic (EM) waves. In this study special cases of trabecular bone phantoms are developed to mimic the dielectric properties of osteoporotic and osteoarthritis patients. Three bone phantoms are used to acquire the experimental data and to access the limitations of the MWI prototype under realistic *in vivo* imaging scenarios. One of the bone phantoms is developed to mimic the dielectric properties of the normal trabecular bone reported in the literature. The remaining two phantoms mimic the dielectric properties of the human trabecular bones from osteoporotic and osteoarthritis patients. The reference dielectric data for trabecular bones of osteoporotic and osteoarthritis patients is acquired from Chapter 3. Each aspect of the imaging system along with the challenges associated with image analysis are also analysed and discussed. The evaluation of experimental phantoms before clinical testing of the MWI system helps to evaluate the robustness of the adopted microwave tomography (MWT) imaging approach for reconstruction of dielectric properties under a realistic *in vivo* imaging scenario. The objective is to evaluate MWT for the assessment of different diseased bone phantoms for bone health monitoring.

This work has been submitted in the journal of *Medical Physics (2021)*. I am the first lead author in the paper, which is co-authored with my supervisors. I designed,

developed, and acquired the experimental data from the imaging prototype. The processing of the measured experimental data and retrieving the spatial distribution of dielectric properties by employing the DBIM algorithm was performed by me. I led all parts of the work with the support of my supervisors.

Abstract

The evaluation of the microwave imaging (MWI) prototype and imaging algorithms on experimental bone phantoms is a precursor step before clinical testing for measuring *in vivo* dielectric properties of human bones. To this end, this paper presents microwave tomographic image reconstruction of experimental phantoms of normal and diseased human calcaneus bone using an MWI prototype and distorted Born iterative method (DBIM) algorithm for bone health monitoring application. A two-layered simplified cylindrical-shaped 3-D printed phantom was used to mimic the human calcaneus bone. The external and internal layers of the bone phantom mimic the cortical bone and trabecular bone, respectively. Liquid tissue-mimicking mixtures (TMM) for normal bone, osteoporotic bone, and osteoarthritis bone were prepared and each layer of the phantom was filled with the respective TMM. The phantoms were then placed in the imaging prototype and the electromagnetic inverse scattering problem was solved using the DBIM to create the complex permittivity images. An L_2-based regularization approach was adopted along with the iterative method with adaptive thresholding for compressed sensing (IMATCS) to overcome the ill-posedness and to solve the underdetermined set of linear equations at each DBIM iteration. The average percentage difference between the relative permittivity of reference data and proposed liquid TMMs was found to be less than ±10%. The reconstruction of dielectric properties of bone phantoms have shown that L_2-IMATCS approach provides a robust reconstruction of diverse bone phantoms with acceptable accuracy. Moreover, the osteoporotic and osteoarthritis bone phantoms were distinguished based on reconstructed dielectric properties with an average percentage difference of 26% at 3 GHz. This two-layered 3-D printed human calcaneus bone phantom and the imaging prototype can be used as a valuable test platform for pre-clinical assessment of calcaneus bone imaging for bone health monitoring. This paper has made the first attempt to validate an MWI prototype for bone imaging application. A DBIM-based iterative method has been employed to classify normal and diseased bone phantoms.

Chapter 7. Experimental Validation of Microwave Imaging Prototype and DBIM-IMATCS Algorithm for Bone Health Monitoring

7.1 Introduction

Osteoporosis is an important and significant bone disease resulting from a loss of minerals from the bone tissue and the resulting fragility giving an increased likelihood of fracture [1]. Indeed almost 8.9 million fractures annually are reported due to osteoporosis worldwide [2], with older patients more susceptible - 50% of the women and 20% of the men over the age of 50 years will suffer an osteoporosis-related bone fracture [3]. Current clinical practices widely employ dual-energy X-ray absorptiometry (DXA) for monitoring osteoporosis. But, due to the cumulative effect of repeated X-ray doses over time, the DXA scan poses long-term health risks [4]. Similarly, quantitative computed tomography (QCT) is rarely used in clinical practice due to the high-intensity X-ray doses (greater than 0.86 mrem), expensive equipment, and cost of test [5]. Therefore, there is a need for safer modalities for osteoporosis monitoring. Microwave imaging (MWI) is a potential imaging modality that relies on the inherent dielectric contrast between healthy and diseased tissues of the target anatomical site in the human body [6]. The target anatomical site to monitor osteoporosis is trabecular bone [7]. Recent studies on dielectric measurements of the bones have found a notable dielectric contrast between healthy and diseased human trabecular bones indicating a potential role for MWI in monitoring pathology in this [1], [8]–[10]. MWI has made significant development towards the diagnosis of breast cancer [11]–[16] and brain stroke monitoring [17]–[19]. Various experimental prototypes have been developed for breast imaging and stroke detection, and some of these have been tested in clinical trials [20]. The key clinical advantages of MWI include non-ionizing radiations, portability, and low cost [1].

While MWI has been proposed to monitor osteoporosis based on the dielectric contrast between healthy and diseased human trabecular bones [9], [10], [21], no dedicated MWI system has been developed to measure *in vivo* dielectric properties of human bone in the microwave frequency range. To date, only two studies have measured *in vivo* dielectric properties of the human trabecular bones. Gilmore *et al*. [22] reported *in vivo* dielectric properties of the human forearms including bone by microwave tomography (MWT). The forearms of five healthy volunteers were imaged to evaluate the image reconstruction quality under the varying thickness of the arm's external adipose tissue layer. The authors found that without the use of prior information a thicker adipose tissue layer leads to a poorer image reconstruction

quality. However, the image reconstruction quality has notable improvement when prior information is incorporated as an inhomogeneous background in the inversion algorithm. While the study demonstrated the successful reconstruction of *in vivo* dielectric properties of the bone, the relation between dielectric properties and bone health was not investigated. Meaney *et al.* [9] reported *in vivo* human heel imaging to assess the dielectric properties of calcaneus bone by using MWT. In this study, the human calcaneus of two patients (suffering from a lower leg injury) was imaged using a breast imaging prototype [9]. The study focused on the investigation of the correlation between the MWT images and corresponding bone mineral density (BMD) values. The (negative) correlation between the MWT images and BMD demonstrated by the authors indicates the potential of MWT for monitoring bone health. However, the study only considered two patients and results need to be further validated in a larger sample size. Despite promising initial results in the reconstruction of bone dielectric properties and evidence of the relationship between dielectric properties and bone health, no clinical MWI system has been developed for bone health monitoring. The authors have previously reported an experimental MWI prototype developed solely for calcaneus bone imaging [23], however, the prototype was not experimentally evaluated by imaging bone phantoms.

The focus of this study is to evaluate the imaging of different diseased bone phantoms using the experimental prototype to demonstrate the feasibility of MWI for use in monitoring osteoporosis. The contributions of this study include:

i) Development of different diseased bone phantoms,

ii) MWT reconstruction of the normal and diseased bone phantoms using the distorted Born iterative method (DBIM) approach and to assess its robustness and accuracy to image a simplistic two-layered bone structure,

iii) Distinguishing between osteoporotic and osteoarthritis bones based on the reconstructed dielectric properties.

To this end, three phantoms representing normal, osteoporotic, and osteoarthritis bone were developed. The bone phantoms representing samples from these two sets of patients would incorporate variation in bone dielectric properties that would be representative of variation between healthy and diseased bones. The human calcaneus bone was modelled with an equivalent simplified two-layered three dimensional (3-D) printed cylinder. The calcaneus bone, in general, resembles an irregular shaped

cylinder, therefore a cylindrical structure is a good approximation for initial imaging evaluation. The external layer of the cylindrical phantom constitutes the liquid tissue-mimicking mixture (TMM) for human cortical bone, whereas the inner layer constitutes the liquid TMM for human trabecular bone. Numerous studies have used 3-D printed breast and head models filled with liquid TMMs for MWI prototype testing [17], [19], [24], [25]. Recent advancements in manufacturing technologies have enabled building complex and relatively easily reproducible 3-D printed structures for use in phantom development. One drawback of 3-D printed moulds is the limited choice of fabricating substrates with acrylonitrile butadiene styrene (ABS) being the most commonly used. The ABS is commonly used despite its electrical permittivity and conductivity is far from the dielectric properties of biological tissues [26]. Therefore, the thickness of these 3-D printed structures should be kept as low as possible to minimize the effect it has on the microwave image [26]. This results in a balancing act between rigidity and low field perturbation. In the current study, the authors have tested ABS structures of 1.5 mm thickness and 2 mm thickness. The thickness of 2 mm for ABS structures ensured that the liquid TMMs do not leak to adjacent layers in a multi-layered 3-D printed structure and provides good mechanical stability. While liquid TMMs for cortical bone and normal trabecular bone have been previously reported by Amin *et al.* [27], TMMs for diseased trabecular bones particularly osteoporosis and osteoarthritis have not been previously reported in the literature. Therefore, new TMMs were developed to simulate the osteoporotic and osteoarthritis conditions. These new TMMs were prepared by varying composition of trabecular bone to achieve the dielectric properties of osteoporotic and osteoarthritis trabecular bones, which have been reported by Amin *et al.* [10]. To scan these phantoms using the MWI prototype, a corresponding cylindrical-shaped 3-D printed phantom holder was designed. To acquire the microwave signals through the bone phantom antennas were mounted in the form of a circular array placed at equidistance to each other.

The acquired microwave signals were then used with the DBIM algorithm for the reconstruction of the dielectric profile of each phantom. The DBIM is a well-known linear approximation technique for solving the electromagnetic (EM) inverse scattering problem [28], [29]. Gilmore *et al*. [29] have used DBIM approximation to reconstruct the numerical leg phantom. However, the authors only considered cortical

bone for leg imaging. Previously, Amin *et al.* [21] reported the reconstruction of numerical bone phantoms by employing the DBIM algorithm with an iterative method with adaptive thresholding for compressed sensing (IMATCS). While Amin *et al.* [21] has used the DBIM-IMATCS approach to reconstruct the numerical phantoms, this study has used the DBIM-IMATCS approach for the first time to reconstruct the experimental phantoms. Further, the EM inverse scattering problem is approximated as linear during the reconstruction process, therefore, the IMATCS algorithm may diverge after some iterations. To address this limitation, an L_2-regularization strategy is employed that leads to stable signal recovery [30].

To quantitatively evaluate the reconstructed tomographic images, most of the previous studies have only used normalized root mean square error (NRMSE) as a performance metric [19], [20], [31]–[33]. The NRMSE computes the difference between two images pixel-by-pixel. The difference is summed and normalized over all pixels. Therefore, it becomes difficult to differentiate between pixels that have higher error values compared to pixels that have lower error values. To address this limitation this study has also used the structural similarity index (SSIM) as an additional performance metric. The SSIM compares two images based on spatially near-pixels [14]. The SSIM reflects the similarity between reference and reconstructed images based on the luminance, contrast, and structure of images. To further evaluate the reconstructed images pixel-by-pixel this study has created histograms of reconstructed images. The reconstructed images having a large number of pixels close to reference value are considered better images. The adoption of three-dimensional quantitative analysis helps to thoroughly compare the reference and reconstructed images. The proposed liquid TMMs are characterized over a frequency range of 1.5 – 4.5 GHz. Further, the average percentage difference between the relative permittivity of reference data and proposed liquid TMMs was found to be less than ±10%. However, a slightly more deviation has been observed for the conductivity values. The findings on the evaluation of the MWI prototype and DBIM based MWT imaging algorithm have demonstrated that the bone phantoms can be reconstructed with acceptable accuracy. Moreover, the reconstructed complex permittivity images are good enough to distinguish between healthy and diseased bone phantoms. This two-layered 3-D printed cylindrical bone phantom and imaging prototype can be used as a tool for pre-clinical assessment of calcaneus bone imaging.

7.2 Methodology

7.2.1 Preparation of Calcaneus Bone Phantom and Liquid TMMs

This study used the two-layered hollow cylinder model previously presented by Amin *et al*. [6] to mimic the human calcaneus bone as shown in Figure 7.1. As the anatomy of the calcaneus bone resembles an extended cylinder, a hollow cylinder model is a reasonable approximation. The dimensions of the inner chambers of the calcaneus model were designed to mimic the dimensions of the cortical and trabecular bone layers of the calcaneus bone [34], [35]. The thickness of the cortical bone was kept at approximately 6 mm, whereas, the trabecular bone was modelled with a thickness of 42 mm to ensure the maximum penetration of the EM field. Moreover, motivation for the use of the human calcaneus was due to the similar cortical to the trabecular ratio of that bone to that found in the femoral head and lumbar spine [34],[35] which are considered as primary targets for monitoring osteoporosis. The 3-D cylindrical models were produced using the Autodesk Fusion 3D software package, with these computational models then printed using an Ultimaker 2+ Extended 3-D printer at 200 °C using a polylactic acid (PLA) filament. Next, the outer and inner layers of the hollow cylinder were filled with cortical bone and trabecular bone liquid TMM respectively. To prevent the leakage of liquid TMM material the cylinder wall thickness was set at 2mm.

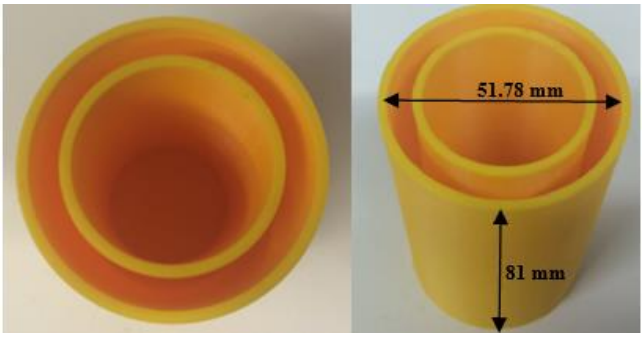

Figure 7.1: 3-D printed cylindrical calcaneus bone structure (a) Top View (b) Side View.

The methodology for the preparation of liquid TMMs has been outlined by Amin *et al*. [6]. The solution of Triton X-100, water, and salt (NaCl) was put in a glass beaker and was thoroughly mixed until the disappearance of air bubbles. While liquid TMMs for normal bone have been previously reported by Amin *et al.* [27], TMMs for diseased bones particularly osteoporosis and osteoarthritis have not been previously reported in the literature. Therefore, this study presents the liquid TMMs for

osteoporotic and osteoarthritis human trabecular bones. The composition of constituents was adjusted until the dielectric properties of TMMs were close to the reference values of osteoporotic and osteoarthritis bones reported by Amin *et al*. [10]. The recipe for cortical bone and trabecular bone TMM was obtained from Amin *et al*. [27]. The composition of TMMs that mimic the dielectric properties of each target tissue is given in Table 7.1.

Table 7.1: Composition of liquid TMMs.

Target Tissue	**TX-100 (vol %)**	**DI water (vol %)**	**NaCl (g/L)**
Cortical Bone [27]	77	23	0.8
Normal Trabecular Bone [27]	69.5	30.5	0.8
Osteoporotic Trabecular Bone	72.70	27.30	0.8
Osteoarthritis Trabecular Bone	65	35	0.8

TX = Triton X, DI = Deionized water. The quantity of NaCl is expressed in terms of grams/litre (g/L).

This study considers a total of three bone phantoms. The outer layer in all phantoms contains liquid TMM of the cortical bone. The inner layer that mimics the trabecular bone was varied to account for the natural pathological changes seen in the clinical conditions (osteoporosis and osteoarthritis) compared to the normal trabecular bone as reported by Amin *et al*. [10]. The sequence of bone tissues for outer and inner layers with their corresponding labels are tabulated in Table 7.2.

Table 7.2: Experimental bone phantoms.

Phantom Label	**Outer Layer TMM**	**Inner Layer TMM**
P1	Cortical Bone	Normal Trabecular Bone
P2	Cortical Bone	Osteoporotic Trabecular Bone
P3	Cortical Bone	Osteoarthritis Trabecular Bone

As, these antennas have been previously used for breast imaging studies [12], [14], [36], and authors have reported that the optimal reconstruction was found at 3 GHz. Therefore, the reconstruction of dielectric properties of all experimental bone phantoms was performed at 3 GHz , the other frequency points were not considered

for the reconstruction of dielectric properties. To this end, the proposed TMMs were prepared for 3 GHz frequency. The relative permittivity and conductivity of the proposed TMMs at 3 GHz are tabulated in Table 7.3.

Table 7.3: The relative permittivity and conductivity for liquid TMMs at 3 GHz.

Target Tissue	ε_r	$\sigma(S/m)$
Cortical Bone	9.93	0.78
Normal Trabecular Bone	17.60	1.02
Osteoporotic Trabecular Bone	16.59	1.24
Osteoarthritis Trabecular Bone	25.19	1.50

7.2.2 Dielectric Properties Measurement

The Dielectric characterization of the liquid TMMs was performed using an open-ended coaxial probe (OECL) over the frequency range of 1.5 – 4.5 GHz. A Keysight slim form probe 85070E was connected directly to the Keysight E5063A vector network analyzer (VNA) [37]. The measurement equipment was first calibrated using a standard three-load one-port calibration (air, short, and deionized water). To verify the calibration, the dielectric properties of the 0.1 M NaCl solution (saline) were measured at 22 ^{o}C, with the saline acting as a reference material [38]. The uncertainty of the accuracy of the equipment is reported in Table 7.4 and is defined as:

$$ACC_{UC}(f) = \left(\frac{y_{meas}(f) - y_{ref}(f)}{y_{ref}(f)}\right) \times 100 \qquad (7.1)$$

where y_{meas} and y_{ref} represents the measured and reference dielectric properties of 0.1 M NaCl respectively [38], and *f* represents frequency. Table 7.4 also reports the uncertainty in repeatability of measurements, with this defined as:

$$REP_{UC}(f) = \left(\frac{y_{meas}(f) - y_{mean}(f)}{y_{mean}(f)}\right) \times 100 \qquad (7.2)$$

where y_{mean} represents the mean of the measured dielectric properties. The y_{mean} is calculated by taking the mean of 6 measurements. Finally, the total combined uncertainty which is the sum of ACC_{UC} and REP_{UC} is also reported in Table 7.4.

Table 7.4: Percent uncertainty in accuracy and repeatability of measurements.

Parameter	$\boldsymbol{\varepsilon_r}$ **(%)**	$\boldsymbol{\sigma}$ $\boldsymbol{(S/m)}$ **(%)**
$\boldsymbol{ACC_{UC}}$	0.12	3.56
$\boldsymbol{REP_{UC}}$	0.04	0.01
Combined	0.16	3.57

7.2.3 Microwave Scanning of the Phantoms

The imaging prototype was designed by modifying the cylindrical model. The height of the imaging tank was 82 mm, whereas the overall width was 54 mm. A total of six holes were fabricated in a plane in a radial pattern to house the flexible microstrip antennas [14]. These antennas have been previously used in a 16-element antenna array with patients for breast imaging applications [12], [14], [36]. In earlier breast imaging studies, these antennas were designed to contact the breast phantom directly [12], [14], [36], therefore, in this study the phantoms were in direct firm contact with the antennas, therefore, no matching medium was used. The microwave signals from the antenna array were measured by a 2-port ZNB40 VNA and ZN-Z84 24-port switching matrix (Rohde and Schartz GmbH, Munich, Germany). Hence, the imaging prototype was composed of these 6 flexible microstrip antennas placed equidistant to each other. An overview of the experimental setup is shown in Figure 7.2. The signals were collected in the frequency range of 1.5 – 4.5 GHz as this is the optimal frequency range for the operation of the antennas with this system [14]. As the imaging prototype is composed of six antennas, a total of fifteen measurements (*N(N-1)/2*, where *N* denotes the number of antennas) were recorded that included the unique measurements from each transmit-receive antenna pair. The redundant data from reciprocal channels and monostatic channels was not recorded. The input power of the VNA was set to 0 dBm.

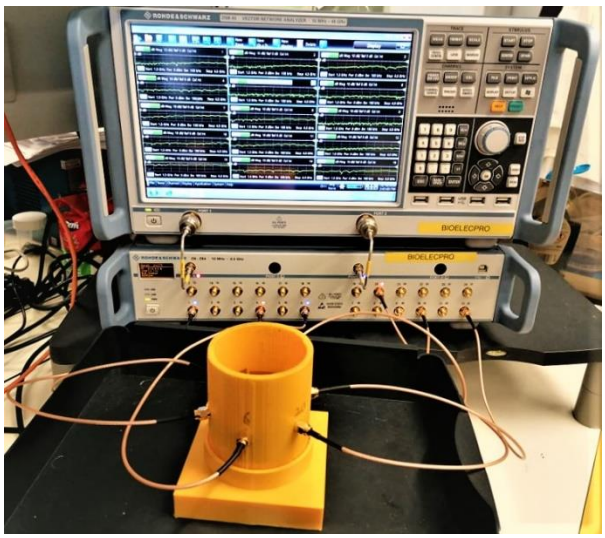

Figure 7.2: Realization of a 3-D MWI system prototype. A VNA is connected to a switching matrix. The switching matrix is connected to the cylindrical imaging prototype through cables.

7.2.4 Image Reconstruction using DBIM Formulation and IMATCS Algorithm

The EM inverse scattering problem is ill-posed and non-linear as the number of measurements is less than the number of unknowns [39]. The dielectric properties of the target region from the measured EM scattered fields are computed by an EM simulation using an inversion of a linear approximation of the EM field [39]. More precisely, this study used the DBIM approximation proposed by Chew and Wang [40]. During each DBIM iteration, the EM scattering wave equation is linearized by replacing the total field with a known incident field which is estimated in the presence of known background [41]. The integral equation of EM field at measurement point r and frequency ω can be expressed as:

$$\Delta E_s(r,\omega) = E_t(r,\omega) - E_i(r,\omega) \tag{7.3}$$

$$= \omega^2 \mu \int_V G_b(r,r',\omega)\, \delta(r',\omega) E_t(r',\omega)\, dr', \tag{7.4}$$

where ΔE_s is the scattered field due to the unknown contrast function $\delta(r,\omega)$ in volume V, E_t is the unknown total field, E_b is the background field, G_b is the dyadic Green's function which denotes propagation from the source located at $r \in V$ to r_R, r_T and r_R representing the transmitter and receiver locations, and ω represents the angular frequency.

To find the *inverse solution*, this study has employed the IMATCS method [30]. The IMATCS method employs an adaptive threshold approach. The initial threshold value is exponentially decreased at each iteration of the IMATCS algorithm. The

measurements in equation 7.4 are not linear which leads to instability and divergence of IMATCS iterations. To overcome this problem, an L_2-regularized approach is adopted [30]. The L_2-IMATCS method can be expressed as:

$$x_{j+1} = \frac{1}{1+\beta_2} A_0 e^{-\alpha i}\left(x_k + \beta_1 M^* (y - M x_k)\right) \quad (7.5)$$

where A_0 is the initial threshold, M^* is the conjugate transpose of measurement matrix, β is the relaxation parameter and controls the convergence, x_k is the unknown vector, α denotes the threshold step size, and i is the iteration number. The initial value of x_k in equation 7.5 starts with zero. The x_k is recovered after the specified number of IMATCS iterations. where β_1 and β_2 controls the convergence of the algorithm. The L_2-IMATCS approach provides a stable and better recovery of x_j from linear measurements given in equation 7.4.

7.2.5 FDTD Modelling and Calibration of Measured Data

The measured data was collected from the imaging prototype composed of 6 flexible microstrip antennas. The scattered EM signals from the bone phantoms were recorded. To perform the numerical simulation a similar imaging model was developed as used in the experimental setup. However, the antennas used in the numerical setup are not realistic. A total of six ideal dipole antennas were placed in a circular array. For the two-dimensional (2-D) geometry, the dipole antennas correspond to point sources. The finite difference time domain (FDTD) method was used to perform the numerical simulations. The initial guess for the DBIM inversion assumes that the actual shape is filled with the homogenous background medium $\varepsilon_\infty = 2.848,\ \Delta\varepsilon = 1.104, \sigma_s = 0.005\ S/m$ [30]. To simplify the FDTD simulation, the relaxation time constant was considered spatially invariant with a constant value of 0.5 ps. Further, no a-priori information regarding the shape of the target was used for the inversion procedure. The evaluated bone phantoms, simulations, and reconstructions are performed for 2-D imaging scenarios. The L_2-IMATCS approach reconstructs the single-pole Debye parameters which were then converted into a complex permittivity profile of bone. The solution of the inverse problem relies on the comparison between the measured experimental data and the simulated scattered EM field data [42],[43]. The FDTD 2-D numerical model is not perfect in comparison to the experimental model due to the use of non-realistic antennas during the inversion procedure. Due to the use of non-realistic antennas in the numerical model, the reconstruction process is prone to propagation and scattering errors. Further, it is often challenging to incorporate a

realistic antenna in the numerical model which requires specialized antenna modelling software and increases computations. However, calibration is a straight forward and robust method to mitigate such errors [32]. Therefore, before the inversion of EM scattered field data, a calibration of the measured data was performed as follows:

$$E_{cal}^{m}(f) = \left(\frac{S_{scat}^{m}(f)}{S_{ref}^{m}(f)}\right) E_{ref}^{s}(f) \qquad (7.6)$$

where $S_{scat}^{m}(f)$ represents the measured transmission coefficients in the presence of the test object, $S_{ref}^{m}(f)$ represents the measured transmission coefficients in the absence of test object, and $E_{ref}^{s}(f)$ is the corresponding simulated reference signal. During the reconstruction process $E_{cal}^{m}(f)$ is used for comparing with the scattered field data from FDTD simulations [42],[43].

7.2.6 Evaluation of Reconstructed Images

To quantitatively evaluate the reconstructed images of bone phantoms this study has considered NRMSE, SSIM, and histogram-based analysis. The histogram-based analysis is the novel analysis proposed in this study to address the limitations of NRMSE and SSIM as described in Section 7.1.

7.2.6.1 Normalized Root Mean Square Error

The NRMSE computes the error between the complex permittivity of reference bone phantom and reconstructed bone phantom. The NRMSE is the standard metric used to evaluate the reconstructed phantoms as reported in the literature [17], [19], [32], [44]. The NRMSE is defined as:

$$\text{NRMSE} = \frac{\|\varepsilon_r(f) - \hat{\varepsilon}_r(f)\|_{L^2}^2}{\|\varepsilon_r(f)\|_{L^2}^2} \qquad (7.7)$$

where $\varepsilon_r(f)$ is the complex permittivity profile of reference bone dielectric properties and $\hat{\varepsilon}_r(f)$ is the complex permittivity profile of reconstructed bone dielectric properties. The NRMSE values range between 0 and 1, a value of 0 indicates no error, however, a value of 1, indicates maximum error between two images under comparison. The NRMSE is separately calculated for both the real (ε') and imaginary (ε'') parts of complex permittivity profile for all bone phantoms.

7.2.6.2 Structural Similarity Index

The SSIM is computed between the reconstructed and reference bone dielectric properties [14]. The SSIM compares two images at a time and considers the luminance, contrast, and structure to produce a similarity value between the two

images. The SSIM values range between 0 and 1, a value of 0 indicates no structural similarity, however, a value of 1, indicates the maximum similarity between two images under comparison. The SSIM is separately calculated for both the real and imaginary parts of the complex permittivity profile for all bone phantoms.

7.2.6.3 Histogram-based Analysis

While NRMSE and SSIM provide a good estimate of the quality of reconstruction, these metrics do not provide insight into pixel-wise error between the reference and reconstructed image. Therefore, to compare the distribution of reconstructed pixels of bone phantoms with corresponding pixels of reference bone phantoms this study has proposed a novel histogram-based analysis as an additional performance parameter. The histogram of reconstructed pixels was created. The reconstructed images having histogram distribution with a large number of pixels close to corresponding reference value are considered better images. The histogram analysis provided an additional tool to evaluate the accuracy of reconstructed images.

7.3 Results and Discussion

This section presents the dielectric properties of liquid TMMs developed to mimic different types of bones. Moreover, the results obtained by L_2-IMATCS approach for bone dielectric properties reconstruction using dielectrically informed experimental bone phantoms are also presented in this section.

7.2.1 Dielectric Properties of Liquid TMMs

The liquid TMMs were made to mimic the dielectric properties of cortical bone, trabecular bone, osteoporotic bone, and osteoarthritis bone. While the recipe for cortical bone and trabecular bone was obtained from Amin *et al*. [27], the recipe for osteoporotic and osteoarthritis was developed in this study as described in Section 7.2. The dielectric properties of all TMMs were analyzed. The composition of TMMs that mimic the dielectric properties of each target tissue is given in Table 7.1.

The measured dielectric properties of liquid TMMs (solid lines) and the reference dielectric data (dashed lines) are shown in Figure 7.3. Each solid curve in Figure 7.3 indicates the mean value of six measurements taken between 1.5 – 4.5 GHz. The measurements were obtained at multiple sites in the liquid. The reference dielectric data for normal human cortical bone and trabecular bone was taken from Gabriel *et al*. [45]. The reference dielectric data for human osteoporotic bone and human osteoarthritis bone was taken from Amin *et al*. [10]. It can be observed from Figure

7.3 (a) and (b), that the mean dielectric properties of all TMMs are well aligned with the reference dielectric properties of modelled tissues and maintain a significant dielectric contrast to each other.

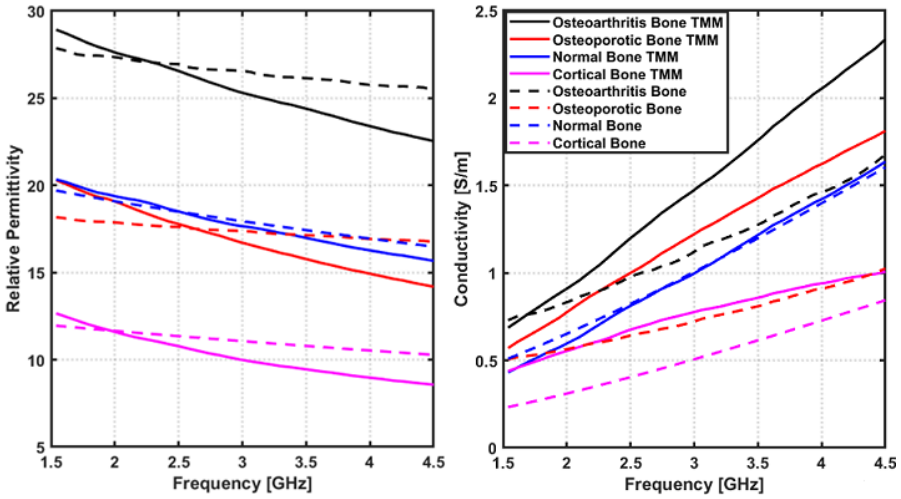

(a) (b)

Figure 7.3: Dielectric properties of liquid TMMs over 1.5 – 4.5 GHz frequency band: (a) Relative Permittivity (b) Conductivity. The measured dielectric data of TMMs (solid lines) are compared with reference data (dotted lines) from Gabriel *et al*. [45] and Amin *et al*. [10].

The average percentage difference between the relative permittivity of TMM and its respective tissue is found to be less than ± 10%, which is within the expected variance in biological tissue [6]. The relative permittivity of liquid TMMs shows very good agreement with the reference data compared to the conductivity values. However, there is a relatively large deviation between the conductivity of liquid TMMs and reference data specifically for osteoporotic bone and osteoarthritis bone TMMs. This large deviation is mainly observed due to the presence of a high amount of water in these TMMs and the variations observed (both in relative permittivity and conductivity) agree with the literature reporting TMMs for human biological tissues [19], [24], [46], [47]. The proposed TMMs maintain a realistic contrast between the conductivities of target bone tissues. Moreover, MWT relies on the contrast in relative permittivity, therefore, the variations observed in conductivity values are not critical to this specific investigation.

7.2.2 Reconstruction of Experimental Bone Phantoms P1, P2, and P3

The two-layered 3-D printed calcaneus structure was placed in the imaging prototype shown in Figure 7.2. The scattered EM signals from all 6 flexible microstrip antennas were measured. These EM signals were used to reconstruct the complex permittivity

profile at 3 GHz. The FDTD simulation was used as a forward solver for the inversion process with a uniform grid cell size of 1 mm. The choice of the number of IMATCS iterations, DBIM iterations, and threshold A_0 was based on the parametric analysis. The minimum value of NRMSE was obtained for five IMATCS iterations. Regarding the DBIM iterations, the minimum value of NRMSE was observed for the first DBIM iteration. Therefore, the reconstruction of all bone phantoms in this study was obtained for the first DBIM iteration. The value of the threshold was kept in the range of 2 – 3 for the reconstruction of all considered bone phantoms. For bone phantoms P1, P2, and P3, the external layer of the 3-D printed calcaneus structure was composed of liquid TMM for human cortical bone. The numerical equivalent models representing reference real and imaginary parts of the complex permittivity were developed as shown in Figures 7.4 (a) and (b), 7.5 (a) and (b), and 7.6 (a) and (b) for the bone phantoms P1, P2, and P3 respectively. The outer layer in all numerical equivalent models mimics the cortical bone, whereas the inner yellow layer mimics the human trabecular bone for P1, human osteoporotic bone for P2, and human osteoarthritis bone for P3.

For the bone phantom P1, the internal layer of the 3-D printed calcaneus structure was filled with the liquid TMM of human trabecular bone. The dielectric contrast between cortical bone and trabecular bone is low [44], due to which reconstructing the dielectric profile of a two-layered bone structure by employing MWT is challenging. To this end, a DBIM based MWT imaging algorithm along with L_2-IMATCS approach was chosen to reconstruct the complex permittivity profiles of bone phantoms. The DBIM algorithm is known to be effective for reconstructing low contrast imaging scenarios, therefore, one of the objectives of this study was to assess the robustness and accuracy of the DBIM approach to image a two-layered bone structure. The reconstructed real and imaginary parts of complex permittivity of bone phantom P1 are shown in Figure 7.4 (c) and (d) respectively. Comparing the reference and reconstructed real and imaginary parts of the complex permittivity profiles, it can be observed that the reconstructed profiles have a relatively low error at the region of interest (central trabecular bone region which significantly deteriorates during osteoporosis) in the reconstructed image. While the shape is not perfectly preserved in reconstruction, it is evident from the reconstructed images that both layers have been reconstructed. The artefacts are prominent at the boundary of the imaging domain as

expected. These artefacts can be attributed to EM field perturbation at the boundaries of two mediums with different dielectric properties.

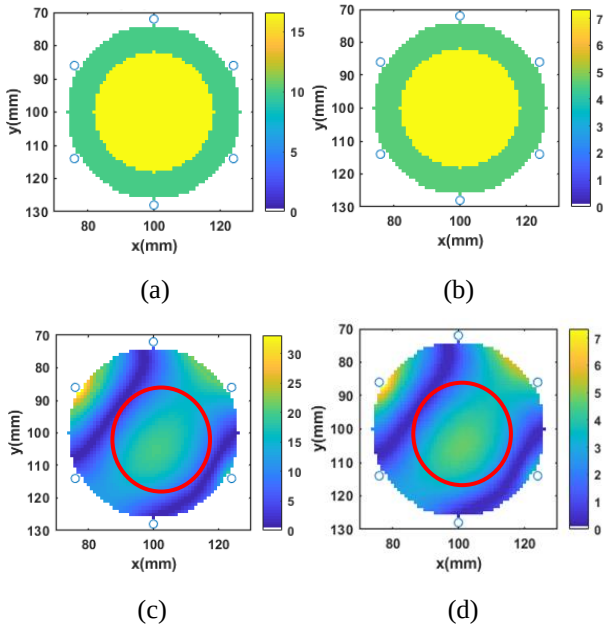

Figure 7.4: Real and imaginary parts of complex permittivity of (a) and (b) reference bone phantom P1, (c) and (d) reconstructed bone phantom P1 at 3 GHz.

For the bone phantom P2, the internal layer of the 3-D printed calcaneus structure was filled with the liquid TMM of human osteoporotic bone. The reference dielectric data for human osteoporotic bone was obtained from Amin *et al.* [10]. The reconstructed real and imaginary parts of complex permittivity of bone phantom P2 are shown in Figure 7.5 (c) and (d) respectively. Comparing the reference and reconstructed real and imaginary parts of the complex permittivity of bone phantom P2, it can be observed that good reconstructions of bone dielectric properties are achieved by using DBIM based MWT imaging algorithm along with L_2-IMATCS approach.

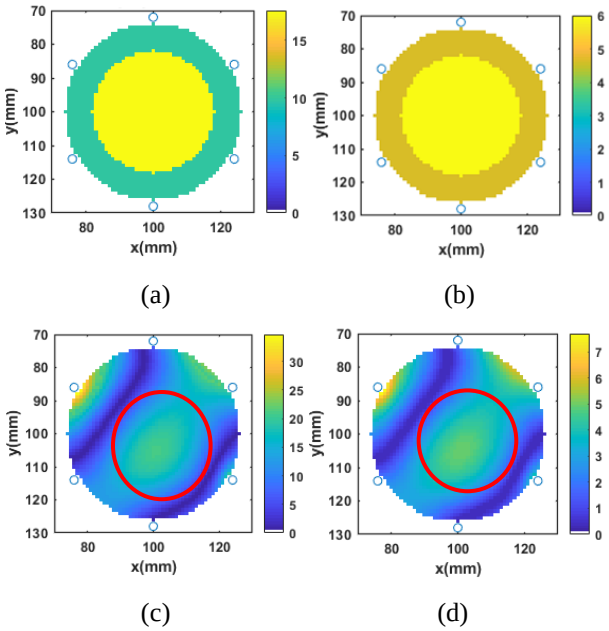

Figure 7.5: Real and imaginary parts of complex permittivity of (a) and (b) reference bone phantom P2, (c) and (d) reconstructed bone phantom P2 at 3 GHz.

For the bone phantom P3, the internal layer of the 3-D printed calcaneus structure was filled with the liquid TMM of human osteoarthritis bone's TMM. The reference dielectric data for human osteoarthritis bone was obtained from Amin *et al*. [10]. The dielectric properties of osteoarthritis bones are higher as compared to osteoporotic bones. The contrast between dielectric properties of outer and inner layers of bone phantom P3 is higher compared to the bone phantoms P1 and P2. The reconstructed real and imaginary parts of the complex permittivity of bone phantom P3 are shown in Figure 7.6 (c) and (d) respectively. Comparing the reference and reconstructed real and imaginary parts of the complex permittivity parts of bone phantom P3, it can be observed that a good reconstruction of experimental bone phantoms can be achieved by using DBIM and L_2-IMATCS approach, even for higher contrast two-layered bone phantom.

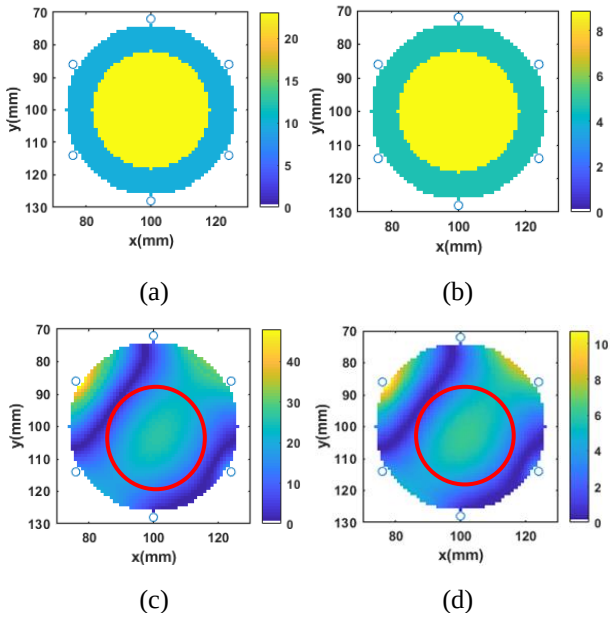

Figure 7.6: Real and imaginary parts of complex permittivity of (a) and (b) reference bone phantom P3, (c) and (d) reconstructed bone phantom P3 at 3 GHz.

7.2.3 Quantitative Evaluation of Reconstructed Profiles

To quantitatively evaluate the reconstructed bone phantoms P1, P2, and P3 this study has used NRMSE, SSIM, and histogram-based analysis. The results of NRMSE for real and imaginary parts of complex permittivity for all reconstructed bone phantoms are tabulated in Table 7.5. The lower error values of NRMSE for all reconstructed bone phantoms indicate the robustness of the L_2-IMATCS approach for the reconstruction of experimental data.

The results of SSIM between real and imaginary parts of reference and reconstructed complex permittivity profiles are tabulated in Table 7.5. Based on SSIM values in Table 7.5, it can be observed that the reference and reconstructed bone dielectric properties have high similarity in terms of real and imaginary parts of complex permittivity for each considered bone phantom. The values of NRMSE and SSIM for the real and imaginary parts of the complex permittivity as tabulated in Table 7.5 suggests that good reconstructions of bone dielectric properties can be achieved by using L_2-IMATCS approach.

Table 7.5: NRMSE and SSIM between original and reconstructed bone phantoms.

Phantom	NRMSE		SSIM	
	ε'	ε''	ε'	ε''
Normal Bone Phantom (P1)	0.456	0.637	0.963	0.920
Osteoporotic Bone Phantom (P2)	0.453	0.674	0.964	0.922
Osteoarthritis Bone Phantom (P3)	0.488	0.622	0.960	0.916

The NRMSE and SSIM do not evaluate the reconstructed images pixel-by-pixel which has paramount significance to evaluate the images in-depth. Therefore, to address this limitation this study has proposed a novel histogram-based analysis. The histogram-based analysis computes the difference between all the corresponding reference and reconstructed pixels. The reconstructed image is classified as a better image if the majority of the pixels are centred at 0. Figure 7.7 (a), (b), and (c) represents the relative error distribution for the relative permittivity of bone phantoms P1, P2, and P3 respectively. The x-axis in the bar plot represents the difference between the relative permittivity of the reference and reconstructed relative permittivity and the y-axis represents the percentage of reconstructed pixels. It can be observed from Figure 7.7 (a), (b), and (c) that the majority of the reconstructed pixels have a low relative error. For bone phantoms, P1, P2, and P3 about 19.28%, 22%, and 17.44% of the reconstructed pixels respectively have relative error values close to 0. Furthermore, it can be observed from Figure 7.7 (a), (b), and (c) that few of the reconstructed pixels have non-zero error value due to non-uniform reconstruction of the imaging domain. This is because the MWI problem is inherently ill-posed and non-linear [39], therefore multiple solutions of the reconstruction domain exist. The reconstruction showed slightly large error values at the edges of the bone phantom and the interface between cortical bone and trabecular bone as can be seen in Figures 7.4, 7.5, and 7.6. The lower error values suggest that the reconstructed real part of the complex permittivity of bone phantoms P1, P2, and P3 can be achieved by using DBIM along with L_2-IMATCS approach.

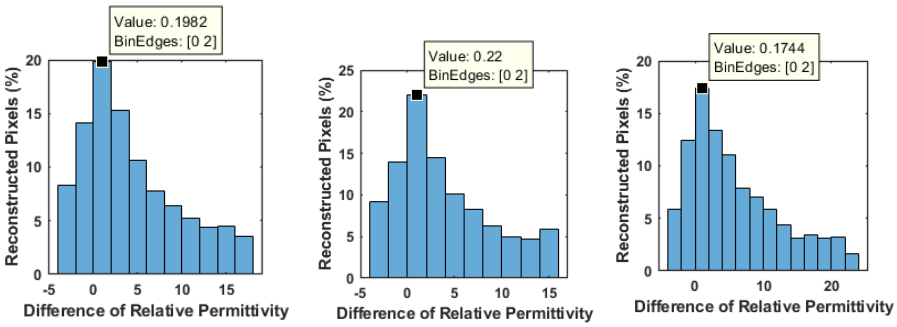

(a) (b) (c)

Figure 7.7: Distribution of reconstructed real part of complex permittivity of (a) bone phantom P1 (b) bone phantom P2 (c) bone phantom P3 at 3 GHz.

7.2.4 Classification of Normal and Diseased Bones Based on Reconstructed Complex Permittivity Profiles

An analysis has been performed to compare the peak values of the complex permittivity of reconstructed bone phantoms with the corresponding reference values. Figure 7.8 (a) and (b) represents the comparison of the peak values of real and imaginary parts of the complex permittivity of bone phantoms P1, P2, and P3 respectively. The blue bars represent the peak value of the complex permittivity of the reference bone phantom, whereas, the brown bars represent the peak value of the reconstructed complex permittivity for each bone phantom. It can be observed from Figure 7.8 (a) and (b) that the differentiation between the different diseased bones is possible using the real part of the reconstructed complex permittivity of bone phantoms. Hence, the adopted approach for the differentiation of osteoporotic and osteoarthritis bone phantoms can be employed for bone health monitoring.

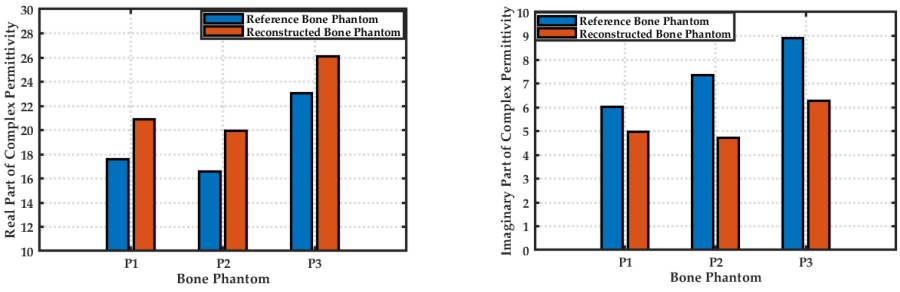

(a) (b)

Figure 7.8: (a) Peak values of the real part of complex permittivity of reconstructed and reference bone phantoms (b) Peak values of the imaginary part of complex permittivity of reconstructed and reference bone phantoms at 3 GHz.

To avoid the possibility during the classification of normal and diseased bones that the detected peak value could be an artefact, this study has performed a histogram-based analysis to analyze the distribution of relative permittivity values of reconstructed pixels. Figure 7.9 (a), (b), and (c) represents the distribution of reconstructed relative permittivity for bone phantoms P1, P2, and P3 respectively. The x-axis in the bar plot represents the relative permittivity distribution and the y-axis represents the percentage of the reconstructed pixels. It can be observed from Figure 7.9 (a), (b), and (c) that the relative permittivity of the majority of the reconstructed pixels for each bone phantom is close to their corresponding reference values which ensures that the peak value used to classify normal and diseased bones is not an artefact. For bone phantom P1, P2, and P3 about 19.33%, 21.51%, and 16.45% of the reconstructed pixels respectively have values close to their respective reference values. The distribution of relative permittivity of each bone phantom compared to the reference profile ensures the robustness of L_2-IMATCS approach for the reconstruction of diverse bone phantoms. Hence, the adopted approach for the differentiation of osteoporotic and osteoarthritis bone phantoms can be employed for bone health monitoring.

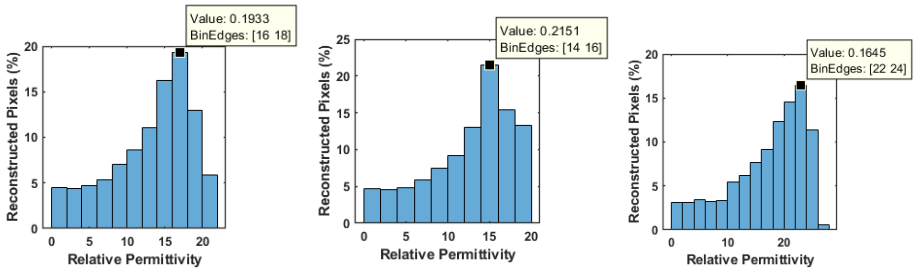

(a) (b) (c)

Figure 7.9: Distribution of reconstructed real part of complex permittivity of the central trabecular bone region (a) bone phantom P1 (b) bone phantom P2 (c) bone phantom P3 at 3 GHz.

7.4 Conclusion

The evaluation of the MWI prototype and imaging algorithms on experimental bone phantoms is a precursor step before clinical testing for measuring *in vivo* dielectric properties of human bones. Moreover, it helps to evaluate the robustness of the adopted approach for the reconstruction of dielectric properties under realistic imaging scenarios. This study has presented the experimental evaluation of the MWI prototype designed to image a simplified calcaneus bone phantom. The shape of the human

calcaneus bone was approximated with a simplified cylindrical model. A two-layered 3-D printed simplified cylindrical calcaneus bone phantom was presented along with its corresponding MWI prototype. The external and internal layers of the cylindrical phantom were filled with liquid TMMs that mimic the dielectric properties of cortical bone and trabecular bone respectively. A total of three bone phantoms with dielectric properties of different diseased human trabecular bones were developed. The TMMs were composed of Triton X-100, water, and salt. The calcaneus bone phantom was placed in the MWI prototype and EM scattered waves were recorded at each antenna. To reconstruct the dielectric properties a DBIM based MWT approach is adopted in conjunction with L_2-IMATCS approach.

The results of reconstructed bone dielectric properties have shown that the adopted approach for linear inversion provides good reconstruction in comparison to the reference bone dielectric properties. The results have shown that the osteoporotic and osteoarthritis bones can be distinguished based on the reconstructed complex permittivity profiles. The results have shown that the osteoporotic and osteoarthritis bones can be distinguished based on the reconstructed complex permittivity profiles. However, the reconstructed MWT images are visually poor and the shape of the two-layered bone structure (cortical-trabecular) has not been preserved completely. The dielectric contrast between the cortical bone and trabecular bone is low, which poses a challenging task during the reconstruction of the low contrast two-layered imaging scenario, this is one of the limitations of MWT reconstruction. Further, the microwave imaging problem is inherently ill-posed and non-linear, therefore multiple solutions of the reconstruction domain exist that makes the reconstructed image visually poor. Moreover, the main difference between our 2-D in-house FDTD model and the experimental prototype is related to the use of realistic antennas which are not properly taken into account in the inversion procedure, introducing propagation and scattering errors. While the considered imaging scenario of a two-layered cylindrical shaped bone phantom is rather anatomically simplistic, the study demonstrates the feasibility of reconstruction of bone dielectric properties using the proposed imaging method and the MWI prototype. Future work will focus on the estimation of dielectric properties of anatomically realistic bone phantoms by employing MWT to ultimately progress towards the measurement of *in vivo* dielectric properties of bone.

Acknowledgements: This work was supported by the European Research Council under the European Union's Horizon 2020 Programme/ERC Grant Agreement BioElecPro n. 637780.

Conflict of Interest: The authors declare that there is no conflict of interest regarding the publication of this article.

References

[1] B. Amin, M. A. Elahi, A. Shahzad, E. Porter, B. McDermott, and M. O'Halloran, "Dielectric properties of bones for the monitoring of osteoporosis," *Med. Biol. Eng. Comput.*, Aug. 2018.

[2] O. Johnell and J. A. Kanis, "An estimate of the worldwide prevalence and disability associated with osteoporotic fractures," *Osteoporos. Int.*, vol. 17, no. 12, pp. 1726–1733, 2006.

[3] S. N. Makarov, G. M. Noetscher, S. Arum, R. Rabiner, and A. Nazarian, "Concept of a Radiofrequency Device for Osteopenia / Osteoporosis Screening," pp. 1–15, 2020.

[4] A. H. Golnabi, P. M. Meaney, S. Geimer, T. Zhou, and K. D. Paulsen, "Microwave tomography for bone imaging," *Proc. - Int. Symp. Biomed. Imaging*, vol. 9, pp. 956–959, 2011.

[5] E.-M. Lochmüller, R. Müller, V. Kuhn, C. A. Lill, and F. Eckstein, "Can Novel Clinical Densitometric Techniques Replace or Improve DXA in Predicting Bone Strength in Osteoporosis at the Hip and Other Skeletal Sites?," *J. Bone Miner. Res.*, vol. 18, no. 5, pp. 906–912, 2003.

[6] B. Amin, A. Shahzad, D. Kelly, M. Ohalloran, and A. Elahi, "Anthropomorphic Calcaneus Phantom for Microwave Bone Imaging Applications," *IEEE J. Electromagn. RF Microwaves Med. Biol.*, no. c, pp. 1–9, 2020.

[7] B. Amin *et al.*, "A feasibility study on microwave imaging of bone for osteoporosis monitoring," *Med. Biol. Eng. Comput.*, 2021.

[8] P. M. Meaney, T. Zhou, D. Goodwin, A. Golnabi, E. A. Attardo, and K. D. Paulsen, "Bone dielectric property variation as a function of mineralization at microwave frequencies," *J. Biomed. Imaging*, vol. 2012, p. 7, 2012.

[9] P. M. Meaney *et al.*, "Clinical microwave tomographic imaging of the calcaneus: A first-in-human case study of two subjects," *IEEE Trans. Biomed. Eng.*, vol. 59, no. 12, pp. 3304–3313, 2012.

[10] B. Amin *et al.*, "Dielectric characterization of diseased human trabecular bones at microwave frequency," *Med. Eng. Phys.*, vol. 78, 2020.

[11] D. O'Loughlin, M. O'Halloran, B. M. Moloney, M. Glavin, E. Jones, and M. A. Elahi, "Microwave breast imaging: Clinical advances and remaining challenges," *IEEE Trans. Biomed. Eng.*, vol. 65, no. 11, pp. 2580–2590, 2018.

[12] D. O. Loughlin *et al.*, "Sensitivity and Specificity Estimation Using Patient-Specific Microwave Imaging in Diverse Experimental Breast Phantoms," vol. 38, no. 1, pp. 303–311, 2019.

[13] M. A. Elahi *et al.*, "Evaluation of image reconstruction algorithms for confocal microwave imaging: Application to patient data," *Sensors (Switzerland)*, vol. 18, no. 6, 2018.

[14] E. Porter, M. Coates, and M. Popović, "An Early Clinical Study of Time-Domain Microwave Radar for Breast Health Monitoring," *IEEE Trans. Biomed. Eng.*, vol. 63, no. 3, pp. 530–539, 2016.

[15] R. C. Conceição *et al.*, "Classification of breast tumor models with a prototype microwave imaging system," *Med. Phys.*, vol. 47, no. 4, pp. 1860–1870, 2020.

[16] A. H. Golnabi, P. M. Meaney, and K. D. Paulsen, "3D microwave tomography of the breast using prior anatomical information," *Med. Phys.*, vol. 43, no. 4, pp. 1933–1944, 2016.

[17] J. A. T. Vasquez *et al.*, "A prototype microwave system for 3d brain stroke imaging," *Sensors (Switzerland)*, vol. 20, no. 9, pp. 1–16, 2020.

[18] S. Ahsan, Z. Guo, Z. Miao, and I. Sotiriou, "Multiple-Frequency Microwave Tomography System," 2018.

[19] O. Karadima *et al.*, "Experimental validation of microwave tomography with the DBIM-twist algorithm for brain stroke detection and classification," *Sensors (Switzerland)*, vol. 20, no. 3, 2020.

[20] S. Ahsan *et al.*, "Design and experimental validation of a multiple-frequency microwave tomography system employing the DBIM-TwIST algorithm," *Sensors (Switzerland)*, vol. 18, no. 10, 2018.

[21] B. Amin, A. Shahzad, M. O'halloran, and M. A. Elahi, "Microwave bone imaging: A preliminary investigation on numerical bone phantoms for bone health monitoring," *Sensors (Switzerland)*, vol. 20, no. 21, pp. 1–21, 2020.

[22] C. Gilmore, A. Zakaria, S. Pistorius, and J. Lovetri, "Microwave imaging of

human forearms: Pilot study and image enhancement," *Int. J. Biomed. Imaging*, vol. 2013, 2013.

[23] B. Amin, C. Sheridan, D. Kelly, A. Shahzad, M. O'Halloran, and M. A. Elahi, "Microwave bone imaging: experimental evaluation of calcaneus bone phantom and imaging prototype," in *2020 IEEE MTT-S International Microwave Biomedical Conference (IMBioC)*, 2020, pp. 1–3.

[24] N. Joachimowicz, B. Duchêne, C. Conessa, and O. Meyer, "Anthropomorphic Breast and Head Phantoms for Microwave Imaging," *Diagnostics*, vol. 8, no. 4, p. 85, 2018.

[25] J. Bourqui, J. M. Sill, and E. C. Fear, "A prototype system for measuring microwave frequency reflections from the breast," *Int. J. Biomed. Imaging*, vol. 2012, 2012.

[26] T. Rydholm, A. Fhager, M. Persson, S. Geimer, and P. Meaney, "Effects of the Plastic of the Realistic GeePS-L2S-Breast Phantom," *Diagnostics*, vol. 8, no. 3, p. 61, 2018.

[27] B. Amin, D. Kelly, A. Shahzad, M. O'Halloran, and M. A. Elahi, "Microwave calcaneus phantom for bone imaging applications," in *2020 14th European Conference on Antennas and Propagation (EuCAP)*, 2020, pp. 1–5.

[28] L. M. Neira, B. D. Van Veen, and S. C. Hagness, "High-resolution microwave breast imaging using a 3-D inverse scattering algorithm with a variable-strength spatial prior constraint," *IEEE Trans. Antennas Propag.*, vol. 65, no. 11, pp. 6002–6014, 2017.

[29] C. Gilmore, S. Member, P. Mojabi, J. Lovetri, and S. Member, "Comparison of an Enhanced Distorted Born Iterative Method and the Multiplicative-Regularized Contrast Source Inversion method," no. September 2009, 2014.

[30] P. Kosmas and F. Marvasti, "Microwave Medical Imaging Based on Sparsity and an Iterative Method with Adaptive Thresholding," vol. 0062, no. MM, pp. 1–9, 2014.

[31] R. Scapaticci, P. Kosmas, and L. Crocco, "Wavelet-Based Regularization for Robust Microwave Imaging in Medical Applications," *IEEE Trans. Biomed. Eng.*, vol. 62, no. 4, pp. 1195–1202, 2015.

[32] M. Ambrosanio, P. Kosmas, S. Member, V. Pascazio, and S. Member, "A Multithreshold Iterative DBIM-Based Algorithm for the Imaging of

Heterogeneous Breast Tissues," *IEEE Trans. Biomed. Eng.*, vol. 66, no. 2, pp. 509–520, 2019.

[33] A. Shahzad, M. O'Halloran, E. Jones, and M. Glavin, "A multistage selective weighting method for improved microwave breast tomography," *Comput. Med. Imaging Graph.*, vol. 54, pp. 6–15, 2016.

[34] J. M. Vogel, R. D. Wasnich, and P. D. Ross, "The clinical relevance of calcaneus bone mineral measurements: a review," *Bone Miner.*, vol. 5, no. 1, pp. 35–58, 1988.

[35] B. Clarke, "Normal bone anatomy and physiology.," *Clin. J. Am. Soc. Nephrol.*, vol. 3 Suppl 3, no. Suppl 3, pp. 1–16, 2008.

[36] B. L. Oliveira and M. O. Halloran, "Microwave Breast Imaging : Experimental tumour phantoms for the evaluation of new breast cancer diagnosis systems Biomedical Physics & Engineering Related content Microwave Breast Imaging : experimental tumour phantoms for the evaluation of new breast can," no. January, 2018.

[37] S. Salahuddin, E. Porter, F. Krewer, and M. O' Halloran, "Optimised analytical models of the dielectric properties of biological tissue," *Med. Eng. Phys.*, vol. 43, pp. 103–111, 2017.

[38] C. Gabriel and A. Peyman, "Dielectric measurement: Error analysis and assessment of uncertainty," *Phys. Med. Biol.*, vol. 51, no. 23, pp. 6033–6046, 2006.

[39] J. D. Shea, P. Kosmas, S. C. Hagness, and B. D. Van Veen, "Three-dimensional microwave imaging of realistic numerical breast phantoms via a multiple-frequency inverse scattering technique," *Med. Phys.*, vol. 37, no. 8, pp. 4210–4226, 2010.

[40] Y. M. Wang, "Reconstruction of Two-Dimensional Permittivity Distribution Using the Distorted Born Iterative Method," vol. 9, no. 2, 1990.

[41] R. Scapaticci, M. Bjelogrlic, J. A. T. Vasquez, F. Vipiana, M. Mattes, and L. Crocco, "Microwave technology for brain imaging and monitoring: physical foundations, potential and limitations," in *Emerging Electromagnetic Technologies for Brain Diseases Diagnostics, Monitoring and Therapy*, Springer, 2018, pp. 7–35.

[42] A. Fhager, S. K. Padhi, and J. Howard, "3D image reconstruction in microwave

tomography using an efficient FDTD model," *IEEE Antennas Wirel. Propag. Lett.*, vol. 8, pp. 1353–1356, 2009.

[43] R. Ciocan and H. Jiang, "Model-based microwave image reconstruction: Simulations and experiments," *Med. Phys.*, vol. 31, no. 12, pp. 3231–3241, 2004.

[44] R. Scapaticci, P. Kosmas, and S. Member, "Wavelet-Based Regularization for Robust Microwave Imaging in Medical Applications," *IEEE Trans. Biomed. Eng.*, vol. 62, no. 4, pp. 1195–1202, 2015.

[45] C. Gabriel *et al.*, "The dielectric properties of biological tissues : III . Parametric models for the dielectric spectrum of tissues The dielectric properties of biological tissues : III . Parametric models for the dielectric spectrum of tissues," 1996.

[46] B. McDermott *et al.*, "Anatomically and dielectrically realistic microwave head phantom with circulation and reconfigurable lesions," *Prog. Electromagn. Res. B*, vol. 78, pp. 47–60, 2017.

[47] B. L. Oliveira, D. O'Loughlin, M. O'Halloran, E. Porter, M. Glavin, and E. Jones, "Microwave Breast Imaging: Experimental tumour phantoms for the evaluation of new breast cancer diagnosis systems," *Biomed. Phys. Eng. Express*, vol. 4, no. 2, p. 25036, 2018.

Chapter 8

Conclusions and Future Work

This chapter summarises the main conclusions and findings of this thesis. The motivation and main findings are summarised in Section 8.1. The future work to further extend and improve the findings of the thesis are discussed in Section 8.2.

8.1 Summary of Main Conclusions

Osteoporosis is one of the major bone diseases that results due to the loss of minerals from bones and hence leads to bone fragility and fractures [1]. Osteoporosis causes more than 8.9 million fractures annually worldwide, resulting in an osteoporotic fracture every 3 seconds [2]. Currently, clinical practices employ X-ray based technologies such as DXA and QCT [3], which have limitations due to expensive equipment, cost of the test, and most importantly potential long-term health risks associated with X-ray doses [4]. MWI has been proposed as a safe alternative to existing imaging technologies for diagnosing and monitoring various diseases such as breast cancer detection and diagnosing brain stroke [4]. The potential of MWI to measure *in vivo* dielectric properties of biological tissue has been demonstrated in several studies. As osteoporosis results in demineralisation of bone and this demineralisation may result in a change in dielectric properties of bones, therefore, MWI can be employed to diagnose osteoporosis. MWI can be comfortable and low-cost, addressing some of the limitations of the imaging modalities used in current clinical practices. MWI has the potential to be repeatable and less operator-dependent than DXA and QCT [1].

Despite the promising initial evidence that MWI can be potentially used for osteoporosis diagnosis, no clinical study has been performed for bone imaging. Further, the literature research suggests that no dedicated MWI system exists to measure *in vivo* dielectric properties of human bone in the microwave frequency range. Therefore, to utilise the potential of MWI for bone health monitoring, this thesis has completed foundational work for the progress of microwave bone imaging technology towards clinical evaluation. To achieve this, firstly, a literature review was conducted. This review sought to establish whether the dielectric properties of bones are influenced by mineralisation levels of bone, and secondly, to determine whether there

is any dielectric contrast between healthy and diseased human trabecular bones. The review suggested that variations do exist in the dielectric properties of bone reported across different studies. The variations were mainly because the studies differ in terms of sources of bone samples, measurement frequency ranges, and measurement protocols. Moreover, some of the previous studies reported the dielectric properties of bones are influenced by BMD but the analysis and comparison of these studies performed in the review found this relationship to be inconsistent [1],[6], hence a comprehensive study is required that should report the relationship between dielectric properties and BMD over a wide frequency range and on large sample size [6],[8],[9]. Further, it was found that none of the studies compared the dielectric properties of healthy and diseased human bones.

To this end, this thesis sought to characterise the dielectric properties of osteoporotic and osteoarthritis human trabecular bones. The availability of healthy human trabecular bones for *ex vivo* dielectric characterisation is scarce, therefore, this thesis has used osteoarthritis bones as a surrogate to healthy bone samples because osteoarthritis patients have compact and dense trabecular bone microarchitecture compared to osteoporotic patients [1],[6],[7],[8]. The findings of this study showed that there exists a significant dielectric contrast between osteoporotic and osteoarthritis bones. However, regression analysis between bone dielectric properties and BVF suggested a weak positive relationship between BVF and relative permittivity. The weak linear regression model suggested that BVF alone cannot predict the dielectric properties. As, studies have found that the dielectric properties are influenced by mineralization and are also expected to be influenced by other bone constituents, including organic matrix, water, and lipids which could not be measured during *ex vivo* dielectric characterization of bone samples. Nevertheless, this study was the first to measure diseased bone tissue and data from this study could be used to investigate the feasibility of MWI.

Once the dielectric contrast between osteoporotic and osteoarthritis bones was established, an initial feasibility study was performed to determine an optimum frequency band, the dielectric properties of tissues present in the human heel, and electric field (E-field) penetration in trabecular bone. The parameters (optimum frequency band, matching medium, and numerical modelling of bone) found in this study served as design inputs into the development of a MWI prototype for monitoring osteoporosis. To assess and determine the spatial distribution of dielectric properties

of the numerical and experimental bone phantoms, a MWT-based imaging algorithm was developed. Firstly, the robustness of the MWT algorithm was evaluated for diverse numerical bone phantoms under different noise levels. The numerical bone phantoms were developed based on the dielectric properties of osteoporotic and osteoarthritis bones reported in this thesis. The simulation results showed that osteoporotic and osteoarthritis bones can be differentiated based on the reconstructed dielectric properties even for low values of the signal-to-noise ratio (SNR). While this study has considered only simplified 2-D numerical bone phantoms, these were the appropriate initial phantoms to assess reconstruction of trabecular bone surrounded by the relatively low permittivity cortical bone using MWT. The anthropomorphic numerical phantoms with additional tissue layers such as skin, muscle, and fat could be considered next. The consideration of additional tissue layers in the imaging scenario may pose challenges during the inversion of the EM inverse scattering problem. The imaging challenge can be simplified by considering a-priori information during the reconstruction process. Further, a more proper decomposition basis should be investigated for enforcing sparsity to reduce the ill-posedness of the EM inverse scattering problem.

The other challenge was to translate imaging of numerical phantoms to imaging of experimental phantoms using a MWI prototype. The experimental system will bring the technology closer to clinical translation, therefore, a MWI prototype was developed in the next step. The findings of the evaluation of numerical bone phantoms supported the development of a MWI prototype for bone imaging, along with a PLA-based simplified two-layered calcaneus bone phantom. The MWT algorithm was evaluated with experimental data obtained from the MWI prototype. The reconstruction of dielectric properties of experimental bone phantoms showed that the developed MWT algorithm provides a robust reconstruction of diverse bone phantoms with acceptable accuracy. The results showed that the osteoporotic and osteoarthritis bones can be distinguished based on the reconstructed complex permittivity profiles. The experimental phantoms considered in this study were simplistic because they would be consistent with numerical study and would validate results from imaging of numerical phantoms. While a simplistic two-layered phantom is used, it is still the first experimental study that performed imaging of bone. Previously, studies have considered bone as a homogenous tissue, however, bone has cortical and trabecular layers with significant different dielectric properties. Therefore, this thesis aimed to

assess whether reconstruction can be achieved when the bone is modelled as a more realistic two-layered structure in contrast to the homogeneous structure and whether diseased trabecular bones can be differentiated based on the reconstruction of dielectric properties using MWT. The shape of the two-layered bone structure (cortical-trabecular) has not been preserved completely. One of the major reasons for this is the main difference between our 2-D in-house FDTD model and the experimental prototype. The 2-D in-house FDTD model does not account for the use of realistic antennas in the inversion procedure, introducing propagation and scattering errors. Future studies should consider realistic antennas for the 2-D in-house FDTD model. Future studies should also consider more realistic bone imaging scenarios that will also include skin, muscle, and fat layers. This will create an additional challenge, however, optimisation of imaging algorithms with a-priori information can address these challenges. The findings of the experimental data have shown that this two-layered 3-D printed human calcaneus bone phantom and the imaging prototype can be used as a valuable test platform for pre-clinical assessment of calcaneus bone imaging for bone health monitoring.

In summary, the *ex vivo* dielectric characterization of different diseased human trabecular bones have shown a significant dielectric contrast between osteoporotic and osteoarthritis bones. An anatomically simplified two-layered bone imaging scenario was considered for numerical and experimental evaluation. The findings of numerical and experimental evaluation have suggested that the adopted MWT imaging approach can differentiate normal and different diseased human trabecular bones based on their reconstructed complex permittivity profiles. The two-layered 3-D printed human calcaneus bone phantom, imaging prototype, and MWT imaging algorithm can be used as a valuable test platform for pre-clinical assessment of calcaneus bone imaging for bone health monitoring, hence, the proposed imaging modality provides a non-ionising and portable solution for monitoring osteoporosis.

To address the current limitations of DXA and QCT such as expensive and non-portable equipment, potential long-term health risks associated with X-ray doses, the proposed MWI technology can be used as a standalone portable solution for monitoring and diagnosing osteoporosis. The MWI device will be portable and will be easily accessed by GPs. MWI system will measure *in vivo* dielectric properties of bones and the temporal change of measured dielectric properties will be observed for each specific patient. Based on the change of dielectric properties the bone health of

each patient will be diagnosed. Due to the non-ionizing nature of this technology, frequent scans are possible which will also allow for monitoring of disease progression. However, the current research findings are based on bench tests. Therefore, future clinical studies with optimised operational systems in combination with improved tomography algorithms such as described in this thesis are needed. The studies will help accelerate the translation of MWI from the research bench to the patient bedside, where tomography-based imaging will hopefully have a real and tangible impact on patient care and outcomes.

8.2 Future Work

The work presented in this thesis can be further extended to assess the potential of the proposed MWT imaging approach to monitor the disease (osteoporosis) progression based on the reconstructed dielectric properties. The suggestions for future work in the area of MWT for monitoring osteoporosis are presented in this section.

A novel tomography-based bone imaging prototype has been developed at the Translational Medical Device Lab (TMDLab), National University of Ireland Galway [10],[11]. Moreover, a MWT imaging algorithm was developed to test both the numerical and experimental bone phantoms. The developed MWT imaging method was tested on anatomically simplified phantoms. The work presented in this thesis is a stepping stone towards the clinical evaluation of microwave bone imaging technology. To further accelerate the translation of MWI from the research bench to the patient bedside the proposed bone imaging modality in this thesis could be extended in several ways to improve the performance and robustness of the method. The recommendations related to future work are listed below:

1. Estimation of the dielectric properties of anatomically realistic bone phantoms by employing the developed MWT imaging method. The realistic bone phantoms should consider the additional layers of skin, fat, and muscle along with cortical bone and trabecular bone. To image the realistic bone phantoms with additional tissue layers, the adopted MWT imaging approach needs to be further optimised. This work will help to progress towards the measurement of *in vivo* dielectric properties of bone.
2. Investigation of the robustness of the proposed DBIM approach by considering the phantoms derived from dielectric properties of patients with different degree of osteoporosis. This analysis will suggest, how well the

adopted DBIM approach maintains the contrast of reconstructed dielectric properties of bone phantoms.

3. Designing of more optimal imaging prototype by considering optimal antenna locations and spacing. Some preliminary numerical studies have suggested that irregular antenna locations may improve the image quality by reducing the amount of redundant information in the collected scan [12],[13]. Hence, more work is needed to determine the factors influencing the optimal antenna locations and the effects of the antenna locations and numbers of channels on the image quality.
4. The future work may also include *in vivo* clinical evaluation of the developed MWI prototype along with the proposed MWT technique for the reconstruction of dielectric properties of bone from patient data. This may include, considering patients from different age groups and suffering from a different degree of osteoporosis. The validation of reconstructed images can be performed using DXA scans.
5. Improvement of the current clinical prototype, the future prototype should consider the regulations and safety standards from the very start of the development process. As, the current clinical prototype has not been verified and compared using any standard phantom, therefore, like other modalities, a realistic standard phantom and standard evaluation criteria to evaluate the fidelity of images and signals is required for MWT.
6. The quality assurance of the MWI prototype also needs to be considered before the clinical investigation to be performed at large. For example, in MRI, standard phantoms have been developed in conjunction with standard evaluation criteria, which allow the fidelity of images and signals to be verified [13].
7. The role of MWI for monitoring bone health in the current patient pathway also needs to be considered. Health Technology Assessments (HTAs) are increasingly used to improve decision making by regulatory and reimbursement bodies and will be required for tomography-based imaging before clinical adoption.
8. Future prototypes should also adhere to the existing standardised framework for image display, 3-D visualisation, and image presentation so that the resultant clinical data should be acceptable by the regulatory authorities.

Further, it will help the clinicians to easily understand the scan results and hence to adopt the proposed imaging modality.

The future clinical studies with optimised imaging prototypes and coupled with MWT-based imaging method as presented in this thesis, will accelerate the translation of MWI from the research bench to patient bedside, where tomographic-based imaging will hopefully have a real and tangible impact on patient care and outcomes.

8.3 References

[1] B. Amin, M. A. Elahi, A. Shahzad, E. Porter, B. McDermott, and M. O'Halloran, "Dielectric properties of bones for the monitoring of osteoporosis," *Med. Biol. Eng. Comput.*, Aug. 2018.

[2] O. Johnell and J. A. Kanis, "An estimate of the worldwide prevalence and disability associated with osteoporotic fractures," *Osteoporos. Int.*, vol. 17, no. 12, pp. 1726–1733, 2006.

[3] A. H. Golnabi, P. M. Meaney, S. Geimer, T. Zhou, and K. D. Paulsen, "Microwave tomography for bone imaging," *Proc. - Int. Symp. Biomed. Imaging*, vol. 9, pp. 956–959, 2011.

[4] E.-M. Lochmüller, R. Müller, V. Kuhn, C. A. Lill, and F. Eckstein, "Can Novel Clinical Densitometric Techniques Replace or Improve DXA in Predicting Bone Strength in Osteoporosis at the Hip and Other Skeletal Sites?," *J. Bone Miner. Res.*, vol. 18, no. 5, pp. 906–912, 2003.

[5] P. M. Meaney, T. Zhou, D. Goodwin, A. Golnabi, E. A. Attardo, and K. D. Paulsen, "Bone dielectric property variation as a function of mineralization at microwave frequencies," *J. Biomed. Imaging*, vol. 2012, p. 7, 2012.

[6] P. M. Meaney *et al.*, "Clinical microwave tomographic imaging of the calcaneus: A first-in-human case study of two subjects," *IEEE Trans. Biomed. Eng.*, vol. 59, no. 12, pp. 3304–3313, 2012.

[7] B. Amin *et al.*, "Dielectric characterization of diseased human trabecular bones at microwave frequency," *Med. Eng. Phys.*, vol. 78, 2020.

[8] B. Amin, A. Shahzad, M. O'halloran, and M. A. Elahi, "Microwave bone imaging: A preliminary investigation on numerical bone phantoms for bone health monitoring," *Sensors (Switzerland)*, vol. 20, no. 21, pp. 1–21, 2020.

[9] B. Amin *et al.*, "Dielectric characterization of diseased human trabecular bones at microwave frequency," in *2020 Medical Engineering and Physics*, 2020, pp.

1–8.

[10] B. Amin, D. Kelly, A. Shahzad, M. O'Halloran, and M. A. Elahi, "Microwave calcaneus phantom for bone imaging applications," in *2020 14th European Conference on Antennas and Propagation (EuCAP)*, 2020, pp. 1–5.

[11] B. Amin, A. Shahzad, D. Kelly, M. Ohalloran, and A. Elahi, "Anthropomorphic Calcaneus Phantom for Microwave Bone Imaging Applications," *IEEE J. Electromagn. RF Microwaves Med. Biol.*, no. c, pp. 1–9, 2020.

[12] M. A. Elahi, "Confocal Microwave Imaging and Artifact Removal Algorithms for the Early Detection of Breast Cancer," 2018.

[13] D. O'Loughlin, "Improving the Sensitivity of Radar-based Breast Imaging Algorithms in Diverse Patient Populations," 2018.